CRANFIELD UNIVERSITY

SCHOOL OF INDUSTRIAL AND MANUFACTURING SCIENCE

DEPARTMENT OF ADVANCED MATERIALS

Ph.D. THESIS

Academic years 1996-1999

JAMES MATHEW ROUTH

PREDICTION OF EXPLOSIVE DECOMPRESSION DAMAGE IN ELASTOMER SEALS

Supervisors	:	Prof Clive Bucknall	: Cranfield University
		Dr Emily Ho	: BHR Group Limited
		Dr Steve Groves	: BP Amoco

JULY 1999

ABSTRACT

Elastomer seals are widely used in industry for containing gases and liquids. Seal failure can have significant environmental and financial implications far beyond the cost of the seal itself. Explosive decompression failure can cause catastrophic cracking of an elastomer seal, causing leakage. The objective of this research was to develop a modelling methodology to predict the onset of crack damage in elastomer seals under various operational conditions.

The modelling methodology uses the finite element method to determine the performance of various elastomers under decompression conditions. The model takes into account seal and groove geometry, the non-linear behaviour of the material and the operational conditions seen by the seal. The model predicts crack initiations, locations and the orientation of the propagation. The model can also calculate the safe decompression time required for no damage in the elastomer seal by using the methodology in reverse.

To carry out the modelling methodology, certain input data are required. The data was determined by designing and constructing specialist test rigs. A permeation testing facility was developed to determine the diffusion, solubility and permeation characteristics of elastomers subject to gas pressure. The physical behaviour of the elastomers was determined through extensive uniaxial and equibiaxial tensile testing. The nature of the failure initiation points is determined by microscopic analysis of seal sections. Decompression tests were performed to validate the output of the model.

Comparison of the model outputs with the decompression tests show a good correlation between the prediction and the occurrences, orientations and positions of cracks.

The ability to predict damage in a quantitative manner was previously not available. The methodology will be developed into a knowledge-based software tool for use in industry to predict damage and develop new materials to resist explosive decompression.

ACKNOWLEDGEMENTS

I would like to acknowledge the assistance and guidance given during this research programme from the following people and institutions:

- The members of the student support panel - Prof Clive Bucknall, Dr Emily Ho and Dr Steve Groves for their advice, help and general encouragement during the duration of the project.

- Mr Phil Embury and Mr Nigel Page of James Walker and Co for supplying materials, data and assisting with the decompression testing.

- Dr Matthew Davies, Dr Emily Ho, Dr Bernard Nau and Mr Bob Flitney for interesting philosophical discussions regarding the theory of explosive decompression in elastomer seals

- BHR Group Limited for giving me guidance and the facilities to carry out the research, while gaining considerable industrial experience.

- BP Amoco, Oil States Industries Inc. and James Walker and Co Ltd for their financial support.

- My partner, Tracey Holland-Smith for putting up with me during the writing of this thesis

LIST OF CONTENTS

		PAGE
ABSTRACT		i
ACKNOWLEDGEMENTS		ii
LIST OF CONTENTS		iii
LIST OF FIGURES		viii
NOTATION		xiii
ABBREVIATIONS		xvi
1.0	**INTRODUCTION**	**1**
2.0	**LITERATURE REVIEW**	**6**
2.1	Introduction to explosive decompression failure	6
2.2	The explosive decompression failure mechanism	9
2.3	Elastomeric stress-strain behaviour and modelling	12
2.4	Gas transport properties of elastomers	22
2.5	Gas induced dilation of elastomers	30
2.6	Gas nucleation and void expansion	32
2.7	Physical property changes in operational environments	39
2.8	Gas induced fracture of elastomers	40
2.9	The effect of design and operational procedures	48
2.10	Summary of literature review	50
3.0	**SEAL DECOMPRESSION TESTING**	**53**
3.1	Introduction	53

	3.2	Test conditions	53
	3.3	The effects of test variables	55
	3.4	Decompression rig design	57
	3.5	O-ring analysis of groove fill and initial compression	62
	3.6	Seal saturation and ageing	64
	3.7	Decompression test procedure	66
	3.8	Results	67
	3.9	Discussion	81
	3.10	Conclusions	83
	3.11	Chapter summary	84
4.0	**VOID AND RIGID INCLUSION ANALYSIS**		**85**
	4.1	Introduction	85
	4.2	Sample preparation	86
	4.3	Image analysis	88
	4.4	Results and statistical analysis	90
	4.5	Discussion	95
	4.6	Conclusions	106
	4.7	Chapter summary	108
5.0	**GAS TRANSPORT TESTING**		**109**
	5.1	Introduction	109
	5.2	Theory of permeation	109
	5.3	Permeation cell design	113
	5.4	Test procedure	122
	5.5	Test results	124
	5.6	Discussion	131
	5.7	Conclusions	133
	5.8	Case study - permeation modelling of gas mixtures through elastomer membranes	135

5.9 Chapter summary 144

6.0 STATISTICAL ANALYSIS OF ELASTOMER QUALITY CONTROL DATA 146

6.1 Introduction 146

6.2 Approach 146

6.3 Results 147

6.4 Conclusions 152

7.0 EQUIBIAXIAL TENSILE TESTING OF ELASTOMER MEMBRANES 154

7.1 Introduction 154

7.2 Experimental procedure 155

7.3 Data analysis 157

7.4 Results 161

7.5 Discussion 164

7.6 Conclusions 168

7.7 Chapter summary 170

8.0 TRANSIENT GAS DIFFUSION MODEL 171

8.1 Introduction 171

8.2 The effect of instantaneous decompression on microscopic gas diffusion 171

8.3 O-ring transient gas diffusion model for linear decompressions 189

8.4 Chapter summary 204

9.0 O-RING STRESS FIELD MODELLING 205

9.1 Introduction 205

9.2 O-ring behaviour under compression and pressure 206

9.3 Non-linear finite element solution procedures 207

9.4 Solution methodology 212
9.5 Results 221
9.6 Discussion 229
9.7 Conclusions 231
9.8 Chapter summary 231

10.0 VOID INFLATION MODELLING 232
10.1 Introduction 232
10.2 The void inflation model 233
10.3 Analysis results 241
10.4 Discussion 253
10.5 Conclusions 259
10.6 Chapter summary 260

11.0 DISCUSSION 261
11.1 The new model 261
11.2 Failure aspects 263
11.3 The effects of diffusion 265
11.4 Stress field 267
11.5 Void inflation 269
11.6 Other factors affecting failure 272

12.0 CONCLUSIONS 276

13.0 FURTHER WORK 280
13.1 Material variability 280
13.2 The effect of geometry 280
13.3 Crack propagations 281
13.4 The effect of decompression cycles 281
13.5 Saturated material properties 281

REFERENCES **282**

APPENDICES **286**

A Transient and steady-state diffusion in a plane sheet

B Permeation testing facility drawings

C Decompression rig drawings

LIST OF FIGURES

		PAGE
CHAPTER 1 - INTRODUCTION		
1.1	Modelling methodology flowchart	5
CHAPTER 2 - LITERATURE REVIEW		
2.1	Compression of O-ring in a standard rectangular groove	9
2.2	Triaxial deformation of rubber	20
2.3	Volume change with time during permeation test	29
2.4	Pressure and elastomer inflation vs time	32
2.5	Gent's void inflation model	35
2.6	Crack growth rate vs tearing energy	47
CHAPTER 3 - SEAL DECOMPRESSION TESTING		
3.1	Test groove schematic	58
3.2	Decompression rig plate with O-rings and pin	59
3.3	Rig assembly schematic	60
3.4	Decompression rig in nitrogenpurge cabinet	61
3.5	Decompression rig showing instrumentation and blowdown monitor	61
3.6	Gas pump system and decompression valve	62
3.7	2 hour linear decompression profile for test 1	68
3.8	Instantaneous decompression profile for test 4	68
3.9	Crack location points	69
3.10	Examples of explosive decompression damage from test 2	75
3.11	Examples of explosive decompression damage from test 4	75
3.12	Test 1, Material B, Sample 2	76
3.13	Test 2, Material C, Sample 2	76
3.14	Test 4, Material A, Sample 1	77
3.15	Test 4, Material D, Sample 1	77
3.16	Test 6, Material A, Sample 2	78

3.17 Test 6, Material A, Sample 4 78
3.18 Test 7, Material A, Sample 1 79
3.19 Test 7, Material D, Sample 2 79
3.20 Average crack length for all test conditions 80
3.21 Average largest crack length for all test conditions 80
3.22 Average number of cracks for all test conditions 81

CHAPTER 4 - VOID AND RIGID INCLUSION ANALYSIS

4.1 O-ring cutting fixture 87
4.2 Example of a void 89
4.3 Example void and rigid inclusion distribution plot 91
4.4 Mean void and rigid inclusion size for elastomers 1-11 93
4.5 Void and rigid inclusion location map for material 2 95
4.6 Summary of evaluation analysis 105
4.7 Location map comparison between materials D and 8 107

CHAPTER 5 - GAS TRANSPORT TESTING

5.1 Diagram of permeation cell layout 115
5.2 Photograph of permeation cell 117
5.3 Permeation cell control program - graphical display of outputs 118
5.4 Permeation cell control program - numerical display of main outputs 119
5.5 Pressure increase vs time for low pressure side 125
5.6 Repeatability of permeation coefficient 128
5.7 Repeatability of diffusion coefficients 128
5.8 Repeatability of solubility coefficients 129
5.9 Effect of temperature on permeation coefficient (Q) 130
5.10 Effect of temperature on diffusion coefficient (D) 130
5.11 Effect of temperature on solubility coefficient (s) 131
5.12 Pressure vs time for gas mixture 139
5.13 Total and partial pressures vs time 143

5.14 %volume of gases on low pressure side vs time 144

CHAPTER 6 - STATISTICAL ANALYSIS OF ELASTOMER QUALITY CONTROL DATA

6.1 Frequency distribution plot of hardness for materials A and B 149

6.2 Mean hardness vs time plot for materials A and B 149

6.3 Tensile strength standard deviation vs time for materials A and B 150

6.4 Stress-strain plot for material A including variability 151

6.5 Stress-strain plot for material B including variability 151

CHAPTER 7 - EQUIBIAXIAL TENSILE TESTING OF ELASTOMER MEMBRANES

7.1 Test arrangement 155

7.2 Equibiaxial stress-strain plot for materials A, B, C and E 161

7.3 Equibiaxial stress-strain plot for material A showing repeatability 162

7.4 Photograph of equibiaxial tensile test in progress 162

7.5 Photograph of test arrangement 163

7.6 Pressure vs extension ratio for material B - sample 2 165

CHAPTER 8 - TRANSIENT GAS DIFFUSION MODEL

8.1 Instantaneous transient diffusion model methodology 176

8.2 Concentration-displacement analogy 179

8.3 Radial position vs displacement for material B 179

8.4 Concentration profile for material B 180

8.5 Concentration surfaces for void diffusion model 182

8.6 Concentration profile for material B at t=1s, 150°C, 100 bar, CH_4 183

8.7 Concentration vs time profile 184

8.8 Void pressure increase due to diffusion vs time 185

8.9 Total void pressure increase vs time 186

8.10 The effect of temperature on the rate of void pressure increase 187

8.11 Linear decompression profile 190
8.12 Concentration calculation points 192
8.13 Concentration vs time plot for points 1-5 193
8.14 Concentration differential vs time for points 1-4 194
8.15 Pressure differential vs time for points 1 to 4 195
8.16 Pressure differential vs time for points 1 to 4 (150°C) 196
8.17 Decompression time vs pressure differential at various locations (100°C) 200
8.18 Decompression time vs pressure differential at various locations (150°C) 200
8.19 Decompression time vs position 1 maximum pressure differential at 100°C and 150°C 201
8.20 Decompression time vs position 4 maximum pressure differential at 100°C and 150°C 202

CHAPTER 9 - O-RING STRESS FIELD MODELLING

9.1 O-ring general arrangements 207
9.2 O-ring stress field model methodology 215
9.3 Compressive stress field and pressure differential during depressurisation 216
9.4 O-ring analysis points and groove arrangement 218
9.5 Comparison of O-ring stress field for compression only and with expansion 222

CHAPTER 10 - VOID INFLATION MODELLING

10.1 Relationship between radius and arc length in an expanded void 234
10.2 Void inflation model definition without compressive constraints 236
10.3 Finite element void inflation model definition with compressive constraints 238
10.4 Void inflation model with compressive constraints analysis locations 238
10.5 Linear increase of compressive stress field with increase in pressure differential 240
10.6 Comparison of FE model and extrapolated prediction 241

10.7 Applied pressure vs maximum wall stress for materials A, B and C 242
10.8 Finite element model of deformed void showing direct stress contours 243
10.9 Typical graph of pressure differential vs maximum wall stress for materials A, B and C 244
10.10 Stress analysis positions 245
10.11 Growth of void at analysis location 5 - analysis number 1 246
10.12 Deformed shape of inflated void under compressive constraints 254
10.13 Expected crack pattern within a standard groove configuration 255

CHAPTER 11 - DISCUSSION

11.1 Proposed groove design with back-up rings 268
11.2 Schematic representation of crack formation owing to rigid inclusions 273
11.3 Initial model of rigid inclusion stress field 274

NOTATION

		UNITS
A	cross sectional area	m^2
C	Neo-Hookean / strain energy function coefficient	MPa
C_p	specific heat at constant pressure	kJ/kgK
c	concentration	mm^3 gas / mm^3 rubber
c_l	crack length	m
D	diffusion coefficient	$cm^2.s^{-1}$
d	diameter	m
E	elastic (Young's) modulus	$N.m^{-2}$
E_d	energy of activation	$kJ.mol^{-1}$
E_r	error measure	-
e	extrusion gap	m
e_m	maximum tensile strain	-
F	force	N
G	Gibbs free energy	$kJ.mol^{-1}$
G	shear modulus	MPa
G_c	characteristic fracture energy	$kJ.m^{-2}$
H_s	heat of solution	$J.mol^{-1}$
h	thickness	m
$I_{1,2,3}$	strain invariant (first, second, third)	-
J	mass flow rate of diffusing substance	$kg.m^{-2}$
J_{el}	elastic volume ratio	-
k_b	Boltzmann's constant	$J.K^{-1}$
k	thermal conductivity	W/mK
K	bulk modulus	MPa
l	length	m
m	mass	kg
n	number of samples	-
N	number of polymer chains per unit volume	-

p	pressure	MPa / bar
q	gas volume	m^3
Q	permeation coefficient	$cm^2.s^{-1}.atm$
r	radius	m
R	characteristic gas constant	kJ/kgK
$R_{1,2}$	radius of curvature	m
s	solubility coefficient	atm^{-1}
S_i	sink term	$[conc]mm.s^{-1}$
S_v	volumetric swell	%
S_l	linear swell	%
S'	cracking stress	MPa
t	time	s
T	absolute temperature	°K
$T_{1,2}$	tension	$N.m^{-1}$
T_{en}	tearing energy	$kJ.m^{-2}$
U	internal energy	kJ
u	displacement	m
V	volume	m^3
W	strain energy density	J
x	applied percentage compression	%
$\bar{x}$	mean value	-
α_i	Ogden material parameter	MPa
α	thermal diffusivity	$m^2.s^{-1}$
γ	surface energy	$N.m^{-1}$
δ_g	solubility parameter of gas	$(J.m^{-3})^{1/2}$
δ_l	solubility parameter of liquefied gas	$(J.m^{-3})^{1/2}$
ϵ	engineering strain	-
λ	extension ratio	-
μ_i	Ogden material parameter	MPa
μ	coefficient of friction	-

μ_{sp}	specific frictional coefficient	$kgf.mm^{-2}$
ν	Poisson's ratio	-
ρ	density	$kg.m^{-3}$
σ	direct stress	MPa
σ_s	standard deviation (statistics)	-
τ	steady-state time lag	s
ϕ	volume fraction	-
∇c	concentration gradient	-

ABBREVIATIONS

ACN	acrylonitrile
BS	British Standard
CCTV	closed circuit television
CH_4	methane
CO_2	carbon dioxide
df	degrees of freedom
ED	Explosive Decompression
EPDM	Ethylene Propylene Diene Rubber
FE	finite element
FKM	fluorocarbon based elastomer
H_2S	hydrogen sulphide
HNBR	hydrogenated nitrile rubber
HP/HT	high pressure / high temperature
IRHD	International Rubber Hardness Degrees
MS	mean square
N_2	nitrogen
NBR	nitrile based elastomer
NH_3	ammonia
PTFE	polytetrafluoroethylene
QC/QA	quality control / quality assurance
SO_2	sulphur dioxide
SS	sum of square of deviations
STP	standard temperature and pressure

CHAPTER 1 - INTRODUCTION

Elastomer seals are widely used throughout many industries to contain fluids in often highly aggressive environments. With the introduction of new materials these seals are being pushed into higher pressure and temperature regimes, often while in contact with more aggressive fluids. Failure of an elastomer seal can have significant financial, safety and environmental consequences.

The ability to understand and model explosive decompression has been required by industry for many years. The capability to predict when and how explosive decompression damage will occur enables industry to reduce emissions and considerably reduce operating costs. There are two main industries where this need has been highlighted, these are oil and gas and nuclear power generation.

The oil and gas industry has expressed concern for many years regarding the implications of explosive decompression damage in elastomer seals. The following gives two recent examples of failure and highlights the implications of seal damage.

The first example involves a major gas injection system where the initial choice of sealing material in various types of valves was inappropriate. The seals were installed in hundreds of top side valves that, when decompressed, failed immediately causing complete shutdown of the gas facility. This has cost implications due to lost production and the re-fitting of suitable elastomer seals.

The second application involves emergency shutdown valves on a North Sea gas development, where the primary cause of failure was decompression damage in large section O-rings. Emergency shutdown valves are used during rapid shutdowns of the system. Obviously, for safety reasons, the valve has to decompress as quickly as possible. However this will cause explosive decompression damage in the elastomer seals and the

system will leak and become a further hazard. Therefore, in this case, there is a need to establish the safe decompression time such that no leakage occurs and the system can be decompressed safely.

The nuclear power generation industry operates a completely leak free policy for obvious reasons. Although the pressures seen in the coolant system of a nuclear reactor are much lower than in the oil and gas industry, the gas (carbon dioxide) affects the physical properties of the elastomer, therefore causing premature failure if the system is rapidly decompressed.

This research programme was carried out in direct response to the needs of the oil and gas industry, hence the emphasis on methane as the pressurising medium. The elastomer seal manufacturers also have an interest in the research as they constantly strive to improve the performance of their materials to resist explosive decompression damage. Therefore, this research has been sponsored by BP Amoco, James Walker and Co. Ltd and Oil States Industries Inc.

When the high pressure system containing the elastomer seal is decompressed, internal cracking and blistering can form within the seal due to the rapid expansion of absorbed gas. It is therefore critical that the conditions under which cracking initiates can be predicted to prevent loss of fluid through seal failure.

Leakage from elastomer seals can cause many problems, in terms of both financial loss and environmental damage. With new European legislation regarding emissions from sealed components becoming ever more stringent, the need for predicting damage and hence leakage due to decompression is paramount.

Previous work in this field has identified many parameters that affect explosive decompression failure, the primary factors being solubility of gas within the elastomer, rate of diffusion of gas and the elastomer physical properties. This work by many authors

produced some qualitative models based on experimental observations.

However the studies were carried out on elastomers that would not normally be used for the types of application previously mentioned and under unrealistic operational conditions. Many studies were carried out on unfilled transparent elastomers to enable observations to be easily carried out. This method was suitable for determining the fundamental mechanisms of explosive decompression failure, however, most materials used today for explosive decompression applications are highly filled and hence extremely hard elastomers. The previous studies were primarily carried out at ambient or low temperatures and at low pressures. The operational conditions encountered in oil and gas production can be approximately 500-1000 bar and 100-250°C while in contact with an aggressive fluid.

This research shows that although the previously identified factors are important to explosive decompression failure, there are other factors that must be taken into account to produce a quantitative model based on real materials under real operational conditions.

This study was therefore developed to address the issues of modelling actual materials used for this type of application to give a quantitative approach to the prediction of failure. Manufacturers of elastomer seals produce 'explosive decompression resistant' materials said to be resistant to decompression. The level of this resistance depends on the application and although they show more resistance to damage than other materials, they are still subject to failure under the extreme conditions commonly encountered in industry.

The model developed uses a combination of experimental data obtained on permeation rates, physical strength and presence of microvoids and rigid inclusions, and finite element modelling techniques to determine the effects of different operational conditions, materials, seal sizes, groove designs and decompression times.

The thesis is structured such that the testing used to generate data for the model is presented initially, followed by details of the modelling methodology. The void and rigid inclusion analysis provides data regarding the shape, size and density of defects found in elastomer seals. The decompression testing programme is used to determine the performance of the selected materials and for validation of the model. The gas transport testing chapter provides details of the permeation testing carried out to provide the pressure differential formed in elastomers during decompression. Data regarding the variability of properties and the equibiaxial tensile strength of the materials are determined in Chapters 6 and 7.

The modelling methodology can be summarised in Figure 1.1 which shows the flowchart of the interacting parameters that are considered in the model. The transient gas diffusion model is used to calculate the pressure differentials formed during various decompression regimes. The O-ring stress field model determines the distribution of stress in seal sections under differing operational conditions. The results of these two models are used as inputs to the void inflation model, which calculates the maximum void wall stress experienced by the seal at various locations in the cross-section. This can be compared with the strength of the material to determine whether fracture initiation will occur.

A further objective of this research is to translate the model into a working tool that a materials scientist or engineer could use in practice. This will involve transferring the technology developed through the research into a software interface that can be easily used and understood to predict under what conditions failure will occur and to provide data on safe decompression times.

Industry can then use this software to predict failure and therefore schedule maintenance programmes and establish safe working practices. This will introduce significant cost savings based on improved efficiency and reduced emissions to the environment.

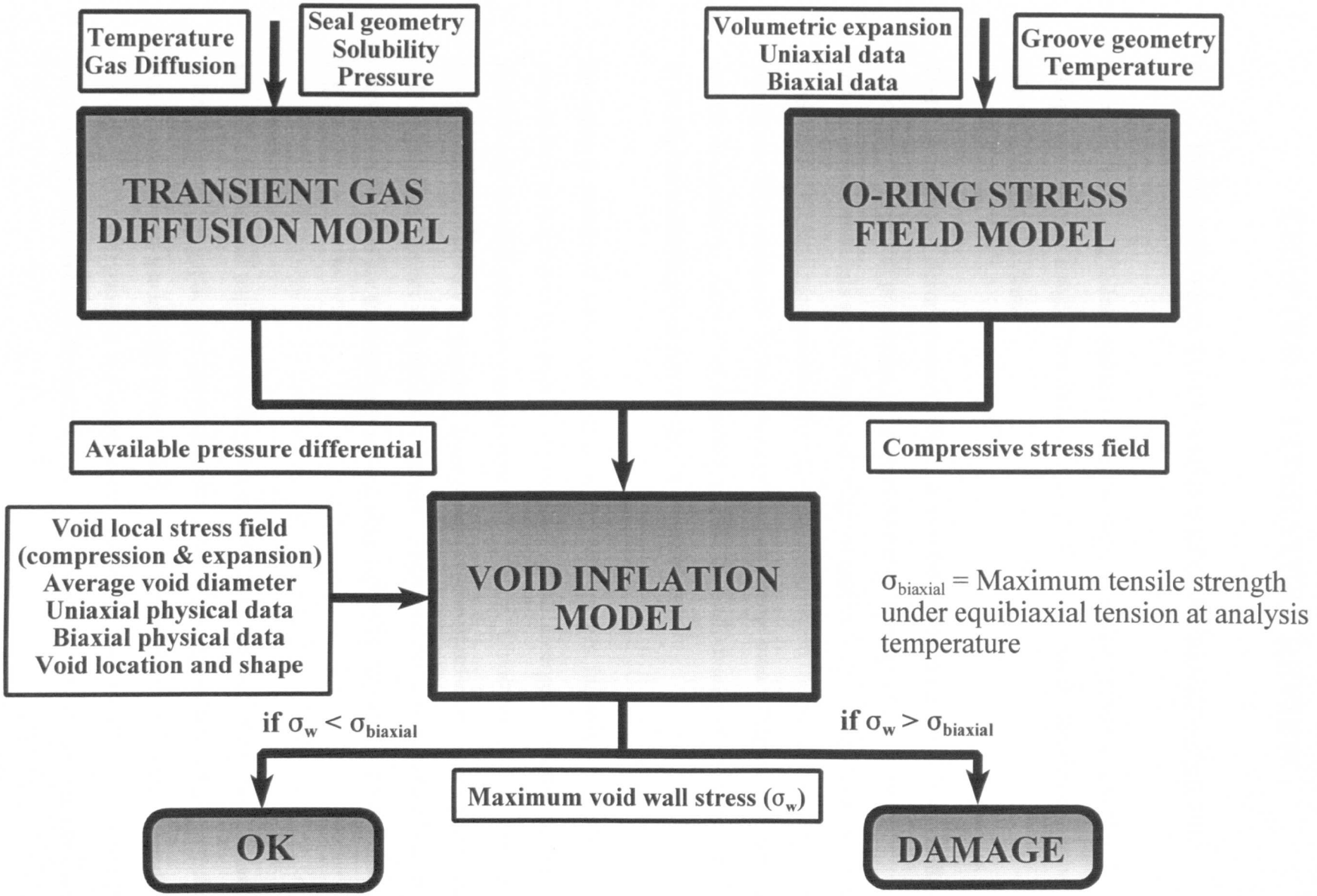

Figure 1.1 - Modelling Methodology Flowchart

CHAPTER 2 - LITERATURE REVIEW

2.1 INTRODUCTION TO EXPLOSIVE DECOMPRESSION FAILURE

An elastomer O-ring failure owing to explosive decompression (ED) in a critical piece of equipment can have a significant impact on the performance, safety and financial aspects of an engineering system.

Therefore explosive decompression failure can cost the oil and gas industry many millions of pounds through lost production and system downtime if the problem is not understood and the correct materials are not specified for given applications. The problem is further compounded by increased pressure from European legislation for the control of gaseous emissions. With increased emphasis being placed on remote monitoring and inaccessible downhole conditions, the need to accurately predict the performance of an elastomer seal in an explosive decompression environment is paramount.

Emergency shutdown valve seals used in the oil and gas industry are particularly susceptible to explosive decompression damage. If an emergency occurs, the valve immediately vents all pressure in the gas processing system. Obviously, for safety reasons, this must occur as rapidly as possible. If the system is decompressed too quickly, the seals will fail and the system will become a hazard. Therefore the need to predict the safe decompression time for these systems is becoming ever more urgent in order to ensure a safe shutdown.

The main problem of explosive decompression exists in industries where there are large fluctuations in the applied gas pressure, particularly in process valves and pig launcher valves in the oil and gas industry [Cox, 1985]. Another primary area of concern regarding explosive decompression is the compressed gas processing industry. The rapidly fluctuating pressure seen by elastomer seals in compressors is considerable and can cause

blistering and crack formation [Shade and Legg, 1988].

The nuclear power generation industry also has problems with explosive decompression. The nuclear industry requires that all seals are leak free in order to prevent any unwanted leakage of radioactive material to the atmosphere. Some limited studies have been carried out on elastomer seals used in 40 bar carbon dioxide, which are used in reactor coolant systems. These have mainly concentrated on the reduction of physical properties at elevated temperature whilst soaked with 40 bar carbon dioxide [Davies, 1997].

The majority of the current literature studies pressures at which explosive decompression is not a practical problem (less than 1500 psi), and often with materials that are not formulated or recommended for explosive decompression applications; and often without considering the effect of housing constraints. If explosive decompression failure is to be predicted, the solution must be made with materials that are actually used in explosive decompression sensitive environments and at realistic pressures, temperatures and gas media.

If industry is able to predict the onset of failure owing to explosive decompression, reduced costs, increased efficiency and safer working environments will be achieved.

2.1.1 The Characteristics of an elastomer O-ring under high pressure

In order to understand how a seal performs during explosive decompression failure, it is necessary to demonstrate how a seal operates as an effective barrier against fluid pressure. There are many types of seal and housing designs available, but for simplicity we will consider the case of a standard O-ring seal with a rectangular groove.

When a seal is installed into a groove for sealing initial pressurisation, it is usually positioned such that the outer diameter of the seal is just in contact with the outer diameter of the groove (see Figure 2.1). The counterface is then brought down such that the seal

is under initial compression. This is often termed the 'assembly compression' and is usually between 5 and 25% of the seal section diameter. The initial compression applies an equal force between the top and bottom counterfaces and the relatively soft seal material conforms to the surface finish of the metallic surfaces. Owing to the near incompressibility of the elastomer, the outer diameter of the seal contacts the outer diameter of the housing. The conformity between the elastomer and the metallic counterfaces eliminates any possible leakage path from one side of the seal to the other.

When high pressure is applied to the inner diameter, the seal is pushed towards the outer diameter of the housing. The pressure applied to the seal will be added to the stress field that already exists in the seal due to the initial compression and will be transmitted to the counterfaces due to the incompressibility assumption. Therefore the contact stress that exists at the counterfaces is always higher than the pressure applied.

Tolerances in the housing design and natural displacement of the counterfaces during pressurisation will form a clearance gap on the low pressure side of the seal. If this gap is very small, the material will not extrude into the gap. If the gap is larger, the seal will extrude into the gap and can cause cracking and seal failure. The pressure, temperature, clearance gap and seal material will determine the extent of damage due to extrusion. Extrusion can occur from surprisingly small clearance gaps. However, extrusion damage can be limited by the use of anti-extrusion rings.

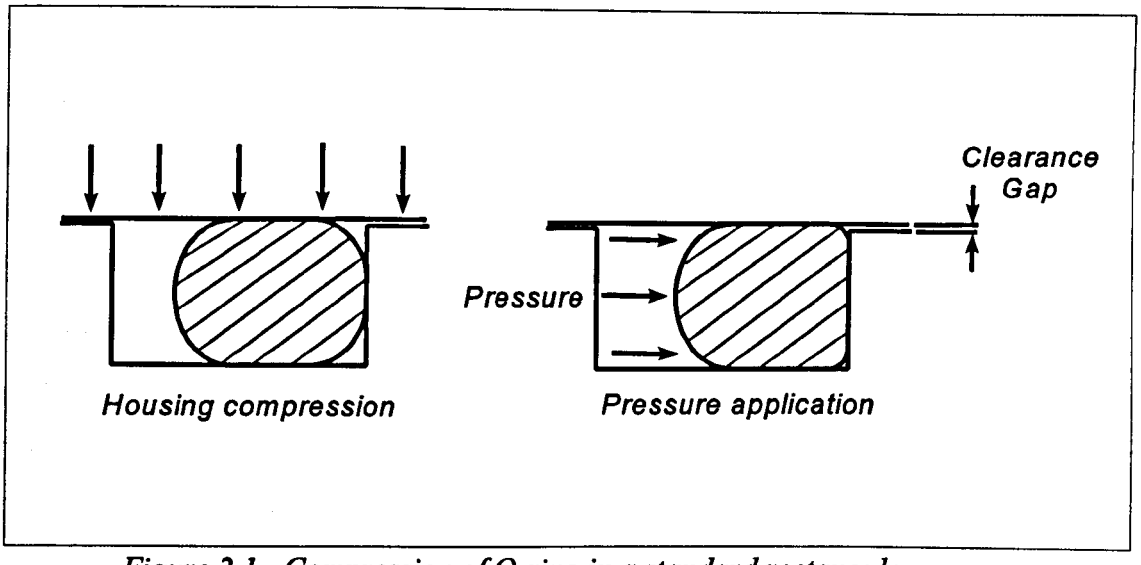

Figure 2.1 - Compression of O-ring in a standard rectangular groove

The effect of fluid contact with the seal can be either physical or chemical. The uptake of fluid can significantly affect the physical properties of the elastomer and cause failure due to compression set, stress relaxation and hardening in the long term.

2.2 THE EXPLOSIVE DECOMPRESSION FAILURE MECHANISM

Damage in elastomers due to decompression takes many forms including cracks, blisters, gross deformation and in some cases catastrophic fragmentation. Examination of failure shows that the splits formed are perpendicular to the pressure gradient [Cox, 1985].

The elastomer absorbs significant quantities of gas in high pressure environments and eventually reaches equilibrium saturation. The gas has two main effects; the first is gas dissolution within the matrix that causes plasticisation, increasing the polymer chain mobility and increasing free volume. The second gas effect is matrix compression due to the applied hydrostatic pressure, which has the opposite effect of the gas dissolution. The net result of these two effects is a gas-polymer solution with unique mechanical and thermal properties [Briscoe, Savvas & Kelly 1994].

Upon decompression, the gas desorbs first from the surface of the elastomer creating steep concentration gradients and initiating diffusion from the interior to the surface. The mechanical and physical properties of the matrix, which are highly concentration dependent, now vary across the elastomer section. There is also a significant temperature gradient developed across the elastomer section due to the adiabatic cooling of the ambient gas upon depressurisation. The gradient also has a significant effect on the gas diffusion profiles and the mechanical properties [Briscoe, Savvas & Kelly, 1994]. This has been observed in laboratory experiments, but in reality the relative conductivity of the surrounding metal work would rapidly heat the elastomer after decompression. Cooling is only likely to occur at the seal surface as the seal is effectively an insulator in comparison with the metal counterfaces.

Upon release of the hydrostatic pressure a pressure differential is formed between the interior and ambient which induces a non-uniform stress condition on the polymer. This stress state, is however, inhibited by the seal housing. The gas transport between the polymer and ambient creates concentration and fugacity profiles which are dependent on the gas diffusion coefficient, concentration, pressure and temperature. The concentration profiles can cause volumetric strain (swelling) which is not uniform across the section, decreasing from interior to the surface. This causes a non-uniform strain field that can be directly related to the overall stress field [Briscoe & Liatsis, 1989].

All of these effects create a stress field within the elastomer structure upon decompression, which is responsible for the initiation and propagation of failure. Each individual process must be fully understood and an estimate of their contribution to the stress field determined [Briscoe, Savvas & Kelly, 1994].

The elastic strain stored in the polymer matrix during compression is then released and the elastomer expands. In practice, the elastomeric matrix cannot accommodate very large strains under a negative hydrostatic pressure. This causes cavitations that grow in an unstable manner when a critical pressure difference (strain) is established. The cavities

inflate during this process against the elastic forces of the matrix. As more cavities are formed, some of which will evolve into cracks, so that larger surface areas become available for gas diffusion. The gas that inflates the bubbles upon depressurisation will diffuse outwards from the cavities to the ambient. Therefore, the cavities are expected to expand and then collapse as the gas contained is depleted [Briscoe, Savvas and Kelly, 1994]. Expansion occurs when the state of equilibrium that existed in the saturated seal is lost.

Gent and Tompkins (1969) proposed that latent bubbles pre-exist in the elastomer in the form of submicroscopic voids, i.e. air trapped during processing or badly wetted particles of dust or dirt. If an inflating cavity reaches the surface, or the bubble wall attains the maximum extensibility of the elastomer, a crack will be formed and begin to propagate [Lindsey, 1967]. In practice, neighbouring bubbles interact with each other and sometimes coalesce while 'satellite' bubbles may be formed in the vicinity of existing growing bubbles due to the local stress field [Gent & Tompkins, 1969].

In filled elastomers, the failure process is much more complex and there are two modes of failure, cohesive and interfacial. Cohesive failure occurs in the matrix due to triaxial tension which is caused by the volumetric expansion of the elastomer [Gent & Park, 1984]. The filler particles behave as stress raisers and increase the local stress field, hence inducing premature cracking. Interfacial failure occurs when the local stress developed at the matrix-filler interface is large enough to separate the polymer from the surface [Gent, 1980]. The diffusing gas is then drawn into these cavities which then expand upon depressurisation.

The crack formations can result in reduced contact stress between the seal and the counterfaces or complete destruction of the seal, both of which can cause leakage.

2.3 ELASTOMERIC STRESS-STRAIN BEHAVIOUR AND MODELLING

It is widely stated that only fluorocarbon based elastomeric materials with a high-structure black and cured to a high cross link density have even reasonable resistance to explosive decompression failure in hydrocarbon fluids [Cox, 1985].

Most elastomeric seals demonstrate a loss of hardness following decompression, usually around 15 IRHD (International Rubber Hardness Degrees). The resistance of an elastomer to ED damage is improved by filling with a reinforcing black of optimum particle size and by curing to a high crosslink density. This however reduces the maximum extensibility of the elastomer [Cox, 1985].

Fillers can greatly affect the explosive decompression resistance of an elastomer. Elastomers are filled with particulate materials to obtain a number of desirable physical and mechanical properties. They generally increase the stiffness of the rubber matrix and have a considerable effect on sorption. The effect is largely dependent on the quality of the matrix-filler interface. A high quality interface will greatly reduce sorption and vice-versa, although this is less important in explosive decompression resistant materials as they are compounded to give a high quality bond [Melikhova, Reitlinger & Kuzina, 1959].

The expansion of filled elastomers is generally lower than that of the unfilled elastomer, but again this depends on the quality of the filler-matrix interface. The transient volume change during decompression depends on the elastomer stiffness and the gas pressure difference developed between the bubbles and the ambient [Hepburn and Reynolds, 1979].

Variations in the strength of interfacial adhesion between the filler particles and the elastomer matrix have been shown to affect not only the magnitude of the critical applied stress at which failure initiates, but also the nature of the failure itself. When a rigid sphere is weakly bonded to the surrounding matrix, a detachment is observed at the poles when the volumetric expansion is applied. If two inclusions are in close proximity, then a cavity

will appear midway between them, lying in the direction of applied tension [Cho & Gent, 1988].

In filled elastomers, the stresses in the matrix are transferred to the filler in two ways: -

- Shear stress at the matrix-filler interface
- Components of the tensile stresses normal to the interface

Therefore, the filler particles act as stress centres. Under an applied triaxial stress, such as that formed under gross volumetric expansion, weakly bonded fillers become detached from the elastomeric matrix and readily form vacuoles. The vacuoles can act as sinks for gas transport and inflate to cause failure. Particles that remain bonded may also act as stress raisers, but do not become nuclei for crack initiation. During the decompression process, failure appears to take place near the rigid inclusions due to the increased levels of tensile and shear stress in those areas [Briscoe & Zakaria, 1990(c)].

The presence of filler particles was found to increase the number of cracks within a specimen, but decrease the average length of crack [Briscoe & Zakaria, 1990(c)]. However, the opposite has been observed in extensive O-ring seal testing [Ho, Nau, Stevenson, Campion, Derham & Morgan, 1989-1997]. Crack formation is dependent upon the type of interface used between the matrix and the filler. Stronger interfaces produce crack patterns with a greater range of orientations, and therefore arrest crack growth [Briscoe & Zakaria, 1990(e)].

During depressurisation, at the vacuoles formed, there are new surfaces being created in the matrix that facilitate the rapid desorption of absorbed gas and relieves the local stress field. This therefore prevents unstable crack growth and reduces the amount of decompression damage [Briscoe & Zakaria, 1990(a)].

2.3.1 Modelling of the explosive decompression failure process

The stress field generated must be modelled in order to determine the position of failure initiation and the subsequent rupture propagation [Briscoe, Savvas & Kelly, 1994]. The total stress condition can be found by adding the individual stress fields acting on the elastomer during decompression, these include: -

- Negative hydrostatic pressure
- Volumetric strain gradient
- Thermal stresses
- Stresses induced by the inhomogeneity of the mechanical properties

In order to model the negative hydrostatic pressure, a knowledge of the gas pressure (fugacity) profile developed across an elastomeric component during decompression is required. This requires a suitable gas transport model which should account for the effects of gas plasticisation and compression of the polymer matrix on diffusion by introducing a concentration and pressure dependent diffusivity.

The desorption model may also account for the effect of gross volumetric strain observed in practice, or for the effect of ambient gas cooling, by estimating the temperature profiles and the gradients in the physical properties of the system (gas solubility, diffusion etc) they induce.

Conversion of the concentration profiles, obtained from such a gas transport model, to the required gas pressure profiles is difficult. A convenient, but approximate method of achieving this is by using equilibrium pressure-concentration experimental data. The prediction of the volumetric strain gradient induced stress field is more problematic as this requires the developed volumetric strain profile and the value of the elastic modulus in the high pressure gas. A simple approach for this is to convert the gas concentration profiles,

to volume, using equilibrium pressure-volume experimental data [Briscoe, Savvas & Kelly, 1994].

To predict failure, the critical conditions for failure initiation and the location where this occurs needs to be determined. Prediction of the subsequent failure processes has not been achieved owing to the lack of materials property data in the swelled state [Briscoe, Savvas & Kelly, 1994]. Some material's property data have been made available recently from the work of Davies (1997), in which the properties of various elastomers were measured when saturated in 40 bar carbon dioxide at up to 200°C.

2.3.2 Elastomer material models

To analyse the behaviour of any elastomeric material, its deformation characteristics and its strain energy distributions are required. This can be achieved through the statistical theory of rubber elasticity [Treloar, 1975]. The statistical theory calculates the entropy associated with the probable separation of the ends of the entwined polymer chains. This is used to develop the force-deformation behaviour in terms of work done to displace the ends of the chains [Treloar, 1975]. It gives an expression for strain energy density, W (elastic strain energy per unit volume) and predicts a linear dependence of strain energy density on absolute temperature T,

$$W = \frac{Nk_bT}{2}(\lambda_1^2 + \lambda_2^2 + \lambda_3^2 - 3) \qquad (2.3.1)$$

where N is the number of chains per unit volume, k_b is Boltzmann's constant and λ_i is the extension ratio. The extension ratio is the ratio of strained to unstrained dimension, i.e. $L/Lo = (1+\varepsilon)$.

Four main approaches are available for modelling the behaviour of elastomeric materials [Leefe, 1993];

Neo-Hookean model

- Mooney-Rivlin model
- Higher order models
- Ogden model

2.3.2.1 Neo-Hookean Model

This uses the single Neo-Hookean constant C_{10} and defines the strain energy density as,

$$W = C_{10}(I_1 - 3) \qquad (2.3.2)$$

where I_1 is the first invariant of the right Cauchy-Green strain tensor and is given by;

$$I_1 = \lambda_1^2 + \lambda_2^2 + \lambda_3^2 \qquad (2.3.3)$$

2.3.2.2 Mooney-Rivlin Model

The strain energy density W is given by;

$$W = C_{10}(I_1 - 3) + C_{01}(I_2 - 3) \qquad (2.3.4)$$

where I_2 is the second strain invariant: -

$$I_2 = \lambda_1^2\lambda_2^2 + \lambda_1^2\lambda_3^2 + \lambda_2^2\lambda_3^2 \qquad (2.3.5)$$

The third strain invariant I_3 is given by equation (2.3.6)

$$I_3 = \lambda_1^2\ \lambda_2^2\ \lambda_3^2 \qquad (2.3.6)$$

Since the volume of elastomers remain virtually constant during compression, I_3 can often be equated to unity. This is because volumetric strains of the order of 0.01 are much smaller than linear strains (which can reach λ=10). The reason for this contrast is that the bulk modulus is typically 2000 MPa for rubbers, whereas the shear modulus is below 1.0

MPa in many rubbers.

2.3.2.3 Higher Order Models

These are models providing further generalisation involving powers of the first and second strain invariants.

$$W = C_{10}(I_1-3)+C_{01}(I_2-3)+C_{20}(I_1-3)^2+C_{11}(I_1-3)(I_2-3)+C_{02}(I_2-3)^2+.....+C_{ij}(I_1-3)^i(I_2-3) \quad (2.3.7)$$

Some finite element packages allow models with up to the first five constants for the definition of the material behaviour model.

2.3.2.4 Ogden model

The Ogden model is defined as follows: -

$$W = \sum_{n=1}^{N} \frac{2\mu_n}{\alpha_n} (\overline{\lambda_1}^{\alpha_i} + \overline{\lambda_2}^{\alpha_i} + \overline{\lambda_3}^{\alpha_i} - 3) + \sum_{i=1}^{N} \frac{1}{D_i}(J^{el}-1)^{2i} \quad (2.3.8)$$

where λ_i are the deviatoric principal stretches: -

$$\overline{\lambda_i} = J_{el}^{-\frac{1}{3}}\lambda_i \quad (2.3.9)$$

J_{el} is the elastic volume ratio, λ_i are the principal stretches; N is a material parameter; and μ_i, α_i, and D are the temperature-dependent material parameters. The Ogden model usually provides a more accurate and stable fit for the material data for finite element modelling.

These strain energy functions are effectively curve-fits and give a reasonable representation of the stress-strain condition over a typical 100% range of strain. However, in practical strain conditions, particularly in explosive decompression, this value is

exceeded and the accuracy then depends on how well the model extrapolates the data [Daley & Mays, 1997]. Therefore testing purely in tension can be a dangerous exercise as the results obtained from the model will be very different in compression and vice-versa.

It is important to ensure that the deformation mode being modelled is accurately replicated during the test data acquisition stage for elastomeric materials [ABAQUS Users Manual, Version 5.6]. If only tension data are measured and used to calculate a strain energy function or curve fit using finite element software, and the actual loading on the component is primarily compression, the results will be inaccurate. Therefore, the measured deformations must be the same as the actual deformations used in the analysis.

Four main physical tests are carried out on rubbers to determine the material's constants necessary for the determination of the strain energy function or for curve fitting algorithms in finite element software. These tests can be carried out in tension and compression and are as follows: -

- Uniaxial
- Equibiaxial
- Volumetric
- Planar (pure shear)

There are some equivalences between the various test types. These are summarised as: -

- Uniaxial tension ⇔ Equibiaxial compression
- Uniaxial compression⇔ Equibiaxial tension
- Planar tension ⇔ Planar compression

The substitutions used for each of the load cases are as follows: -

- Uniaxial : $\lambda_1 = \lambda_u$ and $\lambda_2 = \lambda_3 = 1 / \sqrt{\lambda_u}$
- Equibiaxial : $\lambda_1 = \lambda_2 = \lambda_B$ and $\lambda_3 = 1 / \lambda_B^2$
- Planar : $\lambda_1 = \lambda_S$, $\lambda_2 = 1$ and $\lambda_3 = 1 / \lambda_S$

If these substitutions are made into the general form of the strain energy function (W) and this is then differentiated with respect to λ this will give the nominal stress for the given applied strain condition defined by the extension ratios λ.

2.3.2.5 Choice of Material Model

The following is a reasonable approach to choosing the correct material model for the type of loading and level of accuracy required [Leefe, 1993]

1. Obtain a crude estimate of strain using a linear model
2. If indicated strain is <10% then use linear model
3. Use Neo-Hookean model if compressive, or if tensile with <100% strain
4. Use Mooney-Rivlin or higher order model if the loading is tensile and >100% strain

2.3.2.6 The Edwards and Vilgis Theory

Edwards and Vilgis [1986] developed a complete elastomer material model by considering the consequences of molecular entanglements that form further elastic free energy. However, the model is extremely complex and requires parameters that are very difficult to obtain practically. Therefore, the model will not be studied in any detail.

2.3.3 Elastomer stress-strain relationships

If a cuboidal block is considered with three forces acting in each of the principal directions, the following relationships can be derived [Leefe, 1993]. If the forces F_i are allowed to

increase the side lengths by δ_i, additional strain energy $\delta W.l_1l_2l_3$ is stored because of the work done by the forces moving through their displacements.

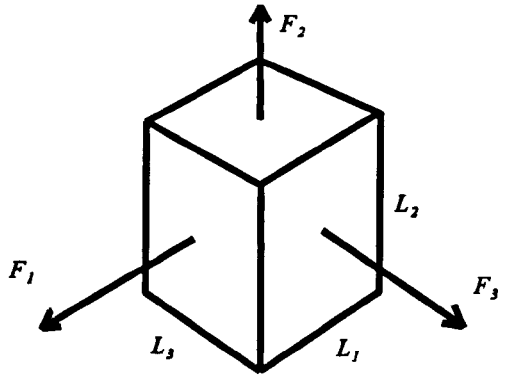

Figure 2.2 - Triaxial Deformation of Rubber

$$\delta W.l_1l_2l_3 = F_1\delta_1 + F_2\delta_2 + F_3\delta_3 \qquad (2.3.10)$$

Dividing through by volume $l_1l_2l_3$: -

$$\delta W = \left[\frac{F_1}{l_2l_3}\right]\left[\frac{\delta_1}{l_1}\right] + \left[\frac{F_2}{l_1l_3}\right]\left[\frac{\delta_2}{l_2}\right] + \left[\frac{F_3}{l_1l_2}\right]\left[\frac{\delta_3}{l_3}\right] \qquad (2.3.11)$$

Note that F_1 / l_2l_3 is the engineering stress σ_1 in direction 1 and δ_1/l_1 is the increment of extension ratio λ_1 in this direction, therefore: -

$$\delta W = \sigma_1\delta\lambda_1 + \sigma_2\delta\lambda_2 + \sigma_3\delta\lambda_3 \qquad (2.3.12)$$

Comparing this with the total differential form: -

$$\delta W = \left[\frac{\partial W}{\partial\lambda_1}\right]\delta\lambda_1 + \left[\frac{\partial W}{\partial\lambda_2}\right]\delta\lambda_2 + \left[\frac{\partial W}{\partial\lambda_3}\right]\delta\lambda_3 \qquad (2.3.13)$$

Yields the result: -

$$\sigma_i = \frac{\partial W}{\partial \lambda_i} \qquad (2.3.14)$$

which relates stress to strain.

If the deformations are small, the start of the stress-strain curve can be assumed to be linear. If we also know the Neo-Hookean constant, it is possible to estimate a corresponding linear stiffness. For uniaxial strain $\lambda_2=\lambda_3$, both equal to $1/\sqrt{\lambda_1}$, therefore

$$W = C_{10}\,(\lambda_1^2 + \frac{2}{\lambda_1} - 3) \qquad (2.3.15)$$

$$\sigma_i = \frac{\partial W}{\partial \lambda_i} = 2C_{10}\,(\lambda_1 - \frac{1}{\lambda_1^2}) \qquad (2.3.16)$$

However, the true stress on the face in direction 1 is the force applied over the actual cross-sectional area, given by $1/\lambda_1$

$$\sigma_{true} = \frac{\sigma_i}{\lambda_1^{-1}} = 2C_{10}\left[\lambda_1^2 - \frac{1}{\lambda}\right] \qquad (2.3.17)$$

If we write $\lambda_1=(1+\varepsilon)$ where ϵ is the engineering strain, using a binomial expansion for the $1/\lambda_1^2$ term and neglecting higher order powers of ε:-

$$\sigma_1 \approx 6C_{10}.\,\varepsilon \qquad (2.3.18)$$

so that the small strain elastic modulus E_s is:-

$$E_s = 6C_{10} \qquad (2.3.19)$$

The material model used for prediction purposes should accurately predict the performance of the material in practice. The strain energy function chosen will vary depending on magnitudes of stress and strain and the deformation mode under which the component is subjected.

2.4 GAS TRANSPORT PROPERTIES OF ELASTOMERS

Gas transport in elastomers during decompression is an important factor in the overall performance of a seal. The worst case for a seal subject to explosive decompression is high solubility and low diffusivity [Davies, 1997]. The high solubility means that the material can absorb large quantities of gas. A low diffusivity means that the gas cannot escape quickly and therefore the gas will be present in the seal to allow failure to occur.

2.4.1 Solubility

Solubility is a primary controlling parameter for explosive decompression performance. Without solubility of gases in elastomers and their variation with temperature and pressure, the phenomenon of explosive decompression would not exist. If the gas were not soluble in the elastomer, explosive decompression would not occur as there would be no stored gas in the seal. The major features which affect solubility include the relative polarity of the elastomer and gas. Polar gases tend to be more soluble in polar elastomers and vice-versa [Van Amerongen, 1964]. Highly soluble gases cause more extensive disruption to the elastomer matrix. Gent and Tompkins (1969) have reported that crack growth is proportional to the extent of gas solubility.

The solubility of gas in elastomers increases with the ambient pressure. At low pressures the concentration c is best described by Henry's law [Van Amerongen, 1964].

$$c = sp \qquad (2.4.1)$$

where p is the ambient pressure and s is the solubility coefficient of the gas in the

elastomer. Deviations from Henry's law are observed at higher pressures in some gases [Ho et al, 1989-1997].

Solubility is also affected by the size, shape and chemical nature of the functional side groups, as these affect the matrix free volume and the gas-polymer interactions. Polar gases (CO_2, NH_3) dissolve more readily in rubbers when polar functional side groups are present [Briscoe, Savvas and Kelly, 1994].

Some polymers crystallise due to the effect of temperature, time and strain that can lead to distinct crystalline and amorphous regions. The solubility of gas in the crystalline regions is thought to be negligible [Treloar, 1975].

Gas sorption in elastomers is closely correlated to the amount of matrix plasticisation and degradation that occurs. It also determines the degree of supersaturation of the gas-polymer solution during depressurisation and the amount of gas coming out of solution as bubbles [Briscoe, Savvas & Kelly, 1994].

2.4.1.1 Effect of Temperature on Solubility

There is a correlation between the solubility and the critical temperature of a gas. Solubility in a polymer increases with more easily condensable gases such as CO_2, NH_3 and SO_2.

Solubility is also largely temperature dependent. For gases with negative heats of solution it has been found that solubility decreases with increasing temperature and vice-versa, most gas-elastomer combinations are negative [Van Amerongen, 1964]. The temperature dependence where Henry's law applies has been expressed by the Van't Hoff relationship [Shah, Hardy & Stern, 1978].

$$s = s_o e^{\frac{-\Delta H_s}{RT}} \qquad (2.4.2)$$

where s is the solubility coefficient, R is the characteristic gas constant, T is absolute temperature and ΔH_s is the heat of solution and s_0 is a constant.

2.4.2 Diffusion and Permeation

The probability of explosive decompression damage is largely dependent on the diffusion of the absorbed gas during depressurisation. If the diffusion rate was infinitely fast, the gas would instantly escape from the seal upon decompression, thereby causing no damage. However, this is not practically possible as if the diffusion rate was this fast it would not make an effective pressure boundary. In practice, the diffusion rates of gases in elastomers are extremely slow.

It has been observed that gas concentration profiles closely matches the stress fields formed within the structure. There are three main categories of diffusion [Crank, 1975].

- Case I - Fickian
- Case II
- Non-Fickian

Case I (Fickian) diffusion is when Fick's first law applies.

$$J = \left[\frac{1}{s}\right]\left[\frac{dm}{dt}\right] = -D\nabla c \qquad (2.4.3)$$

where J is the mass flow rate of the diffusing substance per unit area s, ∇c is the concentration gradient of the substance and D is the diffusion coefficient. This behaviour is usually observed when the diffusion process is much slower than the polymer matrix

relaxation processes. Case II diffusion occurs when diffusion is much faster than relaxation and non-Fickian diffusion occurs when the time scales are comparable. Gas-elastomer systems are usually Fickian in nature, because they are well above the glass transition temperature and chain mobility is high.

With high pressures, the gas dissolves significantly in the rubber matrix, hence causing plasticisation, and the diffusion coefficient is expected to increase. This process is opposed by the matrix compression by the high pressure gas, reducing free volume and hence diffusivity [Campion, 1990].

Usually, the diffusion coefficient increases with a temperature rise. This can be described by an Arrhenius relationship [Van Amerongen, 1964].

$$D = D_o e^{\frac{-E_d}{RT}} \qquad (2.4.4)$$

where E_d is the energy of activation and D_o is a pre-exponential factor.

The effect of the nature of the gas and the polymer on diffusion has been studied in detail by Van Amerongen (1964). Diffusion is largely influenced by the size and shape of gas molecules and their flow through micro cavities, which are constantly created and destroyed by the Brownian motion of segments of the polymer chains [Briscoe & Zakaria, 1992]. If any of the holes open directly on the surface of the material that are in direct contact with the pressurising gas, it is extremely likely that a gas molecule will enter the newly created hole. Once this occurs, the elastomer cannot close the hole and the undissipated kinetic energy will vibrate another hole open between chains. If this newly created hole opens next to the previous hole, the gas molecule may 'jump' into the adjacent hole. Although there is equal probability that the gas molecule will jump in any direction, the net flux of gas migration will be to penetrate the elastomer matrix. This is owing to the initial near infinite concentration gradient between the elastomeric and gaseous regions of the system. Therefore, diffusion in elastomers is primarily polymer mobility and

concentration differential driven [Van Amerongen, 1964].

The diffusional characteristics of a system can be affected by anything that affects the mobility of the polymer chains, hence affecting the opening and closing of holes. Polymers with highly polar side groups will reduce the diffusion coefficient. The mobility of polymer chains can also be affected by side group size, which if large, can produce an effect called 'steric hindrance'. The molecule size of the diffusing substance can affect the diffusion rate. The system temperature can affect diffusion rate as a reduction in temperature will reduce the random thermal fluctuations of the polymer chains and hence chain mobility [Van Amerongen, 1964].

The introduction of chemical cross-links reduces the available movement of the polymer chains and will therefore inhibit diffusion [Briscoe, Savvas & Kelly, 1994]. In general, fillers reduce diffusivity as they are an obstruction to the moving gas and decrease the chain flexibility.

The permeation process is a threefold effect encompassing solution, diffusion and evaporation. The fluid first dissolves into the surface of the seal, then proceeds to diffuse through the bulk and finally evaporates at the low pressure side free surface [Ho et al, 1989-1997].

The rate of permeation of a fluid through an elastomeric seal is dependent upon;

- Material type
- Gas type
- Operational temperature
- Operational pressure
- Design of the seal and the housing

During dissolution almost instantaneous equilibrium is achieved. At equilibrium the chemical potential of the gas dissolved in the elastomer is equal to the chemical potential of that in the gas phase [Ho & Nau, 1996].

Diffusion is governed by Fick's first and second laws. The time-dependent axisymmetric form of the differential equation governing Fickian diffusion in elastomers can be written as:-

$$\frac{\partial c}{\partial t} = \frac{\partial}{\partial z}\left[D\left(\frac{\partial c}{\partial z}\right) + \frac{1}{r}\left[Dr\left(\frac{\partial c}{\partial r}\right)\right]\right] + S_i \qquad (2.4.5)$$

where D is the diffusion coefficient, r is the radial coordinate, z is the axial coordinate and S_i is the sink or source term. The sink term is required for modelling interactions between the gas and the elastomer, due to chemical reactions or swelling for example. The equation gives the time-dependent distribution of gas concentration throughout the seal. The concentration distribution in the steady state condition is given by

$$\frac{\partial}{\partial z}\left[D\left(\frac{\partial c}{\partial z}\right) + \frac{1}{r}\left[Dr\left(\frac{\partial c}{\partial r}\right)\right]\right] + S_i = 0 \qquad (2.4.6)$$

If the low pressure side extrusion space is a closed volume, equilibrium is obtained at the saturated condition. If it is well ventilated, i.e. exposed to atmosphere, then the equilibrium condition is a steady-state governed by the gas concentration gradient in the elastomer near the exposed surface [Ho & Nau, 1996].

There are two analytical models that predict the mass flow rate due to axial permeation through elastomeric seals, the strip model and the arc model [Ho & Nau, 1996]. The strip model considers a strip across a compressed O-ring, having the same width as the extrusion gap. The mass flow rate due to axial permeation of fluid of density ρ through this strip is given by

$$J = \frac{\pi \rho D (r_o^2 - r_i^2)(c_p - c_o)}{L} \qquad (2.4.7)$$

where c_p is the equilibrium concentration at the high pressure side, c_o is the equilibrium concentration at the low pressure side, r_i is the inside radius of the full seal, r_o is the outside radius of the full seal and L is the axial length of the seal.

The arc model treats the O-ring as equivalent to a sector of a circular annulus centred on the low pressure corner of the seal. The annulus has an outer radius equal to the sum of the sides of the square, L, and an inner radius equal to the width of the extrusion gap e. A 45° sector of the annulus is considered. The mass flow rate by this method is

$$J = \frac{\pi^2 \rho D r_o (c_p - c_o)}{2 \ln \left[\frac{L + e}{e} \right]} \qquad (2.4.8)$$

From comparison with experimental and finite element methods for the solution of the Fickian equation, the arc method provides the most accurate results [Ho & Nau, 1996].

2.4.3 Theoretical Considerations for Permeation Testing

Campion (1990) found that Henry's law (eqn 2.4.1) only applies up to a certain pressure in its standard linear form. His experimental work included studying a transparent elastomer to observe the bubble formation process. Initially, due to the high concentrations, bubbles were formed at the outer edges of the sample, but as time elapsed larger bubbles were formed nearer the centre.

During the experiments a thin sheet of an elastomer is used to determine the diffusion, solubility and hence the permeation coefficients. For a plane sheet of an elastomer, Fick's first law becomes

$$\left(\frac{1}{A} \right)\left(\frac{q}{t} \right) = \frac{D(c_1 - c_2)}{h} \qquad (2.4.9)$$

where gas volume q diffuses through thickness h in time t, A is the cross-sectional area, D is the diffusion coefficient and c_1 and c_2 the initial and final concentrations respectively [Campion, 1990]. Therefore by combining equations (2.4.1) and (2.4.9) to give the overall permeation model,

$$\left(\frac{q}{t} \right) = \frac{DsA(P_1 - P_2)}{h} = \frac{QA(P_1 - P_2)}{h} \qquad (2.4.10)$$

where subscript 1 denotes the initial side and subscript 2 denotes the final side. Q is the permeation coefficient and given by

$$Q = Ds \qquad (2.4.11)$$

This permeation model describes only the steady state permeation. A plot of q against t (Figure 2.3) reveals that there is a transient stage in the process before steady-state conditions are reached.

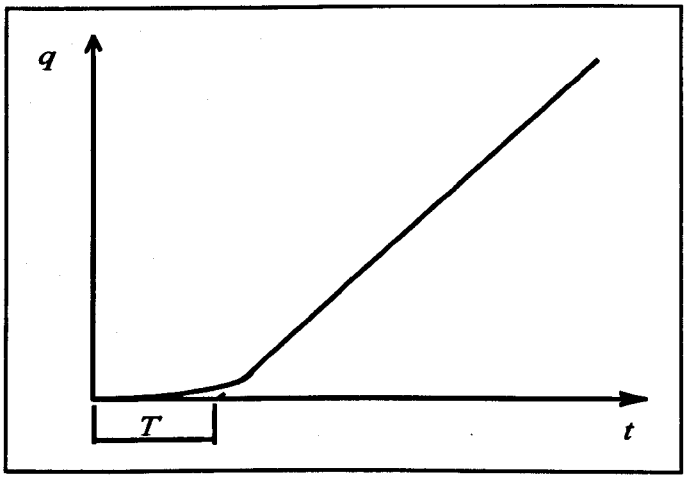

Figure 2.3 - Volume Change with Time during Permeation Test

The transient permeation equation is :

$$Q = \left[\frac{DAc_1}{h}\right]\left[t - \frac{h^2}{6D}\right] \qquad (2.4.12)$$

at the time axis Q=0 and t=τ, so that

$$D = \frac{h^2}{6\tau} \qquad (2.4.13)$$

where τ is the steady-state time lag.

Actual engineering elastomers are fully compounded, which increases the density of the cross-linking and hence reduces the magnitudes of coefficients such as Q [Campion, 1990]. In practice, the determination of the gas transport coefficients by experimental methods is very difficult at high temperatures and pressures.

2.5 GAS INDUCED DILATION OF ELASTOMERS

At high pressures, swelling often accompanies gas sorption of CO_2 and H_2S in EPDM (ethylene-propylene terpolymer) which can be desirable up to around 20-30%, but beyond this becomes undesirable [Ender, 1986, Griffiths, 1985 & Fleming & Koros, 1986]. Gas dilation reflects the amount of plasticisation and hence changes in the elastomer's mechanical properties under pneumatic pressure. The swelling effect is often counteracted by the hydrostatic pressure of the ambient gas. Gases that are highly soluble in elastomers are often strong swelling agents [Ender, 1986].

Expansion is linear with time in the low pressure range [Fleming & Koros, 1986], but becomes a nonlinear function that eventually reaches a limiting value as the hydrostatic compression becomes dominant over the matrix plasticisation at high pressures. The volume change in filled elastomers is lower than that of unfilled elastomers, depending on the quality of the filler-matrix interface [Briscoe & Zakaria, 1992].

There is a distinct similarity between the gas mass sorption and volume dilation curves. Observations of silicone in N_2 [Briscoe & Zakaria, 1990(a)] show a small initial expansion upon decompression followed by a much larger time-dependent dilation and subsequent deflation.

The return to the original dimensions following volumetric swelling is often not immediate, sometimes taking as long as several weeks if explosive decompression failure does not occur [Briscoe & Liatsis, 1989].

The equation converting linear swelling to volumetric swelling is as follows, assuming the swelling is isotropic

$$S_v \approx 3S_l \left(1 + \frac{S_l}{100} \right) \qquad (2.5.1)$$

where S_v is the volumetric swelling and S_l is the linear swelling [Ender, 1986].

If the solubility parameters of the elastomer and the gas are equal, a maximum amount of swelling will occur [Ender, 1986]. Giddings et al extended the Hildebrand solubility parameter concept to gases;

$$\delta_g = \delta_l \cdot \frac{\rho_g}{\rho_l} \qquad (2.5.2)$$

where δ_l is the solubility parameter of the liquefied gas and ρ_g and ρ_l are the densities of the gas and liquid respectively. The solubility parameter varies with pressure. If the seal is subject to only small pressure decreases that do not exceed the supersaturation pressure required for inflation, damage is of no concern [Ender, 1986].

Ender proposed that the inflation of the elastomer corresponds to the pressure cycle in the following graphical form (Figure 2.4).

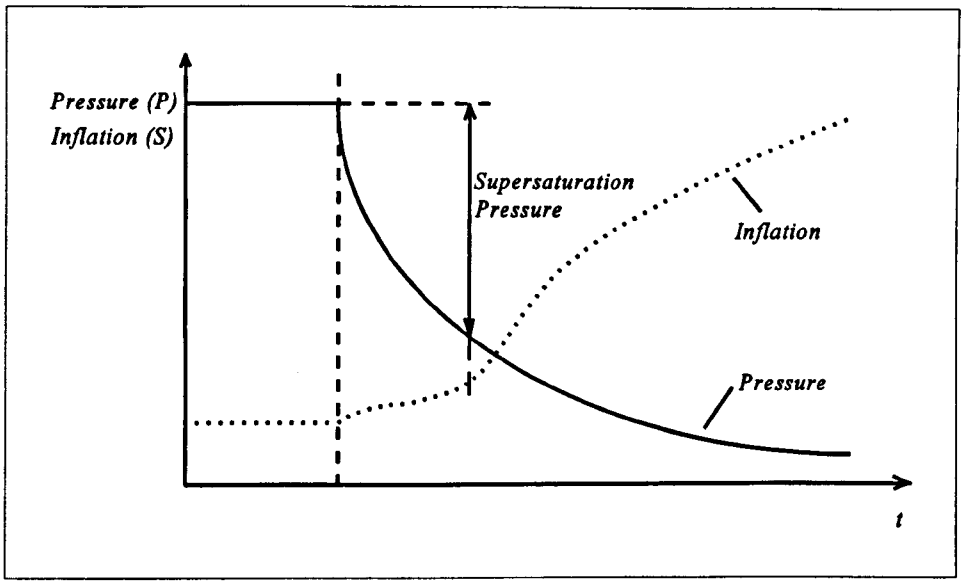

Figure 2.4 - Pressure and Elastomer Inflation Vs Time

Elastomers that are more resistant to gas decompression tend to retain significant volumetric swelling and density changes after gas depressurisation is completed [Briscoe & Zakaria, 1990].

2.6 GAS NUCLEATION AND VOID EXPANSION

Davies (1997) stated that it is probable that the majority of the gross volumetric expansion experienced by a seal during explosive decompression is due to the growth of precursor voids and not network interstices.

Gas bubbles will nucleate at sites of flaws or impurities within the material structure when subjected to high gas pressures. Upon removal of the external pressure the gas will come out of solution and expand into the voids and eventually cause rupture at the void wall.

Gent & Lindley (1958) discussed a material that is assumed to contain an extremely small cavity, small enough for the surrounding region to be regarded as an infinitely thick spherical shell. For an incompressible material which is isotropic in the undeformed state,

the stored energy W is a function of the two strains invariants I_1 and I_2 as discussed in section 2.3.

From this strain energy function the pressure required for the symmetrical expansion of a thick spherical shell is given by [Green & Zerna, 1954].

$$P_m = C\left[5 - \frac{4}{\lambda} - \frac{1}{\lambda^4}\right] \qquad (2.6.1)$$

As λ tends to ∞ (i.e. the diameter of the shell becomes infinite) the equation reduces to:

$$P_m = 5C \qquad (2.6.2)$$

but E = 6C (see section 2.3), therefore :

$$P_m = \frac{5E}{6} \qquad (2.6.3)$$

This value is the critical rupture pressure and it is hypothesised that the cavity will continue to inflate until fracture occurs if this pressure is developed [Gent & Lindley, 1958]. A more complete modelling approach is to take a simple logarithmic form of the strain energy function

$$W = C_1 (I_1 - 3) + C_2 \ln (\frac{1}{3} I_2) \qquad (2.6.4)$$

Gent and Lindley (1958) give E as:

$$E = 6C_1 + 2C_2 \qquad (2.6.5)$$

and through experimental observations, $C_1 = C_2$, therefore,

$$E = 6C_1 + 2C_1 = 8C_1 \qquad (2.6.6)$$

The relationship between P_m and λ is:

$$P_m = W_1\left[5 - \frac{4}{\lambda} - \frac{1}{\lambda^4}\right] + \frac{W_2}{3}\left[\ln\left[\frac{3\lambda^6}{2+\lambda^6}\right] + 2\sqrt{2}\left(\tan^{-1}\sqrt{2} - \tan^{-1}\left[\frac{\sqrt{2}}{\lambda^3}\right]\right)\right] \quad (2.6.7)$$

If C_2 is now substituted with C_1, and $C_1 = E/8$ and λ tends to ∞, the relationship between P_m and λ, is:

$$P_m = 0.783E \quad (2.6.8)$$

Both evaluations of the critical rupture pressure in terms of the elastic modulus are in reasonable agreement, the latter model being the more accurate. However, it is generally accepted that 5E/6 is an accurate enough solution [Gent & Lindley, 1958]. This model is limited as it does not include the effects of surface tension. The empirical approach to the solution was carried out using softer elastomers with no reinforcing filler. Most materials used today, particularly for explosive decompression, contain high quantities of carbon black and would withstand much higher pressure differentials than 5E/6. The model is also limited as it uses the elastic modulus, which is a small strain linear estimation. At the strain levels encountered at fracture the slope of the stress-strain curve will be very different due to material and geometric non-linearities.

Gent and Tompkins (1969) developed the following criteria for the pressure difference to expand a void indefinitely. They considered a simple spherical void of radius r_o which expands in a block of infinite dimensions. The pressure difference ΔP should be large enough to overcome the elastic forces and the surface tension forces of the matrix and was derived as:-

$$\Delta P = \left[\frac{G}{2}\right]\left[5 - 4\left[\frac{r_o}{r}\right] - \left[\frac{r_o}{r}\right]^4\right] + \frac{2\gamma}{r} \quad (2.6.9)$$

where G is the shear modulus, γ is the surface energy of the rubber, r is the radius of the

void and r_0 is the initial radius of the void. However, for voids of sufficiently large radius ($r_0 > 10^{-5}$ cm) the surface tension forces can be neglected, therefore the pressure differential becomes

$$\Delta P = \left[\frac{G}{2}\right]\left[5 - 4\left[\frac{r_o}{r}\right] - \left[\frac{r_o}{r}\right]^4\right] \qquad (2.6.10)$$

The critical pressure difference at which the void expands indefinitely occurs when r tends to infinity is

$$\Delta P_c = \frac{5G}{2} = \frac{5E}{6} \qquad (2.6.11)$$

Because when K (the bulk modulus)>>G (as is the case with elastomers), G = E/3. Note that the value is independent of r_o.

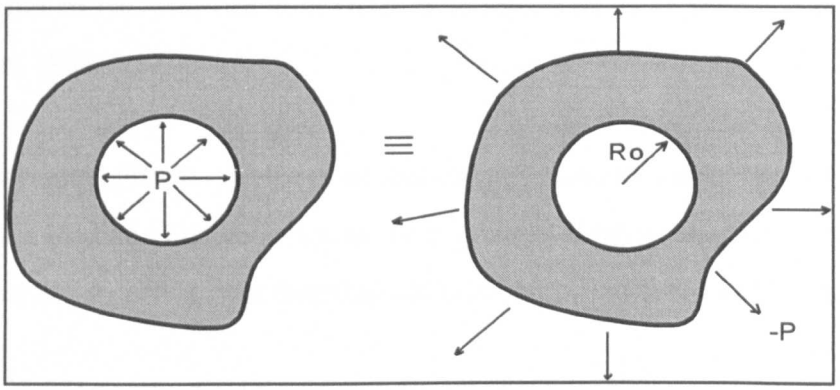

Figure 2.5 - Gent's Void Inflation Model

The pressure within the void will be partly maintained by diffusion of gas into the cavity from the surrounding supersaturated rubber. However, the void will not expand indefinitely because [Gent & Tompkins, 1969a]

- the supply of gas is limited
- in blocks of finite size, diffusion of gas outwards through the edges of the block is competitive with diffusion into the cavity, therefore

the holes collapse back to a closed configuration in the end.

The pressure inside the void will initially be the same as the initial supersaturation pressure. When the external pressure is removed it will drop in accordance with the increased hole volume, but will be partially maintained by inward diffusion [Gent & Tompkins, 1969a].

During the depressurisation phase the inflated voids will behave as 'sinks' and 'sources' for gas transport. The gas will enter and exit the voids driven by the relative concentration gradients and pressures surrounding them. If a void is receiving more gas than it is expelling, it can be termed a 'sink'. Likewise, if a void is expelling more gas than it is receiving, it can be termed a 'source' [Campion, 1990].

When smaller voids are present in the elastomer, the surface tension forces come into account and the critical pressure differential is no longer equal to 5E/6, it is much higher [Cho & Gent, 1988].

Hou and Abeyaratne (1992) developed an analysis technique for cavitation in solids under non-symmetric loading. For cavitation to occur in a neo-Hookean medium, with principal stresses σ_1, σ_2 and σ_3 acting on a material, the following condition must be met:-

$$(4\sigma_1-\sigma_2-\sigma_3)(4\sigma_2-\sigma_3-\sigma_1)(4\sigma_3-\sigma_1-\sigma_2)\geq\frac{125E^3}{27} \qquad (2.6.12)$$

In a condition of pure hydrostatic tension the principal stresses equate to pressure P ($\sigma_1=\sigma_2=\sigma_3=P$). If P is substituted into equation (2 6.12) it gives the critical pressure as 5E/6. However, the condition $\sigma_1=\sigma_2=\sigma_3=P$ can only exist if the elastomer cannot expand.

The rate of bubble growth upon decompression has been shown experimentally and theoretically to be proportional to the square root of the time elapsed after nucleation [Gent

& Tompkins, 1969 and Stewart, 1970].

$$r = kt^{\frac{1}{2}} \qquad (2.6.13)$$

where k is a constant increasing with the diffusivity and solubility of the gas in the matrix and the initial supersaturation pressure.

Williams and Schapery (1965) state that when a hydrostatic tension is applied to the inflating void, the expansion process occurs such that there is an energy balance between the applied work done by the pressure and the internally stored strain energy. The energy balance could be achieved in a different manner, by increasing the cavity wall area arising from the creation of additional surface at fracture. This would require an incremental increase in surface energy. The Williams and Schapery analysis associates the failure in the cavity wall with incremental energy transfers between applied work, internal strain energy and surface energy. However, their subsequent calculations determined that there would not be sufficient strain energy within the system to cause the smallest of the elastomer's intrinsic flaws to propagate. This conclusion seemed unstable as there must be a certain level of internal pressure at which all materials will fail. The study initially used the simple kinetic theory of rubber elasticity which does not apply at the high strains encountered at failure. To solve this problem, Williams and Schapery then used the energy method as previously described. They concluded that a pressure of 3E would be required to fracture a void of 0.5 microns.

The effects of filler particles has received little attention in the open literature. As they will obviously behave as stress raisers under explosive decompression, this is surprising. With respect to void formation due to failure between adjacent filler particles and the surrounding elastomer matrix, Cho and Gent (1988) proposed the following model to predict this failure mode and carried out experiments to validate the theory.

Values of the maximum hydrostatic tension -P set up in the rubber layer around a rigid particle was determined from an approximate stress analysis.

$$\frac{-P_m}{E} = \frac{e_m}{4A\ (A\ -\ 1)^2} \qquad (2.6.14)$$

e_m is the maximum tensile strain set up in the rubber, given by the ratio of the displacement δ of one sphere or cylinder away from the other to the initial separation, h : $e_m = \delta/h$. This is for a layer bonded between two spherical particles, and

$$\frac{-P_m}{E} = \frac{e_m}{2A\ (A\ -\ 1)^2} \qquad (2.6.15)$$

for a layer bonded between two parallel rigid cylinders. The term A denotes,

$$A = 1 + \left(\frac{h}{D}\right) \qquad (2.6.16)$$

where h is the distance between the spheres or cylinders and D is their diameter.

The relationships between e_m and the applied force are,

$$e_m = \frac{\sigma}{E} \qquad (2.6.17)$$

for layers between spherical end-pieces, and

$$e_m = \frac{3\sigma}{4E} \qquad (2.6.18)$$

for layers between cylindrical end-pieces, where σ denotes the mean applied stress.

Experimentally, specimens were prepared with various spacings h so the ratio h/D ranged from 0.02 up to 0.35. The cavities appeared suddenly when the critical load was reached and grew rapidly to a large size. They were formed in the area of maximum tensile strain and maximum hydrostatic tension. The formation of cavities was observed to be time-dependent, in that if the load was held just below the critical value, a cavity would form in much the same manner. This study is only partially relevant to explosive decompression as the ratios of h:D studied means that the distance between the particles is very small incomparison with their diameter. This would only be applicable when considering agglomerations of filler particles.

If the rubber thickness was greater than around 5% of the end piece (filler particle) diameter, then the results agreed with the proposed theory. However, if the thickness was less than 5% the stresses required to form a cavity became considerably larger. These larger stresses, when related to a regular arrangement of spheres on a cubic lattice, correspond to a high volume concentration of filler particles of more than 45% [Cho & Gent, 1988]. Therefore the model should give comparable results with those determined experimentally as the filler content is generally less than 45%.

2.7 PHYSICAL PROPERTY CHANGES IN OPERATIONAL ENVIRONMENTS

The effect of the ambient gas on the molecular motions of elastomers depends on whether the gas acts as a plasticising or pressurising medium. Pressurising media decrease the free volume through matrix compression, and plasticising media increase it. They will compete with each other for dominance [Assink, 1974].

Elastic modulus changes are very much gas dependent as experiments by Briscoe and Zakaria (1990b) show. For example CO_2 induces an initial modulus increase in silicone to applied pressures up to 2 MPa, followed by a decrease due to extensive plasticisation. This is in contrast to N_2 where an increase in modulus was observed under the same conditions.

The glass transition temperature of an elastomer will be decreased if the dominant effect is plasticising and increased if the matrix compression element is dominant. The changes in the glass transition temperature and the internal mobility of the polymer chains, in a high pressure gas, are reflected in the mechanical properties of the polymer matrix.

A reduction in pressure causes marked temperature decreases due to the near adiabatic nature of the process. The magnitude of this reduction depends on the nature of the gas, the initial and final conditions of temperature and pressure and the rate of decompression. Gases with a high Joule-Thompson coefficient undergo a larger temperature decrease during decompression. As an example Liatsis gives data on rapid depressurisation of N_2 from 40 MPa to atmospheric pressure, which caused an ambient temperature reduction from 18°C to -25°C, one minute after depressurisation [Liatsis, 1989].

The physical strength of the elastomer will be considerably reduced at an elevated temperature. A typical reduction in tensile strength of approximately x% can be seen when increasing the temperature from 20°C to 100°C [Davies, 1997].

2.8 GAS INDUCED FRACTURE OF ELASTOMERS

Cavitation and subsequent crack growth in elastomers are usually caused by flaws which grow in response to applied hydrostatic tensile stress. The magnitude of the hydrostatic stress required to produce cavitation can be very small, often of the order of the elastic modulus, around 2MPa [Lake, Thomas & Lawrence, 1991].

Cracks will propagate until the available energy for crack growth falls below a threshold level. A large crack may act as a sink for gas transport and so allow the energy to increase again as gas diffuses into the cavity. This process may repeat itself and cause 'stick-slip' crack propagation [Briscoe and Zakaria, 1990(d)].

Gent and Lindley (1958) observed the formation of internal cracks in bonded rubber cylinders at relatively small tensile loads, and developed a theoretical treatment based on a proposed criterion for crack formation. Equation (2.8.1) has been developed to relate the cracking stress to the applied maximum hydrostatic pressure,

$$S' = \frac{1}{2} P_m \left[1 + \frac{2h^2}{r^2} \right] \qquad (2.8.1)$$

where S' is the cracking stress, P_m is the applied hydrostatic pressure, h is the thickness of the bonded cylinder and r is the cylinder radius.

If cracking occurs at a critical value of P_m, the corresponding cracking stress S', will decrease from a value of P_m for infinitesimally thin test pieces to a value of $P_m/2$ for test pieces of moderate thickness, when $h < a$. Therefore, in simplistic terms, the occurrence of cracks is largely section thickness dependent. A linear relationship between the cracking stress and the value of Young's modulus E has been observed which decreases with test piece thickness. It is also independent of rubber strength of extensibility [Gent & Lindley, 1958].

Large cracks are sometimes axially symmetrical, forming surfaces of the same shape as the test piece, i.e. in a cylindrical system, the cracks are axially symmetrical and circular. The second type of cracks are smaller, randomly oriented cracks [Briscoe & Liatsis, 1989]. The formation of symmetrical internal cracks is attributed to the creation of the stress field through the elastomer section. The position of the maximum shear stress developing from the field is most probably the determining factor in the location of the ruptures. This is in contrast to other observations where cracks were formed perpendicular to the direction of applied pressure. The differences between the observations are probably due to the constraints used in the experiments. The housing designs used the experiments where perpendicular cracks were formed were British Standard designed grooves for the Seal Life Project tests [Ho et al, 1989-1997].

The depth at which cracks occurred in Briscoe and Liatsis' experiments was directly proportional to the saturation time and the pressure. Briscoe and Liatsis (1989) proposed using a thick walled pressure vessel analogy to attempt to explain the induced stress field and hence the cracking pattern. In order to include the effects of a pressure drop across a distance, i.e. a gradient, rather than an instantaneous drop, an alternative modelling approach was taken.

The hypothesis is that at a particular pressure differential an internal crack is formed. The gas then escapes easily through the newly formed crack and a new pressure differential is created. A new crack of smaller radius is then formed and the process continues until the cracks approach the cylinder axis. The model predicts that the ratio of radii between a newly formed crack and the preceding one is constant and equal to K. The model gives a first order estimate of 0.8 for a value of K [Briscoe & Liatsis, 1989]. Shear stresses are then generated between the outer and inner regions and this leads to the formation of large circumferential cracks. The smaller cracks are probably caused by the relatively uniform triaxial expansion of the elastomer [Briscoe & Zakaria, 1990d].

The computed concentration profiles of the gas developed during the depressurisation often exhibit a point of inflexion if the diffusion coefficient is concentration dependent and decreases with increasing concentration. The computed concentrations are S-shaped and hence the curvature of the resulting pressure profile changes at some point across the specimen section. Briscoe et al suggest that there is a strong indication that the existence of a point of inflexion in the pressure profile introduces a discrete maximum in the developed stress field [Briscoe & Liatsis, 1989].

The S-shaped pressure profiles were described reasonably well by a series of slightly modified Gompertz curves, given by:-

$$P = P_o \, (1 - \exp[b.\exp(cr)]) \qquad (2.8.2)$$

where the parameters b and c are used to define the shape of the curve and P_o represents

the initial pressure difference between the centre of the section and the surface [Briscoe & Liatsis, 1989]. The point of inflexion occurs at the point r_p where the second derivative of P with respect to r is zero:-

$$1 + b.\exp(cr_p) = 0 \qquad (2.8.3)$$

The positions of the maxima in the stress plots coincide with the points of inflexion of the pressure profiles remarkably well. Therefore the shape of the pressure profile and the point of inflexion defines the position of the internal cracks. Temperature gradients generated during decompression will tend to prevent the generation of a stress maximum, and will hence improve the explosive decompression performance of the elastomer. A reasonable estimate of the point of inflexion and the sharp drops in the profile would be at around 0.8 of the cylinder radius [Briscoe & Liatsis, 1989].

During decompression two types of stress field are thought to develop within the elastomer. The first, referred to as the overall field, arises from the hydrostatic tension that acts on the specimen, and the second one arises from the internal pressure profiles. Neither can individually explain the crack formation phenomena, however, a combination of the two gives an adequate explanation for the crack formation. The material ruptures because of the hydrostatic tension, but the location and the direction of the cracks is due to the localised stress fields [Briscoe & Liatsis, 1989]. The Briscoe and Liatsis approach holds true if the failure process is studied purely as a function of the stress field. It does not take into account the initiations of cracks due to void inflations.

Cavity expansion involves a fracture process that will obey the Griffiths energy criterion. A spherical cavity of initial volume V_0 will expand to a volume V only if the elastic strain energy released exceeds the characteristic fracture energy G_c of the material.

$$-\left[\frac{\partial(W_{el}+W_p)}{\partial A}\right] \geq G_c \qquad (2.8.4)$$

where W_{el} is the elastic strain energy stored in the matrix, W_p is the work performed by the

pressure and A is the surface area of the cavity [Briscoe, Savvas & Kelly, 1994]. Also, at constant temperature

$$W_p = P dV \qquad (2.8.5)$$

and

$$W_{el} = \int_{V_o}^{V} P dV \qquad (2.8.6)$$

A similar approach was taken by Williams and Schapery (1965) and Gent and Wang (1991), with similar results.

The prediction of the critical negative hydrostatic pressure is largely dependent on the initial radius of the void which means that very small cavities require unrealistically high expansion rates to tear. The kinetic theory of rubber-like elasticity ceases to be valid at the large strains encountered at fracture when the cavities are very small. Therefore the Gent and Wang analysis is valid only for voids such that:-

$$\frac{5x10^{-4}G_c}{E} < r_o < \frac{10^{-1}G_c}{E} \qquad (2.8.7)$$

Tearing is initiated when a critical strain level is reached in the void wall [Gent & Lindley, 1958]. The tearing process can be easily described by the tearing energy T_{en} and the rate of tear. The tearing energy T_{en} is defined, for a sample in sheet form, as the rate of change of energy U, stored elastically in the material, with the crack length, c_l, per unit thickness, h, of the test piece, provided that no external work is done on the sheet:

$$T_{en} = -\left[\frac{1}{h}\right]\left[\frac{\partial U}{\partial c}\right]_l \qquad (2.8.8)$$

where l is the distance between the points of application of the external forces. Briscoe et

al (1994) stated that tear propagation occurs when a threshold tearing energy of the order of 0.1 kJm^{-2} is exceeded.

Gent and Wang (1991) extended their analysis of the critical pressure for inflation to include surface tension effects for small voids. A surface tension factor was included in the bubble inflation equation to give.

$$\frac{P}{E} = \frac{(5 - 4\lambda^{-1} - \lambda^{-4})}{6} + \frac{2\gamma}{Er} \qquad (2.8.9)$$

The energy requirement for crack growth was then derived as;

$$\frac{(1 + \lambda^2 - 2\lambda^{-1})}{3} \geq \frac{G_c}{2r_o E} \qquad (2.8.10)$$

This equation gives the necessary conditions for tearing, which are unlikely to be met for small cracks. The critical internal pressure is largely dependent on the initial radius of the crack or flaw. The values of this pressure were found to be in the relatively narrow range E to 3E, for crack radii in the range $5x10^{-4}G_c/E$ to G_c/E. For conventional rubber materials this corresponds to radii of 0.5μm to about 1mm [Gent & Wang, 1991].

At low tearing energies at constant force, time dependent crack growth occurs [Lake et al, 1991]. This is initially steady but slows down progressively and eventually stops. The torn surface is rough and changes direction, known generally as 'knotty' tearing.

At medium tearing energies, 'stick-slip' crack growth occurs and the crack growth rate fluctuates. At higher tearing energies the crack growth rate is constant and catastrophic failure often occurs. This gives a straight fracture path and a smooth surface, which are typical for non-crystallising rubbers [Lake et al, 1991].

During experiments by Lake, Thomas and Lawrence (1992), a strong dependence of crack growth rate on pressure was observed, decreasing by approximately three orders of

magnitude between 1 bar and 1.3 kbar. There was no evidence from the experiments that the hydrostatic pressure produced any appreciable change in fracture surface roughness. In many cases, there will be an appreciable stress, tensile in nature, acting in the thickness direction at the tip of a propagating crack, arising from geometrical considerations.

Maximum propagation velocity of a running crack is independent of the energy available for tearing. As in other solids, it is shown to be related to the wave velocity of sound within the elastomer and is a strong function of the stored strain in the system [Gent & Marteny, 1982].

Crack propagation is greatly affected by fillers as their addition alters the mechanical properties and hence increases the required tearing energy. They also inhibit the crack growth, this being dependent on the density of filler particles [Greensmith, 1956]. Temperature has a significant effect on the tear properties of elastomers, in general reducing the required tearing energy with temperature increase [Lake et al, 1991].

Lindsey (1967) reported that during the expansion process, sharp cracks may form at two extremities of the expanding cavity which appear to propagate in a direction perpendicular to that of the principal tensile stress. The number of cracks observed in filled elastomers was higher than that of unfilled, however the average crack length was higher for unfilled materials.

It is suggested that high pressure gas nucleates at poor interfacial bonds between filler particles and the matrix and forms vacuoles which are inflated by the gas. The strength of the matrix-filler bond decreases rapidly if the interface is poor when the external gas pressure is removed. Small voids at the interface expand and the matrix pulls away from the filler surface due to the applied tensile stress. The failure surface is generally rough or 'knotty' in filled elastomers and smoother in unfilled elastomers [Briscoe & Zakaria, 1990e].

The appearance of a tear surface changes depending on the rate of failure; for a low rate the surfaces are rough in appearance, but at higher rates a smooth surface is observed [Lake, Thomas & Lawrence, 1992]

The crack propagation velocity is given by:-

$$\frac{dc_l}{dt} = BT^n \qquad (2.8.11)$$

where the constants B and n depend on the linear section of the graph where the system lies (see Figure 2.6).

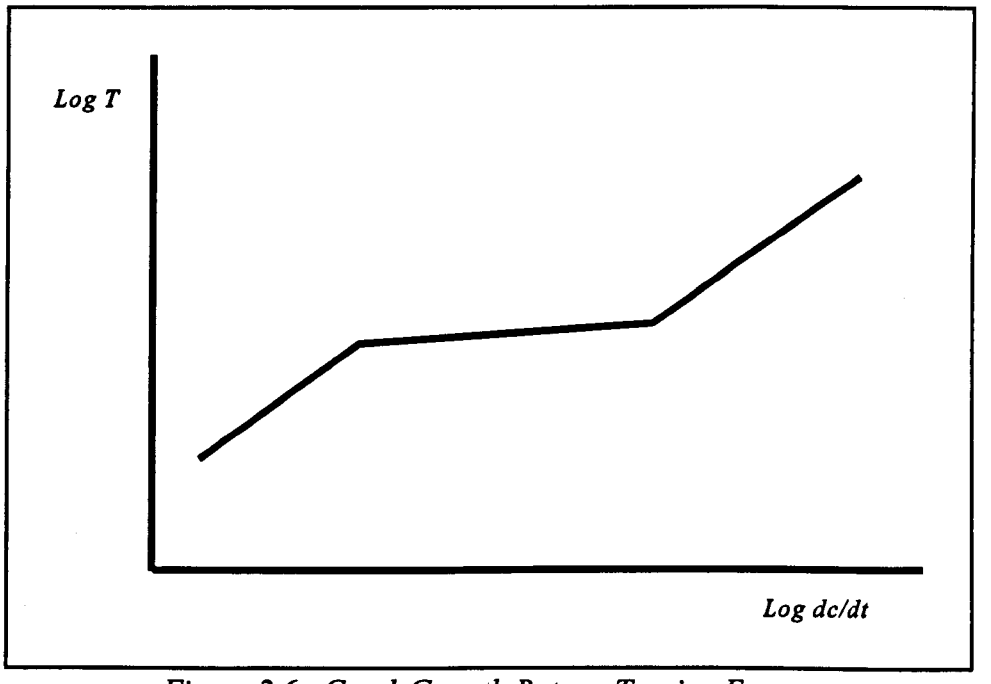

Figure 2.6 - Crack Growth Rate vs Tearing Energy

Andrews and Stevenson (1978) proposed the following criterion for the critical pressure in a penny shaped crack in a plane sheet:-

$$\frac{P_c^2(1 - \nu^2)c}{E}\left[\frac{3}{32}\left[\left[\frac{c}{h}\right]^3 + \frac{c}{h}\cdot\frac{4}{(1 - \nu)}\right] + \frac{1}{\pi}\right] \geq T_{en} \qquad (2.8.12)$$

where c is the radius of the crack and h is half the thickness of the sheet. This process

therefore depends on the gas type as N_2 increases modulus due to compression and CO_2 decreases modulus due to plasticisation. The value of E used in the equation should be the value at temperature, however values of E quoted are at room temperature.

2.9 THE EFFECT OF DESIGN AND OPERATIONAL PROCEDURES

The open literature has no mention in any detail of decompression rate. Obviously, if the decompression rate is slow enough the gas will be able to safely escape without causing any damage. Ideally, it would be of use to users of elastomer seals if they could predict the safe decompression time to inhibit damage.

The open literature puts very little emphasis on the effects of geometry on explosive decompression resistance in elastomers, although some authors have observed that these factors are critical. During the void inflation phase for example the expansion may be limited by high initial groove fill, although this is difficult to achieve because of tolerances and damage on installation.

It is widely stated that large section seals are more susceptible to explosive decompression damage than smaller sections, owing to the longer time required for the gas to diffuse from the section. The explosive decompression resistance of a seal is inversely proportional to the cross sectional area [Cox, 1985].

Explosive decompression characteristics vary depending on the shape of the seal section as the sharp points of a triangular section, for example, would lead to areas of high stress concentration.

The influence of groove design on explosive decompression resistance must be critical in the seal's ability to resist explosive decompression. If the initial groove fill is very high

(i.e. 90-100%), the material does not have any vacant space to expand into and will therefore not exhibit any crack damage. However, excessive groove fill can cause damage by extrusion and high compression set. This has been observed in practice by Ho et al as part of the Seal Life Research Project.

2.9.1 The Effect of Interface Friction

Initially a seal in a groove can be unconstrained laterally, i.e. it is constrained by the top and bottom faces of the housing, but not in contact with the sides of the groove. The seal can then be moved into a constrained position by the action of pressure. This process is very much friction dependent. Chivers and Hunt [1978] derived a simple Coulomb friction model and a specific friction model to determine under what conditions slip will occur.

The determination of the stick or slip condition is very important in determining the overall stress field in a compressed and pressure activated O-ring seal. The Coulomb friction approach provides a slip before leak criterion and requires that:

$$0.41\left[\frac{d}{x}-1\right]\left(\frac{x}{d}\right)^{\frac{1}{2}} > \mu \qquad (2.9.1)$$

where μ is the coefficient of friction, d is the toroid diameter and x is the applied compression. This states that as compression increases, lower coefficients of friction are required if the O-ring is to move to a constrained configuration before leaking. For 20% and 35% compressions the coefficient should be less than 1.1 and 0.6 respectively compared with laboratory measurements of 0.5 and quoted values between 0.2 and 1.0 [Lindley, 1967].

An exponential dependence of frictional coefficient upon time has been shown by Bowns et al [1975], and Sick [1975] has shown that after around 100 hours a pseudo-equilibrium value is reached. In order for the time and area dependence to be taken into account a specific friction model is adopted in which the frictional coefficient is defined in terms of

unit contact area [Chivers and Hunt, 1978]. Using this frictional model, the inequality, for slip to occur before leakage, becomes:

$$\frac{1}{3}\left(1 - \frac{x}{d}\right) > \frac{\mu_{sp}}{E} \qquad (2.9.2)$$

where μ_{sp} is the specific frictional coefficient. Austin and Nau [1974] quote values of up to a maximum of 0.073 kgf/mm^2 for the specific friction of elastomers sliding on a steel surface.

Chivers and Hunt [1978] state that taking a maximum value of x/d of 0.35, and 0.073 for μ_{sp} requires E>0.335 kgf/mm^2. Therefore if compression is less than 35% and hardness is greater than 55 IRHD, slip will occur before leakage. Both of the frictional models show that with few exceptions slip will occur before leakage, so that the seal has the potential of moving from a unconstrained to constrained configuration.

It has been observed experimentally that O-rings do not slide under hydrostatic pressure as previously understood. The compression of the O-ring into the housing is due to internal flexing due to the conservation of volume, assuming Poisson's ratio is near 0.5 [Hörl & Haas, 1997]. However some sliding was observed when the O-ring was pre-lubricated, but this ceased after a number of pressure cycles.

2.10 SUMMARY OF LITERATURE REVIEW

It is clear from the literature review that the basic mechanisms of explosive decompression failure are reasonably well established. However, each of the mechanisms have been considered as separate functions, without giving much consideration as to how they interact with each other. For example, there is no literature regarding how the stress field will affect voids under internal pressure.

The literature includes only limited data on elastomer properties. This data was usually

supplied on materials that are not often used in explosive decompression sensitive environments. Of particular interest is the lack of permeation data of elastomers in high pressure and temperature gas. This data is obviously essential for any explosive decompression model. There is no real data on the size and nature of flaws and defects within elastomers, again particularly for hard materials with high filler content such as fluorocarbons.

The literature discusses in some detail the failure mechanism, but does not take the argument further to consider how the fissures formed affect the overall sealing integrity of the O-ring.

The models that estimate the magnitude of the pressure differential required for crack formations do not consider the effects of material and geometric non-linearities as they make use of the elastic modulus. These models should be developed using a strain energy function, fitted across a range of experimental deformation modes. The literature makes no mention of the pressure differential formed under differing decompression regimes. Obviously, if the decompression was carried out over a long enough period of time, failure would not occur. There will be an minimum time for the safe decompression of a seal, such that no damage occurs. Therefore there is an obvious need for a model to predict the actual pressure differentials formed in unique gas-elastomer combinations.

There is limited data on the physical properties of elastomers in the saturated state and at temperature. The data available is only for carbon dioxide up to 40 bar gas pressure. Most oil and gas sealing systems operate between 100 and 500 bar at 200°C in a methane rich gas. However, the measurement of the physical properties in these conditions would be very difficult and expensive.

In conclusion, it is clear from the literature that although the mechanisms of failure have been described, they have been detailed for irrelevant materials and conditions. Users of seals in explosive decompression sensitive environments use elastomers that are proven

to resist damage under limited conditions. However, these seals do fail under extreme conditions of temperature and pressure and it is these conditions that are of interest.

The literature does not have a complete model detailing the primary causes of explosive decompression failure. Obviously, the explosive decompression failure process is very complex and a model could not cover all variables. However, it is thought that primary variables exist that are responsible for failure. This thesis attempts to determine the relationships between the primary variables to gain a better understanding of the failure process.

CHAPTER 3 - SEAL DECOMPRESSION TESTING

3.1 INTRODUCTION

The programme of seal decompression tests was carried out to determine the extent of damage due to controlled decompression regimes. The seal tests are designed to replicate, as near as possible, the actual conditions seen in operational environments. The results of the tests are used to determine the actual extent of damage. These are then compared with predictions from the model for validation.

The test programme is designed to replicate a wide spread of conditions, with the extremes of each variable used to cover the full range of possibilities. Different factors such as groove fill and installation compression are considered to determine the effects of groove design on decompression damage.

Four materials are studied as part of the test programme. These are the three materials studied throughout the research programme, A, B and C, and material D. Material D is a standard nitrile based elastomer with approximately 36% ACN (acrylonitrile) content. This material is known to fail readily under decompression conditions and is therefore used as a control.

Observations of failure made in industry have noted that larger section seals are more susceptible to decompression damage. Therefore, two different section seals are used in the test programme to determine their effect on the extent of damage.

3.2 TEST CONDITIONS

A total of six test environments is used to cover the full range of extremities. The variables used in the test matrix are as follows: -

- Installation compression
- Groove fill
- Seal section diameter
- Decompression period
- Temperature
- Pressure

Three replicates of each material under each test condition are used for the 5.33mm section seals, and four replicates are used for the 10mm section seals. The replication is used to ensure repeatability in the results. There will be some inherent variability in the results due to the variable nature of the physical properties of the elastomers being studied. The test matrix is shown in Table 3.1. Note that all groove fill and initial compression values are nominal, based on housing and O-ring tolerances. The actual initial compression and groove fill values at the test temperature are also given.

Table 3.1 - Test matrix

Test Parameter	**Test Number**					
	1	2	4	5	6	7
Compression (aim)	15%	15%	25%	25%	15%	15%
Compression (cold)	12.8%	12.8%	24%	23%	12.8%	13.7%
Compression (hot)	13.9%	14.7%	25.2%	24.9%	13.9%	15.6%
Groove fill (aim)	70%	70%	70%	90%	70%	90%
Groove fill (cold)	68.7%	67.4%	70.3%	84.4%	69.8%	84.6%
Groove fill (hot)	71.1%	71.2%	72.7%	89.0%	72.2%	89.3%
Section diameter (mm)	5.33	10.0	5.33	10.0	10.0	5.33
Decompression time	2 hours	Instant	Instant	2 hours	2 hours	Instant
Temperature	100°C	150°C	100°C	150°C	100°C	150°C
Pressure	100 bar	400 bar	500 bar	100 bar	100 bar	500 bar

Test three, which does not exist in the test matrix, was not included. From test parameters and experience, no failure would clearly take place because it was at low pressure, with a small seal section and a decompression period of 48 hours.

The size specifications for the elastomer O-rings are: -

5.33mm section	:	BS312 (1" OD x 5.33mm section)
10mm section	:	53mm OD x 10mm section (nominal)

The groove dimensions are then varied to adjust the installation compression and groove fill variables specified in the test protocols. The groove dimensions take into account the differential thermal expansion of the elastomer and metal work.

3.3 THE EFFECTS OF TEST VARIABLES

3.3.1 The Effect of Installation Compression

The amount of installation compression is thought to affect the explosive decompression resistance of an elastomer O-ring. If the initial compression is low, the stress field created within the seal section is considerably lower than that of a higher compression. Therefore a void that undergoes inflation will not have a high compressive stress in the surrounding matrix. If the local compressive stress is low, the void can expand more freely.

3.3.2 The Effect of Groove Fill

Groove fill has not been documented in great detail as a controlling parameter in explosive decompression resistance. However, it is clear that the higher the groove fill, the lower the possibility of damage. This is because the seal must undergo gross volumetric expansion for damage to occur. If the initial groove fill is very high, the seal can only physically expand a small amount into the constraints of the groove. This situation will remain until

the gas has diffused out the seal section. The voids, which would normally inflate under the internal pressure, now have an additional local compressive stress field. The additional stress field is generated as the seal contacts the seal housing.

This enables the seal to maintain its physical integrity. However, there are major problems with designing for a high initial groove fill. If the groove fill is high and the initial compression is low, the section size will often be larger than the available groove width and the seal cannot be installed. If the seal is installed and then compressed, the seal will push outwards into the corners of the groove and may result in cracking due to the large stress concentrations.

3.3.3 The Effect of Section Diameter

It has been widely observed that larger section seals are more susceptible to damage through explosive decompression than smaller seals. The tests carried out in this study aim to confirm this observation. The reasons for the higher probability of damage with larger section seals are threefold. The first reason is due to gas transport. If the seal is fully saturated with gas upon decompression, the gas cannot escape as rapidly from a large section seal. This is because the gas has a greater quantity of material to diffuse through in the larger section seal.

The second reason is due to the higher probability of discovering a void or a rigid inclusion with a larger section seal. The void and rigid inclusion analysis detailed in Chapter 4 clearly shows that larger sections seals exhibit a larger and higher number of defects than smaller section seals. Besides this, most voids are found near the centre of seal sections, and this is even more apparent with larger sections.

The third reason is due to the stress field generated in larger sections. The compressive stress field generated due to contact with the counter faces of the housing do not penetrate as far through a larger section seal. Therefore the voids near the centre of these seals have

less constraint and so are allowed to expand more readily.

3.3.4 The Effect of Temperature

Temperature will greatly affect the performance of elastomer seals under explosive decompression conditions. An increase in temperature will increase the gas transport activity within the seal, therefore allowing the gas to escape more rapidly and reduce the pressure differential available for void expansions. However, the physical strength of the material is also greatly reduced at elevated temperatures that may cause the material to increase its elasticity and fracture at lower critical stress levels.

Therefore elevated temperature is both an advantage and a hindrance to the performance of elastomer seals, but one function will be dominant. This dominance must be determined before judgement can be made on whether increased temperature is an advantage or not.

3.4 DECOMPRESSION RIG DESIGN

The rig was designed such that twelve samples can be tested in any one test condition. The test rig consists of a series of stacked plates each containing a test O-ring. Outside each test O-ring are a leakage grooves and ports, which transports any leaked gases through to a water column. This groove is sealed with an additional O-ring (Figure 3.1).

Different plates (see Figure 3.2) are used depending on the required initial compression upon installation. The groove depth in the plates is varied to achieve the compression. Pins are positioned in the centre of the test groove to achieve the desired groove fill. The diameters of the pins vary according to the specified groove fill.

Careful consideration of initial compression and groove fill was required when designing the test plates. To achieve the specified test parameters, the tolerance placed on design dimensions were very tight. Taking worst case scenarios on upper and lower limits of

tolerance sometimes meant a variation of the test parameter by 20-30%.

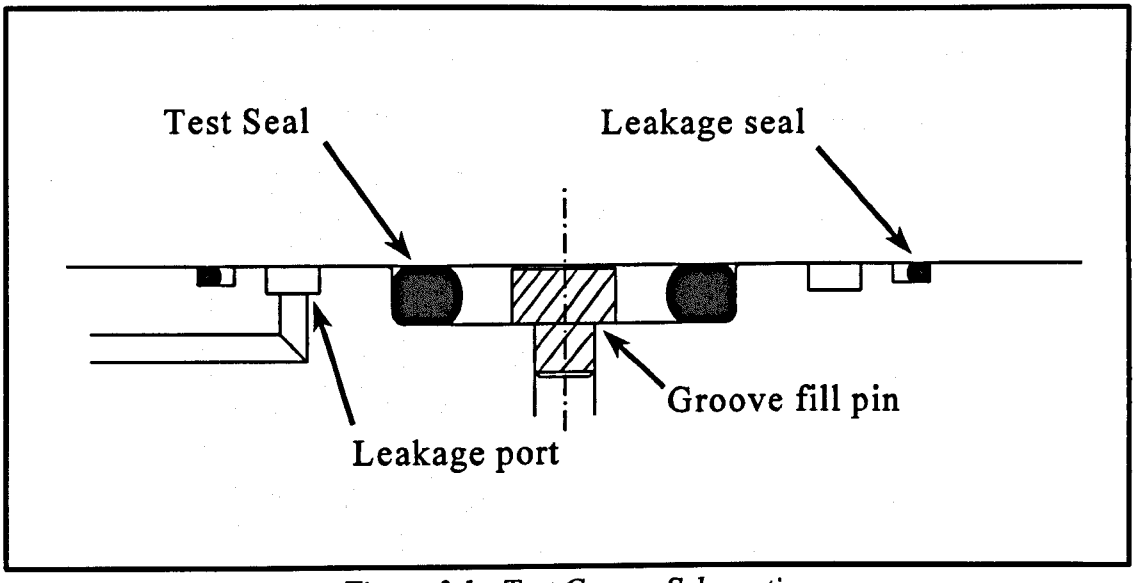

Figure 3.1 - Test Groove Schematic

A schematic view of the rig assembly is shown in Figure 3.3. Ten standard test plates are used, in addition to a thicker mid plate and a bottom plate. A top plate is used to allow the test gas to enter and to act as a counter face for the first standard test groove. On each of the thicker test plates (top, mid and bottom) are electrical band heaters to achieve the desired test temperature.

Three thermocouples are used under each band heater to monitor local temperature for the temperature controller. The three thermocouples are connected in parallel to ensure that the average temperature is taken over the whole rig. This is necessary because, if one band heater was used as a control and the band heater failed, the others would continue to apply heat and may cause localised heat damage.

The rig is placed in a cabinet purged with nitrogen to maintain a low oxygen content. The cabinet contains both an oxygen and a hydrocarbon sensor. The nitrogen is automatically switched on and off as the hydrocarbon and oxygen levels change within the cabinet to maintain a safe operating condition.

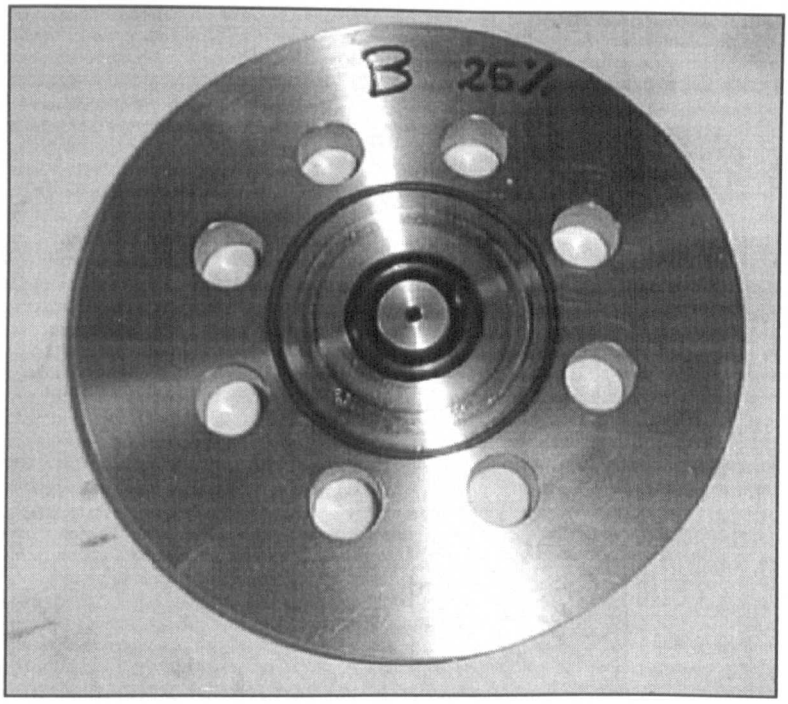

Figure 3.2 - Decompression rig plate with O-rings and pin

The pressure is applied using a high pressure gas pump, the pressure system is shown in Figure 3.6. The decompression regime is either instantaneous or a linear decompression over a 2 hour period. For the instantaneous case, the gas pressure is removed as quickly as possible. The two hour linear decompression is performed manually by monitoring the pressure using a data acquisition system. The system shows the pressure vs time plot and the required linear decompression line is superimposed on the plot. The operator is required to follow the line over the 2 hour decompression period by manually opening and closing the decompression needle valve. Having a monitor in the room with the valve during blowdown is necessary so that the operator can perform the decompression accurately (see Figure 3.5).

The degassing stage is carried out at the test temperature. This ensures that the gas will escape quickly to minimise the test time. Figures 3.4 and 3.5 show photographs of the test arrangement within the safe room.

After the decompression period and the degassing time, the seals are pressure tested to determine the level of damage. This is carried out by applying low pressure (35 bar) nitrogen. The leakage is determined by monitoring the number of bubbles formed in the water columns. This re-pressurisation test was not carried out on the 10mm section seals as these were tested at James Walker and Co. Ltd.

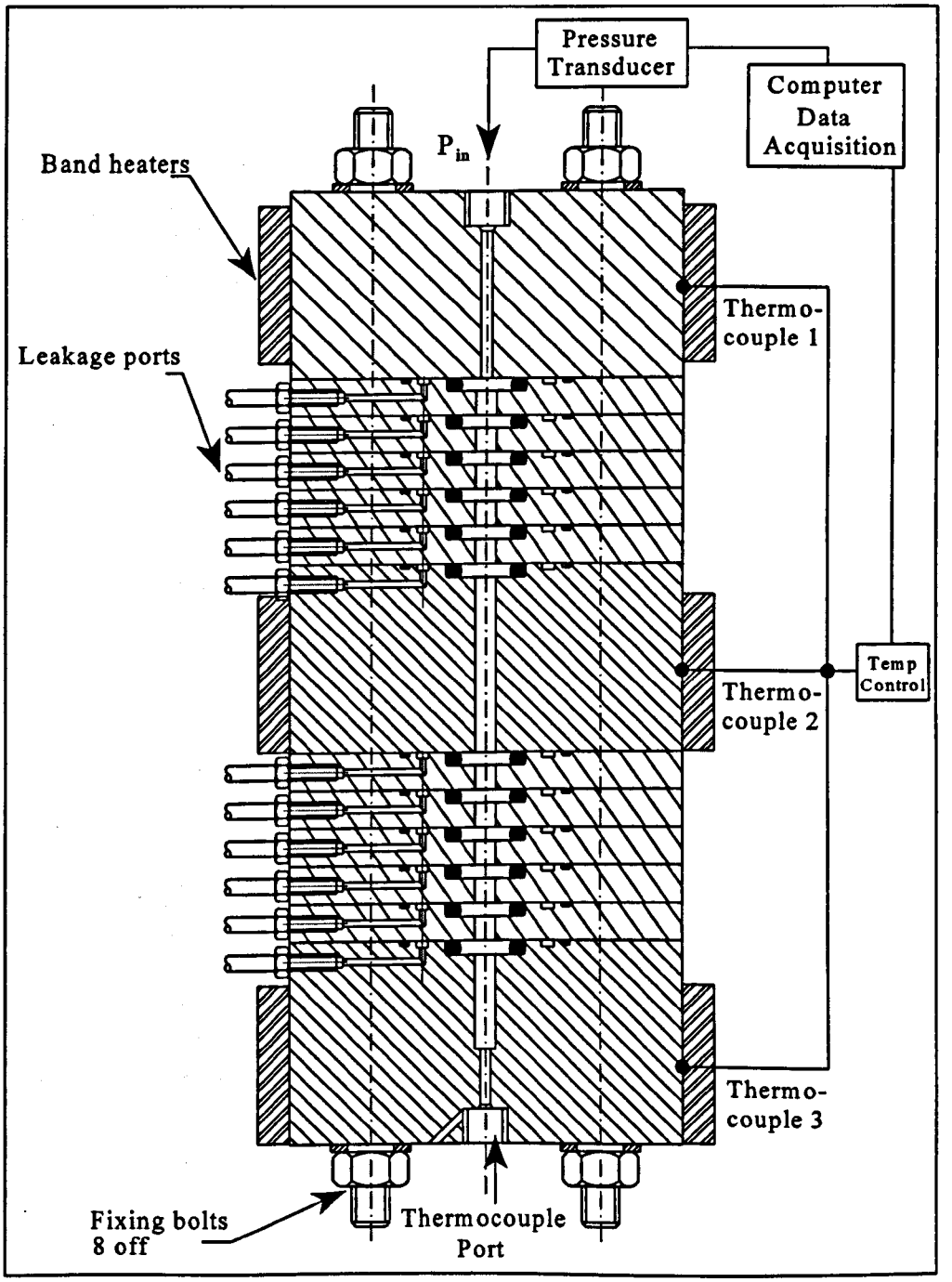

Figure 3.3 - Rig Assembly Schematic

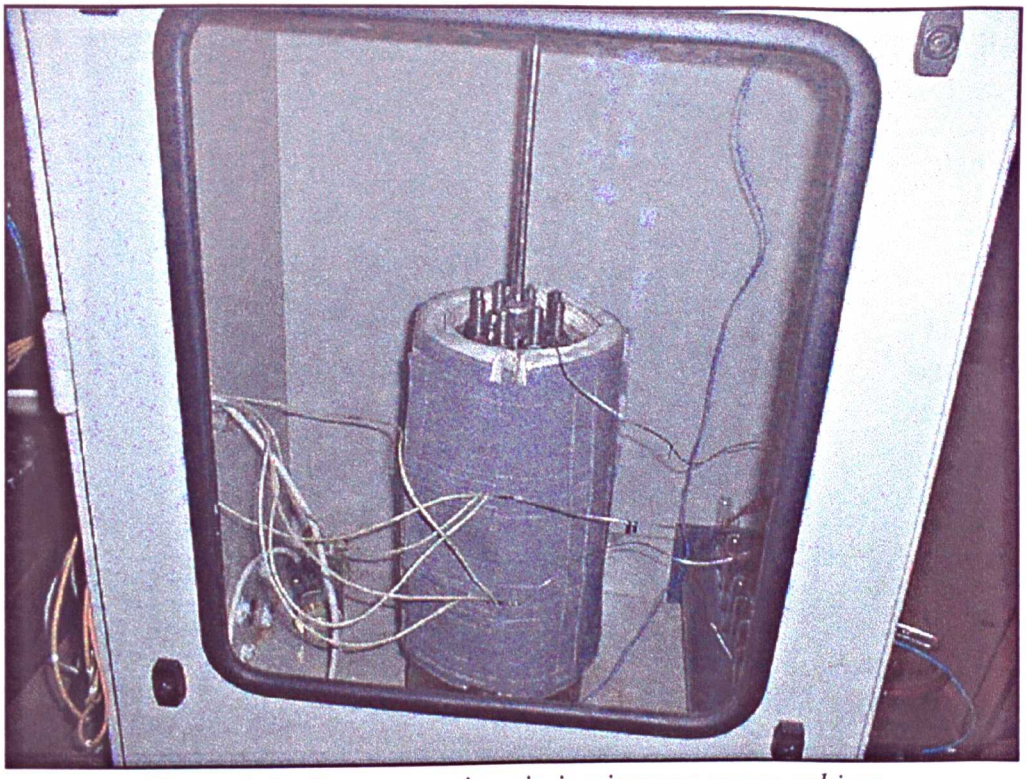

Figure 3.4 - Decompression rig in nitrogen purge cabinet

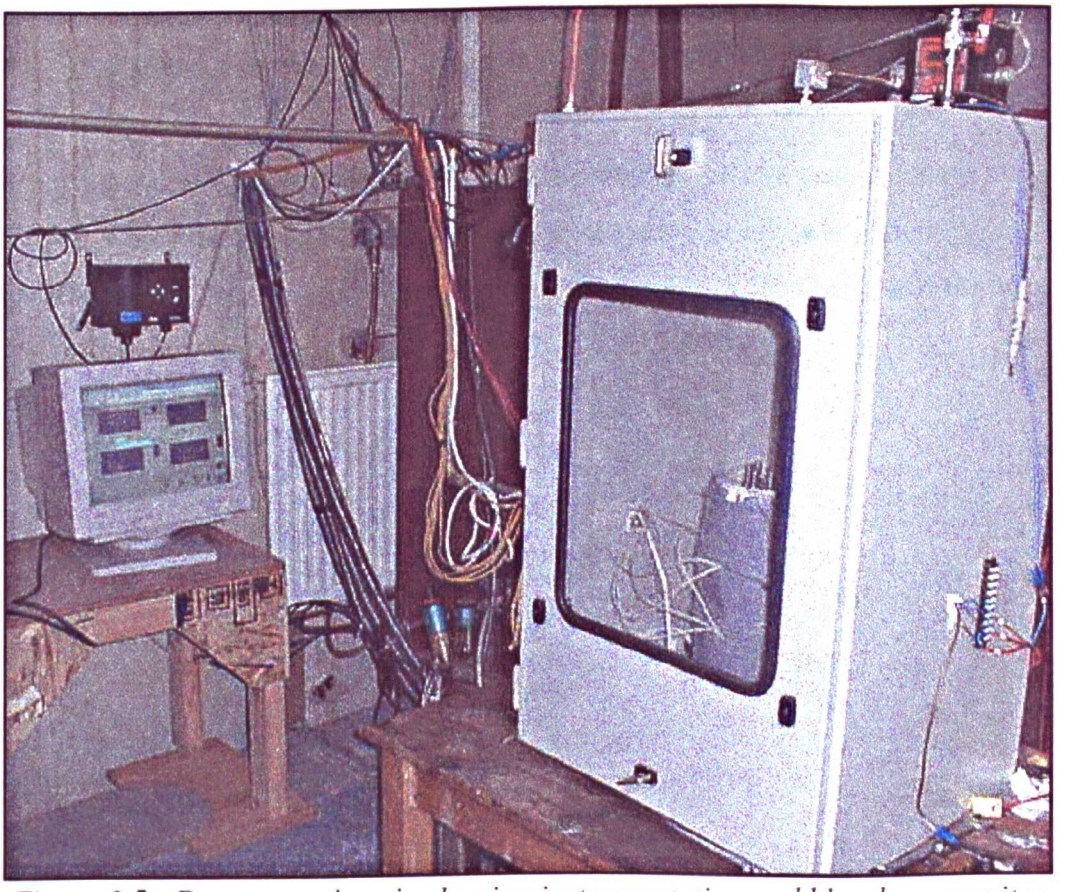

Figure 3.5 - Decompression rig showing instrumentation and blowdown monitor

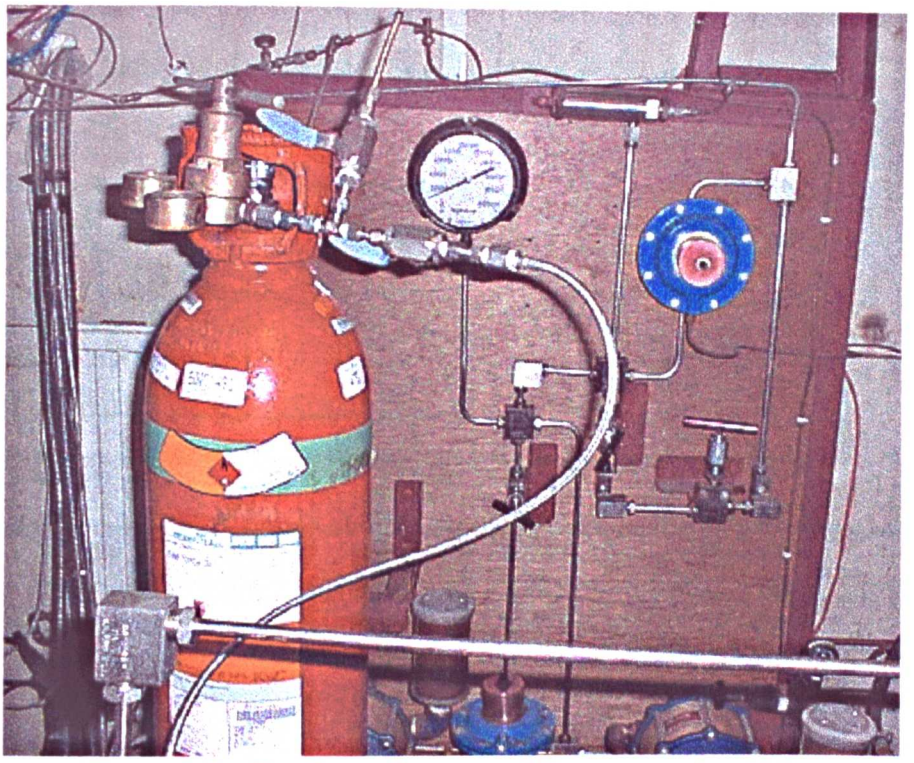

Figure 3.6 - Gas Pump System and Decompression Valve

3.5 O-RING ANALYSIS OF GROOVE FILL AND INITIAL COMPRESSION

The equations used for the calculation of initial compression and groove fill are shown in the Table 3.2. This spreadsheet determines the necessary groove dimensions, taking into account thermal expansions and dimensional tolerances of both the O-ring and the housing.

Table 3.2 - Spreadsheet example for the calculation of groove dimensions

Material		*fluoroelastomer*
O-RING SIZES	mm	inches
i.d.	**15.240**	*0.600*
i.d. tolerance,±	**0.230**	*0.0090551*
section diam.	**5.330**	*0.210*
section tolerance,±	**0.127**	*0.005*

INPUT DATA	Dimensions			
	min	max	nominal	Notation
Rod diam.	**8.000**	**8.200**	**8.100**	Dr
Bore diam.	**8.000**	**8.200**	**8.100**	Db
Groove diam.	**25.400**	**25.600**	**25.500**	Dg
Groove-length	**4.550**	**4.650**	**4.600**	L
O-ring i.d.	15.010	15.470	15.240	d
O-ring cord.	5.203	5.457	5.330	c
Max temp,°C	**100**	**100**	**100**	T
Vol.Exp. : Metal	***5.00E-05***	***5.00E-05***	***5.00E-05***	Em
Rubber	***4.80E-04***	***4.80E-04***	***4.80E-04***	Er

CONCENTRIC COMPONENTS

Seal volume: cold	1350.488	1538.039	1442.252	Vsc=(pc^2/4)*p .(d+c)
hot	1402.347	1597.099	1497.634	Vsh=Vsc*(1+Er*(T-Ta))
hot and swollen	1402.347	1597.099	1497.634	Vssw=Vsc*sw%+Vsh
Av volume: cold	2065.501	2159.987	2112.480	Vac=(p/4) .(Dg^2-Dr^2)*L
hot	2073.763	2168.627	2120.930	Vah=Vac*(1+Em*(T-Ta))
%-fill: cold	62.5%	74.5%	68.3%	Vc%=Vsc/Vac
hot	64.7%	77.0%	70.6%	Vh%=Vsh/Vah
hot and swollen	64.7%	77.0%	70.6%	Vsw%=Vssw/Vah

Seal wkg-height	8.600	8.800	8.700	h=(Dg-Dr)/2
Radial ext gap	-0.100	0.100	0.000	e=(Db-Dr)/2
Wkj O-ring cord.	5.203	5.457	5.330	c!=v (8*Vsc/p/(Dg+Dr)/p)
Linear int : cold	0.553	0.907	0.730	Ic=c!-h
hot	0.614	0.971	0.792	Ih=Ic+(T-Ta)*(c!*Er-h*Em)/3
hot and swollen	0.614	0.971	0.792	Isw=Ih+c!*sw%/3
swollen, cold & set	0.614	0.971	0.792	Isc=Isw*(1-s)/(1+Em/3)
% int : cold	10.6%	16.6%	13.7%	ic%=100*Ic/c
hot	11.8%	17.8%	14.9%	ih%=100*Ih/c
hot and swollen	11.8%	17.8%	14.9%	isw%=100*Isw/c
swollen, cold & set	11.8%	17.8%	14.9%	is% = 100*Isc/c

3.6 SEAL SATURATION AND AGEING

Before the decompression of the system can occur, it is necessary to ensure that the seal is fully saturated with gas. This occurs when the chemical potential of the gas within the seal equals the chemical potential of the pressurising gas. That is, when there is no net flow of gas in any direction.

To determine the time required for full saturation of the O-ring with the test gas, a transient gas permeation model was used. The method for this analysis is given in Chapter 8 - Transient Gas Diffusion Modelling. It was found that for a 5.33mm section seal, 48 hours in required for full saturation of the seal section. For the 10mm sections seal, this time is increased to 96 hours. This time determines the soak time required before the decompression can take place.

However, if the 10mm section seal is required to soak for a longer period of time, ageing effects could take place. Materials A and D are both nitrile based elastomers, material A being a hydrogenated nitrile. These elastomers are particularly susceptible to temperature ageing. If the 10mm and 5.33mm section decompression tests are to be directly comparable we need to ensure that no significant ageing has taken place as this can affect the explosive decompression performance of the seals. If ageing does take place between 48 and 96 hours, both sections should be soaked for 96 hours.

To determine if significant ageing takes place between 48 and 96 hours, a temperature ageing test was carried out. Both material A and D were placed in a test housing to replicate the conditions seen during the decompression tests. Two samples of each material were used for repeatability. Two test fixtures were used, one for the 48 hour test and the other for the 96 hour test. Both test fixtures were purged of air with nitrogen to ensure that no air ageing takes place. The fixtures were placed in an oven at 150°C (the decompression test upper temperature). One test fixture was removed after 48 hours and the second after 96 hours.

To determine if any significant ageing has taken place, the hardness of the seals was measured before and after the test. The results of the hardness tests of both the 48 and 96 hour aged samples are shown in Table 3.3.

Table 3.3 - Results of Temperature Ageing

Material	Time (hours)	Arrangement	Hardness (IRHD)				
			1	2	3	4	Average
D	0	New seal	75	74	74	74	74.25
D	48	Flange	77	77	76	78	77.00
D	96	Flange	78	77	77	77	77.25
D	48	Spigot	76	75	75	76	75.50
D	96	Spigot	76	74	77	77	76.00
A	0	New seal	90	89	91	90	90.00
A	48	Flange	87	87	86	87	86.75
A	96	Flange	86	86	87	87	86.50
A	48	Spigot	87	89	85	86	86.75
A	96	Spigot	84	87	84	85	85.00

The results clearly suggest that there is no significant hardness change between the 48 and 96 hour samples. Small variations in the results are due to experimental error and the inherent variability of the materials studied. As there is no hardness change, the 5.33mm section seals can be decompressed after a saturation time of 48 hours, with the 10mm section remaining at 96 hours.

The degas period required after the decompression will still be 48 hours for the 5.33mm section and 96 hours for the 10mm section seals.

3.7 DECOMPRESSION TEST PROCEDURE

1. Fit test and leakage O-rings to all plates (dry)
2. Fit groove fill adapters to all plates to achieve the desired groove fill.
3. Assemble the plates, end units and middle units and tighten bolts to required torque.
4. Fit high pressure fitting, thermocouples and band heaters.
5. Fit leakage connections
6. Fit insulation
7. Turn on nitrogen purge
8. Apply desired test pressure
9. Apply desired test temperature
10. Adjust pressure according to specification due to the temperature increase
11. Allow gas to saturate seal for 48/96 hours (depending on seal section)
12. Decompress according to test specification
    - 12a. Instantaneous - as rapidly as possible
    - 12b. Linear - linear reduction over decompression period
13. Allow to degas at test temperature for 48/96 hours (depending on seal section)
14. Turn off band heaters.
15. Turn off nitrogen purge.
16. Allow the rig to cool to room temperature.
17. Repressurise slowly with nitrogen to 35 bar and monitor any leakage through the leakage ports by monitoring the number of bubbles per minute.
18. Disassemble rig one plate at a time
19. Take a photo of each individual seal
20. Remove samples individually.
21. Place samples in a labelled bag with material, sample number and test condition.

3.8 RESULTS

The results of the decompression testing programme consist of observations of: -

- Average crack length
- Largest crack
- Number of cracks
- Orientation of cracks
- Leakage
- Position of cracks

These observations are taken over all samples and all test conditions. The average crack length, size of the largest crack and number of cracks are measured using a microscope and image analysis software. The general orientation of the cracks is observed during the microscopic analysis and is either radial, lateral or random. The leakage performance is determined from the repressurisation of the seals after the degassing period.

Typical decompression profiles for instantaneous and linear decompressions are shown in Figures 3.7 and 3.8. Note the step nature of the linear decompression due to the opening and closing of the decompression needle valve. The instantaneous decompression actually occurs over a period of approximately 20 seconds. This is due to the relatively small diameter of the vent pipework. The pipework diameter must be small to withstand the high pressures produced upon decompression. The results of the decompression tests are shown in Tables 3.4 to 3.9. The observations of crack locations correspond to the diagram in Figure 3.9.

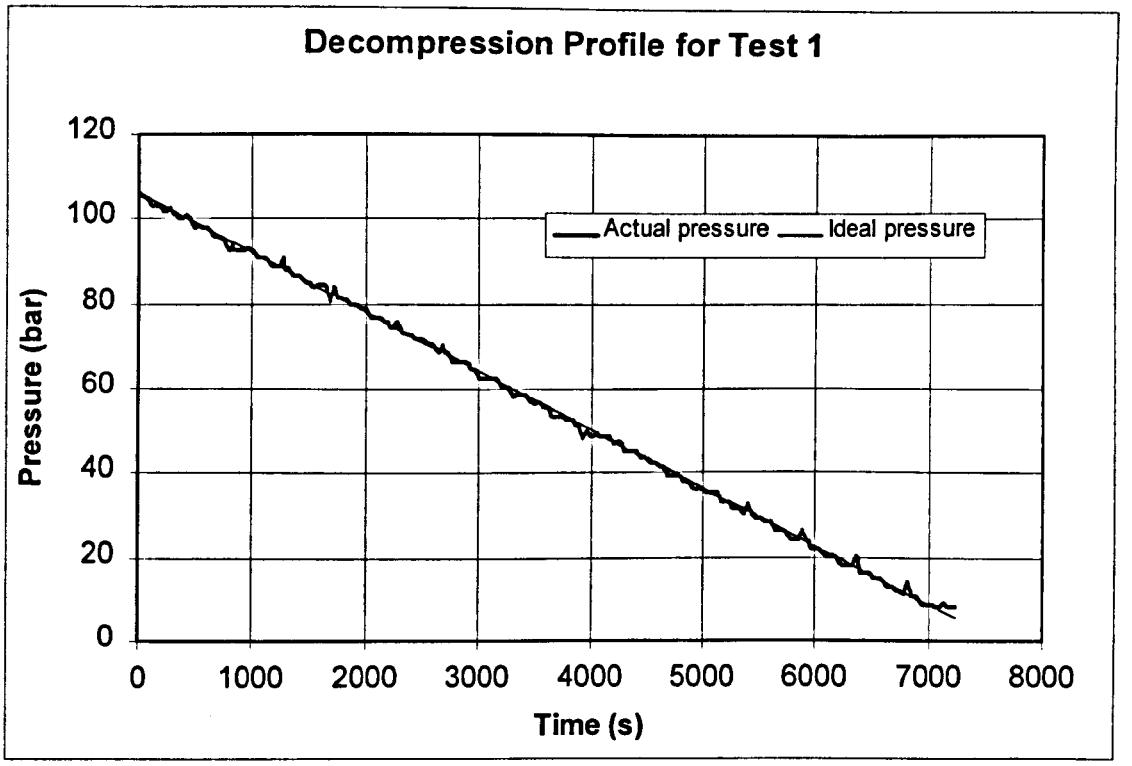

Figure 3.7 - 2 hour linear decompression profile for test 1

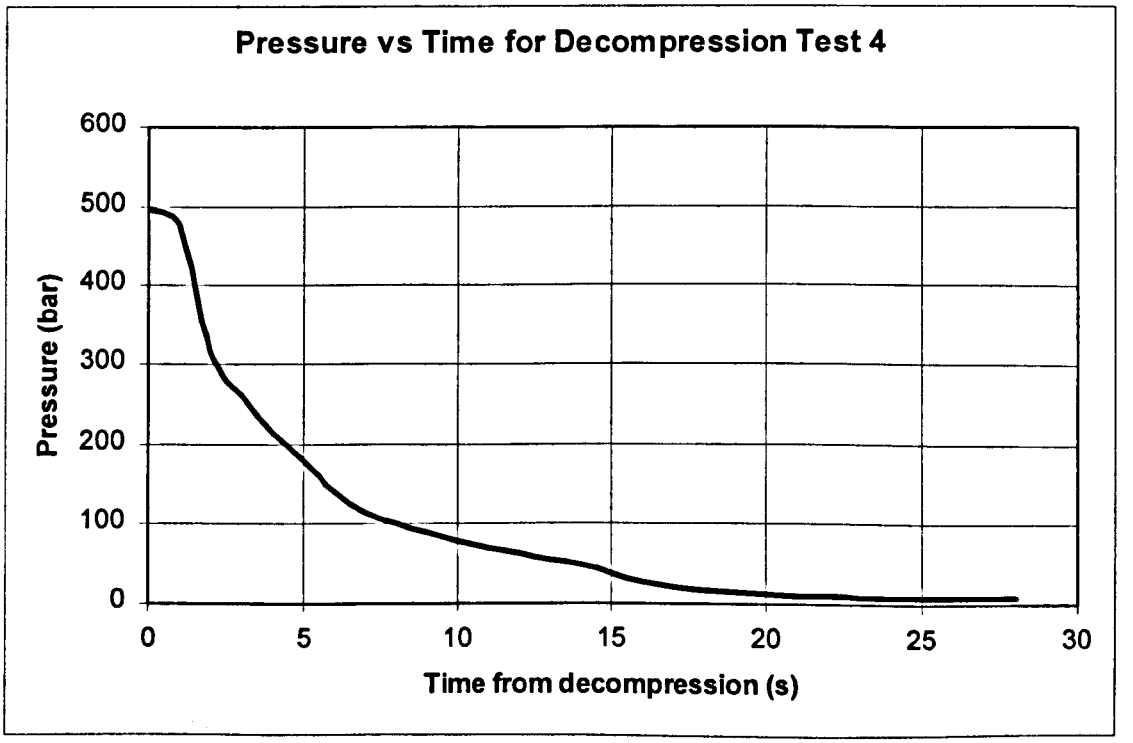

Figure 3.8 - Instantaneous decompression profile for test 4

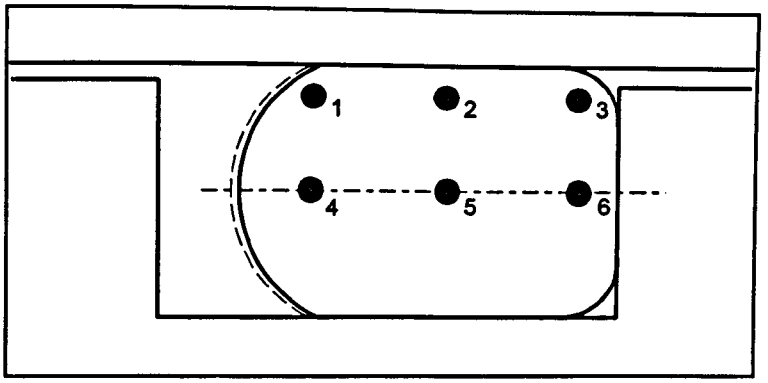

Figure 3.9 - Crack location points

Table 3.4 - Results of decompression test 1

Section = 5.33mm		*Groove fill = 70%*		*Compression = 15%*		
Pressure = 100 bar		*Temperature = 100°C*		*Decompression = 2 hours*		
Mat. Code	**Sample Number**	**Average Length (mm)**	**Largest Crack (mm)**	**Number of Cracks**	**Leakage?**	**General Observations**
A	1	0	0	0	No	-
A	2	0	0	0	No	-
A	3	0	0	0	No	-
A	**Average**	**0**	**0**	**0**	**No**	**-**
B	1	0	0	0	No	-
B	2	4.3	4.3	1	No	position 5, lateral
B	3	2.4	2.4	1	No	position 2, radial
B	**Average**	**3.4**	**3.4**	**1**	**No**	**-**
C	1	0	0	0	No	-
C	2	0	0	0	No	-
C	3	0	0	0	No	-
C	**Average**	**0**	**0**	**0**	**No**	**-**
D	1	0	0	0	No	-
D	2	0.2	0.2	1	No	position 5, lateral
D	3	0	0	0	No	-
D	**Average**	**0.2**	**0.2**	**1**	**No**	**position 5, lateral**

Table 3.5 - Results of decompression test 2

Section = 10mm		*Groove fill = 70%*		*Compression = 15%*		
Pressure = 400 bar		*Temperature = 150°C*		*Decompression = instantaneous*		
Mat. Code	**Sample Number**	**Average Length (mm)**	**Largest Crack (mm)**	**Number of Cracks**	**Leakage?**	**General Observations**
A	1	4.6	10	5.5	No	position 5, lateral
A	2	5.3	10	4.0	No	position 5, lateral
A	3	5.2	10	5.0	Yes	position 5, lateral
A	4	5.3	9.3	4.8	No	position 5, lateral
A	**Average**	**5.1**	**9.8**	**4.8**	**No**	**position 5, lateral**
B	1	6.1	Full	3.0	unknown	position 5, lateral
B	2	8.1	Full	2.8	unknown	position 5, lateral
B	3	6.3	8.5	2.8	unknown	position 5, lateral
B	4	8.2	9.3	2.8	unknown	position 5, lateral
B	**Average**	**7.2**	**9.5**	**2.9**	**unknown**	**position 5, lateral**
C	1	2.6	7.3	>20	No	position 5, lateral
C	2	3.0	6.3	>20	No	position 5, lateral
C	3	3.0	6.0	>20	No	position 5, lateral
C	4	3.0	7.8	>20	No	position 5, lateral
C	**Average**	**2.9**	**6.9**	**>20**	**No**	**position 5, lateral**
D	1	2.2	3.4	>50	unknown	all locations, lateral
D	2	2.8	3.6	>50	unknown	all locations, lateral
D	3	3.2	3.9	>50	unknown	all locations, lateral
D	4	2.9	3.5	>50	unknown	all locations, lateral
D	**Average**	**2.8**	**3.6**	**>50**	**unknown**	**all locations, lateral**

Table 3.6 - Results of decompression test 4

Section = 5.33mm		*Groove fill = 70%*		*Compression = 25%*		
Pressure = 500 bar		*Temperature = 100°C*		*Decompression = instantaneous*		
Mat. Code	**Sample Number**	**Average Length (mm)**	**Largest Crack (mm)**	**Number of Cracks**	**Leakage?**	**General Observations**
A	1	3.3	4.0	2	No	position 5, lateral
A	2	0.7	1.0	2	No	position 5, lateral
A	3	3.5	3.5	1	No	position 5, lateral
A	**Average**	**2.5**	**2.8**	**1.7**	**No**	**position 5, lateral**
B	1	Full	Full	2	No	position 5, lateral
B	2	3.7	Full	5	No	position 5, lateral
B	3	3.7	Full	3	No	position 5, lateral
B	**Average**	**4.2**	**Full**	**3.3**	**No**	**position 5, lateral**
C	1	3.4	Full	6	No	position 5, lateral
C	2	4.5	Full	7	No	position 5, lateral
C	3	Full	Full	4	No	position 5, lateral
C	**Average**	**4.4**	**Full**	**5.7**	**No**	**position 5, lateral**
D	1	2.4	Full	>40	Yes	all positions, lateral
D	2	Full	Full	>40	Yes	all positions, lateral
D	3	Full	Full	>40	Yes	all positions, lateral
D	**Average**	**4.4**	**Full**	**>40**	**Yes**	**all positions, lateral**

Table 3.7 - Results of decompression test 5

Section = 10mm		*Groove fill = 90%*		*Compression = 25%*		
Pressure = 100 bar		*Temperature = 150°C*		*Decompression = 2 hours*		
Mat. Code	**Sample Number**	**Average Length (mm)**	**Largest Crack (mm)**	**Number of Cracks**	**Leakage?**	**General Observations**
A	1	0	0	0	unknown	-
A	2	0	0	0	unknown	-
A	3	0	0	0	unknown	-
A	4	0	0	0	unknown	-
A	**Average**	**0**	**0**	**0**	**unknown**	**-**
B	1	0.3	0.4	5	unknown	surface, very small
B	2	5.2	5.5	2	unknown	position 5, lateral
B	3	0.3	0.4	5	unknown	surface, very small
B	4	0	0	0	unknown	-
B	**Average**	**1.9**	**2.1**	**4**	**unknown**	**-**
C	1	6.0	10.0	3	unknown	position 5, lateral
C	2	0	0	0	unknown	-
C	3	2.0	7.0	2	unknown	position 5, lateral
C	4	7.8	10.0	4	unknown	position 5, lateral
C	**Average**	**5.3**	**9.0**	**3**	**unknown**	**position 5, lateral**
D	1	0	0	0	unknown	-
D	2	1.5	1.5	1	unknown	radial - mould line
D	3	0	0	0	unknown	-
D	4	5.5	5.6	2	unknown	position 5, lateral
D	**Average**	**3.5**	**3.6**	**1.5**	**unknown**	**-**

Table 3.8 - Results of decompression test 6

Section = 10mm		*Groove fill = 70%*		*Compression = 15%*		
Pressure = 100 bar		*Temperature = 100°C*		*Decompression = 2 hours*		
Mat. Code	**Sample Number**	**Average Length (mm)**	**Largest Crack (mm)**	**Number of Cracks**	**Leakage?**	**General Observations**
A	1	0.3	0.3	1	unknown	position 4, radial
A	2	6.0	6.0	1	unknown	position 5, lateral
A	3	0.5	0.5	1	unknown	position 6, radial
A	4	0.1	0.1	2	unknown	position 5, lateral
A	Average	1.7	1.7	1.3	unknown	-
B	1	0.1	0.1	3	unknown	position 5, lateral
B	2	0.2	0.3	7.5	unknown	surface, radial
B	3	0.2	0.3	1.5	unknown	position 5, lateral
B	4	1.5	3.5	3	unknown	position 5, lateral
B	**Average**	**0.5**	**1.1**	**3.8**	**unknown**	**position 5, lateral**
C	1	7.2	8.0	1.3	unknown	position 5, lateral
C	2	4.5	4.5	1.0	unknown	position 5, lateral
C	3	7.0	7.0	1.0	unknown	position 4&5, lateral
C	4	6.3	7.3	1.5	unknown	position 5, lateral
C	**Average**	**6.3**	**6.7**	**1.2**	**unknown**	**position 5, lateral**
D	1	3.4	4.1	6.3	unknown	position 5, lateral
D	2	3.4	4.8	6.0	unknown	position 5, lateral
D	3	3.3	4.9	6.0	unknown	position 5, lateral
D	4	3.1	5.3	5.8	unknown	position 5, lateral
D	**Average**	**3.3**	**4.8**	**6.0**	**unknown**	**position 5, lateral**

Table 3.9 - Results of decompression test 7

Section = 5.33mm		*Groove fill = 90%*		*Compression = 15%*		
Pressure = 500 bar		*Temperature = 150°C*		*Decompression = instantaneous*		
Mat. Code	**Sample Number**	**Average Length (mm)**	**Largest Crack (mm)**	**Number of Cracks**	**Leakage?**	**General Observations**
A	1	3.5	3.6	1.3	No	position 5, lateral
A	2	4.2	4.2	1.0	No	position 5, lateral
A	3	3.6	3.9	1.3	No	position 5, lateral
A	**Average**	**3.8**	**3.9**	**1.2**	**No**	**position 5, lateral**
B	1	0	0	0	No	-
B	2	0	0	0	No	-
B	3	0	0	0	No	-
B	**Average**	**0**	**0**	**0**	**No**	**-**
C	1	0	0	0	No	-
C	2	0	0	0	No	-
C	3	0	0	0	No	-
C	**Average**	**0**	**0**	**0**	**No**	**-**
D	1	2.8	3.0	1.5	No	position 5, lateral
D	2	3.1	3.8	2.0	No	position 5, lateral
D	3	3.6	3.6	1.0	No	position 5, lateral
D	**Average**	**3.2**	**3.5**	**1.5**	**No**	**position 5, lateral**

Some examples of decompression damage before sectioning of the seals are shown in Figures 3.10 and 3.11. Photographs of sample seal sections, clearly showing cracks, are given in Figures 3.12 to 3.19.

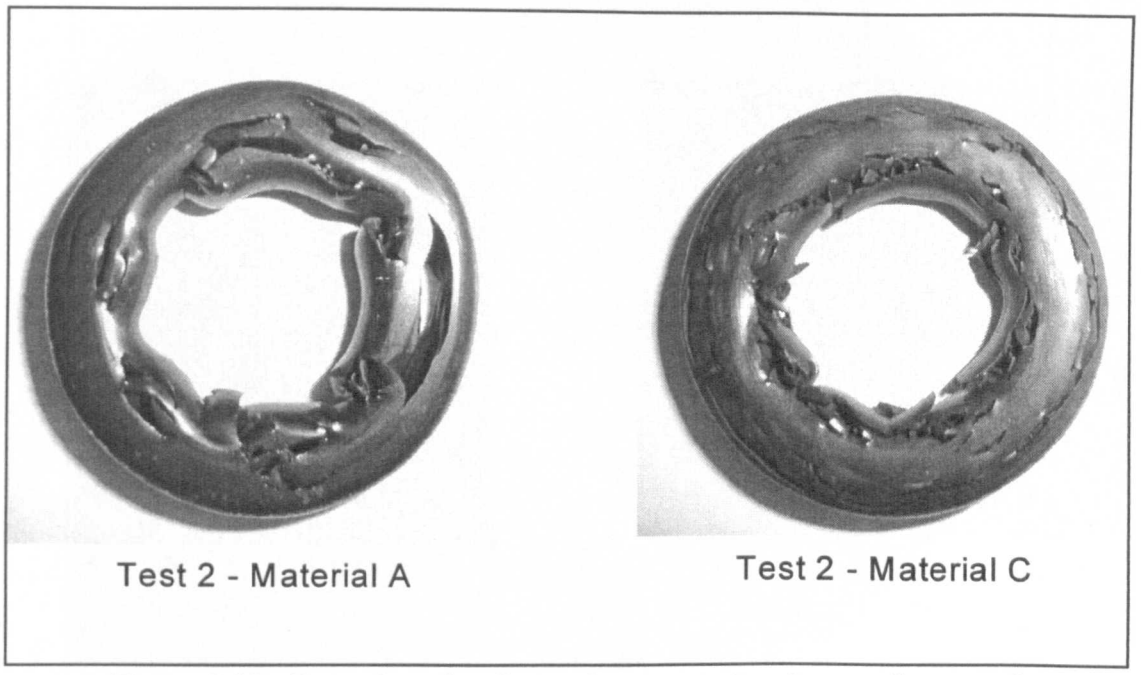

Figure 3.10 - Examples of explosive decompression damage from test 2

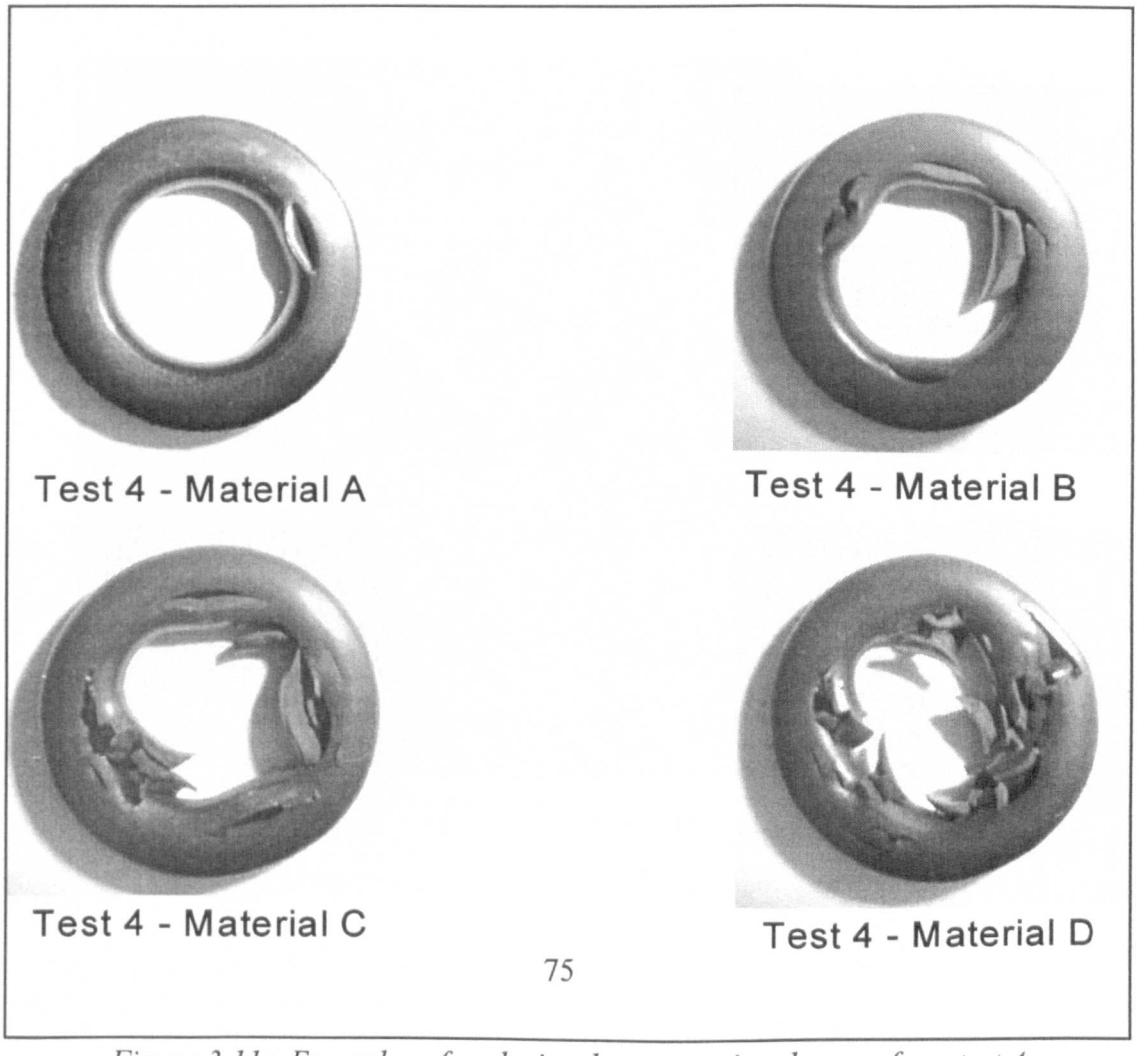

Figure 3.11 - Examples of explosive decompression damage from test 4

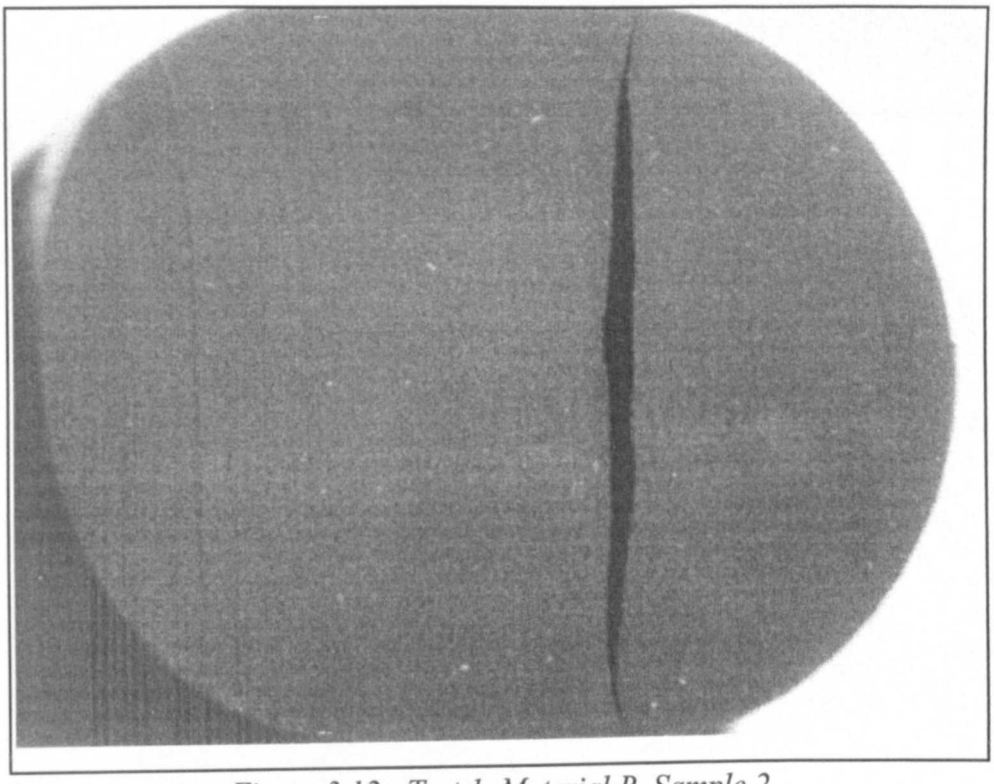

Figure 3.12 - Test 1, Material B, Sample 2

Figure 3.13 - Test 2, Material C, Sample 2

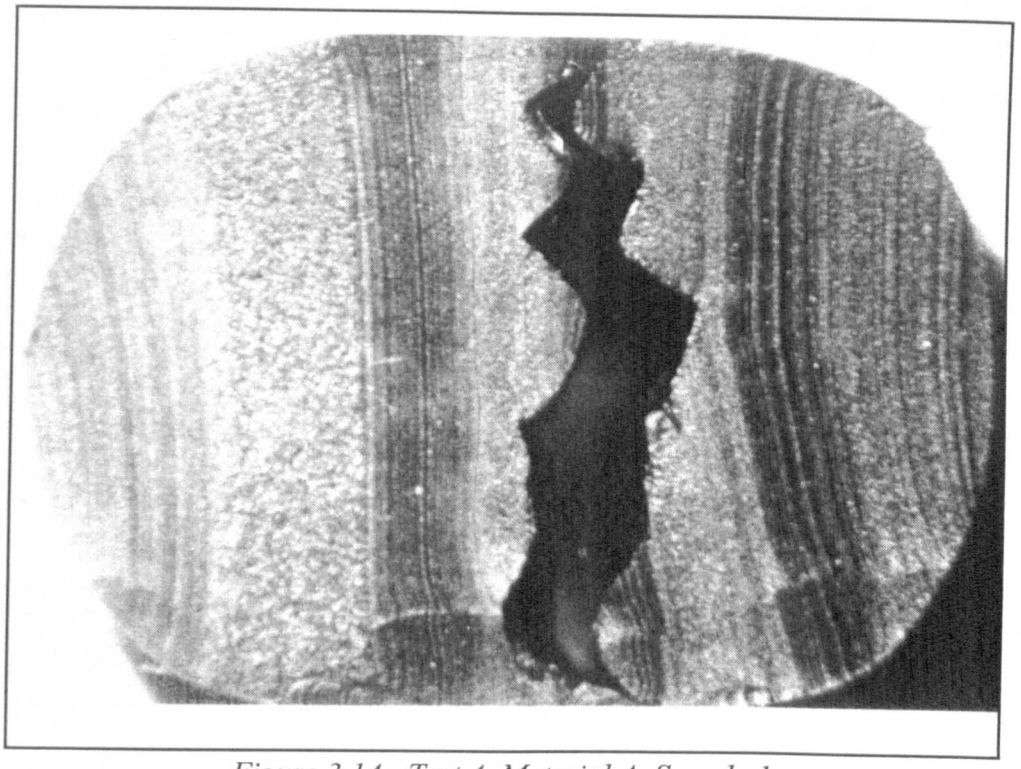

Figure 3.14 - Test 4, Material A, Sample 1

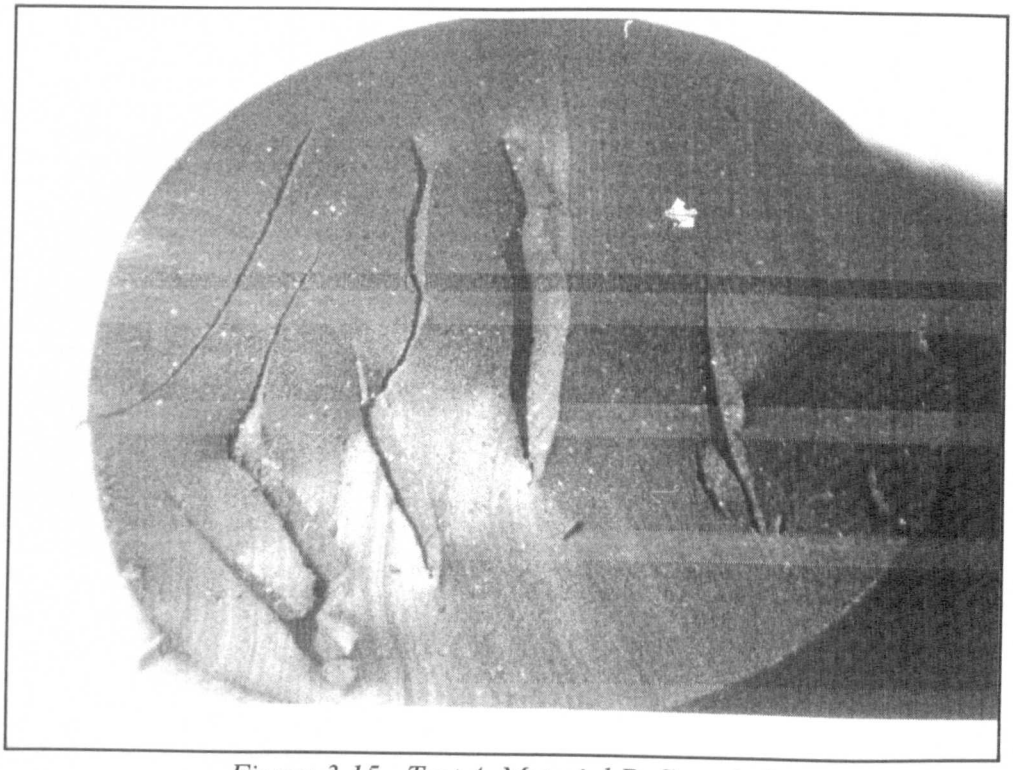

Figure 3.15 - Test 4, Material D, Sample 1

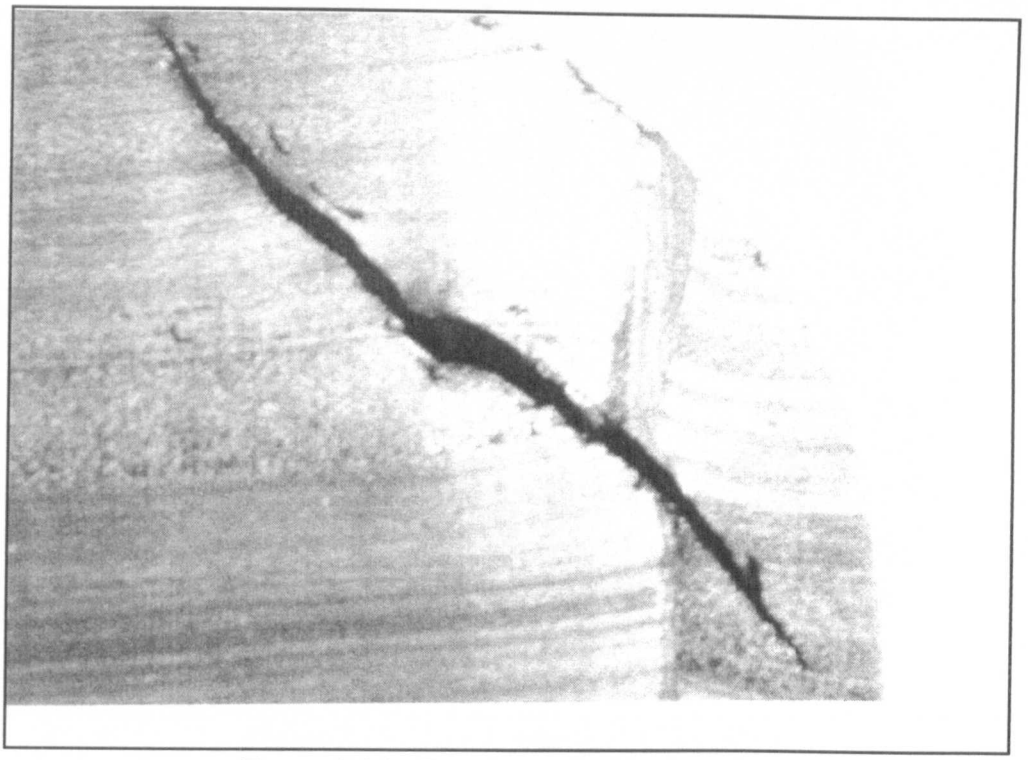

Figure 3.16 - Test 6, Material A, Sample 2

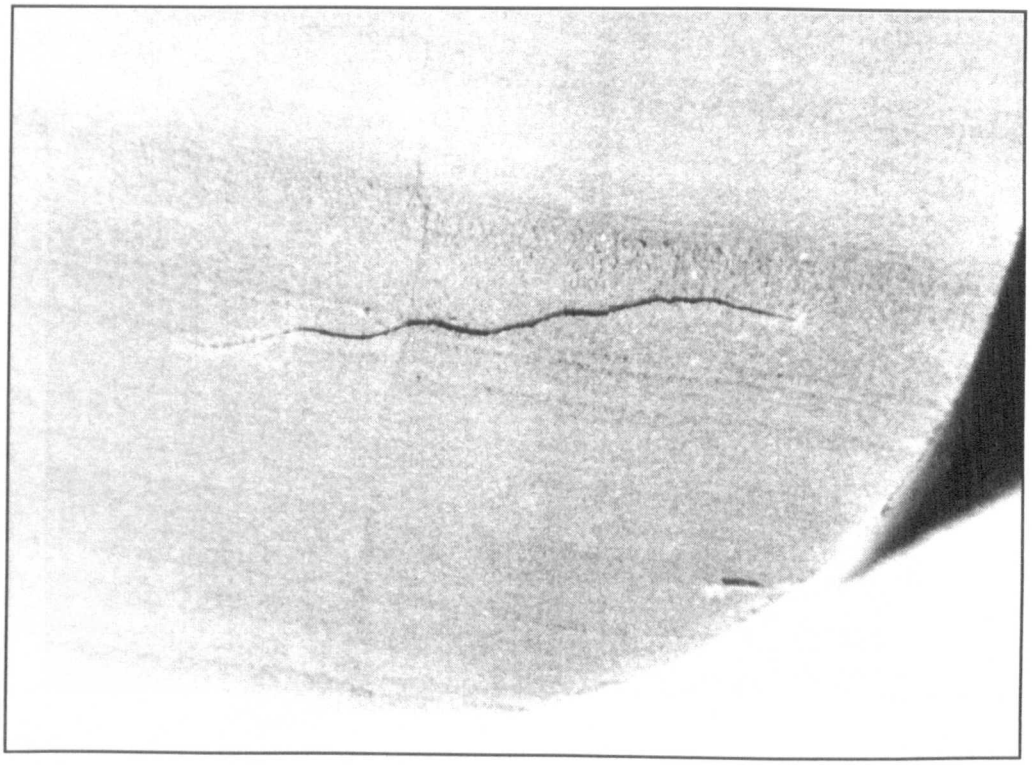

Figure 3.17 - Test 6, Material B, Sample 4

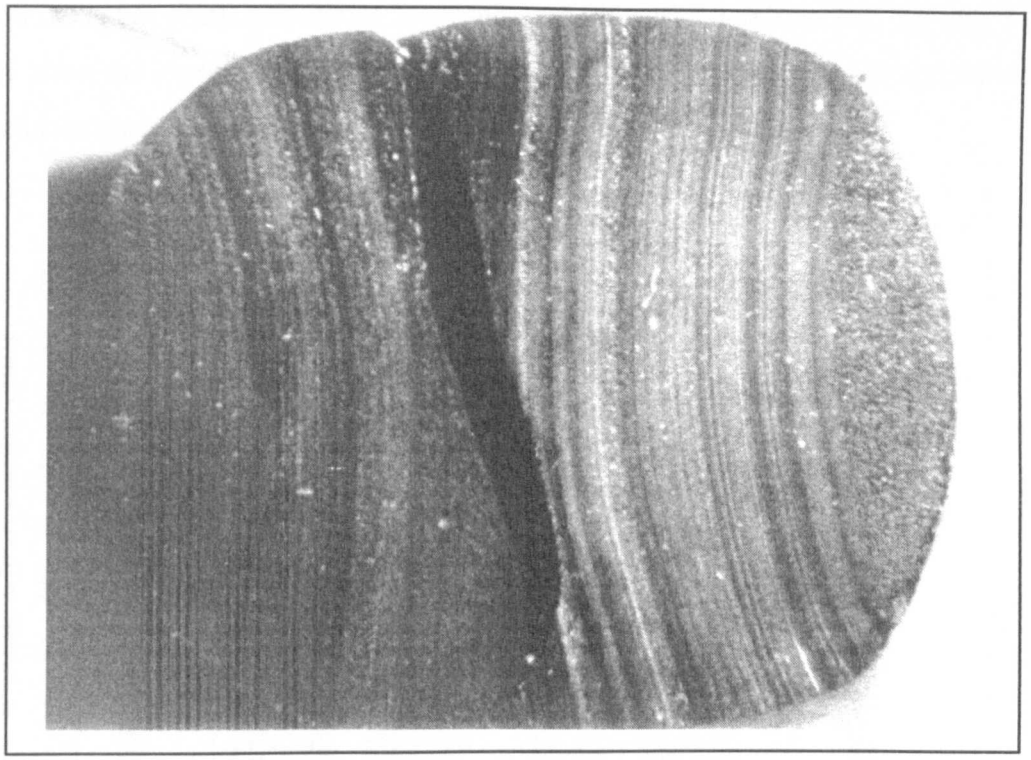

Figure 3.18 - Test 7, Material A, Sample 1

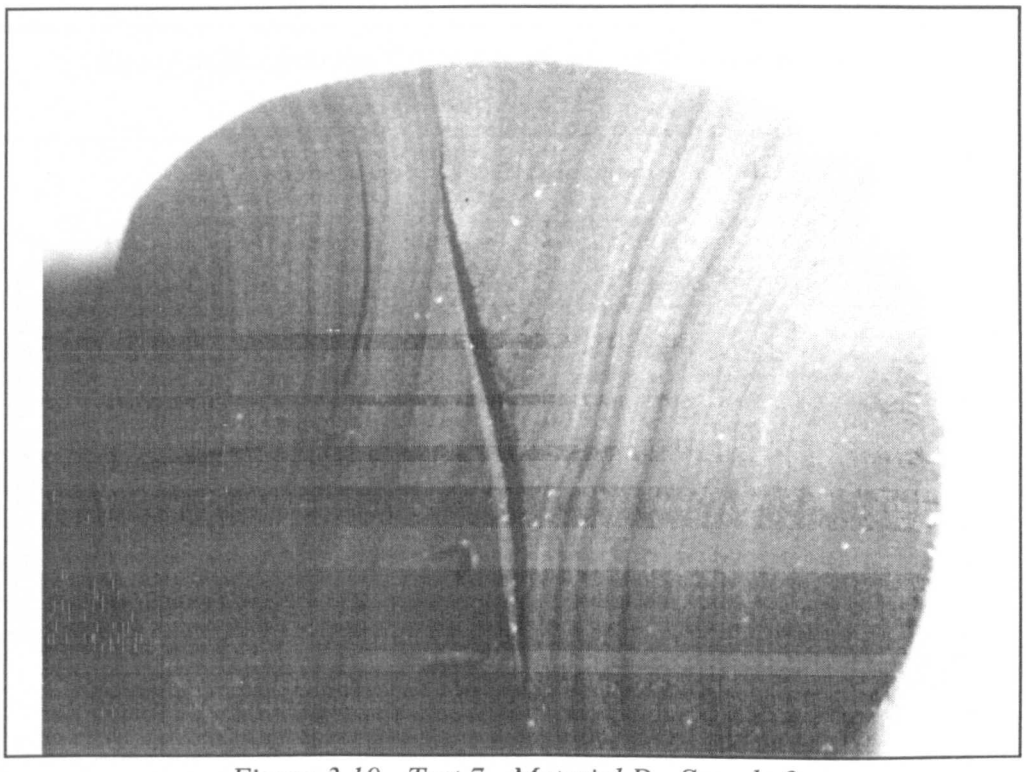

Figure 3.19 - Test 7 - Material D - Sample 2

The following bar charts summarise the results shown in Tables 3.4 to 3.9. Figures 3.20 to 3.22 show the average crack length, average largest crack length and average number of cracks for each test condition.

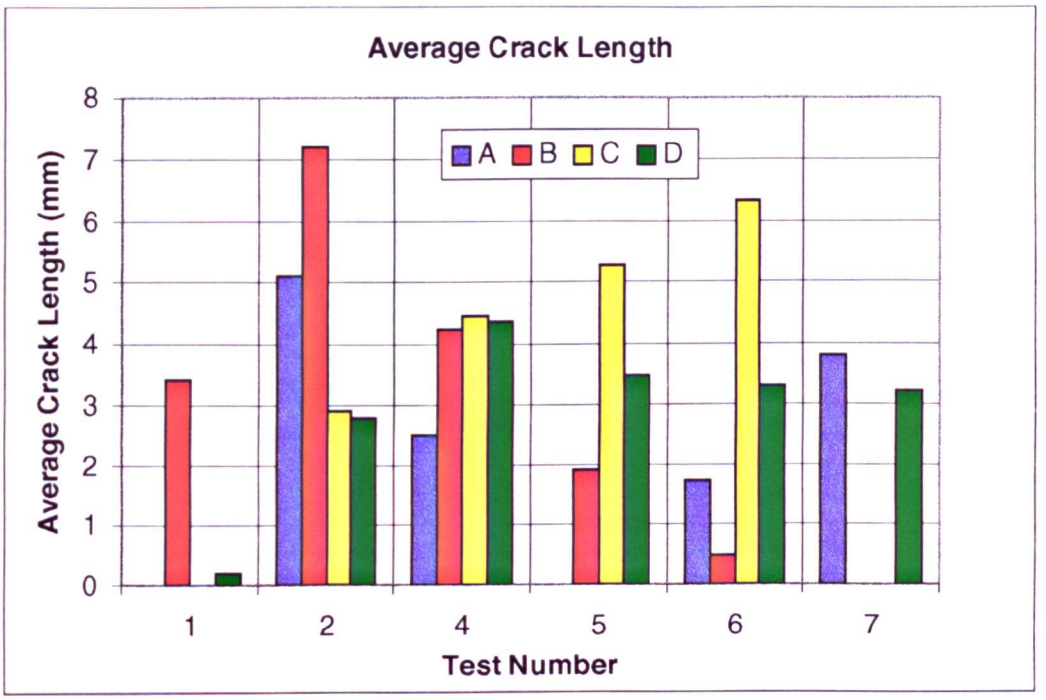

Figure 3.20 - Average Crack Length for all Test Conditions

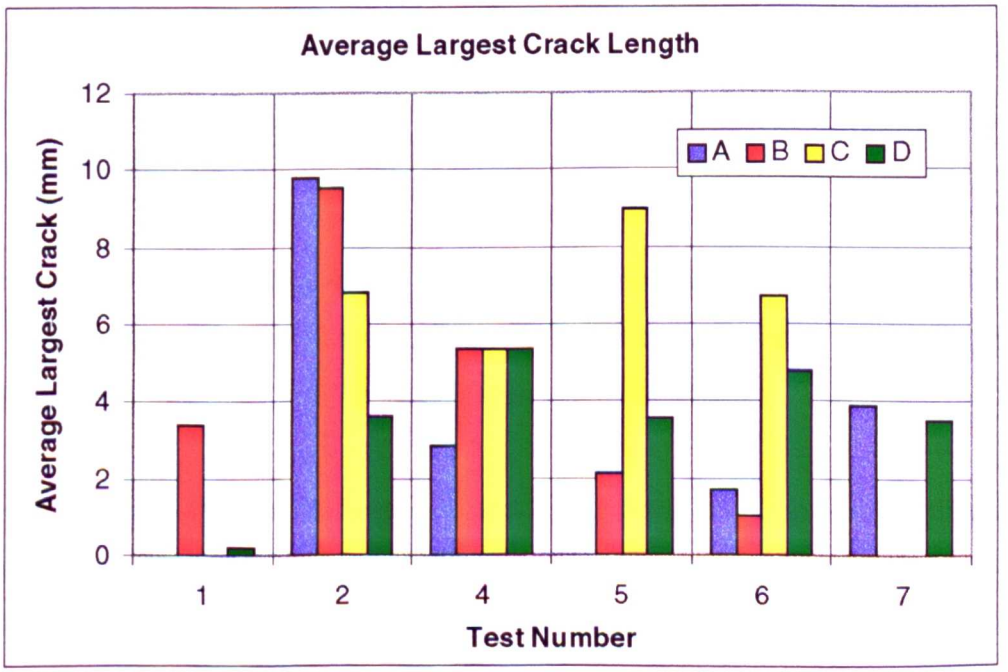

Figure 3.21 - Average Largest Crack Length for all Test Conditions

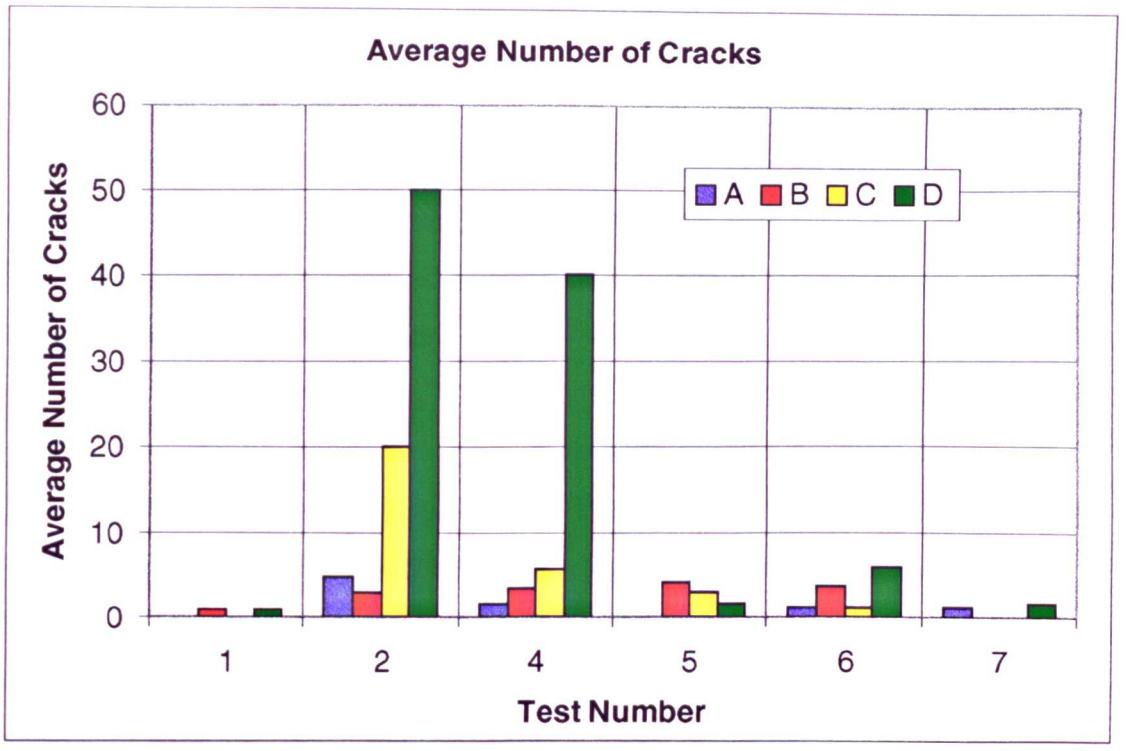

Figure 3.22 - Average Number of Cracks for all Test Conditions

3.9 DISCUSSION

This testing programme was devised to determine how the seals under study perform under explosive decompression conditions. The information gathered from the testing programme is used to validate the modelling methodology.

The results clearly show that, in general, material A showed the best resistance across the test programme. Material D clearly shows the lowest resistance to damage. The number of cracks was much higher for material D than for all others.

In general cracks were formed perpendicular to the direction of pressure application and usually in the centre of the seal section. Very few seals actually caused a measurable leakage when re-pressurised with nitrogen at 35 bar. It is possible that after several decompression cycles, which is generally what occurs in practice, leakage will occur.

The theory regarding section size affecting the performance of elastomer seals under decompression conditions has been confirmed. Tests 1 and 6 have the same operational environments except for the seal section. The comparison of the results from tests 1 and 6 shows that the larger section seal exhibits much higher crack numbers and lengths than the smaller section. All materials failed for the 10mm section seal whereas only material B failed with the 5.33mm section.

Obvious controlling parameters such as decompression time and pressure show a considerable effect on the extent of damage. The results from test 5, which is a high initial compression and high groove fill test, show that damage has occurred. However, it is thought that the cracks formed in the seals are due to stress cracking and not explosive decompression. The stresses induced in the seal section under high compression and groove fill are considerable and may therefore cause premature failure.

The effect of ageing and therefore degradation of the physical properties was confirmed as negligible between the 48 and 96 hour tests. This enabled direct comparison between the 5.33mm and the 10mm section tests.

The definition of instantaneous decompression used in the testing programme is inaccurate as the actual decompression period is approximately 20 seconds. However, this is thought to be negligible in comparison with the longer period of 2 hours.

The testing programme has provided the necessary data to compare directly with the model to determine the model accuracy in predicting explosive decompression damage.

3.10 CONCLUSIONS

The main conclusion from this programme of testing work is that material A gives the greatest resistance to explosive decompression damage over the range of differing environments. As expected, material D shows the least resistance to damage. Materials B and C show similar levels of resistance, although material C is much more prone to stress cracking as the material is much harder and therefore less elastic.

It is clear from the test results that the primary failure position and direction is lateral, initiating at the centre of the seal section. If multiple cracks exist, the orientation of the crack propagation remains perpendicular to the direction of pressure application. In general, the cracks are very large and in all but the most extreme cases, exhibit only a small number of cracks.

The larger section seals are more likely to fail under explosive decompression conditions than the smaller section seals. Decompression time has a significant impact on the damage resistance of the elastomer with the instantaneous decompression causing much greater levels of damage than the two hour decompression.

Most of the seals tested did not cease to function as a sealing medium. Only one seal tested actually caused leakage upon re-pressurisation, suggesting that explosive decompression damage does not necessarily imply failure of the seal function.

The tests carried out with a high groove fill showed limited damage. The downside of high groove fill and/or high initial compression is that stress cracking could occur within the seal section due to the increased deformation.

3.11 CHAPTER SUMMARY

The testing programme has determined the resistance of materials A, B, C and D to various operational environments and decompression regimes. Material A (hydrogenated nitrile) showed the greatest resistance and material D (nitrile) showed the least resistance.

Most cracks were formed perpendicular to the direction of applied pressure. Larger section seals are more likely to develop cracks than smaller section seals. The single decompression carried out during the test programme did not, in general, cause the seal to stop functioning as a seal. Groove fill and initial compression affect the explosive decompression resistance.

The data from the test programme is used to validate the model.

CHAPTER 4 - VOID AND RIGID INCLUSION ANALYSIS

4.1 INTRODUCTION

Voids and rigid inclusions within the elastomer matrix of O-ring seals are considered a major contributing factor to failure under explosive decompression conditions. It was necessary, therefore, to analyse a number of representative materials to study the size and distribution of voids and rigid inclusions.

The theory surrounding explosive decompression failure puts great emphasis on the 'critical pressure' required for void expansion. If this critical pressure is exceeded or maintained the precursor void will expand indefinitely. In reality, as the void volume increases, the pressure maintaining the expansion will decrease accordingly and so the void may inflate and deflate without causing damage. This is dependent on the competitive diffusion of gas into and out of the void. The critical pressure will be largely dependent on the initial radius of any precursor sites for void inflation due to the surface tension effects of smaller voids. Therefore, the smaller the void, the higher the pressure required to overcome the surface tension forces.

The location of voids and rigid inclusions within the seal section is also an important aspect of the modelling process. The voids and rigid inclusions that are close to the pressure face of the O-ring will be subjected to a much lower pressure differential. This is owing to the gas transport process during decompression. The gas first diffuses out of the seal from the pressure interface (free surface) and then progressively through the seal section. Voids and rigid inclusions that are farthest away from the pressure face will be subjected to a much higher pressure differential as the gas cannot diffuse out as quickly.

As part of the modelling section of the research, it is necessary to know the initial size, location and proximity of voids within an elastomer matrix. The purpose of the void and

rigid inclusion analysis is to determine statistically the average size density and location of voids in each of the commercially available materials being studied.

The results are studied and conclusions drawn based on the material's overall performance with respect to parameters believed to cause damage in elastomers.

4.2 SAMPLE PREPARATION

The void and rigid inclusion size distribution analysis programme involved the study of eleven representative materials, generally for use in HP/HT (High Pressure/High Temperature) environments such as downhole applications. One material (material D) is a standard nitrile-based elastomer, which is used as a comparator as it is known to fail readily under explosive decompression conditions. The other materials are all commercially available materials of differing section sizes.

Table 4.1 - Material Identification

MAT ID CODE	MATERIAL ID No.	BASE MATERIAL	NUMBER OF SAMPLES	SECTION DIA. (mm)
C	1	Fluorocarbon (FKM)	6	5.33
	2	Fluorocarbon (FKM)	3	10.50
B	3	Fluorocarbon (FKM)	6	5.33
	4	Fluorocarbon (FKM)	3	10.50
	5	Fluorocarbon (FKM)	4	14.00
-	6	Ethylene Propylene Diene Rubber (EPDM)	6	5.33
-	7	Hydrogenated Nitrile Rubber (HNBR)	5	5.33
-	8	Fluorocarbon (FKM)	6	5.33
D	9	Nitrile (NBR)	6	5.33
A	10	Hydrogenated Nitrile Rubber (HNBR)	6	5.33
	11	Hydrogenated Nitrile Rubber (HNBR)	4	10.50

Six samples of each of the 5.33mm section O-rings were prepared, and either three or four of the larger section seals. The material identification codes (i.e. A, B and C) are used in further testing programmes and indicate the same material, but of differing section sizes.

4.2.1 Sample cutting technique

An initial study of cutting techniques for elastomer O-rings revealed that upon slicing through the section with a scalpel blade, the surface of the material flattened, masking the surface features. Therefore a technique was devised by which the material surface features were not affected.

The technique involves cutting the O-ring radially and opening it out into a single length. The O-ring is then placed under tensile strain and clamped in position using the cutting fixture shown in Figure 4.1. The cut is then made perpendicular to the length with a lubricated scalpel blade such that the surface of the elastomer section is always pulling away from the cutting blade. From experimental observations it was found that a tensile strain of between 15-20% was adequate to give a surface where the features were not obscured. If the strain was increased beyond this level, tearing occurred during the cutting process.

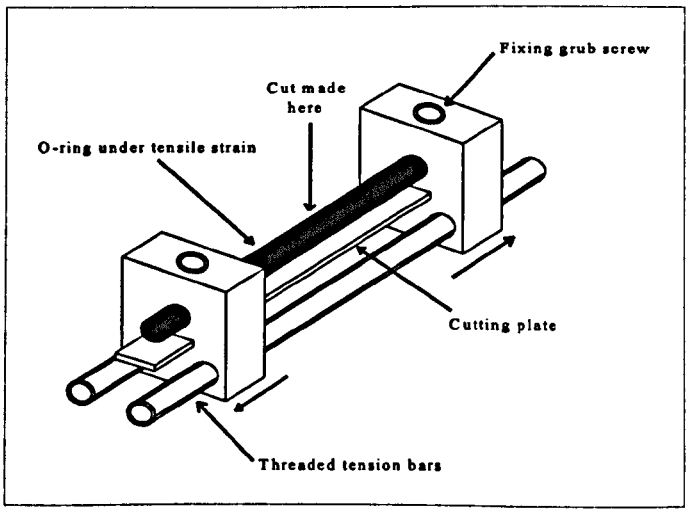

Figure 4.1 - O-ring Cutting Fixture

The surfaces of the elastomer section are then dried with compressed air and the sample is removed. A thin section is then cut as normal from the sample and an identification mark is applied to the normally cut side of the specimen. This circular section is then cut into quadrants and one section is retained for analysis. The single quadrant is then sprayed with cleanser and dried using compressed air to remove any surface contaminants or charged dust particles. The samples are then handled with anti-static tweezers and placed in a labelled sample bag.

4.3 IMAGE ANALYSIS

The analysis of voids and inclusions in elastomeric materials is difficult by virtue of the nature of the material itself. With respect to elastomer seals, the standard colour of an O-ring is black and the void or rigid inclusion is also black or a shade of grey. Therefore using any microscopic analysis technique is difficult.

4.3.1 Analysis Methodology

The approach for the analysis of voids and rigid inclusions was to use a standard optical microscope with a CCTV camera attached to allow images to be captured into image analysis software. The sample is attached to a slide by means of plasticine and made square using a press. The O-ring quadrant is then scanned systematically using a grid system and the number, sizes and location of voids and rigid inclusions are recorded for each grid square.

Each grid is examined with the optical microscope set at 40x magnification that through calibration gives a resolution of 1 pixel = 0.208 μm on the image analysis software. The software includes many image transformation functions used to enhance the image if required. Upon capturing and enhancing the image, the software is then used to detect any features on the image at a set level of grey scale. The setting of the grey scale is at the discretion of the user and could be a source of error. Alternatively, the void or rigid

inclusion can be measured semi-automatically by defining two points on the circumference of a void or rigid inclusion. To determine whether the subject is a void or a rigid inclusion, the fine focus is used on the microscope. An example of an observed void is shown in Figure 4.2. The x-y coordinate of each void or rigid inclusion is also measured and recorded for some of the final analyses.

Once the image has been scanned for voids and rigid inclusions, the software then counts and measures the equivalent circle diameters of all detected areas. The reason for using an equivalent circle diameter for the measurement parameter is the nature of the void shapes. All of the void shapes are different and for simplicity the void inflation model assumes a spherical void. The data are then recorded to a text file for subsequent analysis.

The results of the optical microscopy and image analysis were compared with those from a scanning electron micrograph of one sample for correlation purposes. This was to ensure that the defects measured by the optical method were defects and not a mistake in the software or inaccurate user interpretation.

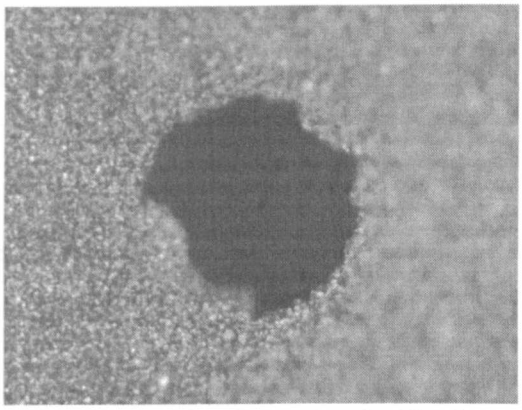

Figure 4.2 - Example of a Void

4.3.2 Analysis assumptions

To measure the presence of voids and rigid inclusions within an elastomeric material, some assumptions are necessary. The main assumptions are as follows: -

- the analysis is subjective - it is at the user's discretion to determine what is and what is not a void or rigid inclusion
- small areas (i.e. 1-2 pixels) are often ignored owing to a high local density
- the measurement process assumes an equivalent circle diameter of any measured void or rigid inclusion. The void is also assumed to be spherical.

The process of subjectively choosing the voids from an image was kept as consistent as possible throughout the measurement process, although there will be some discrepancies between measurements. It may be the case that the small areas of 'black' on the image were actually voids or rigid inclusions and these were ignored.

4.4 RESULTS AND STATISTICAL ANALYSIS

The void and rigid inclusion size distribution analysis results in: -

- Void and rigid inclusion size distribution plots
- Statistical information including mean, mode and confidence range
- Percentage area of voids
- Occurrences of larger voids (>20μm)
- Void and rigid inclusion location maps

The data are analysed using a spreadsheet package to determine distributions and statistical summaries.

4.4.1 Void size distribution plots

The void size distribution plots are for the total of the number of samples used for the particular material. The plots show the distribution up to a maximum value of 20μm equivalent circle diameter, all larger voids are presented in Table 4.3. An example of a void and rigid inclusion size distribution plot is shown in Figure 4.3.

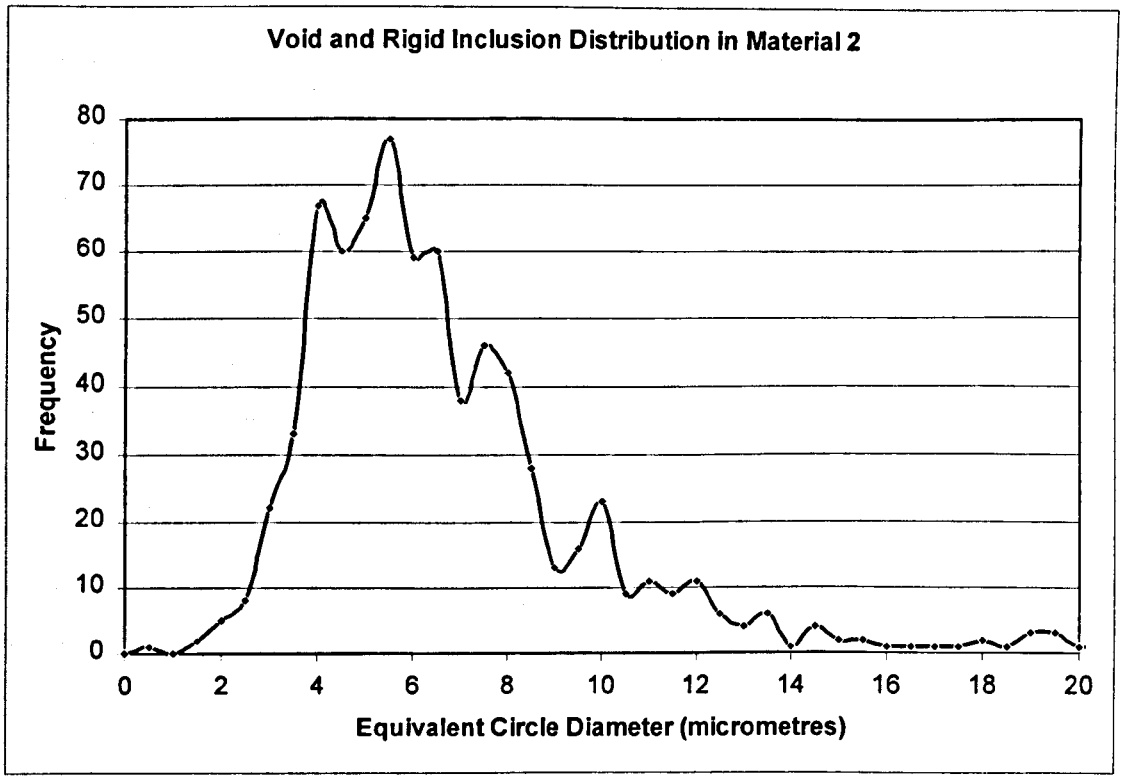

Figure 4.3 - Example void and rigid inclusion distribution plot

4.4.2 Statistical information

The results of the summary statistics based on a population of the number of samples for each material are given in Table 4.2. As can be seen from the table, the mean void size, distribution mode and a 95% confidence range for the mean size are given. These parameters are defined as follows: -

- Mean : arithmetic average
- Mode : value that corresponds to the highest frequency

The percentage area of voids per sample is an averaged value taken over all samples of a given material.

Table 4.2 - Statistical analysis results

MAT ID CODE	MAT ID No.	SECTION DIA. (mm)	MEAN VOID DIA. (μm)	DISTRIBUTION MODE (μm)	95% CONFIDENCE RANGE (μm)	%AREA OF VOIDS PER SAMPLE
C	1	5.33	3.6	3.1	3.5 - 3.7	0.057
	2	10.50	6.8	5.2	6.5 - 7.1	0.060
B	3	5.33	3.9	1.5	3.5 - 4.2	0.024
	4	10.50	5.2	1.1	4.9 - 5.5	0.014
	5	14.00	5.9	3.7	4.9 - 7.0	0.118
-	6	5.33	4.2	4.0	3.9 - 4.5	0.047
-	7	5.33	2.4	1.3	2.3 - 2.5	0.055
-	8	5.33	3.2	1.9	3.1 - 3.4	0.012
D	9	5.33	8.1	2.2	7.7 - 8.5	0.129
A	10	5.33	5.2	3.1	4.9 - 5.4	0.064
	11	10.50	5.1	3.7	4.0 - 5.3	0.043

Assuming $\alpha = 0.05$ (the areas at the tails of the normal distribution curve), the area under the standard normal curve is calculated as equals $(1-\alpha)$, or 95%. This value is ± 1.96. The confidence interval is therefore given as;

$$\bar{x} \pm 1.96 \left(\frac{\sigma_s}{\sqrt{n}} \right) \qquad (4.1)$$

In this case, this means that we can be 95% confident of the range of void sizes given in Table 4.2. The standard deviation is given as;

$$\sigma = \sqrt{\frac{n\Sigma x^2 - (\Sigma x)^2}{n\,(n-1)}} \qquad (4.2)$$

where σ_s is the standard deviation, n is the number of samples in a population and x is the mean value. The bar chart for mean void size is shown in Figure 4.4.

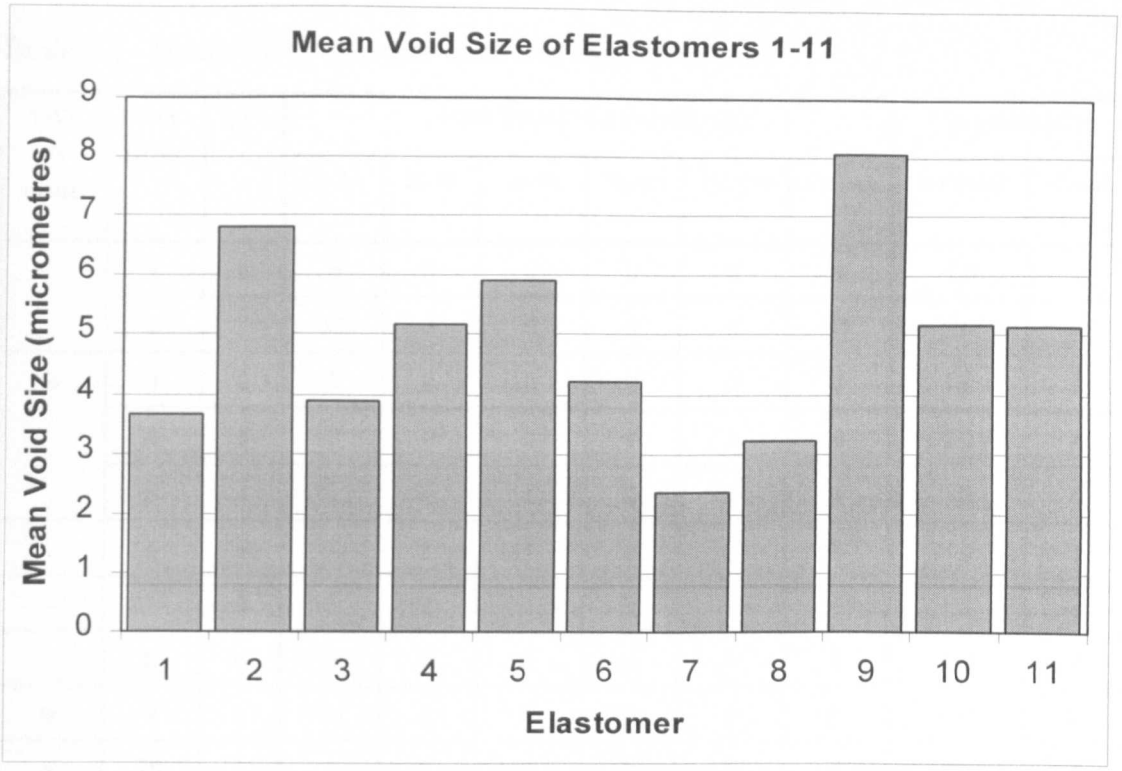

Figure 4.4 - Mean Void and Rigid Inclusion Size for Elastomers 1-11

4.4.3 Occurrences of larger voids

The number of observed larger voids and rigid inclusions (>20μm) was far less than the number of smaller voids and rigid inclusions, being almost nonexistent on the void size distribution plots. However, these are considered potentially very important for decompression resistance. The results of the larger voids and rigid inclusions are presented in tabular form for ease of reference and give the total occurrences of voids over all samples measured. Therefore, the total value needs to be weighted according to the number of samples measured to give a true representation of the probability of encountering a larger void. The occurrences of voids are grouped together in ranges of sizes as shown in Table 4.3.

Table 4.3 - Occurrences of larger voids and rigid inclusions

MAT ID CODE	MAT ID No.	QTY	VOID DIAMETER RANGE (μm)						WEIGHTING	
			20-30	31-40	41-50	51-100	101-500	TOTAL	WEIGHT	FINAL TOTAL
C	1	6	0	0	0	0	0	0	1.0	0
	2	3	13	4	0	0	0	17	2.0	34
B	3	6	3	0	0	0	0	3	1.0	3
	4	3	0	0	0	0	0	0	2.0	0
	5	4	0	2	1	2	1	6	1.5	9
-	6	6	1	3	1	0	0	5	1.0	5
-	7	5	3	2	0	0	0	5	1.2	6
-	8	6	0	0	0	0	0	0	1.0	0
D	9	6	16	1	0	0	0	17	1.0	17
A	10	6	5	0	0	0	0	5	1.0	5
	11	4	3	1	0	0	0	4	1.5	6

4.4.4 Void and Rigid inclusion Location

An example location map is given in Figure 4.5. The maps show rigid inclusions and voids in the range 0-20μm and greater than 20μm. Several very large voids were found, particularly in the larger section fluorocarbon based materials. In general the voids were roughly circular, but a few (~1%) were elliptical and some, although circular, were flat 'penny shaped' voids.

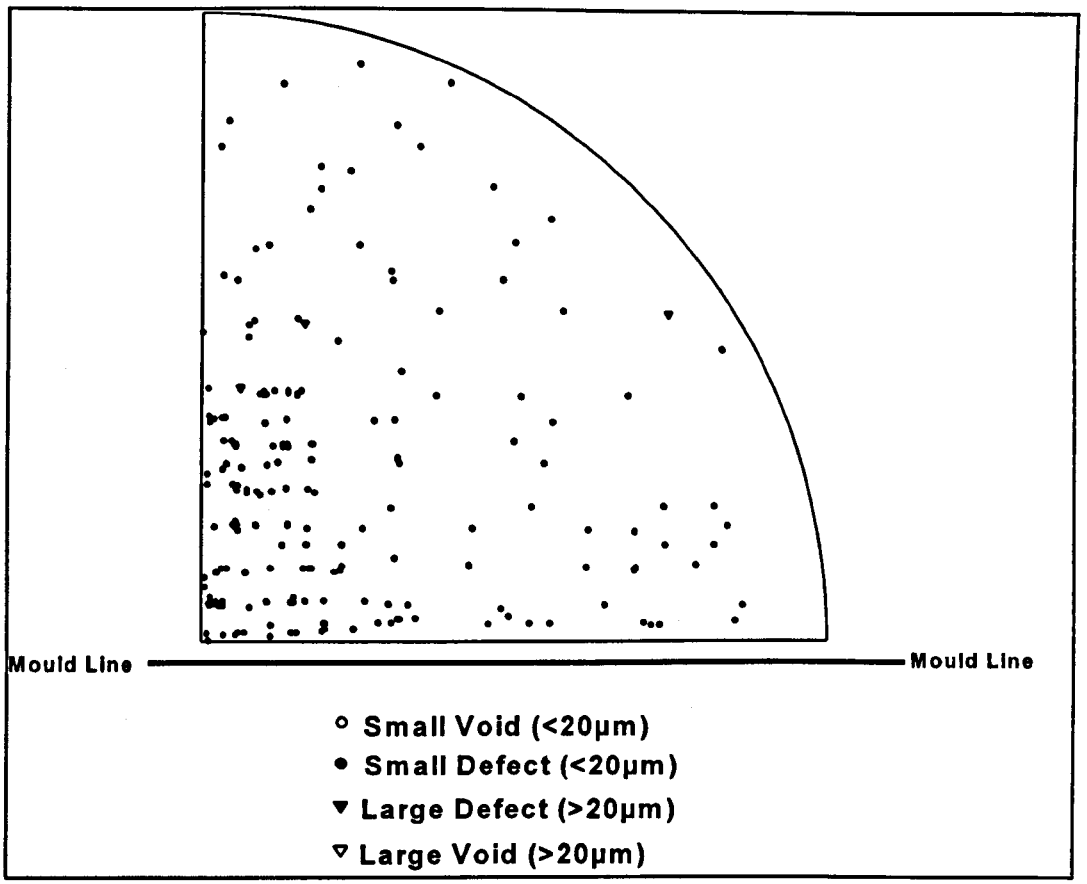

Figure 4.5 - Void and Rigid Inclusion Location Map for Material 2

4.5 DISCUSSION

Owing to the nature of the void and rigid inclusion analysis there are many parameters that could cause errors in the results obtained. The measured voids and rigid inclusions are assumed to be spherical in nature, although the depth of the image is sometimes quite flat. This would indicate that some of the recorded defects may be 'penny-shaped', which would behave quite differently under explosive decompression conditions.

4.5.1 Operator variability

As stated in section 4.3.2, the void and rigid inclusion analysis is subjective. It is at the operators discretion to determine: -

a. what is and what is not a void or rigid inclusion.

b. the two points on the circumference of a void or rigid inclusion from which the diameter is obtained.

In total, 5 operators have been used to analyse the eleven O-ring materials to gain an appreciation of the effects of operator variability. To study the effect of operators, the following have been performed:

- An analysis of variance for some representative results produced by each operator on the total void and rigid inclusion area

- A comparison of results of repeat inspections of three randomly selected samples produced by different operators on the total void and rigid inclusion area

- A comparison of the sizes of the largest voids found in one sample measured by two different operators

4.5.1.1 Comparison of repeated results on total void area

The operators are denoted by the numbers 1 to 5. To clarify the repeatability of results, pairs of operators have measured the same sample randomly selected. The results are as follows:

Table 4.4 - Repeated results on void area

Operator	Sample	Total Area (μm^2)	Average	Deviation (%)
2	material 8, sample 2	961	1070.5	-10.2
3	material 8, sample 2	1180	1070.5	+10.2
3	material 9, sample 1	15826	15497	+2.1
4	material 9, sample 1	15168	15497	-2.1
4	material 9, sample 3	6018	5702.5	+5.5
5	material 9, sample 3	5387	5702.5	-5.5

We can conclude that different operators can have up to ±10% variation in measuring the same sample.

4.5.1.2 Comparison of repeated results on individual void size

When measuring material 9 (material D) sample 1, operators 3 and 4 are asked to record the location and the size of the voids or rigid inclusions. The total void and rigid inclusion areas measured by operator 3 and 4 on this sample are very close. However, it is found that operator 4 would record many smaller size voids, and therefore a larger total number of voids or rigid inclusions. Operator 4 tended to record a smaller size for the same void or rigid inclusion, shown in the ten largest measured voids or rigid inclusions as follows:

Material 9 sample 1

Table 4.5 - Repeated results on individual void size

	Operator 3	Operator 4
Total number of voids or rigid inclusions	112	199

Void Number	Dia.(operator 3) (μm)	Dia.(operator 4) (μm)	Average (μm)	Deviation (%)
1	30.3	27.4	28.85	±5.0
2	31.1	26.5	28.80	±8.0
3	32.0	25.9	28.95	±10.5
4	17.5	25.3	21.40	±18.2
5	22.5	19.1	20.80	±8.2
6	22.0	20.3	21.15	±4.0
7	22.0	17.2	19.60	±12.2
8	20.1	16.1	18.10	±11.0
9	19.5	18.0	18.75	±4.0
10	19.4	Too close to edge	n/a	±9.0

The average deviation for the largest ten voids/rigid inclusions is therefore ±9.0%. For void number 10, the deviation given is the average of the previous nine measurements as operator 4 suggested that it was not valid as it was too close to the edge of the sample.

Theoretically, the largest possible variation occurs between an operator who discards the smaller voids/rigid inclusions and records lower sizes for voids/rigid inclusions and an operator who measures all the smaller voids/rigid inclusions and records larger sizes for voids/rigid inclusions. The average deviation will then be approximately ±35%.

4.5.1.3 Analysis of variance

The analysis of variance is based on the method of testing a statistical hypothesis. It is a statistical procedure in which samples from a population are used to determine whether we may accept the hypothesis. The hypothesis in our case is 'operator does not affect total void and rigid inclusion area'.

4.5.1.3(a) Material 10

Measurements on material 10 are as follows:

Table 4.6 - Total void areas

Operator	Sample	Total Area (μm^2)
1	1	1059 (x_1)
1	2	1819 (x_2)
1	3	5318 (x_3)
1	4	3879 (x_4)
2	5	5312 (x_5)
2	6	4150 (x_6)

We can see that the same operator measuring samples 1 to 4 recorded the total area for each sample varying from 1059- 5318μm^2, and another operator measuring samples 5 and 6 recorded the total area for each sample varying from 4150 - 5312 μm^2. These are the 'background noise' in statistical terms, and we have to consider these when comparing the differences in values produced between operators.

Table 4.7 - Analysis of Variance - Material 10

	Number of samples	Sum (μm^2)	Average (μm^2)	Degrees of freedom (df)
Operator 1	4	12075	3019 ($\bar{x}_1$)	3
Operator 2	2	9462	4731 ($\bar{x}_2$)	1
Total	6	21537	3589 ($\bar{x}_{t10}$)	-

	df	Sum of square of deviation (SS)	Mean square (MS)=SS/df
Between operators	1	$(\bar{x}_1 - \bar{x}_{t10})^2 x4 + (\bar{x}_2 - \bar{x}_{t10})^2 \times 2 = 3.909 \times 10^6$	3.909×10^6
Same operator	4	$\sum_{I=1,4}(x_i - \bar{x}_1)^2 + \sum_{I=5,6}(x_i - \bar{x}_2)^2 = 11.982 \times 10^6$	2.996×10^6

If the operator does not affect the total void/rigid inclusion area, both MS values estimate the same variance in different sections of the same O-ring material, and so their ratio will be a random value of the F-distribution. However, if the operator does have an effect, the between-operators MS value will reflect this difference and be an estimate of a larger variability than the same-operators MS value. Therefore their MS ratio (F) will tend to be high.

$$F(matl\ 10) = \frac{MS\ (betwn\ operators)}{MS\ (same\ operators)} = 1.3$$

from the standard F distribution table, FDIST(1.3,1,4) = 0.318

This means that there will be a 31.8% probability of having an error by discarding the hypothesis 'operator does not affect total void and rigid inclusion area'. In statistical practice, the critical value of F for rejection is 5%. Therefore, there is not enough evidence to reject the hypothesis.

4.5.1.3(b) Material 8

Measurements on material 8 are as follows:

Table 4.8 - Analysis of Variance - Material 8

Operator	Sample	Total Area (μm^2)
3	1	1882 (x_1)
3	2	1180 (x_2)
2	2	961 (x_2)
2	3	1210 (x_3)

	Number of samples	Sum (μm^2)	Average (μm^2)	Degrees of freedom (df)
Operator 1	2	3062	1531 ($\bar{x}_1$)	1
Operator 2	2	2171	1086 ($\bar{x}_2$)	1
Total	4	5233	1308 ($\bar{x}_{t8}$)	-

	df	Sum of square of deviation (SS)	Mean square (MS)=SS/df
Between operators	1	$(\bar{x}_1-\bar{x}_{t8})^2 \times 2 + (\bar{x}_2-\bar{x}_{t8})^2 \times 2 = 0.198 \times 10^6$	0.198×10^6
Same operator	2	$\sum_{I=1,2}(x_i-\bar{x}_1)^2+\sum_{I=3,4}(x_i-\bar{x}_2)^2 = 0.277 \times 10^6$	0.139×10^6

$$F(matl\ 8) = \frac{MS\ (betwn\ operators)}{MS\ (same\ operators)} = 1.424$$

from the F distribution table, FDIST(1.424,1,2) = 0.355

This means that there will be a 35.5% probability of having an error by discarding the hypothesis 'operator does not affect total void and rigid inclusion area'. Again, there is not

enough evidence to reject the hypothesis.

4.5.1.3(c) Material 9

Measurements on material 9 are as follows:

Table 4.9 - Analysis of Variance - Material 9

Operator	Sample	Total Area (μm^2)
3	1	15826 (x_1)
3	2	20909 (x_2)
4	1	15168 (x_3)
4	3	6018 (x_4)
5	3	5387 (x_5)
5	4	8380 (x_6)

	Number of samples	Sum (μm^2)	Average (μm^2)	Degrees of freedom (df)
Operator 3	2	36735	18368 ($\bar{x}_1$)	1
Operator 4	2	21186	10593 ($\bar{x}_2$)	1
Operator 5	2	13767	6884 ($\bar{x}_3$)	1
Total	6	71688	11948($\bar{x}_{t9}$)	-

	df	Sum of square of deviation (SS)	Mean square (MS)=SS/df
Between operators	2	$(\bar{x}_1 - \bar{x}_{t9})^2 \times 2 + (\bar{x}_2 - \bar{x}_{t9})^2 \times 2 + (\bar{x}_3 - \bar{x}_{t9})^2 \times 2 = 68.7 \times 10^6$	34.35×10^6
Same operator	3	$\sum_{I=1,2} (x_i - \bar{x}_1)^2 + \sum_{I=3,4} (x_i - \bar{x}_2)^2 + \sum_{I=5,6} (x_i - \bar{x}_3)^2 = 59.3 \times 10^6$	19.75×10^6

$$F(matl\ 9) = \frac{MS\ (betwn\ operators)}{MS\ (same\ operator)} = 1.739$$

From the F distribution table, FDIST(1.739,2,3) = 0.315

This means that there will be a 31.5% probability of having an error by discarding the hypothesis 'operator does not affect total void and rigid inclusion area'. Again, there is not enough evidence to reject the hypothesis.

The conclusion of the analysis of variance is that the observed probability does not provide enough evidence of a major operator effect. However, further analysis would be useful to study the possibility of minor operator effects.

4.5.1.4 Summary of operator variability analysis

The observed probability does not provide enough evidence of major operator effect. However, minor operator effect can cause up to ±35% variation in the worst possible scenario. The largest known variation in the measurement of the eleven O-ring materials is ±10%

4.5.2 Evaluation of results

To ascertain which materials have the least probability of failure due to decompression damage with respect to void and rigid inclusion content, an evaluation matrix method was used. This involves a ranking system of each parameter measured and analysed during the microscopic and statistical studies. The four parameters are: -

- percentage area : (0.25 weighting)
- mean void size : (0.25 weighting)

- distribution mode : (0.25 weighting)
- occurrences of large voids : (0.25 weighting)

The weighting method is a draft method and is subject to discussion, pending further information regarding the significance of the various parameters. The equal values are included based on current knowledge. Should further information become known regarding which of the above parameters is most dominant, the evaluation matrix should be revised with the appropriate weighting values.

The materials were ranked in order from one to ten on each parameter and given a score corresponding to their ranking position, 1 for the lowest value and 10 for the highest. The values are multiplied by the weighting factor to give a weighted score. The sum of the four weighted scores is then the final score, the lowest value being ranked first. Table 4.10 shows the evaluation matrix for all elastomers.

Table 4.10 - Evaluation matrix

MAT ID CODE	MAT ID No.	%AREA 0.25 weighting		MEAN 0.25 weighting		MODE 0.25 weighting		LARGE VOIDS 0.25 weighting		TOTAL
		Score	Weight	Score	Weight	Score	Weight	Score	Weight	
C	1	7	1.75	3	0.75	4	1.00	1	0.25	**3.75**
	2	8	2.00	10	2.50	11	2.75	11	2.75	**10.00**
B	3	3	0.75	4	1.00	3	0.75	4	1.00	**3.50**
	4	2	0.50	7	1.75	1	0.25	1	0.25	**2.75**
	5	10	2.50	9	2.25	8	2.00	9	2.25	**9.00**
-	6	5	1.25	5	1.25	10	2.50	5	1.25	**6.25**
-	7	6	1.50	1	0.25	2	0.50	7	1.75	**4.00**
-	8	1	0.25	2	0.50	4	1.00	1	0.25	**2.00**
D	9	11	2.75	11	2.75	5	1.25	10	2.50	**9.25**
A	10	9	2.25	7	1.75	6	1.50	5	1.25	**6.75**
	11	4	1.00	6	1.50	8	2.00	7	1.75	**6.25**

Where two values have the same score, this is due to their parameter value being equal. Based on the values given in the totals column, the final ranking is given in Table 4.11.

Table 4.11 - Final ranking of materials

RANKING	MATERIAL ID	MAT ID No.	BASE POLYMER
1	Material 8	8	Fluorocarbon (FKM)
2	Material B (10.5mm)	4	Fluorocarbon (FKM)
3	Material B (5.33mm)	3	Fluorocarbon (FKM)
4	Material C (5.33mm)	1	Fluorocarbon (FKM)
5	Material 7	7	Hydrogenated nitrile rubber (HNBR)
6	Material 6	6	Ethylene propylene diene rubber (EPDM)
6	Material A (10.5mm)	11	Hydrogenated nitrile rubber (HNBR)
8	Material A (5.33mm)	10	Hydrogenated nitrile rubber (HNBR)
9	Material B (14mm)	5	Fluorocarbon (FKM)
10	Material D	9	Nitrile rubber (NBR)
11	Material C (10.5mm)	2	Fluorocarbon (FKM)

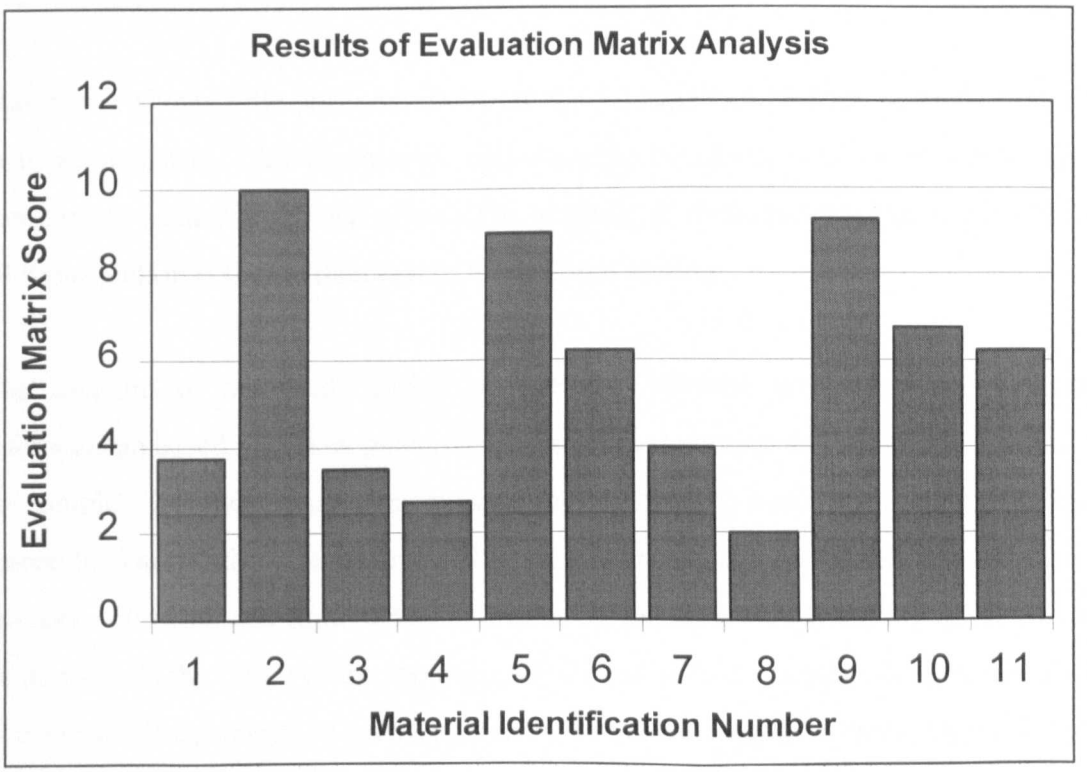

Figure 4.6 - Summary of Evaluation Analysis

4.6 CONCLUSIONS

Based on the evaluation matrix method the results indicate that, in general, the fluorocarbon based materials have the least quantity and size distribution of voids and rigid inclusions from the range of materials selected, in particular materials 8, 3, 4 and 1. This is the case for the smaller 5.33mm section materials, however, sometimes the larger sections of the same material perform less well.

One fluorocarbon material, a 14mm section sample, was ranked lower. This was primarily due to the inclusion of one particularly large void of approximately 450μm diameter. This caused all of the measured parameters to be much higher, except the distribution mode.

It is interesting that in the cases where a 5mm and a 10.5mm section material were studied, the 10.5mm section ranked higher than the 5mm sample of the same material, with the exception of material C. The 14mm sample ranked far lower, perhaps suggesting that there may be an optimum section diameter for a reduction in void and rigid inclusion content.

Material A shows little difference between the 5.33mm and 10.5mm sections from the evaluation matrix. All parameters, including the occurrences of larger voids, show comparable values with each other. The quantity of voids and rigid inclusions in the 10.5mm section is higher than that of the 5.33mm section.

The location of the voids varied considerably between material types, with the fluorocarbon based materials (materials B and C) containing voids towards the centre of the sample. The hydrogenated nitrile samples (material A) were found to contain voids nearer the outer surface of the sample. This may indicate a difference in the manufacturing process. The void and rigid inclusion location maps show clearly the higher density of voids towards the centre of the specimen. The rigid inclusion content is more randomly distributed. The comparison between material 8 and material D is shown in Figure 4.7 and the density and distribution difference between the two materials can be clearly seen.

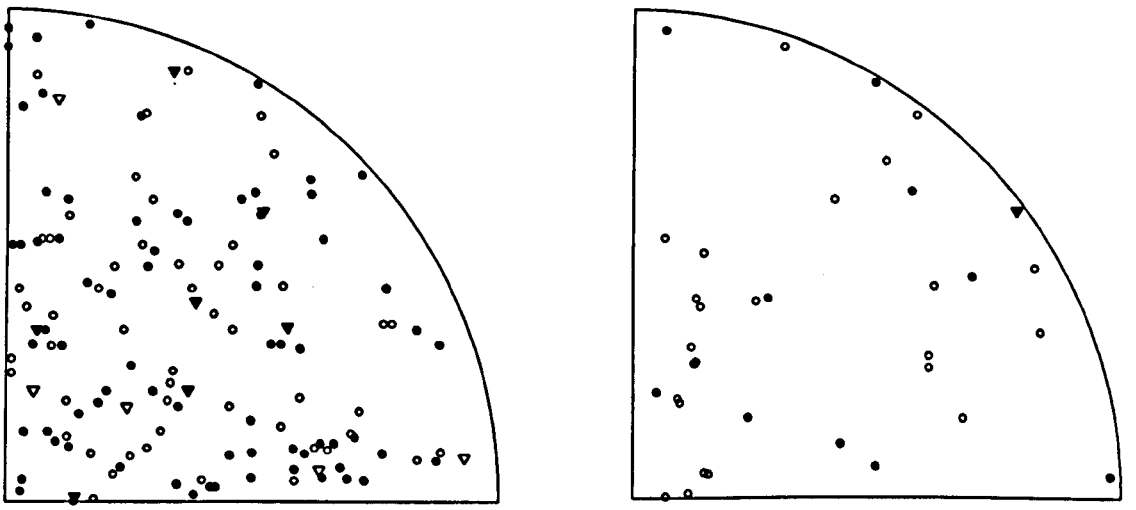

Figure 4.7 - Location Map Comparison between Materials D and 8

There is no evidence that the mould line has a significant influence on the presence of voids and rigid inclusions within the sections.

The effect of operator variability was studied as part of this analysis and it was concluded that, although the process is subjective and there is inherent variability between operators, the variance could not be termed significant. The maximum observed variance in the repeated measurement of a single void was ±10%. A possible worst case scenario could be ±35% due to operator variability.

A review of the manufacturing process for elastomer seals revealed many possible variables that could introduce voids and rigid inclusions into elastomeric seals. The details of this study cannot be given in depth owing to the confidentiality of the manufacturing process. This may need to be investigated further to ascertain which variables are dominant. In particular, it seems that gas release during curing is significant, and this correlates well with the observations made during the microscopic analysis. Other factors such as the mixing and moulding method are also of primary interest.

4.7 CHAPTER SUMMARY

A new method to determine the size, density and location of voids and rigid inclusions within elastomers has been developed. The size distribution generally exhibits a skewed normal distribution and the main concentration of voids in primarily towards the centre of an O-ring section. Rigid inclusions tended to be distributed randomly through the section.

These data regarding size, location and density can now be used to develop the void diffusion and expansion models that rely on the initial sizes and locations of voids and rigid inclusions. The location is important as the pressure differential formed across the seal during decompression varies considerably from one side of the seal to the other. Unfortunately this was discovered after much of the analysis had already been carried out and so the location data are limited to a few materials and sections.

The data on the rigid inclusion distribution are also important as this will determine how these defects can act as stress raisers under gross material deformation during decompression.

CHAPTER 5 - GAS TRANSPORT TESTING

5.1 INTRODUCTION

To determine how gas transport behaves during explosive decompression it is necessary to ascertain the solubility, diffusion and evaporation properties of a particular gas in a given elastomer. This can only be determined experimentally as the chemical interactions between the elastomer and fluid are unique.

The gas transport properties are calculated from the results of a permeation test. The permeation test involves applying pressure to the gas on one side of an elastomer membrane and measuring the pressure increase in a fixed volume on the other side of the membrane. Diffusion and solubility are highly temperature dependant and therefore the test requires the ability to vary the temperature.

The explosive behaviour of some gases found in oil and gas applications require that the test cell should also be intrinsically safe. The permeation data is used in the transient gas diffusion model to determine the gas transport activity within the seal section during differing decompression regimes.

5.2 THEORY OF PERMEATION

Gas transport through elastomers by pressure driven movement can take three main routes, these are: -

- Rapid passage through a massive hole, i.e. a leak
- Micro-corridor, such as the result of a manufacturing fault, i.e. a continuum of open pores etc. This depends on the inverse of a gas's molecular weight and the size of the fault.

- Permeation involving either: -
  - Movement of gas molecules between polymer chain molecules
  - Movement of gas molecules between polymer chain molecules in addition to passage across separate closed pores inside the polymeric material.

High pressure permeation is a combination of the dissolution of a gas in the elastomer surface, followed by diffusion through the bulk and finally evaporation at the low pressure side surface. The dissolution at the surface is highly pressure dependant. Diffusion of gas through the bulk is pressure independent at normal pressure, but some changes at higher pressure have been observed, primarily due to compaction of the elastomer matrix. The diffusion process occurs due to random thermal fluctuations of the polymer chains, known as Brownian motion. During this motion, open pores appear at the surface of the elastomer. If the elastomer is in contact with a gaseous medium there will be a high probability that a gas molecule will enter the pore. The gas molecules are then trapped and released as the polymer chains rotate, allowing the molecules to migrate through the structure.

The concentration of gas adsorbed at either membrane surface is directly proportional to the applied gas pressure p according to Henry's law;

$$c = sp \qquad (5.2.1)$$

where c is the concentration and s is solubility coefficient.

5.2.1 Diffusion in a plane sheet

The full solution of the equations for diffusion in a plane sheet is given in Appendix A. The following is a summary of the derivation. The rate of diffusion is governed by Fick's law of diffusion: -

$$F = -D \frac{\partial c}{\partial x} \qquad (5.2.2)$$

where F is the rate of transfer per unit area, c is the concentration, D is the diffusion coefficient and x is the space coordinate measured normal to the section.

For a plane sheet, steady state diffusion of adsorbed gas from one surface through to another is given by a simple integrated version of Fick's first law: -

$$\left[\frac{1}{A}\right]\left[\frac{q}{t}\right] = \frac{D\ (c_1 - c_2)}{h} \qquad (5.2.3)$$

where q is the gas volume at STP (Standard Temperature and Pressure), A is the cross-sectional area in contact with the gas, h is the sheet thickness, t is time in seconds and c_1 and c_2 are the initial and final concentrations.

If we substitute Henry's law (eqn 5.2.1) into the modified Fick's law equation (eqn 5.2.3) for diffusion in a plane sheet, we may write: -

$$\left[\frac{q}{t}\right] = \frac{QA\ (p_1 - p_2)}{h} \qquad (5.2.4)$$

where Q is the permeation coefficient, which is given by Q = Ds. Equation (5.2.4) gives the steady-state conditions. For transient permeation the equation is: -

$$q = \left[\frac{DAc_1}{h}\right]\left[t - \frac{h^2}{6D}\right] \qquad (5.2.5)$$

At the time axis q=0 and t = τ (the time lag), such that: -

$$D = \frac{h^2}{6\tau} \qquad (5.2.6)$$

This equation is used to determine the diffusion coefficient.

5.2.2 The Effects of Temperature

Both the diffusion and solubility coefficients are highly temperature dependant, exhibiting Arrhenius type behaviour. The increase in temperature causes the random Brownian motion of the polymer chains to increase, therefore allowing the gas molecules to migrate through the material at an increased rate. The solubility coefficient's temperature dependence is described by: -

$$s = s_o \exp\left[\frac{-\Delta H_s}{RT}\right] \qquad (5.2.7)$$

where s_o is the original solubility coefficient, ΔH is the heat of solution, R is the characteristic gas constant and T is the absolute temperature. The governing equations are similar for the diffusion and permeation coefficients: -

$$D = D_o \exp\left[\frac{-E_d}{RT}\right] \qquad (5.2.8)$$

$$Q = Q_o \exp\left[\frac{-E_q}{RT}\right]$$

where E_d and E_q are the activation energies of diffusion and permeation respectively. E_q itself has little physical significance as

$$E_q = E_d + \Delta H_s \qquad (5.2.9)$$

If a mixed gas is used as the diffusion medium, the equation is modified according to the rule of mixtures

$$\left[\frac{q}{t}\right] = (Q_a\phi_a + Q_b\phi_b)\,\frac{A\,(p_1 - p_2)}{h} \qquad (5.2.10)$$

where ϕ is the volume fraction and a and b are the two gases.

The rate of gas diffusion through elastomer plane sheets depends greatly, as can be seen from the above equations, on the sheet thickness. During testing at high pressures this thickness can change due to: -

- differential expansion of the metalwork and the elastomer
- compaction due to high pressure
- creep
- swelling effects - due to gas density approaching that of a liquid at high pressure

5.3 PERMEATION CELL DESIGN

The permeation cell must be designed around the material as it is supplied in thin sheet (nominally 2.2mm thick) form. Figure 5.1 shows a diagrammatic view of the permeation cell. Appendix B shows the detail and assembly drawings of the permeation cell. The required specification for the operational conditions of an elastomer seal in an oil and gas application is as follows: -

- Operational temperature : up to 200°C (392°F)
- Operational pressure : up to 1000 bar (14,500 psi)
- Gas types : CH_4, CO_2, Air

Therefore, the components of the cell are required to withstand these conditions and the instrumentation is required to control them.

The principle of the permeation cell is that the high pressure gas is supplied via a gas diaphragm pump into a cavity above the elastomer membrane. The membrane is held in place by a support ring that compresses the membrane approximately 20%. Beneath the membrane, a porous ceramic filter disc is employed to allow the permeated gas that has passed through the membrane to pass through to the low pressure side. The ceramic disc also acts as a support to the membrane while under pressure. The gas must be able to pass through the ceramic disc freely. Otherwise, it will affect the rate of pressure increase in the low pressure cavity.

Beneath the ceramic disc is a stainless steel support disc with numerous holes machined through its thickness. It also has grooves machined into the base to allow the gas to pass through and into the low pressure cavity. This support is required as the ceramic disc cannot withstand the bending stresses generated by the maximum 1000 bar pressure without additional support underneath.

Once the gas has passed through into the low pressure cavity, the pressure increase of the fixed volume is measured by means of a low range pressure transducer. This pressure increase can then be related to the permeation rate through the membrane by equation (5.2.4).

Figure 5.1 - Diagram of Permeation Cell Layout

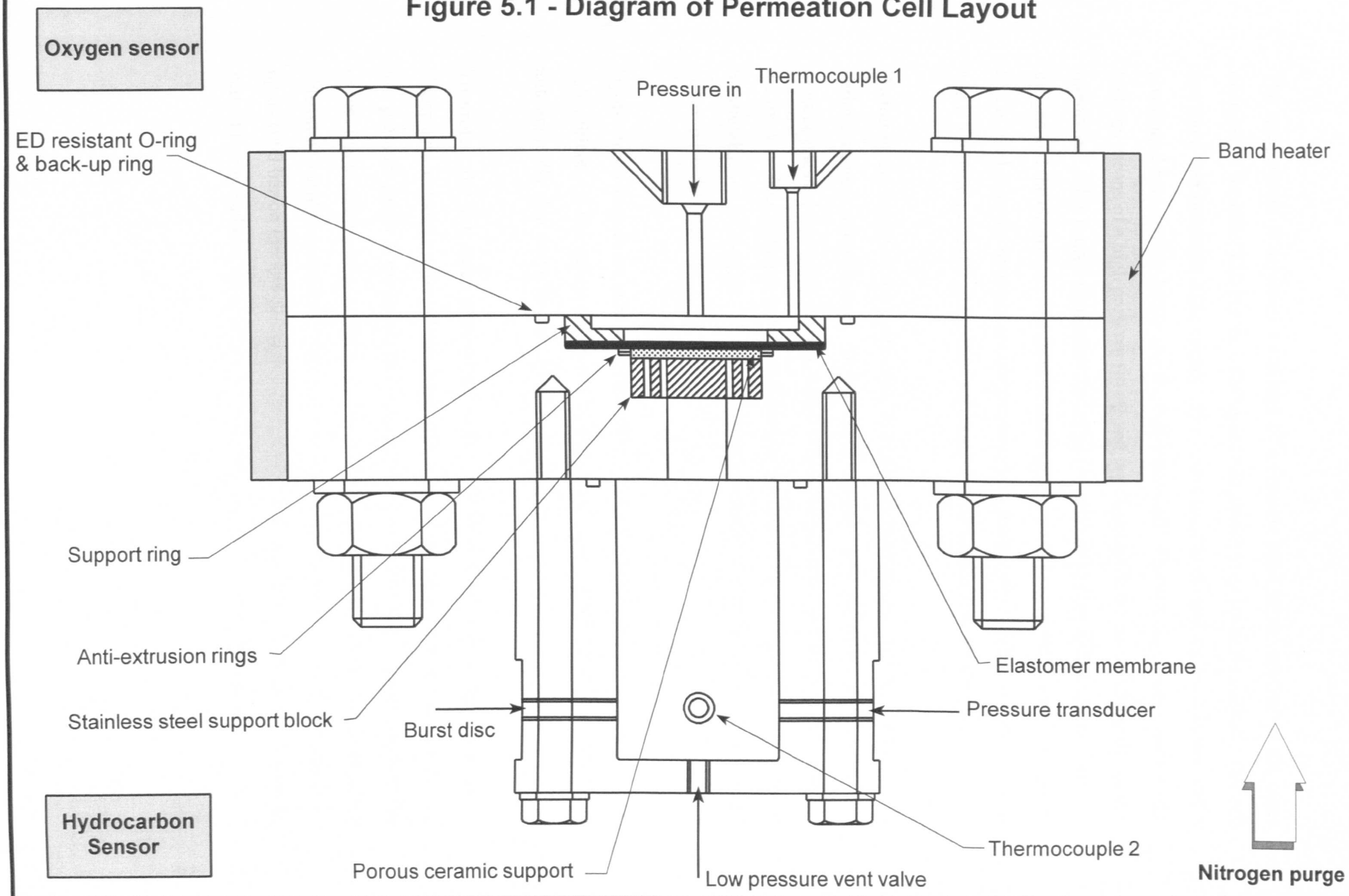

The temperature is achieved by means of a ceramic band heater applied to the outer diameter of the cell. This is then fully lagged and placed in an isolation cabinet. The cell has three thermocouple attachments. The first is used to control the band heater and is positioned between the heater and the cell outer wall. The second is machined into the body by means of a high pressure fitting and is positioned in the cavity above the rubber membrane. This is used to monitor the actual temperature at the point of contact between the gas and the elastomer. The final thermocouple is positioned in the low pressure cavity and is used to make temperature compensations in the pressure transducer output and to add a temperature factor in the final calculation to obtain the permeation rate.

Owing to the nature of the gases used, in particular methane, the cell is required to use various intrinsic safety features. Methane is an explosive gas. Therefore, the complete cell must be encased in a safety cabinet, which is then purged with nitrogen to remove most of the oxygen. The principle is that the explosive potential of the methane is greatly reduced by the absence of oxygen. This is particularly important with the use of the electrical ceramic band heater.

Hydrocarbon sensors are used to monitor the hydrocarbon levels within the room and the cell cabinet. If the values monitored by the sensors reach predefined limits, the rig is automatically shut down by the control program.

To protect the low range pressure transducer, and for safety reasons, the low pressure cavity also includes a solenoid valve and a burst disc. If the maximum safe pressure in the low pressure cavity is exceeded, the solenoid valve will automatically open and vent the excess gas to atmosphere, safely away from the operating environment. However, if the elastomer membrane suddenly fails and there is an instantaneous increase in pressure of up to 1000 bar on the low pressure side, the burst disc will fail and the gas will again be vented to atmosphere, while simultaneously shutting down the gas pump.

Figure 5.2 shows a photograph of the permeation cell outside the cabinet.

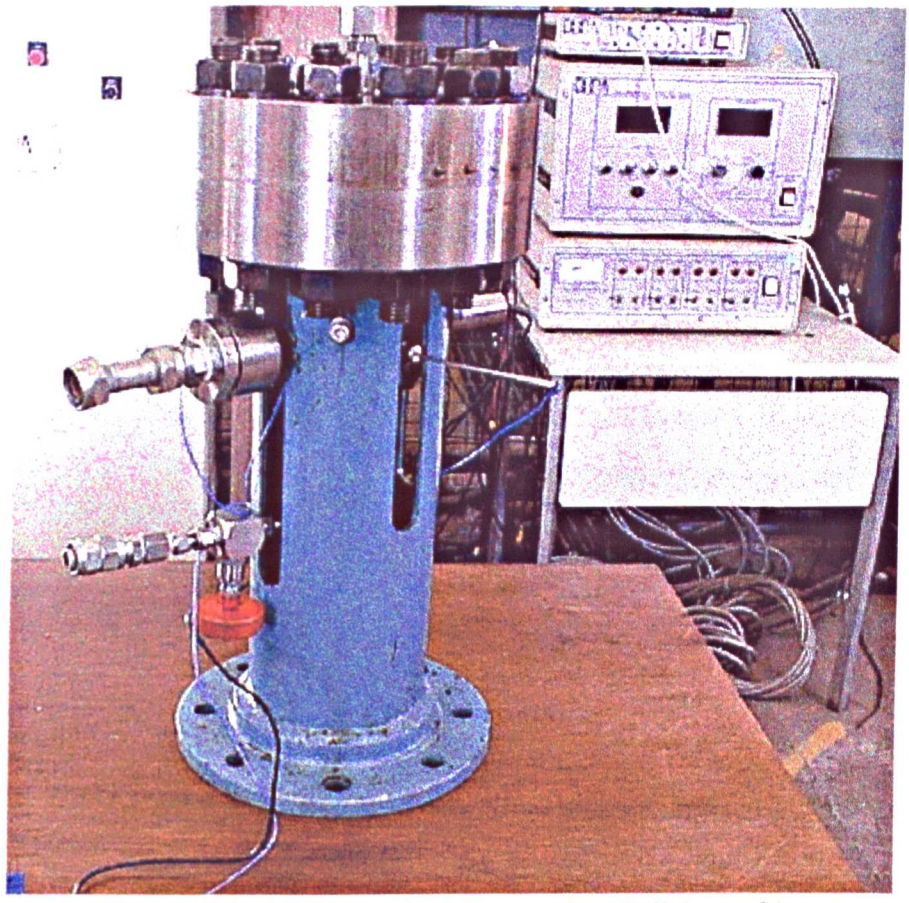

Figure 5.2 - Photograph of Permeation Cell Assembly

The cell is rated on a 2x factor of safety regarding the bolt loads holding the two sections of the cell together. The complete system is controlled via a data acquisition and control program developed specifically for the requirements of the rig. The program performs the following functions:-

- Controls all parameters including:-
  - gas pump
  - nitrogen purge
  - band heater
- Controls the rig trip-out limits
- Monitors and records:-

- Oxygen content
- Temperatures (low pressure and high pressure sides)
- Pressures (low pressure and high pressure sides)
- Hydrocarbon content

Some sample screens of the software are given in Figures 5.3 and 5.4.

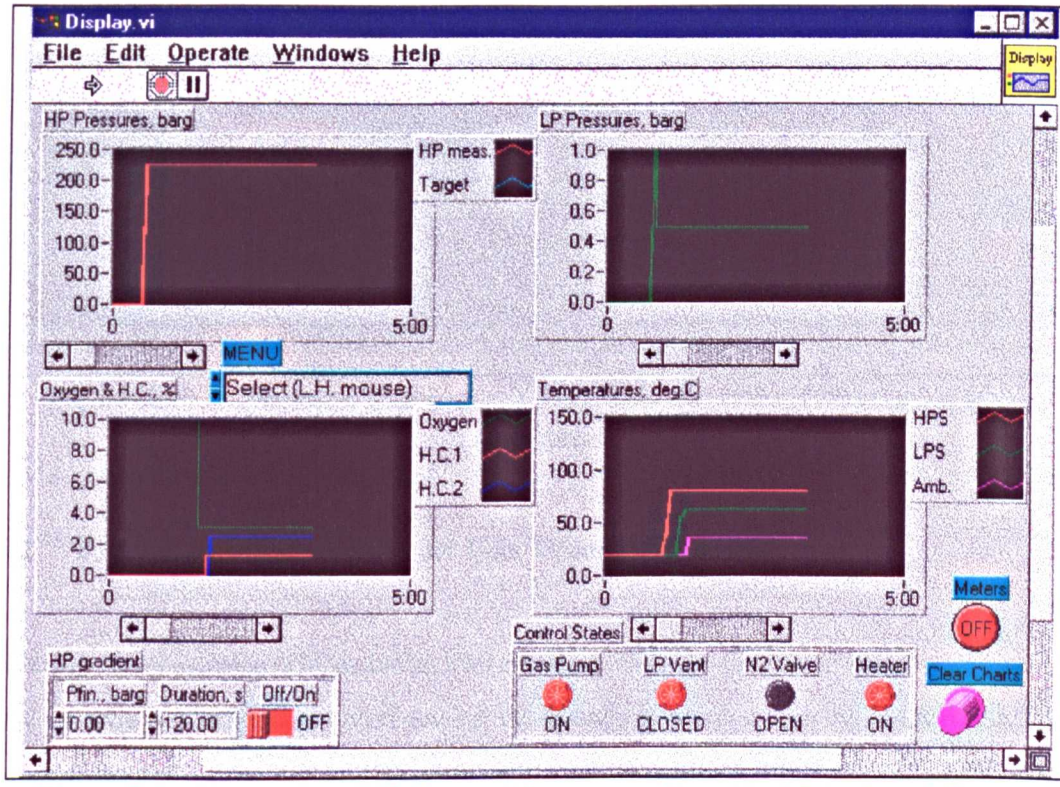

Figure 5.3 - Permeation Cell Control Program - Graphical Display of Outputs

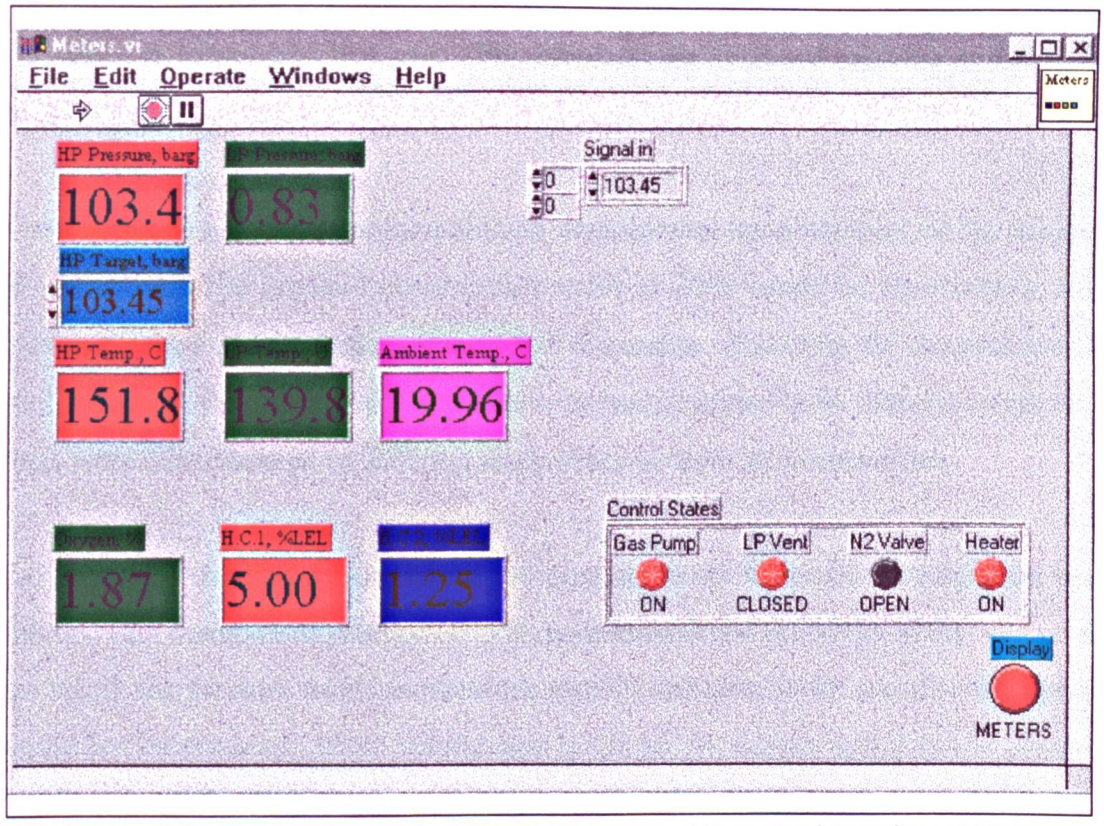

Figure 5.4 - Permeation Cell Control Program - Numerical Display of Main Outputs

5.3.1 Practical Considerations for Gas Transport Testing

There are many considerations taken into account with the design of the permeation cell, many of which were encountered during the commissioning of the rig. The variation in temperature across the cell and the differing thermal expansions of the various materials employed leads to problems with limits and fits. The elastomer membrane is required to be as flat as possible across the ceramic filter disc, however, due to the differential thermal expansion in the area and the tolerances involved in the component parts, there will be a slight curvature to the membrane.

There are two anti-extrusion rings mounted beneath the elastomer membrane and around the ceramic disc to prevent any extrusion damage. Extrusion damage occurs when there is a small gap available on the low pressure side of an elastomer sealing device and the

elastomer is forced into this gap. This often causes localised cracking and therefore premature failure.

The membrane supplied from the elastomer manufacturer has a tolerance on the thickness of ±0.15mm. The required compressive strain of 20% would be significantly either increased or reduced depending on the actual dimension. Therefore the compression ring applied to hold the membrane in place has to be manufactured to fit. Several compression rings were manufactured of differing thicknesses to cover all eventualities.

Estimating the required volume for the low pressure cavity involved estimating the worst and best case scenarios of permeation rates, temperatures and pressures. If the volume was too small, the pressure would increase too rapidly and an accurate pressure-time profile would not be obtained. If the volume was too large, the output would not be changing rapidly enough for the pressure transducer to record the changes.

Therefore the estimated permeation rates were calculated using the following empirical formulations [Ho et al, 1989-1997]:-

$$\frac{dq}{dt} = \left[\frac{\delta P_2}{\delta t}\right]_V \left[\frac{273}{T_{LP}}\right] V_{LP} \qquad (5.3.1)$$

and

$$\frac{q}{t} = \frac{QA(P_1 - P_2)}{h} \qquad (5.3.2)$$

Equating the two equations gives:-

$$\frac{QA(P_1 - P_2)}{h} = \left[\frac{\delta P_2}{\delta t}\right]_V \left[\frac{273}{T_{LP}}\right] V_{LP} \qquad (5.3.3)$$

where Q is the permeation coefficient, A is the cross-sectional area of the membrane in contact with the gas, P_1 is the high pressure side of the membrane, P_2 is the low pressure

side of the membrane, h is the membrane thickness, T_{LP} and V_{LP} are the temperature and the volume of the low pressure side.

The permeation coefficient estimates at given temperatures and pressures were sourced from earlier permeation test work detailed in the Seal Life Project Reports (Ho et al, 1989-1997). The calculated volume was overestimated and a volume reducer had to be manufactured which would fit into the low pressure cavity. This enabled the pressure transducer to measure pressure increases more accurately.

During the commissioning of the permeation cell, many problems were encountered that are too numerous to list. One main problem was finding a material for the filter disc. The specification devised for the filter disc stated that the disc had to be around 3mm thick and withstand a compressive stress of 100 MPa, while simultaneously allowing free gas flow. This was very difficult and various options were tested in the rig, many of them failing due to either cracking or not allowing any gas flow at all. Eventually a reaction bonded, silicon nitride material was used with a built-in porosity that satisfied the specification.

Another major problem was the sealing of the low pressure side reservoir. The low pressure side reservoir had to seal very low pressures, which were increasing over a long period of time. The low pressure side reservoir also has many fittings for instrumentation. Initial tests showed that many of these fittings and the main seal between the reservoir and the cell were leaking. The leak rates were very slow, but were significant enough to cause errors in the pressure increases being recorded during the tests.

The PTFE (polytetrafluoroethylene) seal had to be examined to determine why the leak was occurring, and it was found that the surface finish between the reservoir and the main cell was too rough. Once the surfaces had been hand lapped and the fittings locked in with an appropriate sealant, the leak was eliminated.

The initial tests carried out at 100 bar showed no problems. However, when the pressure was increased to 500 bar, leakages of methane occurred which automatically shut down the cell. It was found that the high pressure side main seal was leaking due to extrusion damage. This meant that an extrusion gap had been formed between the top and bottom halves of the cell. The only explanation for this was that the top plate was deflecting under the pressure and the bolts were stretching. After calculating the bolt stretch and the top plate displacement it was found that this was the case.

The solution to this was to redesign the membrane compression ring to accommodate a second inner O-ring and to increase the fitting torque on the fixing bolts. The second O-ring would reduce the area available for the pressure to act over and therefore reduce the applied force. The increased torque, coupled with high tensile steel bolts and hardened steel washers, would reduce the bolt stretch and creep.

Initial commissioning tests also highlighted the importance of obtaining temperature stability in the cell before any testing was carried out, particularly in the low pressure reservoir. During temperature increase the low pressure vent is opened to allow any pressure build up to dissipate. The temperature is then allowed to settle and become stable before the test is started and the low pressure vent valve is closed. If the temperature was not allowed to become stable, the pressure increase in the low pressure reservoir would be inaccurate, owing to the additional pressure caused by the temperature increase.

5.4 TEST PROCEDURE

The procedure for a standard permeation test is as follows:-

1. Measure and record the thickness of the elastomer membrane sample.
2. Mount the sample in the fixture along with the ceramic disc and anti-extrusion rings.
3. Install a new high pressure O-ring and anti-extrusion ring.

4. Fit top section ensuring that the high pressure O-ring is not twisted by this operation.
5. Fit main bolts and tighten to a torque of 300 lb.ft.
6. Fix high pressure inlet fitting in place and tighten.
7. Ensure that all high pressure fittings are secure.
8. Fit band heater, thermocouple and insulation.
9. Open the low pressure vent valve.
10. Close cabinet door and activate all locking mechanisms.
11. Turn on nitrogen supply.
12. Open the high vent valve.
13. Switch on all rig and control limits on the computer.
14. Turn on heater and set temperature controller to test temperature.
15. Clear computer displays and start recording data.
16. Allow both the high and low pressure side temperature levels to stabilise.
17. Switch off upper rig limit for cabinet oxygen content.
18. Open cabinet door and close the low pressure vent valve. Close cabinet door and activate all locking mechanisms.
19. Close the high pressure vent valve.
20. Check instrumentation and ensure that all operational parameters are within rig limits.
21. Open the test gas supply bottle.
22. Turn on the gas pump via the computer.
23. Set the test pressure on the gas pump. Adjust the pump control until the pressure has stabilised.
24. Allow the test to run until the rate of pressure increase within the low pressure volume is increasing at a constant rate. When the pressure increase has remained constant for some time the test may be stopped.
25. Switch off the data recording.
26. Close the test gas supply bottle.
27. Switch off gas pump.
28. Switch of the band heater.

29. Open the high pressure vent valve slightly to allow the rig to decompress as slowly as possible to avoid explosive decompression in the test sample and the high pressure O-ring.
30. Open the cabinet and open the low pressure vent valve.
31. Switch off the nitrogen purge.
32. Remove insulation and high pressure fitting.
33. Remove main bolts and separate the top and bottom sections of the cell.
34. Remove compression ring and sample and inspect for damage.
35. Place the sample in a labelled bag.

5.5 TEST RESULTS

The result which comes directly from the test rig is primarily the rate of pressure increase within the low pressure cavity with time. This allows us to calculate the permeation coefficient, the diffusion coefficient and the solubility coefficient, providing we know the test temperature and the sample thickness.

The pressure within the cavity is plotted against time from which we can determine the steady state rate of pressure increase (dP_2/dt). An example is given in Figure 5.5. The plot clearly shows the initial transient diffusion process and the steady state section. Also from the plot we can obtain the time lag (τ) for the system. The rate of pressure increase is determined from the slope of the steady state permeation and the time lag (τ) is determined by back extrapolating the steady state line until it intersects with the time scale on the x-axis. The time at which the line crosses the x-axis is the system time lag which describes the transient diffusion process.

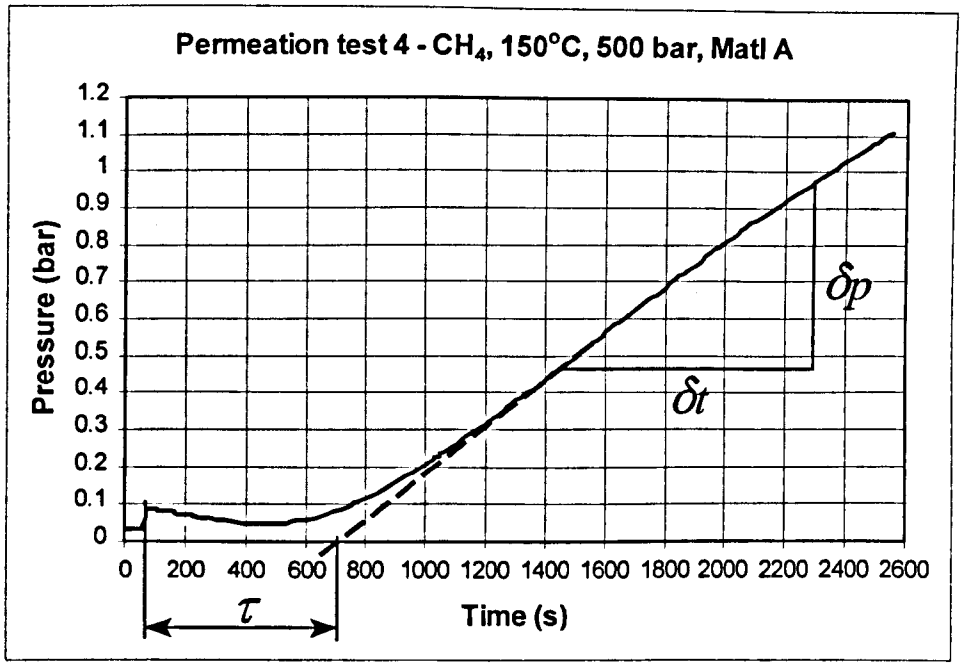

Figure 5.5 - Pressure increase vs time for low pressure side

This information allows us to calculate the various coefficients for the gas-polymer system based on the relationships previously described. The test programme is detailed in Table 5.1. The results of each test are summarised in Table 5.2.

The testing programme includes repeat tests for validation purposes. Obtaining repeatable test results from the test cell is important. Confidence in further test results will then be obtained. The superscript (*) denotes a first repeat test and (**) denotes a second repeat test.

Table 5.1 - Permeation test programme

Test No	Material	Temperature (°C)		Pressure (bar)		Gas
		100	150	100	500	CH_4
1	A	✓		✓		✓
2	A	✓			✓	✓
3	A		✓	✓		✓
4	A		✓		✓	✓
5	B	✓		✓		✓
6	B	✓			✓	✓
7	B		✓	✓		✓
8	B		✓		✓	✓
9	C	✓		✓		✓
10	C		✓		✓	✓
11	B		✓	250		✓
5*	B	✓		✓		✓
3*	A		✓	✓		✓
10*	C		✓		✓	✓
10**	C		✓		✓	✓

Table 5.2 - Test results

Test No.	Material	Temperature (°C)	Pressure (bar)	Gas	dq/dt ($cm^3.s^{-1}$) $x10^{-3}$	Q ($cm^2.s^{-1}.atm^{-1}$) $x10^{-6}$	D ($cm^2.s^{-1}$) $x10^{-6}$	s (atm^{-1})
1	A	100	100	CH_4	0.88	0.11	2.72	0.04
2	A	100	500	CH_4	4.09	0.12	2.97	0.04
3	A	150	100	CH_4	8.29	1.10	12.29	0.09
4	A	150	500	CH_4	24.49	0.69	10.93	0.06
5	B	100	100	CH_4	0.63	0.09	4.39	0.02
6	B	100	500	CH_4	3.38	0.10	1.55	0.06
7	B	150	100	CH_4	4.56	0.63	8.02	0.08
8	B	150	500	CH_4	18.66	0.53	5.79	0.09
9	C	100	100	CH_4	0.69	0.09	1.63	0.05
10	C	150	500	CH_4	9.80	0.27	3.69	0.07
11	B	150	250	CH_4	9.41	0.53	6.42	0.08
5*	B	100	100	CH_4	0.47	0.07	2.12	0.03
3*	A	150	100	CH_4	2.96	0.40	5.02	0.08
10*	C	150	500	CH_4	8.96	0.25	3.52	0.07
10**	C	150	500	CH_4	8.75	0.24	3.37	0.07

5.5.1 Repeatability of results

The repeatability of the results generated by the gas transport testing is of particular interest as they effectively determine the accuracy of the measurement technique. It was thought that during testing, the initial results from test 3 were inaccurate. The repeat test shows a large difference in the results obtained. The other repeatability tests show good agreement with the previous tests. The repeatability of the results is shown in Figures 5.6 to 5.8.

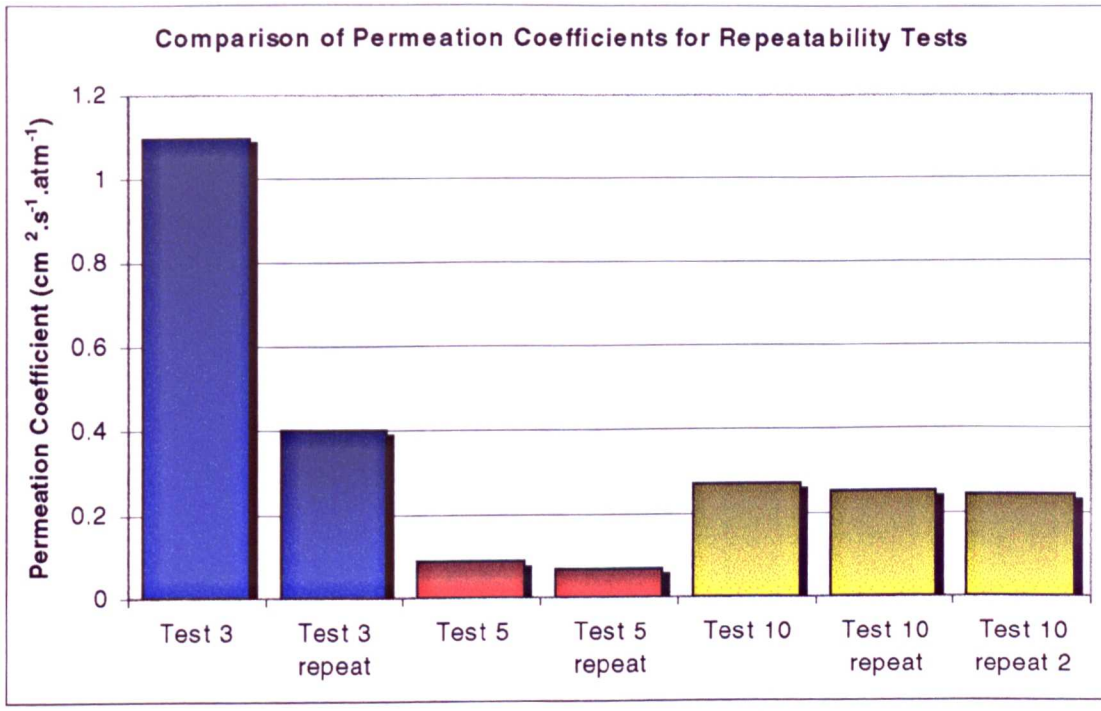

Figure 5.6 - Repeatability of Permeation Coefficient

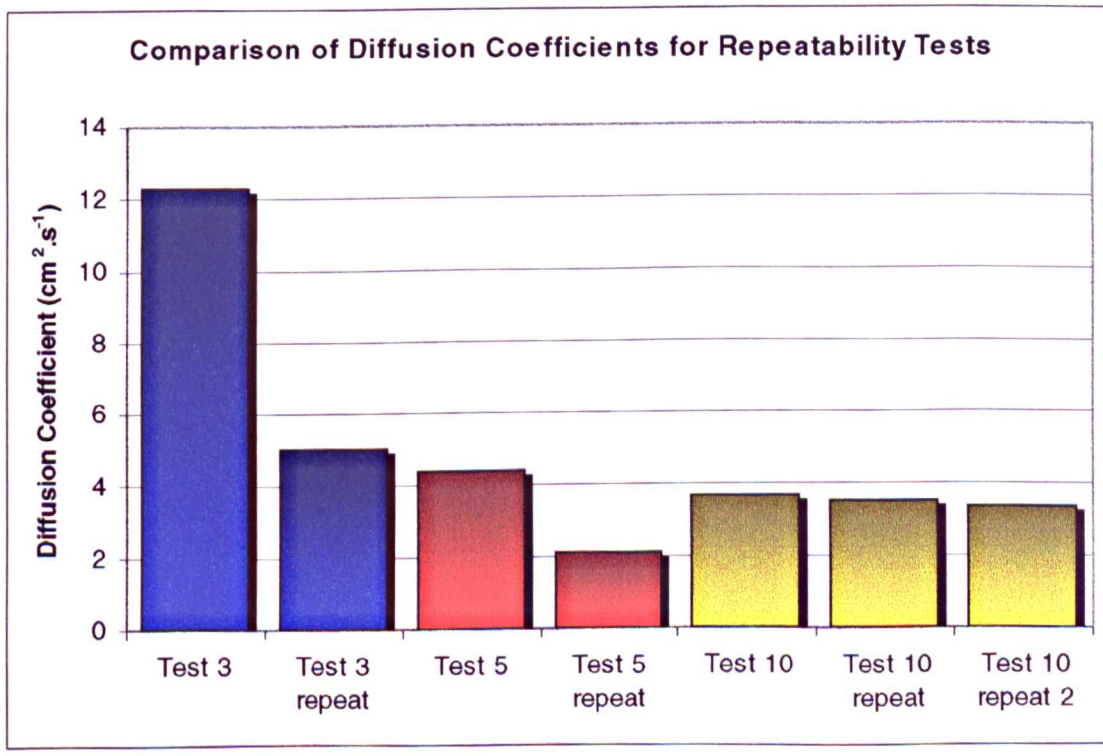

Figure 5.7 - Repeatability of Diffusion Coefficients

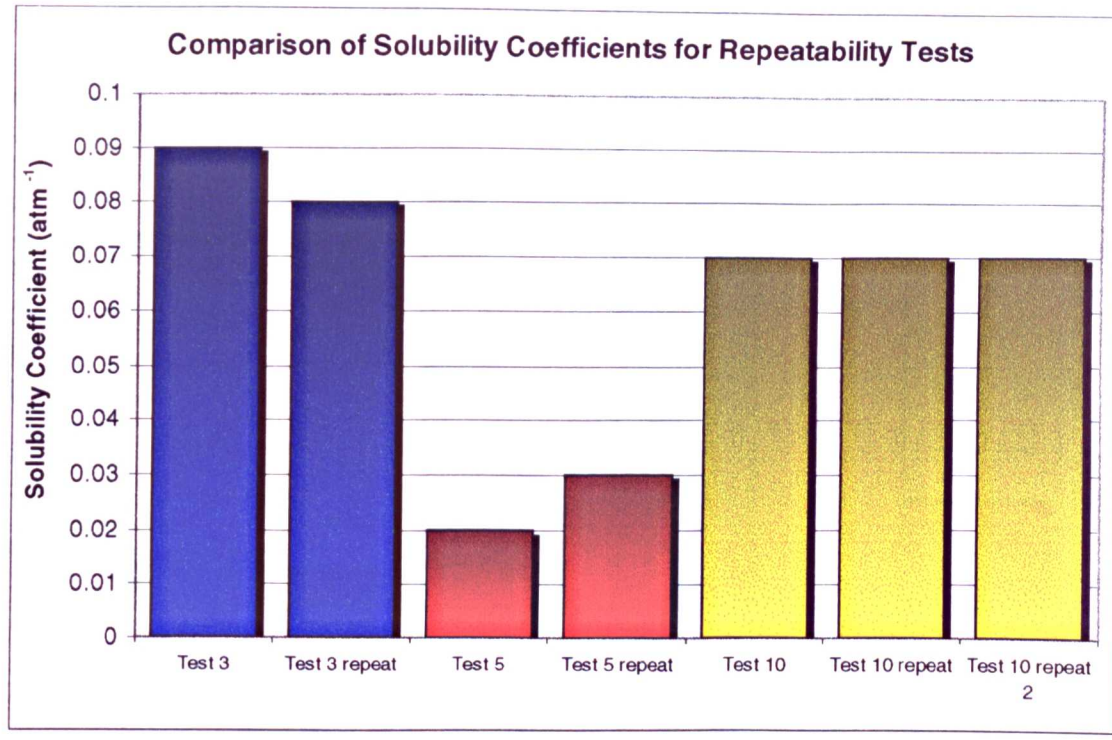

Figure 5.8 - Repeatability of Solubility Coefficients

5.5.2 The Effect of Temperature on Permeation, Diffusion and Solubility

The theory of permeation states that temperature affects the diffusion and solubility of gases in elastomers. The results obtained from the gas transport tests confirm this theory. Figures 5.9 to 5.11 show the effect of temperature on the permeation, diffusion and solubility coefficients for materials A, B and C.

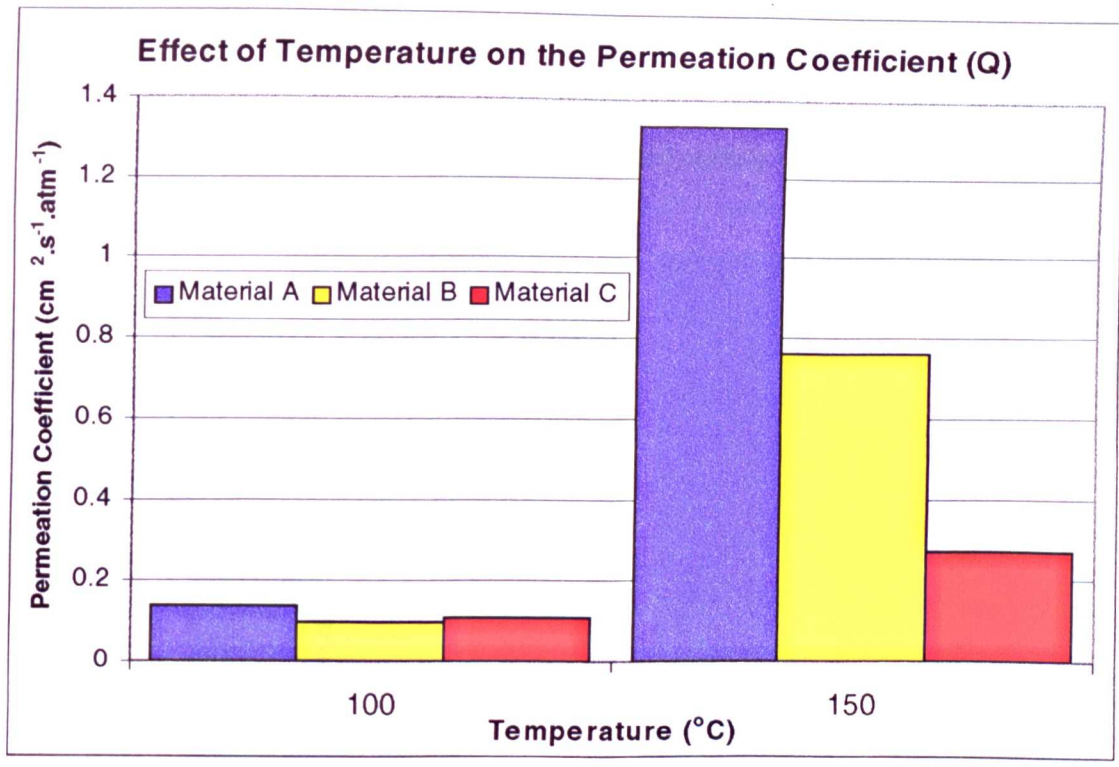

Figure 5.9 - Effect of Temperature on Permeation Coefficient (Q)

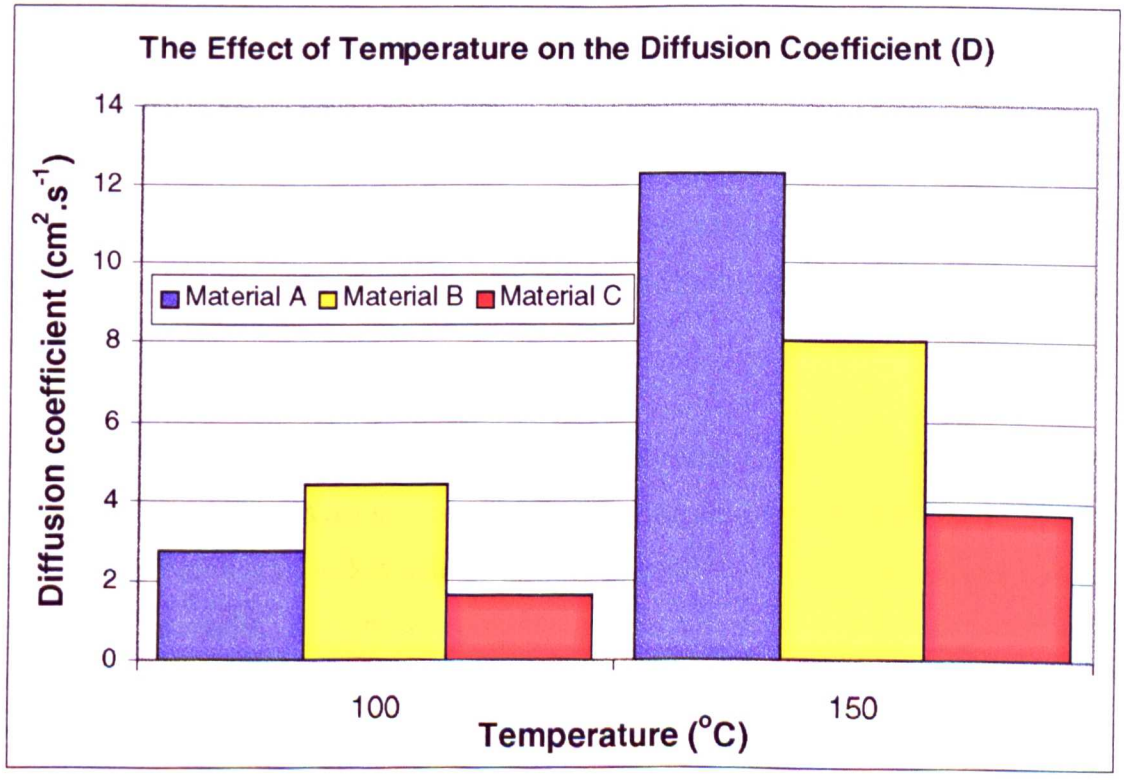

Figure 5.10 - Effect of Temperature on Diffusion Coefficient (D)

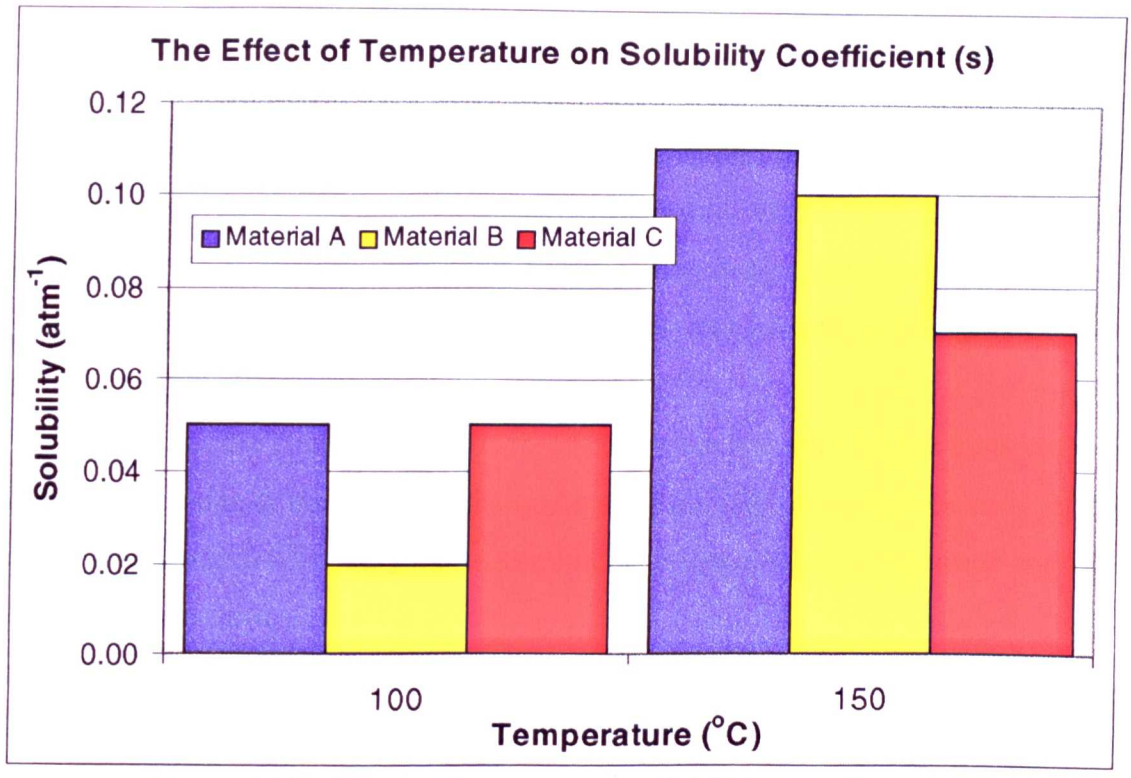

Figure 5.11 - Effect of Temperature on Solubility Coefficient (s)

5.6 DISCUSSION

The gas transport testing method developed is considered accurate and repeatable. However, there are sources of error in both the test and subsequent analysis which should be considered.

Regarding the testing itself, one main area of possible error is the low pressure reservoir. This fixed volume collects the gas as it diffuses through the elastomer membrane. As the rate of gas diffusion is very slow and the pressure increase is relatively small, any leakage could affect the results. The pressure transducer in the low pressure reservoir records the pressure increase with time. The sources of leakage could be slow permeation through either the PTFE 'U' seal or the polymeric burst disc. The low pressure side was pressure tested to ensure that no leakage occurred. The results of this test showed that no measurable leakage was taking place. However, the leakage could be extremely slow and therefore undetectable.

Temperature fluctuations in the low pressure reservoir could also lead to variability in the results. From experiments carried out during commissioning to determine the effects of temperature increase on the low pressure side, it was found that a very small increases in temperature (<1°C) can increase the pressure considerably. The test procedure shows that the temperature is allowed to stabilise before testing begins, often over many hours. However, small fluctuations may occur during testing that will affect the results slightly.

The thickness of the elastomer sheet is measured before and after the gas transport test. The average value is used in the subsequent analysis. However, the thickness of the sample once under test can vary due to swelling, differential thermal expansion and high pressure compaction.

The variable thicknesses of the samples supplied by the manufacturer forced the manufacture of different size compression rings, which hold the sample in place. Only a small number of compression rings were manufactured to cover all eventualities and so the compression of the elastomer sheet was variable. This may have a small effect of the rate of permeation through the sample.

The coefficients determined from the test are not determined directly. They are derived from known mathematical functions using the steady-state and transient pressure increases on the low pressure side. The test therefore assumes that the mathematical functions are correct and hold true under extremes of pressure and temperature.

The analysis of the results of the permeation test could also be a source of error. The slope of the steady-state pressure increase and the time lag are determined graphically from the graph of pressure increase vs time. The analyst may interpret the slope of the curve incorrectly or make errors in measuring quantities directly from the graph.

5.7 CONCLUSIONS

A permeation testing facility has been developed to measure the solubility, diffusion and permeation coefficients of gas-elastomer systems. These parameters can be determined at high temperature and pressure using volatile gases. The facility is designed to be intrinsically safe using features such as a nitrogen purge, a burst disc and computer control. The facility uses the standard sheet form of elastomer, rather than having to mould a sample into a holder.

The permeation test resulted in a plot of pressure increase in the low pressure cavity with time. All tests show the characteristic transient increase followed by the linear steady state increase in pressure. The steady state increase in pressure [dP_2/dt] is determined from the linear portion and the system time lag (τ) is determined by back extrapolating the steady state line until it reaches the time axis. The time from the start of the test to this point is then the time lag. The solubility, diffusion and permeation coefficients are then calculated.

Additional tests were carried out to determine the repeatability of the test method. The repeatability was good except for one test. This showed considerable variation from the original test.

In all cases, temperature increased the solubility, diffusion and permeation as expected from the theory of permeation. Temperature had the largest effect on diffusion coefficient for material A and the largest effect on solubility for material B. Material C showed, in general, the lowest temperature effects. Material A showed the largest effect of temperature on the overall permeation coefficient.

The effect of temperature on the gas transport properties of the elastomer is important when determining the rate of diffusion out of the seal during decompression.

Increase of pressure resulted in little difference in the gas transport properties. In some cases, the rate of diffusion actually decreased. This could be due to matrix compaction, so reducing the available free volume and inhibiting the random thermal fluctuations of the polymer chains.

Some sources of error were determined during the commissioning of the rig. These were reduced through design and procedural changes.

The data generated from the gas transport testing is used in the transient gas transport model (Chapter 8). The data will effectively determine the pressure available for void expansions during decompression.

5.8 CASE STUDY - PERMEATION MODELLING OF GAS MIXTURES THROUGH ELASTOMER MEMBRANES

5.8.1 Introduction

This was developed to meet the requirements of a major oil and gas company to determine the permeation of gas mixtures through elastomer membranes. It shows an alternative application for the data generated during the gas transport testing programme. The requirement of the model is to predict the composition of the gas on the low pressure side of an elastomer membrane under various temperatures and pressures and to determine the gas composition change with time. The company required a spreadsheet-based modelling tool that can be used to assess various operational parameters.

The model incorporated the following factors:

i. the slowing down of permeation due to the rising pressure in the low pressure side (i.e. a reduction in the pressure differential between each side of the membrane).
ii. the facility to maintain the pressure on the low pressure side at a fixed value, in order to simulate the effect of a vent valve.
iii. the capability for users to assess various operational parameters.

5.8.2 Solution

The solution to the problem of modelling permeation of gas mixtures was divided into two sections. The first section was used to determine the volumetric gas flow rates of each of the constituent gases into the low pressure cavity. The second section was used to determine the gas composition and partial pressures on the low pressure side with time as the gas diffuses through the membrane.

5.8.2.1 Permeation modelling

The solution to the permeation modelling problem was to produce a spreadsheet to enable the user to determine the volumetric flow rates of the gas mixture and the individual gases through the elastomer membrane.

The gas mixture is assumed to be composed of three gases, primarily methane (CH_4), carbon dioxide (CO_2) and hydrogen sulphide (H_2S), all of which make up a total pressure P_1. In order for the permeation of each gas to be modelled, the partial pressures of the constituent gases must be calculated. From Dalton's law of partial pressures the total pressure must equal the sum of the partial pressures. If we denote the methane by the subscript A, the carbon dioxide by subscript B and the hydrogen sulphide by C, the total pressure is given by equation (5.6.1).

$$P_1 = \partial P_A + \partial P_B + \partial P_C \qquad (5.8.1)$$

where ∂P is the partial pressure of the constituent gas. If the densities of the gases are similar, we can use the rule of mixtures to determine the partial pressures

$$\partial P_{A,B,C} = \phi_{A,B,C} P_1 \qquad (5.8.2)$$

where $\phi_{A,B,C}$ is the volume fraction of the constituent gas.

The total estimated permeation coefficient for the gas mixture, Q_T, is calculated by using the rule of mixtures.

$$Q_T = \phi_A Q_A + \phi_B Q_B + \phi_C Q_C \qquad (5.8.3)$$

where $Q_{A,B,C}$ is the permeation coefficient of the constituent gas.

During any model carried out using the spreadsheet, the fastest diffusing gas (in this case C), must be entered as gas C, the second fastest as gas B and the fastest as gas A. This is important as the model assumes this is the case.

From equation (5.8.3) the rate of pressure increase on the low pressure side $[\delta P_2/\delta t]_v$ can be calculated using the following relationship

$$\frac{Q_T\ A\ (P_1 - P_2)}{h} = \left[\frac{\delta P_2}{\delta t}\right]_V \left[\frac{273}{T_2}\right] V_2 \qquad (5.8.4)$$

where A is the cross-sectional area of the membrane, h is the membrane thickness and P_2, V_2 and T_2 are the pressure, volume and temperature on the low pressure side respectively. $[\delta P_2/\delta t]_v$ is the rate of change of the low pressure side volume with time at constant volume.

The rate of volumetric gas flow for the complete gas mixture is calculated by

$$\left[\frac{dq}{dt}\right]_{ABC} = \frac{Q_T\ A\ (P_1 - P_2)}{h} \qquad (5.8.5)$$

For the calculation of the volumetric gas flow of each constituent gas, the partial pressures of each gas must be used. The calculation of $[\delta P_2/\delta t]_v$ then becomes

$$\frac{Q_{ABC}\ A\ (\partial P_1 - \partial P_2)_{A,B,C}}{h} = \left[\frac{\delta P_2}{\delta t}\right]_{A,B,C} \left[\frac{273}{T_2}\right] V_2 \qquad (5.8.6)$$

where $\partial P_{1,2}$ is the partial pressure and $Q_{A,B,C}$ is the permeation coefficient of the constituent gases. The rate of volumetric gas flow for the constituent gases is then given by

$$\left(\frac{dq}{dt}\right)_{A,B,C} = \frac{Q_{ABC}\ A\ (\partial P_1 - \partial P_2)_{A,B,C}}{h} \qquad (5.8.7)$$

The rate of volumetric gas flow for each constituent gas should equal the rate for the complete gas mixture.

$$\left(\frac{dq}{dt}\right)_T = \left(\frac{dq}{dt}\right)_A + \left(\frac{dq}{dt}\right)_B + \left(\frac{dq}{dt}\right)_C \qquad (5.8.8)$$

In order to calculate the time for gas to emerge on the low pressure side the solubility

coefficient (s) of the constituent gas in the elastomer is assumed to be known. From this the diffusion coefficient is calculated as

$$D = \frac{Q}{s} \qquad (5.8.9)$$

where D is the diffusion coefficient and Q is the permeation coefficient. The time lag (τ) is then given by

$$\tau = \frac{h^2}{6D} \qquad (5.8.10)$$

where h is the membrane thickness. This quantity is then used to determine the time at which each constituent gas first emerges on the low pressure side.

5.8.2.2 Evaluation of gas composition with time on the low pressure side

It is assumed that the rate of pressure increase due to gas diffusion on the low pressure side is constant and is therefore a linear increase with time. The first gas to diffuse through the membrane will build up pressure within the cavity. This will occur after a time lag (τ). After a period of time the second and third gases will diffuse through the membrane, again adding to the total pressure within the low pressure cavity. The resultant pressure increase is of the form shown in Figure 5.12.

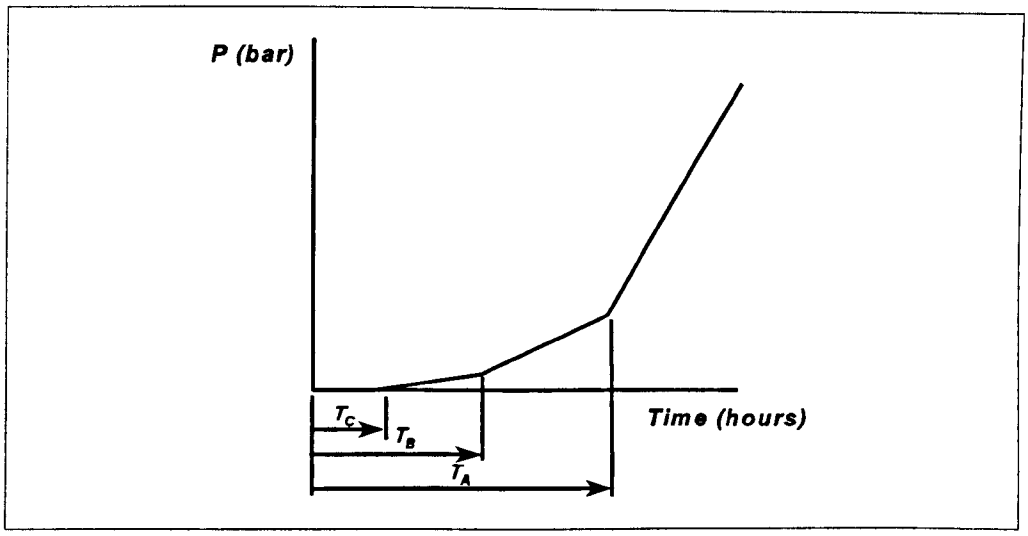

Figure 5.12 - Pressure vs Time for Gas Mixture

The spreadsheet calculates the constants for the straight line equation of the form (y=mx+c) for each of the constituent gases. The constants are given by

$$c_C = 0 - \left[\frac{dP_2}{dt}\right]\tau_C \qquad (5.8.11)$$

The subscripts A, B and C denote the pressure for each constituent gas. The partial pressures of each constituent gas are then calculated with time using equations (5.8.12) at each stage of the gas diffusion through the membrane, assuming that gas C diffuses first, then B and finally A from the permeation data provided.

until time = τ_C, $\quad P_{CBA} = P_{CB} = P_C = 0$

then

$$P_{C_t} = \left(\frac{dP_2}{dt}\right)_{C_t} \delta t + P_{C_{t-1}}$$

until time = τ_B, $\quad P_B = 0,\ P_A = 0,\ P_{CBA} = P_{CB} = P_C$

then

$$P_{B_t} = \left(\frac{dP_2}{dt}\right)_{B_t} \delta t + P_{B_{t-1}} \qquad (5.8.12)$$

until time = τ_A, $P_A = 0$, $P_{CBA} = P_{CB}$

then

$$P_{A_t} = \left(\frac{dP_2}{dt} \right)_{A_t} \delta t + P_{A_{t-1}}$$

where δt denotes the time interval in seconds, subscript t indicates the current time step, subscript t-1 indicates the last time step, and

$$\frac{Q_T A (P_{1_t} - P_{2_{t-1}})}{h} = \left[\frac{\delta P_2}{\delta t} \right]_{V_t} \left[\frac{273}{T_2} \right] V_2 \qquad (5.8.13)$$

From these relationships the pressure increase within the low pressure cavity can be calculated. The sum of the partial pressures should equal the total pressure within the cavity.

$$P_{ABC} = \partial P_A + \partial P_B + \partial P_C \qquad (5.8.14)$$

In order to determine the percentage volume of gas in the low pressure cavity, the partial pressure is divided by the total pressure.

$$[\%vol]_{ABC} = \frac{\partial P_{ABC}}{P_{ABC}} \qquad (5.8.15)$$

5.8.2.3 Venting the low pressure side

If the pressure on the low pressure side is higher than the venting pressure, the following equations are used instead of those from (5.8.12).

$$P_{C_t} = \left(\frac{dP_2}{dt} \right)_{C_t} \delta t + \left(\frac{P_{re-seat}}{P_{vent}} \right) P_{C_{t-1}}$$

$$P_{B_t} = \left(\frac{dP_2}{dt}\right)_{B_t} \delta t + \left(\frac{P_{re-seat}}{P_{vent}}\right) P_{B_{t-1}} \qquad (5.8.16)$$

$$P_{A_t} = \left(\frac{dP_2}{dt}\right)_{A_t} \delta t + \left(\frac{P_{re-seat}}{P_{vent}}\right) P_{A_{t-1}}$$

where P_{vent} is the pressure at which the vent valve opens, and $P_{re\text{-}seat}$ is the pressure at which the vent valve closes after releasing excessive pressure.

5.8.3 GUIDELINES FOR USE OF THE MODEL

The model is split into four worksheets within the spreadsheet file, these are as follows:-

- Permeation calculations
- Partial pressure calculations
- Partial pressure graph
- %volume graph

The spreadsheet is protected to avoid any unwanted deletion of any of the equations or relationships. Only data which is required to be entered by the user can be changed.

5.8.3.1 Permeation calculations

The input data required for the permeation calculations are as follows:-

- Gas composition (% volume)
- Membrane thickness
- High pressure side temperature
- Low pressure side temperature

- Pressure on the high pressure side
- Pressure on the low pressure side
- Volume of the low pressure side (per unit area of membrane)
- Cross sectional area of membrane (can be set to unity for results per unit area)
- Permeation coefficients of the constituent gases
- Solubility coefficients of the constituent gases

The model requires the percentage volume of carbon dioxide and hydrogen sulphide and then calculates the remaining volume of methane. The system pressure, P_1, is entered and the partial pressures are automatically calculated.

The membrane thickness, temperatures and low pressure side pressure are entered as normal. The volume of the low pressure side is entered for the cross-sectional area of membrane specified. The model is currently set with a cross-sectional area of membrane at $1 cm^2$ for simplicity which will give results per unit area. This value may be varied for specific cases.

The user has to adjust the time steps over which the analysis is performed. The time scale is changed in seconds and the column labelled 'hours' will be automatically updated. If the time step is too large, this will reduce the accuracy. If the time step is too small, the spreadsheet will require more computational power for the spreadsheet to be updated.

The model carries out a check under which the volumetric flow rates for the constituent gases are summed. This value should be in line with the volumetric flow rates for the gas mixture. Small differences will be observed between the two values due to rounding errors.

5.8.3.2 Partial pressure calculations

This worksheet calculates the partial pressures and percentage volumes of each of the constituent gases with time on the low pressure side of the membrane. The only data which can be changed in this part of the model are the vent pressure and the re-seating pressure. If the pressure vent is not considered, the vent pressure and the re-seating pressure values are set higher than the pressure on the high pressure side.

The model produces the two graphs showing partial pressures and percentage volumes vs time (see Figures 5.13 and 5.14). If the model is changed, these graphs are automatically updated. The scales on the graphs can be manually changed as normal with spreadsheet graphs if closer examination is required.

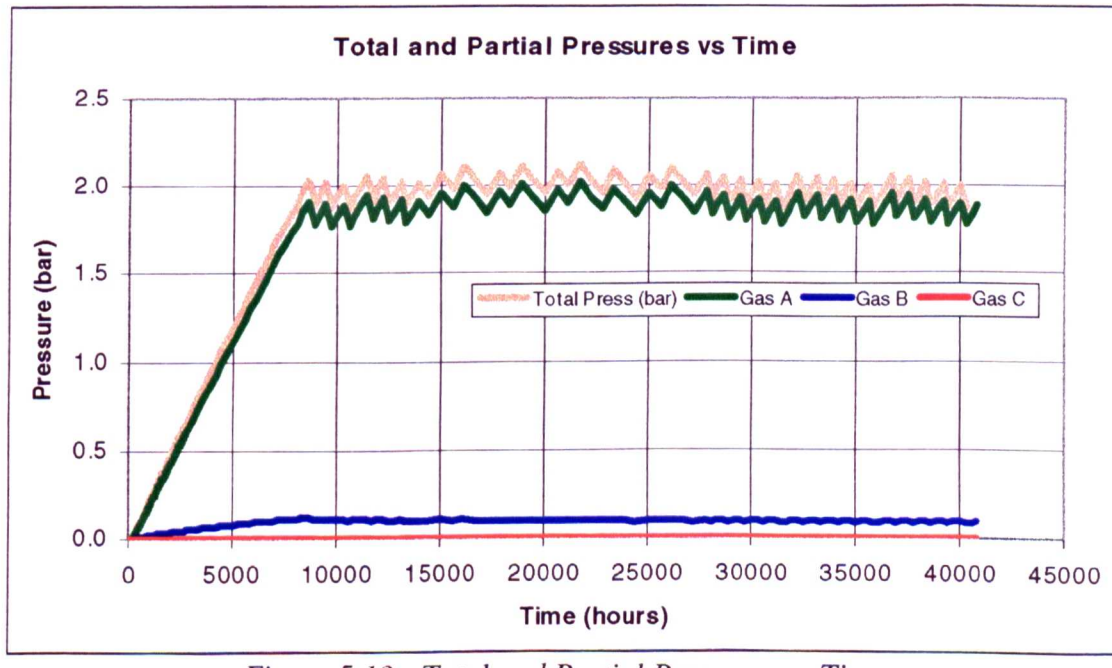

Figure 5.13 - Total and Partial Pressures vs Time

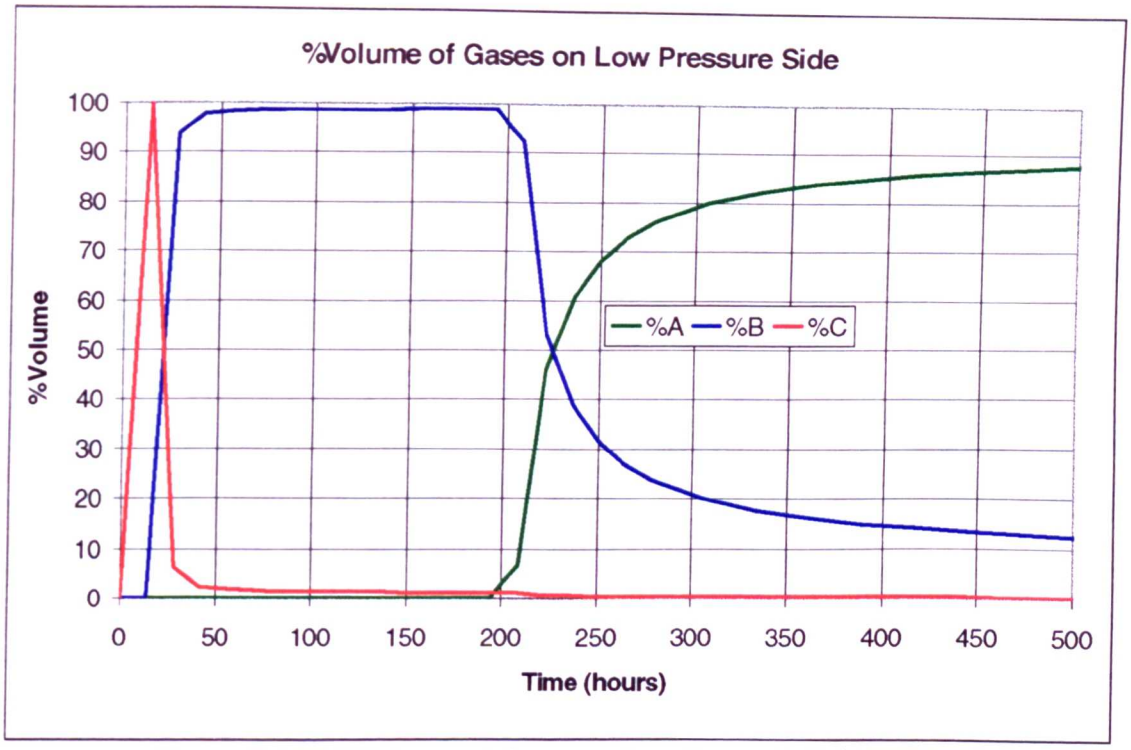

Figure 5.14 - %Volume of Gases on Low Pressure Side vs Time

5.8.3.3. Case study conclusion

The model provided gives the volumetric flow rate for both the gas mixture and the constituent gases permeating through a polymer membrane. It allows the user to change the variables to establish the effect on the overall volumetric flow rate. The second section of the model allows the user to establish the partial pressure changes and percentage volumes of the constituent gases with time.

5.9 CHAPTER SUMMARY

The permeation characteristics of any given elastomer-fluid combination are unique and cannot be accurately predicted by analytical methods. Therefore, a permeation cell was designed and built to enable the permeation characteristics of elastomer membranes to be determined at high pressure and temperature in volatile gases.

The rig was designed such that a standard elastomer test sheet as supplied by material

manufacturers could be used within the rig, rather than moulding special test pieces.

Many problems, which were encountered during the design and building of the rig, had to be evaluated and solved as they arose. These problems caused the scheduled cell commissioning time to be almost doubled.

The diffusion, solubility and permeation data obtained for each material under different operational conditions are then used in the transient diffusion model to determine available pressure differentials within the O-ring during decompression.

The data generated from the testing programme can be used for various applications. The data is used for the transient gas diffusion modelling section of the explosive decompression model. The data for individual gases can be used together to simulate the effects of gas mixtures. This is shown in a case study for the prediction of the transport of gas mixtures through elastomer membranes. The model can be used for the prediction of pressure buildups in the annulus between pipes and polymeric liners. The low pressure vent part of the model is used to simulate the effects of periodically reducing the annulus pressure in polymer lined pipes. If the pressure buildups can be determined, the probability of liner collapse can be easily predicted.

CHAPTER 6 - STATISTICAL ANALYSIS OF ELASTOMER QUALITY CONTROL DATA

6.1 INTRODUCTION

To determine the variability of elastomer material properties, and therefore variability in the output from computational models developed under the research programme, historical data of physical properties were analysed.

The data supplied by elastomer material manufacturers for materials A and B were obtained from quality control tests carried out over the period 1992-1997. The data obtained for material C are limited to a small number of batches over a one year period. The purpose of the statistical analysis is to determine the spread and time based trends of various physical properties of commercially available, explosive decompression resistant materials.

The results of the analysis will provide a confidence limit in the input data used in finite element models.

6.2 APPROACH

The analysis was approached by initially gathering the data and then using statistical methods to arrive at conclusions regarding spread and trends. The physical properties analysed were;

- Hardness
- Stress at 25% strain (Material B only)
- Stress at 50% strain
- Stress at 100% strain (Material A only)

- Tensile strength
- Elongation at break

The three materials studied were : -

- Material A : Hydrogenated nitrile rubber (HNBR)
- Material B : Fluorocarbon (FKM)
- Material C : Fluorocarbon (FKM)

The quantity of data available for Material A was considerably less than that available for Material B. The data was analysed using a spreadsheet package to arrive at both descriptive statistics and histogram based distributions.

6.3 RESULTS

Tables 6.1 to 6.3 show the summary of descriptive statistics for materials A, B and C. The standard deviation value gives a measure of the variation of results about the mean for a given physical property. The results observed were, in general, a normal distribution about a mean value. From this data, assuming a normal distribution, the following can be observed.

- 68% of the values will fall within ±1 standard deviation (σ)
- 95% of the values will fall within $\pm 2\sigma$
- 99.7% of the values will fall within $\pm 3\sigma$

The bands for 95% confidence are also given in Tables 6.1 to 6.3. The confidence bands are based on the hypothesis that 95% of samples tested will fall within ±2 standard deviations of the mean. This assumes that the distribution of samples is normal about a mean value. The table gives the minimum and maximum values in the 95% confidence range.

Table 6.1 - Summary of descriptive statistics for Material A

Property	Units	Mean	Mode	σ	Confidence Range		% Var
					Min	Max	
Hardness	IRHD	90.7	91.0	1.4	87.9	93.5	±3%
Stress at 50% strain	MPa	5.9	5.9	0.7	4.5	7.3	±24%
Stress at 100% strain	MPa	12.6	14.2	1.7	9.2	16.0	±27%
Tensile strength	MPa	32.1	32.2	1.8	28.5	35.7	±11%
Elongation at break	%	216.9	210.0	22.4	172.1	261.7	±21%

Table 6.2 - Summary of descriptive statistics for Material B

Property	Units	Mean	Mode	σ	Confidence Range		% Var
					Min	Max	
Hardness	IRHD	89.2	90.0	1.5	86.2	92.2	±3%
Stress at 25% strain	MPa	3.7	3.4	0.5	2.7	4.7	±27%
Stress at 50% strain	MPa	5.8	5.5	0.9	4.0	7.6	±31%
Tensile strength	MPa	14.1	13.7	1.2	11.7	16.5	±17%
Elongation at break	%	185.4	180.0	17.7	150.0	220.8	±19%

Table 6.3 - Summary of descriptive statistics for Material C

Property	Units	Mean	Mode	σ	Confidence Range		% Var
					Min	Max	
Hardness	IRHD	92.7	94.0	1.1	90.5	94.9	±2%
Stress at 50% strain	MPa	9.5	-	0.7	8.1	10.9	±15%
Tensile strength	MPa	19.1	-	0.9	17.3	20.9	±9%
Elongation at break	%	105.9	107.0	4.2	97.5	114.3	±8%

Figure 6.1 shows an example of a frequency distribution comparison plot of hardness between material A and B.

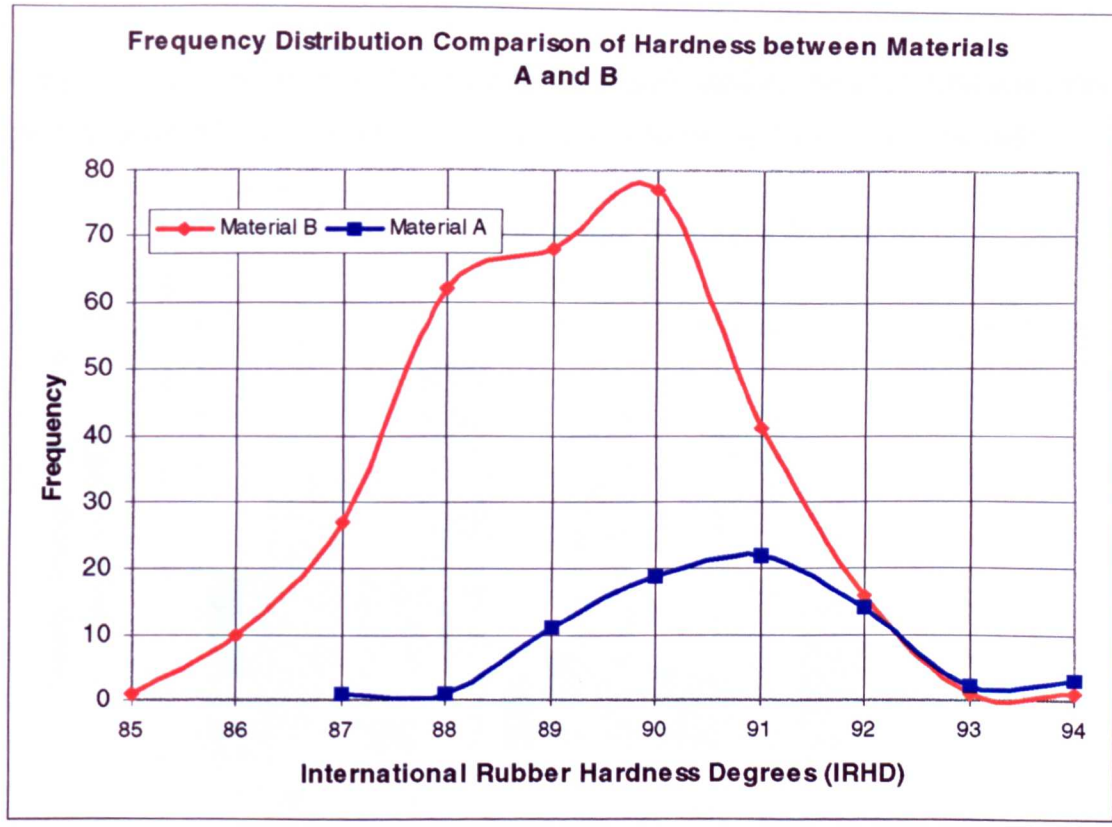

Figure 6.1 - Frequency distribution plot of hardness for materials A and B

Figure 6.2 shows an example chart of mean hardness vs time for materials A and B.

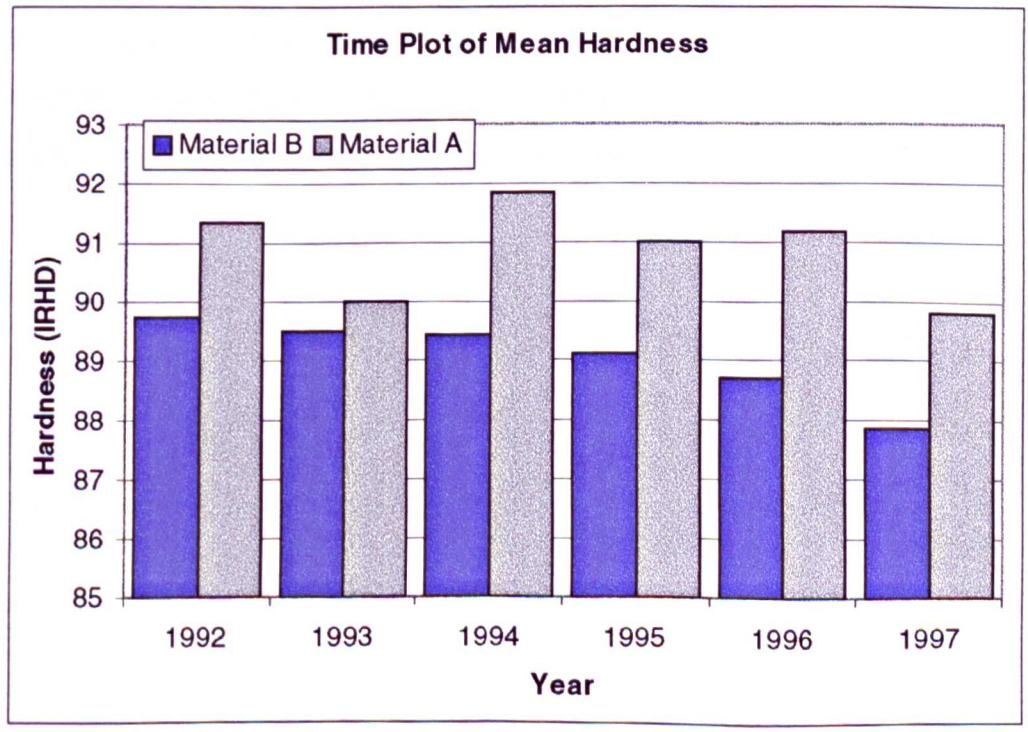

Figure 6.2 - Mean hardness vs time plot for materials A and B

Figure 6.3 shows an example chart of tensile strength standard deviation with time, which gives a direct indication of whether the process is becoming more or less variable.

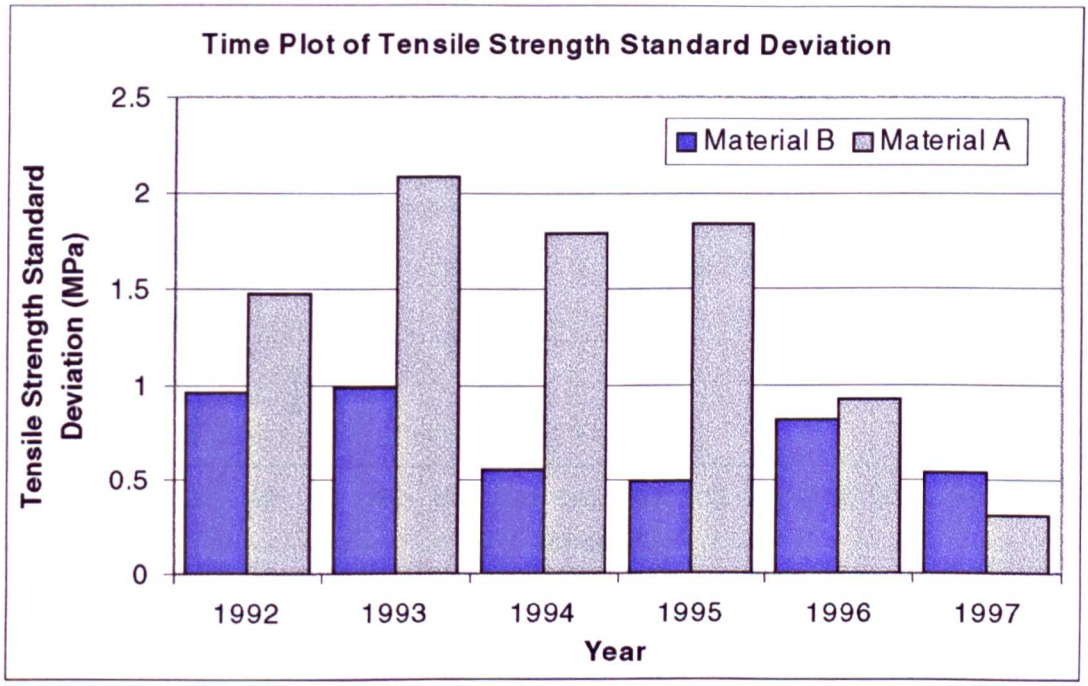

Figure 6.3 - Tensile Strength Standard Deviation vs with time for materials A and B

Using the stress at strain, tensile strength and elongation at break values, an approximate stress-strain curve can be constructed. Figures 6.4 and 6.5 show the inherent variability in the stress-strain characteristics of the materials, in particular at failure. Note that the region at failure is both variable in terms of elongation at break and tensile strength.

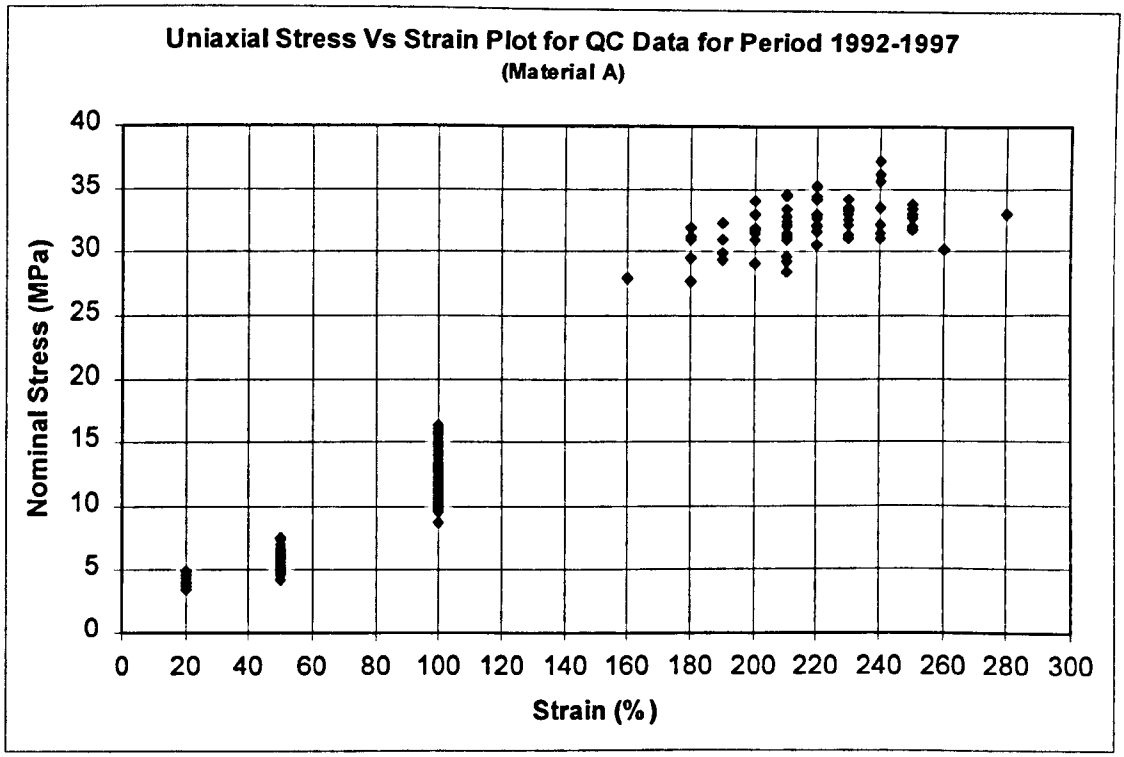

Figure 6.4 - Stress-strain plot for material A including variability

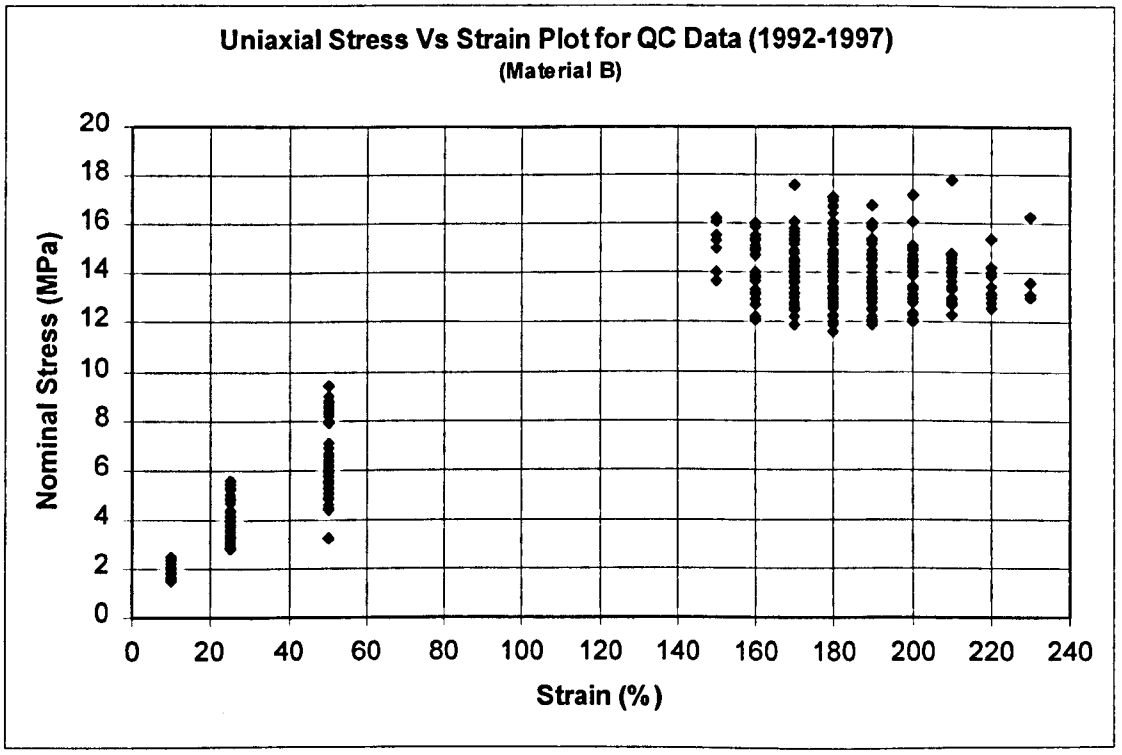

Figure 6.5 - Stress-strain plot for material B including variability

6.4 CONCLUSIONS

6.4.1 Hardness

The frequency distribution plots show that the hardness of both materials A and B vary considerably. Both materials show approximate normal distributions with the mean values being around 90 IRHD. The spread in the values of material B is much larger than that of material A, suggesting that it is much more probable that a higher or lower hardness material will be produced. In general, the mean hardness of material C is higher at 92.7 IRHD and is also less variable than materials A and B.

The time plot of mean hardness shows that over the five year time period, the hardness of material B has steadily reduced. The variation in hardness of material A over the time period is cyclic in nature, with no particular trend. The time plot of hardness standard deviation over the time period shows that the standard deviation has steadily reduced in material B and is cyclic in material A. This would suggest that the spread of values in material B is slowly decreasing, i.e. the hardness is becoming less variable. The cyclic nature of the standard deviation in material A shows that the spread in values is reasonably constant.

6.4.2 Stress at 50% strain

This property is used as a measure of elastic modulus of the material. The frequency plots show that the variance of materials A and B are similar at around 30%. However, the value for material C is much higher and again less variable at 15%.

The time plots for materials A and B shows that there has been very little variation in the mean stress at 50% strain over the five year period. The standard deviation has varied over the five year period in material B. Initially, for the first two years, the standard deviation was high compared with the final three years, whereby it remained reasonably constant.

The standard deviation in material A has been cyclic in nature with no apparent trends.

6.4.3 Tensile strength

The tensile strength of the materials B and C are much lower than material A, with material A exhibiting over twice the strength of materials B and C. However, the spreads of values are similar, suggesting that they possess a similar variance about a different mean value. Again, material C is much less variable than A and B.

The time plots of mean tensile strength over the five year period show that there was very little variation in the mean value. The tensile strength standard deviation for material A has reduced significantly over the last two years indicating a reduction in the spread of values. The standard deviation for material B has shown a tendency to reduce over the five year period, although this is more variable.

6.4.4 Elongation at break

The mean value of elongation at break for material C is much lower than A and B. Material A has a mean value of 217%, material B has a value of 185%, whereas material C is 106%. Material C is less variable than materials A and B.

The time plot of mean elongation at break shows that there is little variation. There are no trends in the mean value over the time period. The time plot of elongation at break standard deviation shows that for material A there was a trend for a reduction between 1992-1994 that has since started to rise again during 1996 and 1997. The value for material B shows a steady value over the period 1992-1996, but in 1997 shows a considerable rise of around 40% from the previous year. This may suggest that the process is becoming more variable, but this may be part of a cycle and the value may reduce again in the coming years.

CHAPTER 7 - EQUIBIAXIAL TENSILE TESTING OF ELASTOMER MEMBRANES

7.1 INTRODUCTION

To obtain relevant material physical data regarding stress-strain profiles and critical stress to failure for finite element modelling purposes, carrying out representative material testing was necessary. Finite element models are as accurate as the material data used in them, and are often misinterpreted. It is a requirement of the finite element modelling process to use test data that represent the loading conditions experienced by the component.

For the modelling areas of the research, using ABAQUS finite element software, stress-strain characteristics derived from a range of test data are most suitable for running an analysis. However, this is not always practicable or cost effective. The optimum set of data would include: -

- Uniaxial test data
- Biaxial test data
- Planar (pure shear) test data
- Volumetric test data

In the analysis programme it was envisaged that only uniaxial and biaxial data would suffice to give a good representation of the stress field in both the O-ring model and the void expansion model.

In addition to the stress-strain data for the selected materials, the critical stress at failure under equibiaxial extension is also required. This data would be used as a failure indicator in the void expansion modelling phase of the project.

A test method was devised where both the stress-strain conditions for the elastomer and the critical stress to failure were determined under equibiaxial extension.

7.2 EXPERIMENTAL PROCEDURE

The material test programme requires that five materials are studied under equibiaxial extension, these are designated by material codes A, B, C, D and E. Materials B and C are both fluorocarbon based elastomers. Material A is a hydrogenated nitrile (HNBR) based material and material D is a standard nitrile elastomer. Material E is a very hard fluorocarbon based elastomer (98 IRHD). The test is carried out on an elastomer membrane, nominally 2mm thick. The membrane is inflated by gas pressure to failure.

The elastomer membrane is inflated using the test arrangement shown in Figure 7.1. The membrane is clamped between two steel plates by a series of bolts on a pitch circle diameter. The pressure is applied to the bottom plate using bottled nitrogen. The top plate has a very large radius machined onto the clamping contact area between the plate and the membrane. This is used to reduce the local stress concentration around this point during inflation and therefore prevent premature failure.

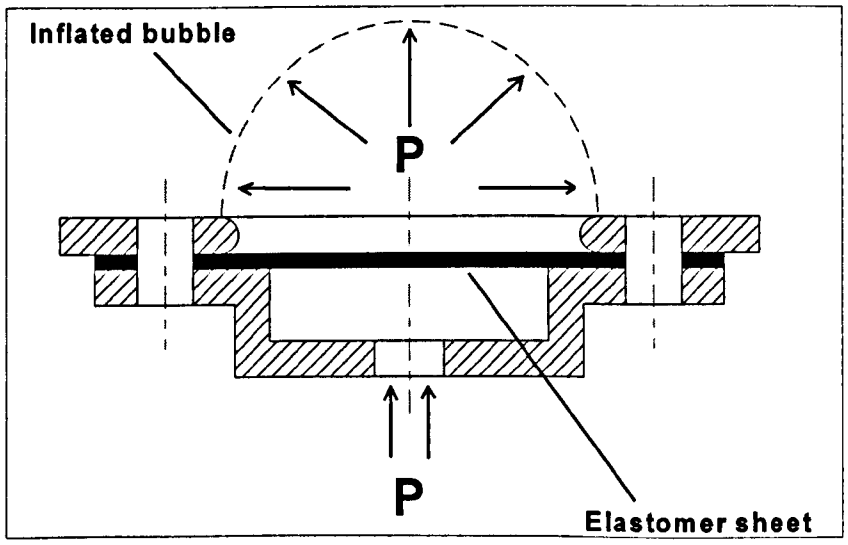

Figure 7.1 - Test arrangement

A pressure transducer is affixed to the bottom plate to monitor the applied pressure to the membrane; these data are recorded at a rate of 10 Hz. The assembly is mounted in a cabinet to support the fixture and to allow all recording equipment to be easily mounted.

The inflation process is monitored by means of two video cameras mounted to the side and above the fixture. The camera on the side is used to measure the height and the radius of curvature of the membrane with time and pressure. This is achieved by mounting a grid behind the inflating membrane.

The top camera is used to determine the variation in extension ratio (strain) with pressure and time. Before testing, a grid is printed onto the top of the elastomer membrane and its size is calibrated using the video equipment. The small element at the crown of the inflated membrane will be under equibiaxial extension and will also coincide with the position of maximum stress. As the membrane is inflated, the grid will stretch and so the extension ratio can be determined. Using the radius of curvature, the pressure and the extension ratio, the stress can be calculated for a given strain.

The strain, pressure and radius of curvature data are then correlated using video editing and data acquisition equipment. The ambient temperature and thickness of the sample are also measured.

7.2.1 Test assumptions

It is assumed that during the inflation phase of the test the membrane remains equally loaded, symmetric about the vertical axis. The clamping arrangement is not assumed to affect the resultant stress levels at the crown. As the extensibilities of the elastomers being studied are quite low in comparison with lower hardness materials, the shape of the inflated membrane never increases above that of a hemispherical form. The majority of the testing carried out shows that the shape of the membrane at failure is approximately hemispherical in nature. Therefore the radius of curvature can be assumed to be that of the

radius of the undeformed membrane.

7.3 DATA ANALYSIS

The method used to calculate the stress values for a given strain are based on the observations of Flint and Naunton (1937), Treloar (1943) and James, Green and Simpson (1975)

If an element at the crown of an inflated, infinitesimally thin membrane is considered, the tensions in the latitudinal (T_1) and the longitudinal (T_2) directions and the respective radii of curvature R_1 and R_2, are related to the inflation pressure P according to the equation: -

$$P = \frac{T_1}{R_1} + \frac{T_2}{R_2} \qquad (7.3.1)$$

At the crown, $T_1=T_2=T$ and $R_1=R_2=R$, therefore

$$P = \frac{2T}{R} \qquad (7.3.2)$$

If the thickness of the strained material is t, then the stress at the crown is given by: -

$$\sigma = \frac{T}{t} \qquad (7.3.3)$$

Combining equations (7.3.2) and (7.3.3) gives

$$\sigma = \frac{PR}{2t} \qquad (7.3.4)$$

For an incompressible material stretched equibiaxially by λ, the third dimension is reduced by $\frac{1}{\lambda^2}$, thus

$$t = \frac{t_o}{\lambda^2} \qquad (7.3.5)$$

where t_0 is the original thickness. Therefore, the crown stress can be found for a particular crown strain by: -

$$\sigma_c = \frac{PR\lambda^2}{2t_o} \qquad (7.3.6)$$

The crown strain at failure is then used to determine the crown stress at failure by using the above relationship. All data points on the stress-strain curves are calculated using this technique. Equation (7.3.6) gives the true stress, the force per unit strained area. The finite element software requires that the nominal stress is used as input, that is the force per unit unstrained area. This is calculated from: -

$$\sigma_n = \frac{\sigma_t}{\lambda^2} \qquad (7.3.7)$$

where σ_n is the nominal stress and σ_t is the true or Cauchy stress.

7.3.1 Calculation of Strain Energy Function Coefficients

To calculate the stress from a given extension ratio, the finite element software uses a strain energy function. The stress can then be calculated as the partial differential of the strain energy function with respect to the extension ratio. The strain energy function can be defined in two ways, using either the polynomial or Ogden form. The polynomial function is given by

$$U = \sum_{i+j=1}^{N} C_{ij} (I_1 - 3)^i (I_2 - 3)^j + \sum_{i=1}^{N} \frac{1}{D_i} (J_{el} - 1)^{2i} \qquad (7.3.8)$$

where U is the strain energy per unit reference volume; N is a material's parameter; C_{ij} and D are temperature dependent material's parameters; J_{el} is the elastic volume ratio and I_1 and

I_2 are the first and second deviatoric strain invariants, given in Chapter 2, section 2.3.

If we take the form of the polynomial function where N=1, we form the classical Mooney-Rivlin law

$$U = C_{10}(I_1 - 3) + C_{01}(I_2 - 3) \qquad (7.3.9)$$

The Ogden strain energy function is given by

$$U = \sum_{i=1}^{N} \frac{2\mu_i}{\alpha_i^2} (\lambda_1^{-\alpha_i} + \lambda_2^{-\alpha_i} + \lambda_3^{-\alpha_i} - 3) + \sum_{i=1}^{N} \frac{1}{D_i} (J_{el} - 1)^{2i} \qquad (7.3.10)$$

where μ_i, α_i and D_i are temperature dependent material's parameters. The second term may be neglected on the basis on the incompressibility approximation.

For simplicity, if we take the N=1 form of the polynomial strain energy function (equation (7.3.9)), the following conditions exist in equibiaxial extension.

$$\lambda_1 = \lambda_2 = \lambda_b, \qquad \lambda_3 = \frac{1}{\lambda_b^2} \qquad (7.3.11)$$

Where λ_b is the extension ratio in the two perpendicular loading directions. If we use the principle of virtual work, assuming the stress perpendicular to the two loading directions is zero.

$$\delta U = 2\sigma_b \delta\lambda_b \qquad (7.3.12)$$

The nominal equibiaxial stress if therefore given by

$$\sigma_b = \frac{1}{2} \frac{\partial U}{\partial \lambda_b} = 2(\lambda_b - \lambda_b^{-5}) \left[\frac{\partial U}{\partial I_1} + \lambda_b^2 \frac{\partial U}{\partial I_2} \right] \qquad (7.3.13)$$

If we take the partial differential of the strain energy function with respect to I_1 and I_2, equation (7.3.13) becomes

$$\sigma_b = 2(\lambda_b - \lambda_b^{-5})(C_{10} + \lambda^2 C_{01}) \qquad (7.3.14)$$

This function was used to create fitted stress-strain curves. The strain energy function coefficients were calculated using the ABAQUS finite element software. For each stress-strain pair the software generates an equation for the stress in terms of the strain invariants or stretches and the unknown hyperelastic constants, assuming the incompressibility approximation. The hyperelastic constants are materials parameters that define the magnitude of stress for a given value of strain.

Since the number of stress equations will be greater than the number of unknown constants, a least squares fit must be performed to determine the hyperelastic constants. For the n stress-strain pairs comprising all of the test data, the following error measure E_r is minimised.

$$E_r = \sum_{i=1}^{n} \left[1 - \frac{T_i^{th}}{T_i^{test}} \right]^2 \qquad (7.3.15)$$

where T_i^{test} is a stress value from the test data and T_i^{th} is a theoretical stress expression as described above. The polynomial potential is linear in the coefficients C_{ij}, therefore a linear least squares fit is used. The Ogden potential (equation 7.3.10) is linear in the coefficients μ_i, but highly nonlinear in the exponents α_i, therefore a nonlinear least squares fit is performed.

When a set of constants are derived, the software performs a material stability check along the primary deformation modes using the Drucker stability criterion:-

$$d\sigma : d\varepsilon > 0 \quad \Rightarrow \quad d\varepsilon \,.\, D : d\varepsilon > 0 \qquad (7.3.16)$$

where dσ is the change in stress due to an infinitesimal change in strain dε, and D is the tangential material stiffness. For an isotropic elastic formulation the inequality can be expressed in terms of the principal stresses and strains

$$d\sigma_1 d\varepsilon_1 + d\sigma_2 d\varepsilon_2 + d\sigma_3 \varepsilon_3 > 0 \qquad (7.3.17)$$

7.4 RESULTS

The results will be divided into two sections for ease of reference, equibiaxial stress-strain results and critical stress-strain results.

7.4.1 Equibiaxial stress-strain tests

The averaged equibiaxial stress-strain plots for each material are shown in Figure 7.2. Figure 7.3 shows the repeatability of the testing procedure. Figure 7.4 shows a photograph of a test in progress, clearly showing the inflated membrane.

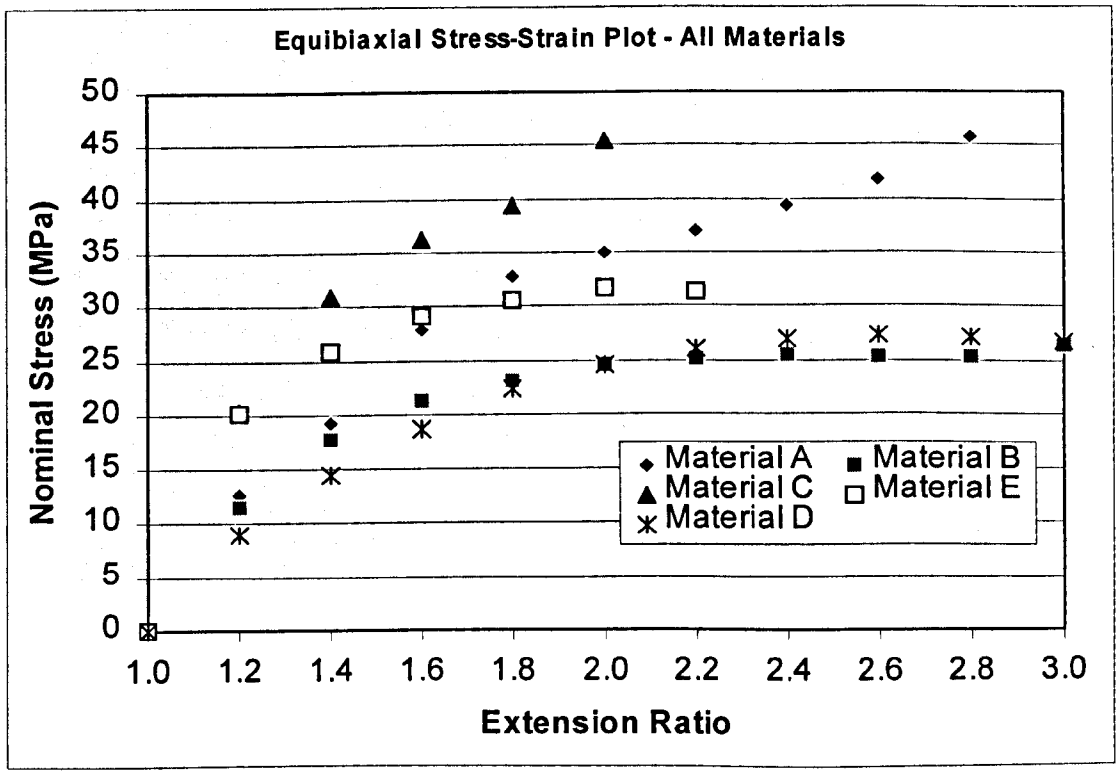

Figure 7.2 - Equibiaxial stress-strain plot for materials A, B, C, D and E

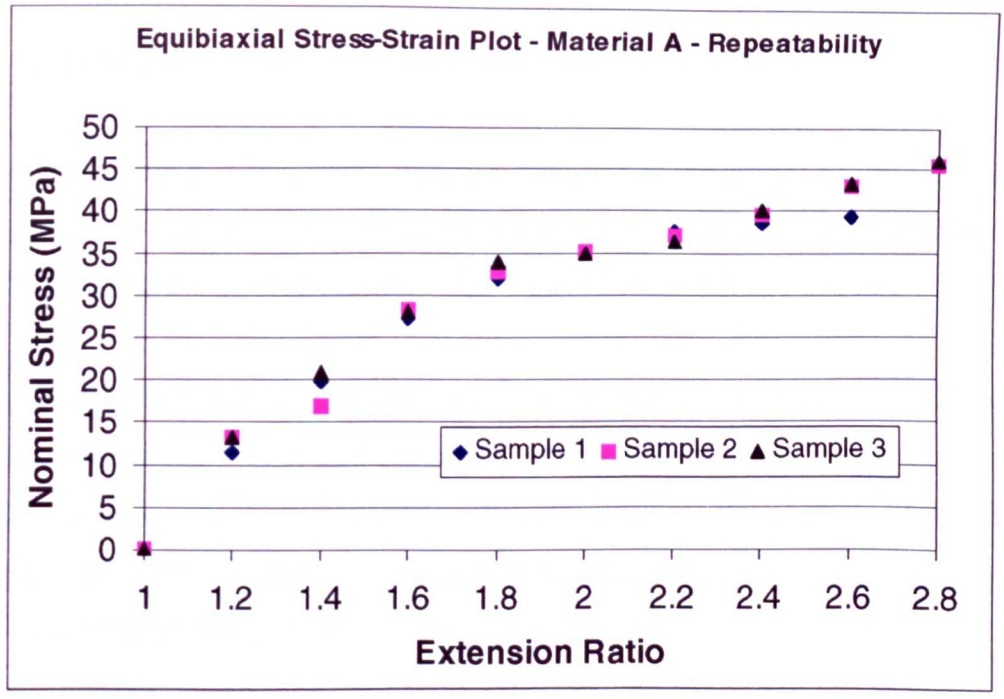

Figure 7.3 - Equibiaxial stress-strain plot for material A showing repeatability

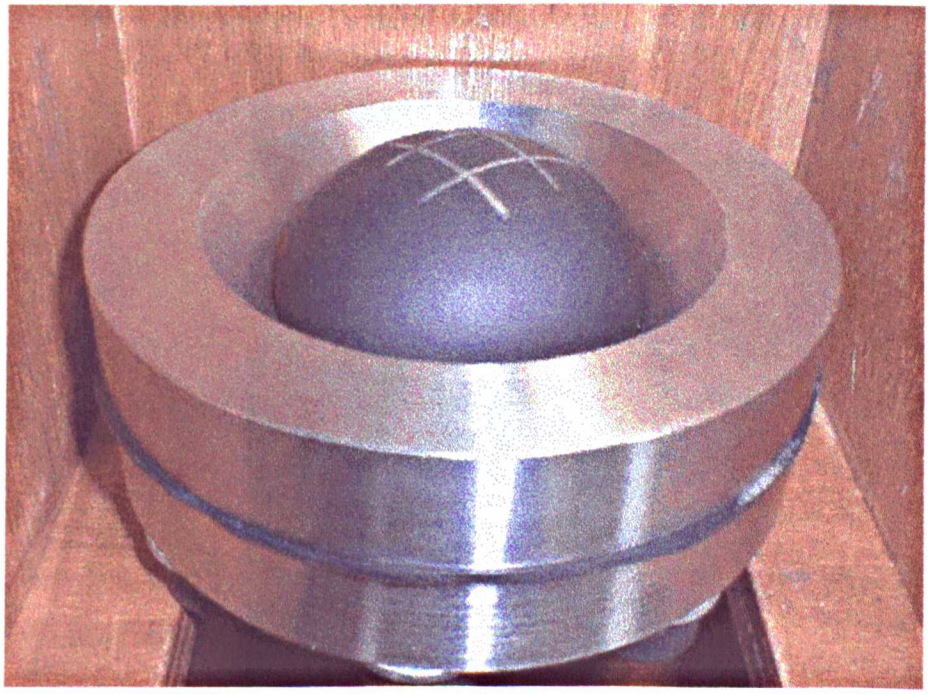

Figure 7.4 - Photograph of equibiaxial tensile test in progress

7.4.2 Critical Stress-Strain Test Results

The nominal stress at which failure occurs is regarded as the critical stress. The stress-strain plots show that the critical stress and corresponding strain are repeatable from the three tests carried out on each material. The results are summarised in Table 7.1.

Any variation in the results between the tests could be due to several factors. Elastomers are notoriously inconsistent in their physical properties, even within a single batch, due to differing cure rates and the presence of voids and inclusions. For example, if the critical strained region of the diaphragm contained a rigid defect, it would act as a stress raiser, therefore causing premature failure.

During failure it was observed that failure occurred in the region surrounding the crown at the top of the inflated membrane. The failure pattern often formed 'petal' shaped pieces. Figure 7.5 shows a photograph of a failed membrane in the test arrangement.

Figure 7.5
Photograph of Test Arrangement

Table 7.1 - Summary of Critical Strain and Stress Values

MATERIAL	HARDNESS (IRHD)	CRITICAL STRAIN (%)		CRITICAL STRESS (MPa)	
		MEAN	% VARIABILITY	MEAN	% VARIABILITY
A	91	160	12.5	42.7	8.2
B	90	190	5.3	25.5	3.9
C	95	105	4.8	42.8	12.9
D	70	190	10.5	27.0	1.1
E	98	110	9.1	30.9	3.6

7.4.3 General observations

During the test programme is was observed that, as the elastomer approaches the critical strain value, the rapid increase in strain at the crown of the membrane required very little increase in pressure. Figure 7.6 shows the relationship between applied pressure and strain at the crown of the inflated membrane for material A. For all materials there is a rapid increase in strain for either a small increase in pressure or no pressure increase at all.

7.5 DISCUSSION

The material data gathered during the measurement process are for equi-biaxial tension conditions only and should be used as input data only for finite element models incorporating this deformation mode. If other deformation modes are present, the appropriate materials data should be included in the input data to calculate the revised hyperelastic coefficients.

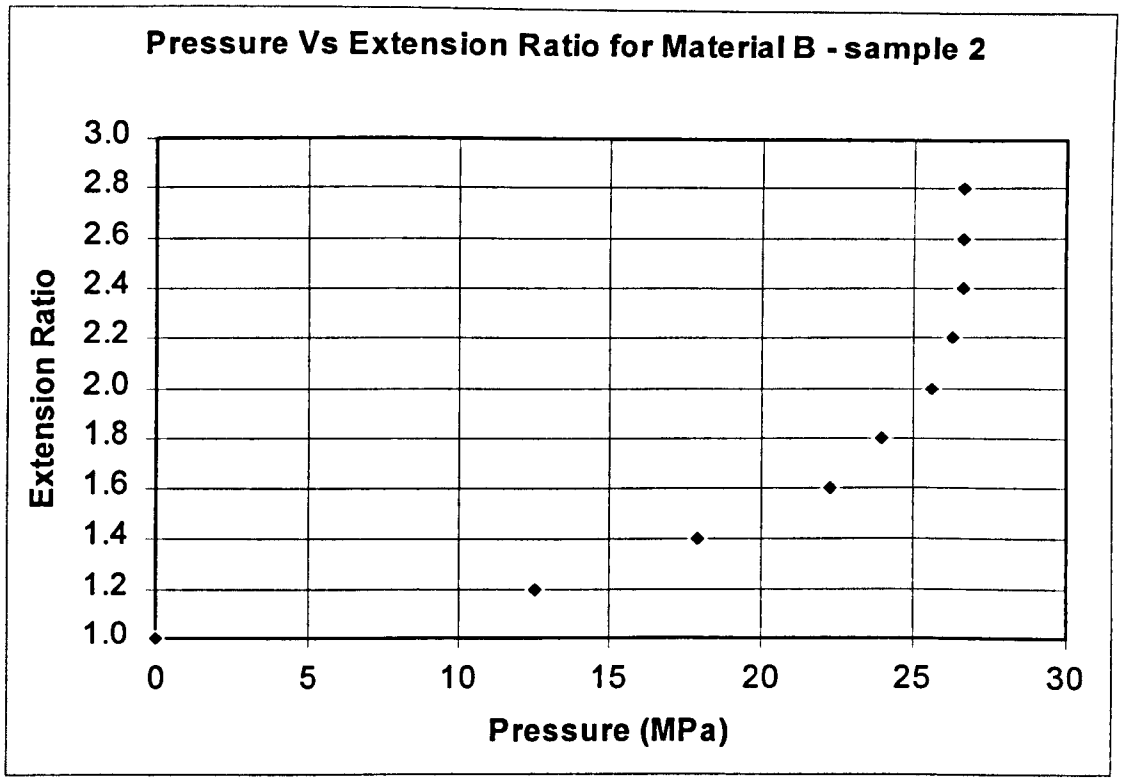

Figure 7.6 - Pressure vs extension ratio for material B - sample 2

This is not always practicable, therefore the minimum input data required to develop the model should be used. Many elastomeric components are subject to various loading conditions and will therefore require the appropriate input data. The superposition of a tensile or compressive hydrostatic stress on a loaded, fully incompressible material such as rubber results in different stresses, but does not change the deformation. Thus, apparently different loading conditions are, in fact, equivalent in their deformations. (ABAQUS Users Manual, 1996)

- Uniaxial tension ⇔ equibiaxial compression
- Uniaxial compression ⇔ equibiaxial tension
- Planar tension ⇔ planar compression

The equibiaxial tension test is equivalent to the uniaxial compression test, therefore as the majority of an O-ring under hydrostatic pressure is in compression, the test data are valid. The wall of an inflating void is also under biaxial tension, therefore the test data are again valid.

There are some possible sources of error during the test. The strain measurement depends on the accuracy of the initial grid marking and the alignment of the cameras. The correlation between pressure and strain is determined using a time based technique, working back from the point of failure. There may be a disparity between the time recording method on the data acquisition system and that on the video editing equipment.

The observation of a rapid strain increase with very little or no increase in pressure concurs with the Gent model for void inflation. This states that the radius of an inflating void will tend to infinity at a given pressure. This radius increase will obviously be halted when the stress in the wall reaches a critical value and failure occurs.

There is a significant difference between the levels of stress measured during this experiment and that measured in uniaxial extension. This difference can be explained as follows.

If a cylindrical rod of diameter D is considered under uniaxial extension, the diameter will reduce to d in accordance with the increase in length L due to the Poisson's ratio of the material tending towards 0.5.

$$d = \frac{D}{\sqrt{\lambda}} \qquad (7.5.1)$$

Where λ is the extension ratio, given by $\lambda=1+(\Delta L/L)$, and ΔL is the change in length. This allows the extension of the rod to occur relatively freely.

If the crown element at the top of an inflated membrane is considered, the applied extensions in the two mutually perpendicular directions are equal. Therefore, the material cannot contract as with the uniaxial extension. Owing to the conservation of volume approximation of elastomers, the only manner in which the element can extend is by reducing the thickness.

$$\lambda_1\lambda_2\lambda_3 = 1 \qquad (7.5.2)$$

In equibiaxial extension, the extension ratios λ_1 and λ_2 are equal and can therefore be denoted as λ_b. This yields the relation

$$\lambda_3 = \frac{1}{\lambda_b^2} \qquad (7.5.3)$$

Therefore, the thickness of the membrane will reduce by a factor of λ_b^2.

The theory of deformation of the two arrangements matches the actual extensions observed experimentally. The stress levels under equibiaxial extension are much higher.

This behaviour difference can also be explained mathematically. The stress-strain relation in uniaxial extension can be expressed as the partial derivative of the Mooney-Rivlin strain energy function. The uniaxial strain conditions are

$$\lambda_1 = \lambda \quad ; \quad \lambda_2 = \lambda_3 = \frac{1}{\sqrt{\lambda}} \qquad (7.5.4)$$

Substituting these conditions into the strain energy function and differentiating with respect to λ gives the relation for uniaxial stress. From virtual work principles

$$\delta U = \sigma_u \delta\lambda \qquad (7.5.5)$$

Rearranging and carrying out the partial differentiation

$$\frac{\partial U}{\partial \lambda} = \sigma_u = 2(1 - \lambda^{-3})(\lambda C_{10} + C_{01}) \qquad (7.5.6)$$

where λ is the uniaxial extension ratio and C_{10} and C_{01} are material constants. The corresponding function for equibiaxial extension can be expressed as

$$\delta U = 2\sigma_b \delta\lambda \qquad (7.5.7)$$

$$\frac{1}{2}.\frac{\partial U}{\partial \lambda} = \sigma_b = 2(\lambda - \lambda^{-5})(C_{10} + \lambda^2 C_{01}) \qquad (7.5.8)$$

The substitutions defining the strain conditions are different in this case, being $\lambda_1=\lambda_2=\lambda$ and $\lambda_3=1/\lambda^2$.

Comparing the equations for uniaxial and biaxial stress (7.5.6 and 7.5.8) and depending on the value of λ used, the difference between the uniaxial and equibiaxial stress levels will vary as a power function (i.e. $x.\lambda^n$). However, if the material constants are estimated from known stress-strain plots by the following relations, the stress levels at given strains can be evaluated and compared with the experimental values.

$$E = 6C_{10} \qquad (7.5.9)$$

and

$$C_{01} = 0.25C_{10} \qquad (7.5.10)$$

Taking an approximate value of elastic modulus (E) to be 20-25 MPa for the materials of interest, the corresponding stress plots match very well with the experimental values. The differences between the uniaxial and equibiaxial stress-strain plots match the theory very well, indicating that the results and the assumptions regarding the equibiaxial tensile testing are reasonable.

7.6 CONCLUSIONS

The results measured from the five materials are consistent with the expected form of the stress-strain curve for elastomeric materials. The low extensibility of materials C and E is marked in comparison with that of materials A, B and D. However, the low critical stress to failure of materials B and D could be of some concern in relation to explosive decompression.

Material C does show a high critical stress to failure. This, in conjunction with its low extensibility, suggests that this material is much stiffer the other than materials. This stiffness correlates reasonably well with the indicated hardness values given in Table 7.1. The high initial stiffness of material E becomes lower as the strain is increased.

Interestingly, although the extensibilities of materials A and C are considerably different, the critical stress to failure is the same. The extensibilities of materials B and D are higher than the other materials. The stress-strain curves for materials B and D are very similar, although their relative hardness are considerably different. In relation to explosive decompression damage, it is not clear which parameter, if any, is more dominant in resisting damage. It is probably a combination of both extensibility and ultimate strength.

Repeatability in the test results was very good, indicating that the testing technique was acceptable.

The failure process observed at the burst point indicated that the inflated membrane develops several radial tears starting just outside the region of the crown and terminating on a well-defined circle at the clamp. This failure mode could be due to a type of cleavage resulting from an orientation of the molecules along the line of latitude of the inflated sheet (Flint & Naunton, 1937).

The fitted curves calculated using the least-squares regression technique are reasonably concurrent with the curves measured during the test programme. Material A does have some errors at moderate strain levels ($\sim\lambda = 1.8 - 2$).

The observation that the strain at the crown increases rapidly with very little or no increase in inflation pressure is important as it matches the Gent theory of explosive decompression failure.

The data generated during this test programme are used as input data to the finite element models of void inflation, as this is a multi-axial deformation mode. The critical stress measured during these tests can be used as a failure criterion in the modelling process.

All values given in the graphs and tables are based on the nominal stress, meaning that the calculations are based on the original cross sectional area. The input requirements of the ABAQUS software state that nominal stress must be used for input data, the output is then Cauchy or true stress.

7.7 CHAPTER SUMMARY

A test rig has been designed and built to measure the equibiaxial tensile properties of elastomer membranes to simulate the deformation mode of an inflating microvoid. The test rig is designed to be simple to use using standard material test sheets as supplied by the manufacturer.

The test produces data on stress-strain characteristics and ultimate stress and strain at failure for the materials studied. This data are then used in the finite element model to produce the appropriate strain energy function to describe the behaviour of the material.

CHAPTER 8 - TRANSIENT GAS DIFFUSION MODEL

8.1 INTRODUCTION

To predict the pressure available for void expansions under explosive decompression conditions, it is necessary to determine the gas transport activity within the seal section. This chapter studies two cases, the first being instantaneous decompression at a microscopic level, to determine whether the void pressure remains constant as the void expands. The second case studies the effects of linear decompressions on the macroscopic concentration profiles formed across the seal section. This gives the pressure differential available for void expansions at various locations across the seal.

It is important to determine the pressure differentials on a location basis as the void content and local stress field vary considerably across the section and will therefore determine the crack patterns upon decompression.

The available pressure differential versus decompression period relationship can then be used as an input variable to the void expansion model that evaluates the critical wall stress and therefore fracture initiation from an expanding void.

8.2 THE EFFECT OF INSTANTANEOUS DECOMPRESSION ON MICROSCOPIC GAS DIFFUSION

Before decompression occurs, the pressure of the saturated gas within the seal is equal to the applied system pressure, therefore the system is in equilibrium. Under instantaneous decompression, the pressure differential created must be equal to the system pressure, as there is no time for any gas to diffuse out of the seal section, so reducing the concentration and pressure within the seal. Therefore, voids will expand under this pressure differential.

Upon expansion, the pressure within the void decreases in accordance with the increase in volume, unless the diffusion of gas into the void is extremely rapid. This will create steep concentration gradients between the void and the surrounding matrix and initiate gas diffusion into the expanded void.

This model determines the time required for the pressure within the void to recover the near system pressure. If the time to reach a constant pressure is small, the applied void pressure can be assumed to be constant and not variable (due to the increased volume) for the purposes of the void expansion model.

The rate of pressure increase within an expanded void due to an instantaneous decompression is evaluated by means of the finite element method using a thermal diffusivity analogy. Thermal diffusivity and transient heat transfer analysis can be considered directly analogous to transient gas diffusion. The relationships can be summarised as follows: -

diffusion coefficient	⇔	thermal diffusivity
concentration	⇔	temperature

Using these relationships, the finite element method can be used to evaluate the transient diffusion of gas through an elastomeric matrix to an inflated void.

To understand the gas transport process in elastomer seals, it is necessary to understand the concept of chemical potential. The chemical potential μ_A of a substance *A* (e.g. methane) is a measure of the potential energy of chemical species A in a given volume element. It is defined as $(\partial G/\partial n_A)_{T,\,P,\,nB}$, the rate of change in the Gibbs free energy of the volume element, with respect to the quantity of the substance (number of moles of *A*) that the element contains, when the change takes place at constant temperature and pressure, without loss of other chemical species n_B, n_C,etc.

$$\mu_A = \left(\frac{\partial G}{\partial n_A} \right)_{T,\, p,\, n_B}$$

where μ_A is the chemical potential of the chemical species *A*, G is the Gibbs free energy of the chosen volume element, and n_A is the number of moles of species *A* contained in the element. Chemical potential effectively determines the distribution of species *A* throughout the system, and a difference in chemical potential for species A between two points in the system is the driving force for net flow of *A* molecules from one point to another.

For any change taking place in the system under equilibrium conditions (e.g., boiling of water at 100°C under 760mm atmospheric pressure) the change in Gibbs free energy is zero. Molecules can still move between two points at equilibrium, but there will be no net increase or decrease at either point. When a chemical potential gradient is created, the tendency is for the substance to migrate from regions of high chemical potential to regions of lower μ until equilibrium is reached.

When an elastomer seal is subjected to high gas pressures, the chemical potential of each gas species is much greater outside the seal than in the elastomer matrix. This causes a net inward potential flow of gas into the seal section via the diffusion process. Eventually, the chemical potentials on each side of the phase boundary will become equal.

Upon depressurisation, the chemical potential of the pressurising gas is rapidly reduced. This creates a new difference in chemical potential, and initiates net outward flow of gases from the seal. The gas flow will continue until the supply of gas within the seal is exhausted, assuming that the ambient volume is much larger than the seal volume.

This process effectively drives the transport of gas through the seal during decompression and therefore the pressure differential available for void expansion. It should be noted that

the chemical potential of a species is determined not simply by its concentration, but also by its activity, which is affected by whether the components of the mixture are compatible.

For an instantaneous decompression the sequence of events for modelling purposes is as follows: -

1. Void and surrounding matrix in equilibrium at concentration C_o
2. Instantaneous decompression occurs.
3. External pressure drops from p_0 to p_1(external). The gas expands until p_1(gas) is in equilibrium, taking into account the surface tension and rubber stretching).
4. The void expands to an increased diameter.
5. The increased volume and therefore the corresponding drop in void pressure causes the concentration of gas to drop accordingly (a cubic function of the expanded radius)
6. The drop in concentration causes a discontinuity in chemical potential of gas species to be set up between the void and the surrounding elastomer matrix.
7. The gas then diffuses towards the void until the system reaches an equilibrium chemical potential throughout the surrounding matrix.
8. This causes the concentration within the void to increase again, therefore increasing the pressure within the void according to Henry's law.

8.2.1 Model assumptions

- Voids are equi-spaced within the material in a square lattice, approximately 0.4mm apart (taken from void and rigid inclusion analysis, Chapter 3)
- Initial void diameter is 40μm.
- The void will undergo instantaneous expansion to a value not exceeding λ=3 in the worst case condition
- Volume increase will cause a corresponding pressure and concentration reduction by a factor of 27 for λ=3

- Temperature remains constant during expansion and diffusion process
- The matrix is fully saturated with gas at the time of decompression
- The gas stored in the surrounding matrix at initial equilibrium conditions is the only gas available for diffusion into the void
- The concentration gradient caused by void expansion is a logarithmic function of the form $c_r=A+B\ln(r)$ where A and B are constants and r is the radial distance from the void. (See displacement-concentration analogy model)
- The chemical potential at the void wall is assumed to be the equal to the chemical potential within the void. A surface heat transfer coefficient is not included in the model as the relative volume between the void and the surrounding material is very small
- The concentration at a point in the surrounding matrix is a direct analogy to the displacement at that point due to the void expansion
- The elastomer matrix is assumed to be homogenous with no rigid inclusions or filler particles to disrupt gas diffusion

8.2.2 Modelling Procedure

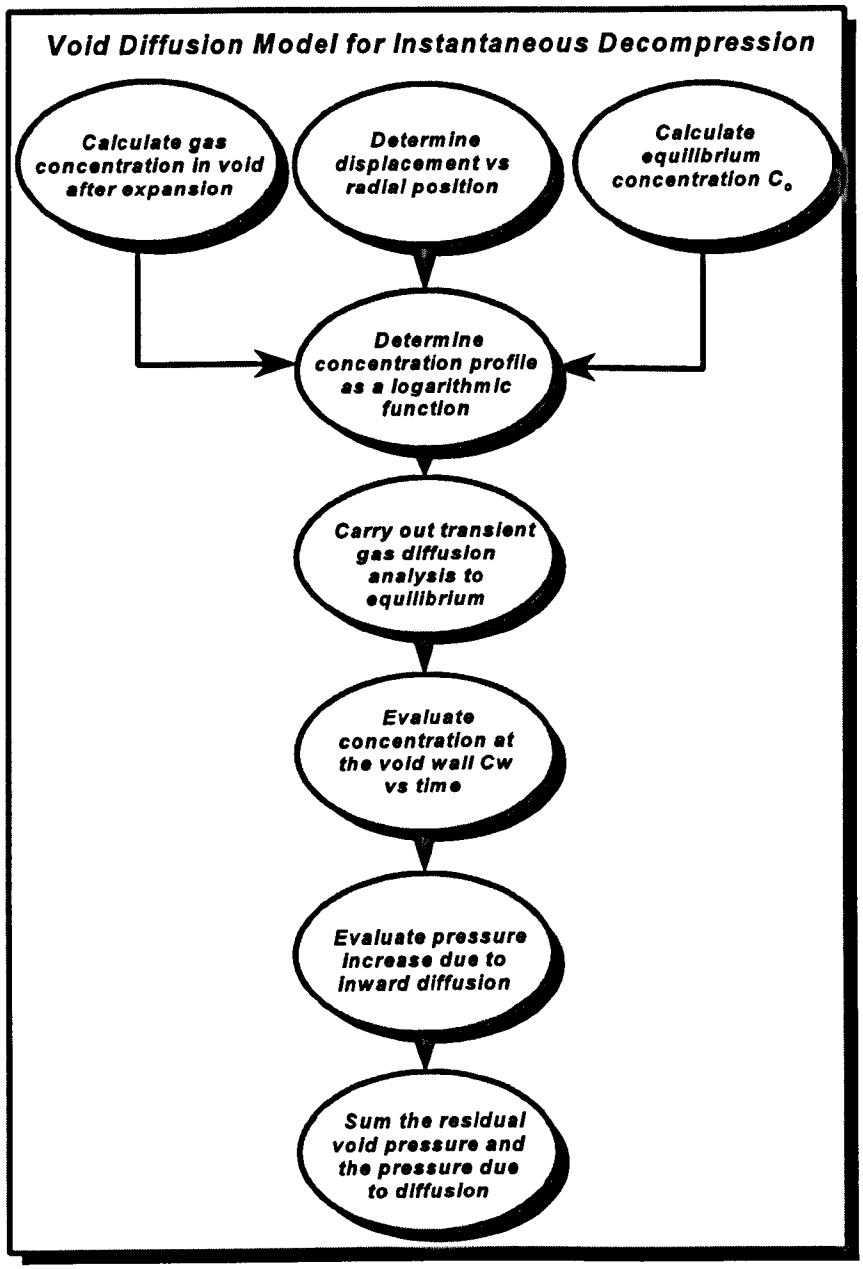

Figure 8.1 - Instantaneous Transient Diffusion Model Methodology

8.2.3 Calculation of void concentration after expansion

The void will expand almost instantaneously under instantaneous decompression conditions and its volume will increase. For most of the materials being studied the failure extension ratio under equibiaxial extension is around λ=3, indicating a 200% strain. Following this expansion, if the pressure is not maintained, the void will then begin to collapse if fracture has not occurred. Using standard perfect gas relationships: -

$$\frac{p_1 V_1}{T_1} = \frac{p_2 V_2}{T_2} \qquad (8.2.1)$$

where p is the pressure, V is the volume and T is the temperature and the subscripts 1 and 2 denote initial and final conditions. If we assume that temperature is constant (T_1=T_2) and that the volume of a sphere is given by $4/3\pi r^3$, the relationship becomes: -

$$\frac{4}{3}\pi r_1^3 p_1 = \frac{4}{3}\pi r_2^3 p_2 \qquad (8.2.2)$$

Rearranging:

$$\frac{p_1}{p_2} = \frac{r_2^3}{r_1^3} \leftrightarrow \frac{p_1}{p_2} = \left(\frac{r_2}{r_1}\right)^3 \qquad (8.2.3)$$

Let:

$$\lambda = \frac{r_2}{r_1} \qquad (8.2.4)$$

Assuming that the extension ratio λ reaches a maximum of 3

$$r_2 = 3r_1 \qquad (8.2.5)$$

Substituting back into equation (8.2.3) yields

$$p_2 = \frac{p_1}{27} \qquad (8.2.6)$$

As concentration levels are directly pressure dependant, the concentration within the void will also fall by a factor of 27 if the radius of the void is trebled under expansion.

8.2.4 Calculation of equilibrium concentration c_0

The evaluation of the equilibrium concentration c_0 is made by using Henry's law, which relates pressure, concentration and solubility. If the system pressure and the solubility at that pressure are known, the saturated concentration can be evaluated by the following relationship.

$$c = sp \qquad (8.2.7)$$

Where c is the concentration and s is the solubility at pressure p. The solubility values under temperature and pressure are known from the gas transport testing (see Chapter 5).

8.2.5 Analysis of displacement vs radial position

To predict how the concentration gradient changes away from the void after void expansion, a displacement analogy is used. As the concentration within the void falls in proportion to the radial displacement of the void, the chemical potential in the surrounding material must also vary according to the displacement.

The displacement analysis is carried out using the finite element method. A fixed displacement of λ=3 was applied to the void and the resulting displacement through the surrounding material evaluated. Boundary conditions were applied as shown in Figure 8.2 to allow the displacement to take place in the desired directions and to prevent rigid body motion.

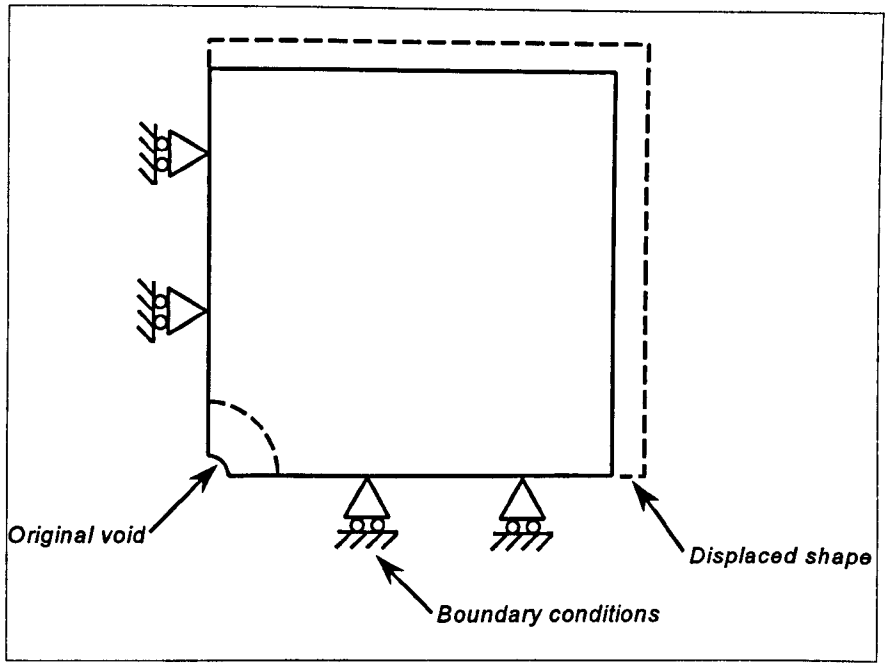

Figure 8.2 - Concentration-displacement analogy

The resulting displacement vs radial position away from the void curve is shown in Figure 8.3. The concentration gradient can then be determined from this curve as it is the inverse, i.e. when the displacement is high the gas concentration is low.

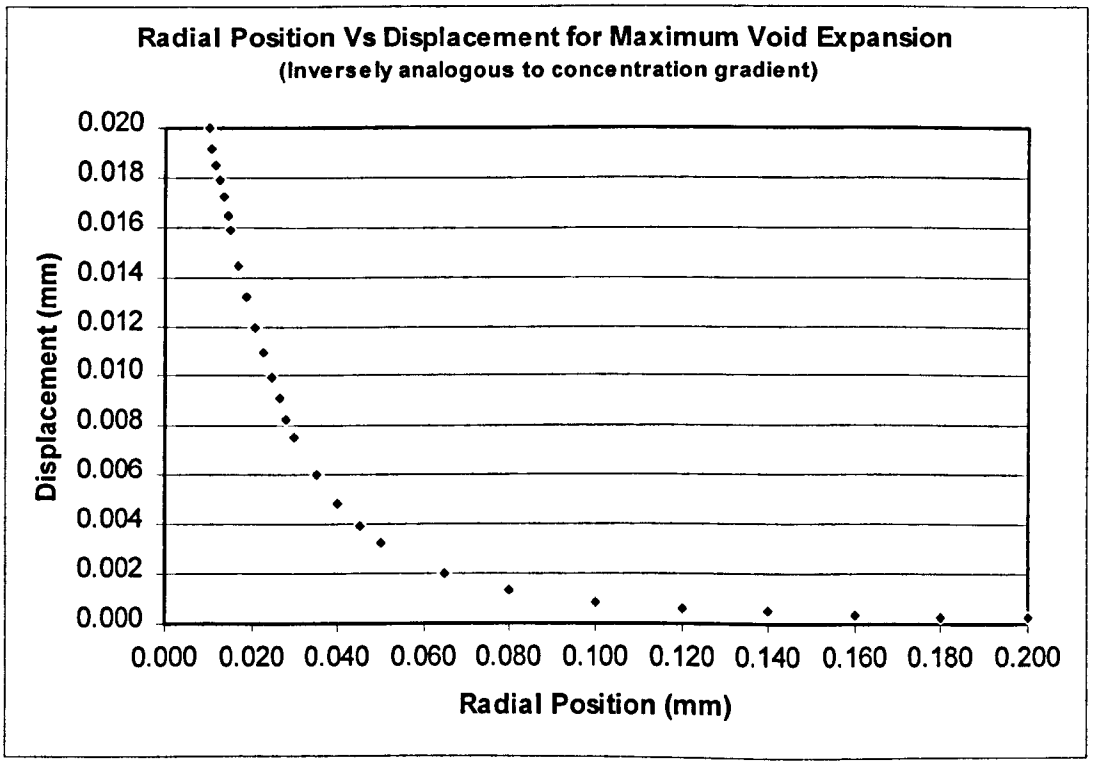

Figure 8.3 - Radial position vs displacement for material B

8.2.6 Determination of the concentration profile

The concentration profile is determined from the displacement analogy. The function which best fits the inverse of the displacement-radial position curve is a logarithmic function of the form:

$$c_r = 1.2c_0 + 0.15.c_0.\ln(r) \qquad (8.2.8)$$

where c_r is the concentration at radius r and c_0 is the equilibrium concentration at time t=0. The concentration profile for Material B at 100 bar, 150°C and CH_4 (methane) is shown in Figure 8.4. The concentration-radial distance relationship is then used as an input to the finite element model for transient gas diffusion analysis.

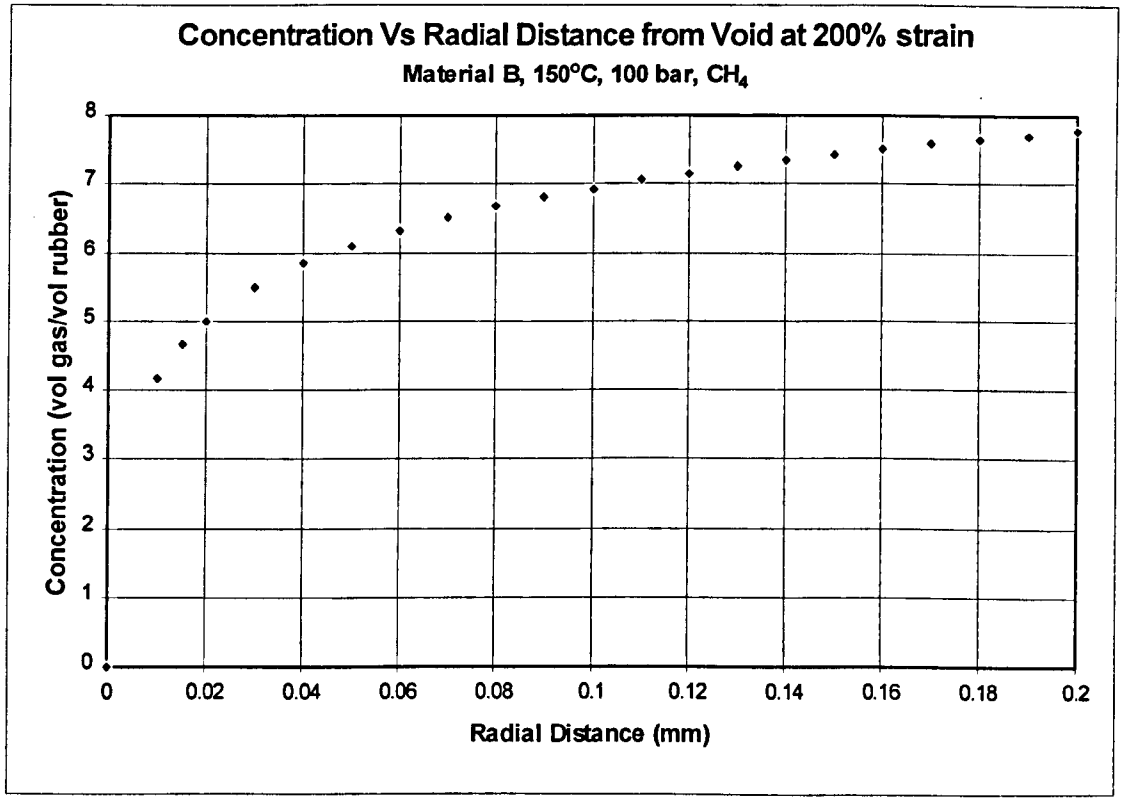

Figure 8.4 - Concentration profile for material B

8.2.7 Transient gas diffusion analysis

The transient gas diffusion analysis is carried out using the finite element method, using a thermal diffusivity analogy. The model uses the equivalence of thermal diffusivity and the gas diffusion coefficient to determine the transient response of the system until it reaches steady state conditions.

The thermal diffusivity (α) is equivalent to the diffusion coefficient (D) and is given by:

$$\alpha = \frac{k}{\rho C_p} \qquad (8.2.9)$$

where k is the conductivity, ρ is the density and C_p is the specific heat at constant pressure. The finite element model requires values for all three of the variables to define thermal diffusivity. If C_p and ρ are set to 1 in the model and only the conductivity is defined, the diffusion coefficient D can be assumed to be equivalent to the conductivity k. The mesh density used in the model is higher nearer the void as this is where the greatest accuracy is required and more gas transport activity takes place at this location. The concentration gradient is applied to the model as initial conditions of temperature over different surfaces across the elastomer matrix as shown in Figure 8.5.

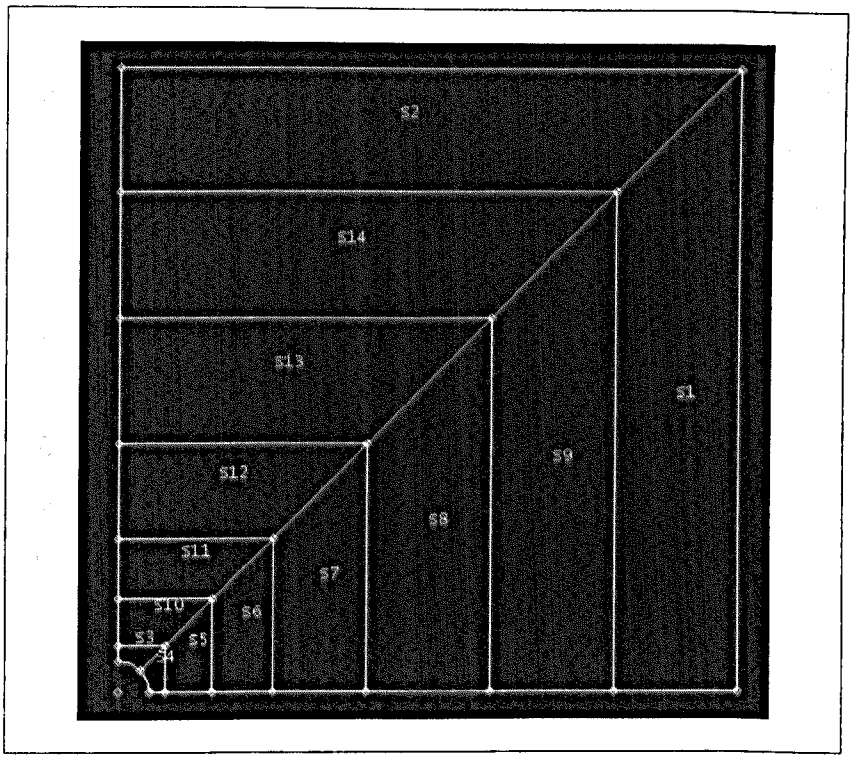

Figure 8.5 - Concentration surfaces for void diffusion model

The fourteen surfaces used in the model (s1 to s14) are each applied an initial concentration value, depending on their radial distance from the void. The thermal diffusivity analogy used means that the concentration is applied as an initial temperature. The model was run as a transient heat transfer analysis until steady state conditions were reached. The results of nodal temperature variation were then written to a results file.

8.2.8 Evaluation of void wall concentration vs time

From the results of the finite element transient gas diffusion analysis, the concentration of gas at the void wall can be determined as a function of time. The results of the analysis clearly show (Figure 8.6) the gas diffusing towards the void as time progresses, increasing the concentration within the void. It is assumed that the chemical potential between the void and the void boundary are equal as the volume of the void is relatively small and would only have a negligible effect on the surface mass.

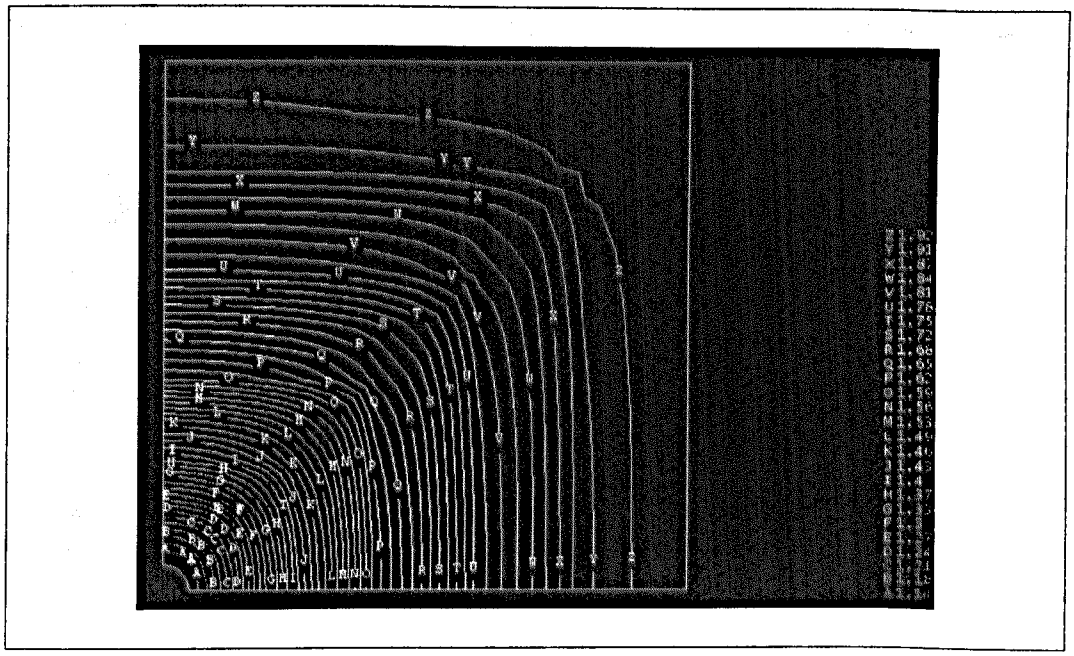

Figure 8.6 - Concentration profile for Material B at t=1s
150°C, 100 bar, CH_4

Figure 8.7 shows the concentration vs time plot for Material B at 100°C, 100 bar and CH_4. The y-axis label 'NT' denotes nodal temperature which is directly analogous to gas concentration. The x-axis value is time in seconds. The graph shows a rapid increase in concentration in a relatively short period of time.

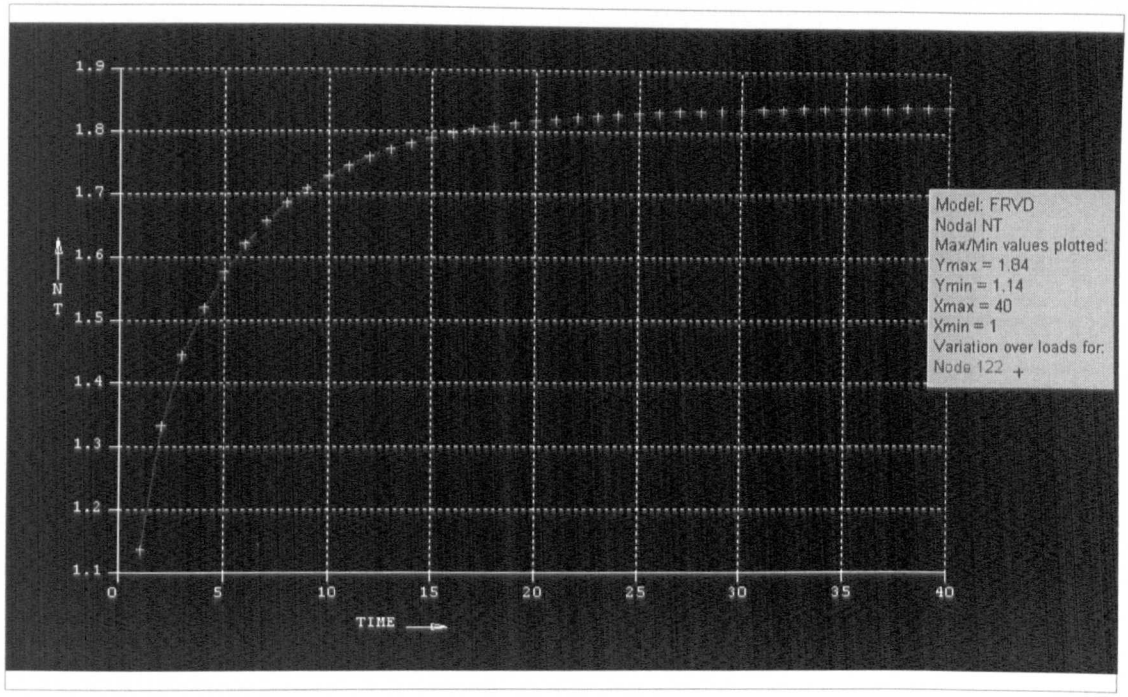

Figure 8.7 - Concentration vs time profile

8.2.9 Evaluation of pressure increase due to inward diffusion

The resulting concentration vs time relationship from the transient gas diffusion analysis can then be used to determine the pressure increase within the void. Again using Henry's law we can evaluate the pressure at each time step by using the following relation

$$p = \frac{c}{s} \qquad (8.2.10)$$

This results in a pressure increase vs time plot for the void as shown in Figure 8.8.

To obtain an estimate of the time taken to return to approximate system pressure, a critical time can be evaluated based on time to reach 90% of the steady state value. The time for this example was $t_c = 6.8$s. This parameter can be used as a comparative measure against other materials and operational parameters.

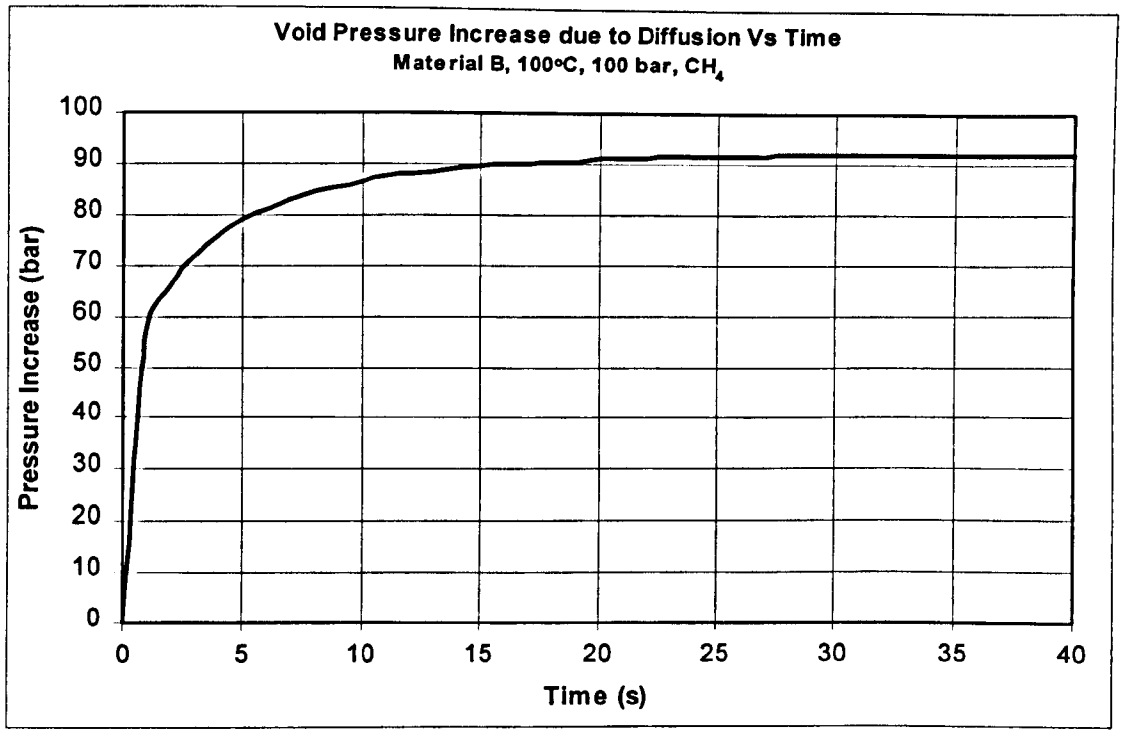

Figure 8.8 - Void pressure increase due to diffusion vs time

8.2.10 Calculation of total pressure within the void

The pressure increase due to inward diffusion must be summed with the residual pressure remaining in the void after expansion, which was calculated to be $p_o/27$. Therefore, the total pressure can be expressed as

$$p(t) = p_d(t) + p_r \qquad (8.2.11)$$

where p(t) is the pressure as a function of time, $p_d(t)$ is the pressure increase due to diffusion as a function of time and p_r is the residual void pressure after expansion. The final pressure increase with time plot is shown in Figure 8.9.

The critical time for pressure increase (t_c) as previously calculated does not change significantly with the inclusion of the residual pressure.

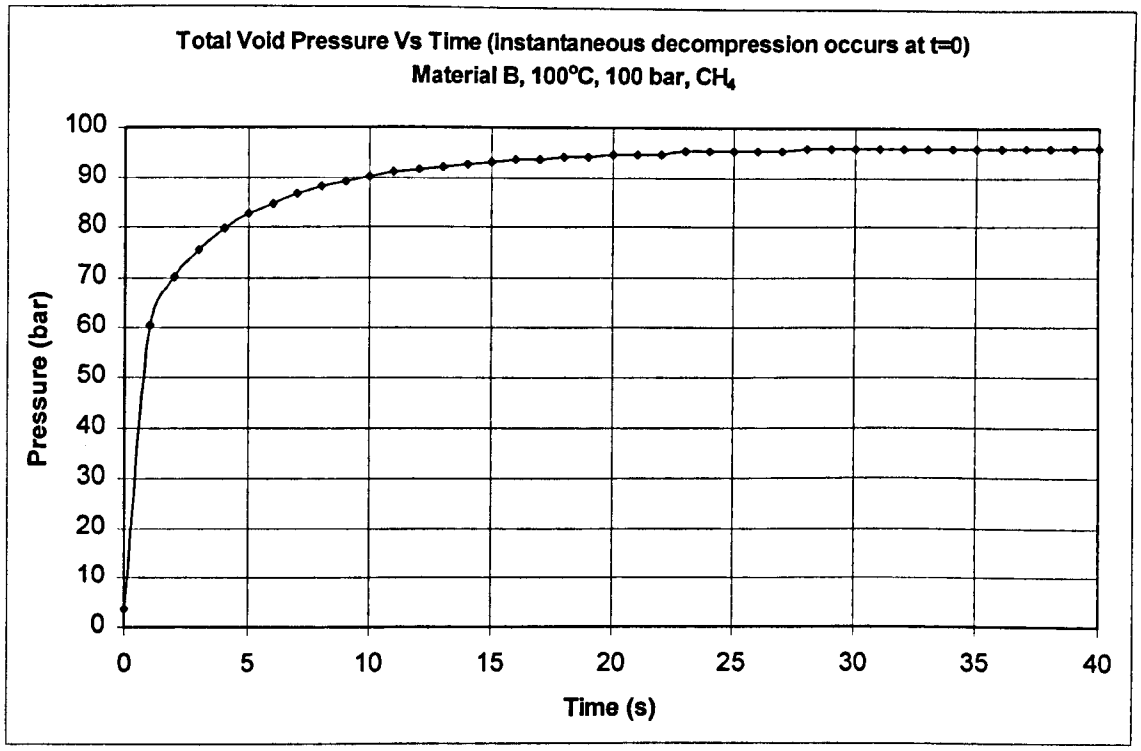

Figure 8.9 - Total void pressure increase vs time

An analysis of the same material, gas and pressure was carried out, but at a temperature of 150°C to determine the effects of temperature increase on the rate of pressure increase within the void.

As figure 8.10 shows, the increase in temperature results in a marked increase in the rate of pressure increase within the void. After t = 1s the pressure at 100°C is approximately 61 bar, at 150°C the pressure is around 78 bar.

8.2.11 Analysis results

The results of the analysis of transient gas diffusion due to instantaneous decompression are summarised in Table 8.1. The effect of temperature increase is shown in Figure 8.10.

Table 8.1 - Results of instantaneous decompression analysis

Material	Temperature (°C)	Pressure (bar)	Gas	Critical time for 90% of steady state (t_c) (s)
A	100	100	CH_4	7.0
A	150	100	CH_4	1.7
B	100	100	CH_4	6.7
B	150	100	CH_4	2.4

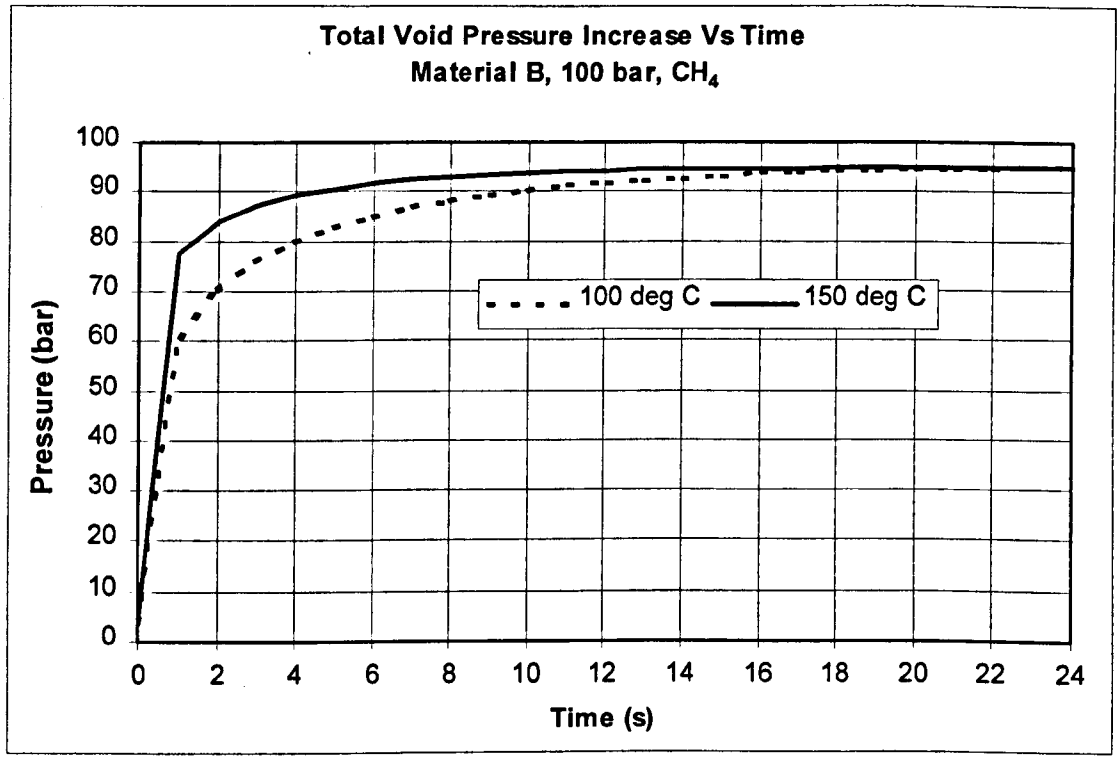

Figure 8.10 - The effect of temperature on the rate of void pressure increase

8.2.12 Discussion

The assumption of an inversely proportional concentration drop with radial distance is an approximation, owing to the incompressibility assumption of elastomers. If the material

deforms, the volume effectively must stay the same (except for a small volume change of ~1%) and as concentration is a volume related quantity, the concentration will not drop in the material. The only concentration drop will be in the void itself where the volume is decreased by a factor of 27. If this is the case, the concentration in the surrounding material will be higher and the rate of pressure increase within the void will be even closer to instantaneous.

The model assumes that the diffusion of gas into the void occurs after the expansion. However, in practice, the a concentration gradient will be created as the void expands and the pressure starts to drop. This will allow the gas to diffuse into the void during expansion. Depending on the rate of diffusion, the pressure might remain constant.

The magnitude of the expansion applied to the void was fixed in the model. However, this will depend on the initial size of the void and the elasticity of the material. The initial void size will also affect the area of void wall available for gas diffusion. If the initial void size is small, the available area for gas diffusion will be much lower, reducing by the square of the void radius.

8.2.13 Conclusions

As the critical time to 90% of equilibrium is so rapid in most cases, the applied pressure for the void inflation model can be assumed to be constant for the instantaneous decompression case.

Due to the increased diffusion rate at elevated temperature, there was no requirement to carry out the full set of analyses at the higher temperatures and pressures. This was because the pressure within the void will achieve a constant value almost instantaneously at the lower temperature and pressure. As the diffusion coefficient increases with an increase in temperature, the resulting pressure increase within the void would have occurred more rapidly.

8.3 O-RING TRANSIENT GAS DIFFUSION MODEL FOR LINEAR DECOMPRESSIONS

To model the actual decompression process as it usually occurs, it is necessary to consider the effect of slower decompression. For the purposes of this model it is assumed that the decompression occurs linearly over a time period. From industry sources, it is assumed that the average decompression time is 2-4 hours. Therefore, as a worst case, we will study linear decompression over 2 hours. In addition to this, we will also study longer decompressions over 24 and 48 hours to establish the safe decompression time for a given system.

The data generated from this model will give the pressure differential for the void expansion model. For a linear decompression of the form shown in Figure 8.11, the sequence of events is as follows: -

1. Void and surrounding elastomeric matrix have equal chemical potential and are in equilibrium at concentration c_o.
2. Decompression occurs linearly over the decompression time.
3. During decompression a concentration gradient is developed across the seal section, the concentration being zero at the pressure interface (the external surface of the seal) and concentration c(t) at all other points within the seal section.
4. As time continues the concentration profile will change as the gas diffuses out of the seal.
5. At differing points within the section, different concentrations of gas will exist depending on the decompression rate.
6. The maximum concentration differential will occur when the time elapsed equals the decompression time.
7. The corresponding maximum pressure differential will also exist at this point in time.
8. Therefore at each point in the seal section we can evaluate the pressure differential.

9. Owing to the longer time periods available for expansion and inward diffusion, the chemical potential within the void can be assumed to be equal to the chemical potential in the surrounding elastomeric matrix at that point in the seal.

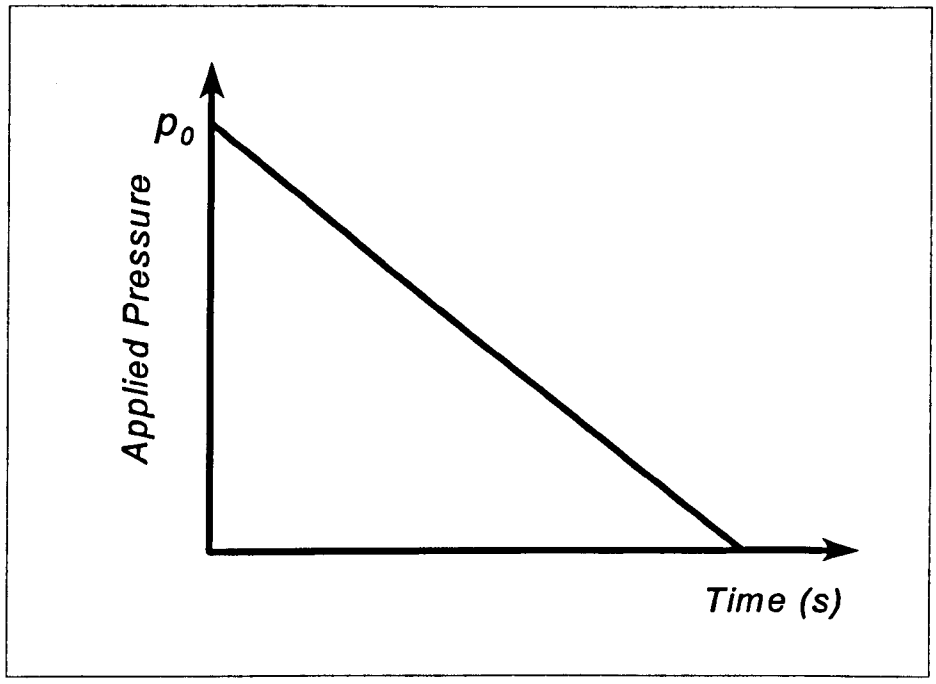

Figure 8.11 - Linear decompression profile

8.3.1 Model assumptions

- Ambient temperature remains constant during the decompression process. If a very rapid decompression occurs, the gas will expand adiabatically and induce a temperature drop. This will cause some temperature reduction at the external surface of the seal, but owing to the thermal conductivity and stored heat in the seal, the effect of this will be small.
- The matrix is fully saturated with gas at the time of decompression
- The elastomer matrix is assumed to be homogenous with no rigid inclusions or filler particles to disrupt the gas diffusion
- The concentration at the pressure boundary and the pressure decay linearly to zero at the pressure interface over the decompression time

- The concentration boundary at the pressure interface is the surface available after 15% compression of the O-ring
- The chemical potential formed in the elastomeric matrix is equal to the chemical potential within any void at that location. The time required for the decompression and therefore change in gas concentration is long enough to allow equilibrium conditions to exist between void and surrounding material. The previous instantaneous analysis shows that equilibrium is achieved very rapidly in comparison with the decompression time.
- The only surface available for gas transport is the pressure interface.

8.3.2 Modelling procedure

The model is based on the differential equation for axisymmetric transient diffusion of gas [Ho, 1993]: -

$$\frac{\partial c}{\partial t} = \frac{\partial}{\partial z}\left[D_z \left(\frac{\partial c}{\partial z} \right) \right] + \frac{1}{r}\left(\frac{\partial}{\partial r}\left[D_r r \left(\frac{\partial c}{\partial r} \right) \right] \right) + S_i \qquad (8.3.1)$$

where: D_z and D_r are the diffusion coefficients in the specified direction

c is the concentration of gas

dt is the time interval

r is the radius

z is the longitudinal length in the axisymmetric model

x, y, z are the rectangular Cartesian coordinates

S_i is the sink term

Steady state conditions are reached when

$$\frac{\partial c}{\partial t} = 0 \qquad (8.3.2)$$

This equation has been incorporated into a software program [Ho, 1993] to predict the life of elastomer seals. The software can be used to evaluate the change of concentration at various points within a seal section to establish a concentration gradient change with time.

If we consider five points within a seal section as shown in Figure 8.12 we can evaluate how the concentration profile changes with time at different points. From this we can compare the concentration profile with that of the profile at the pressure boundary to establish the concentration differential at the five points.

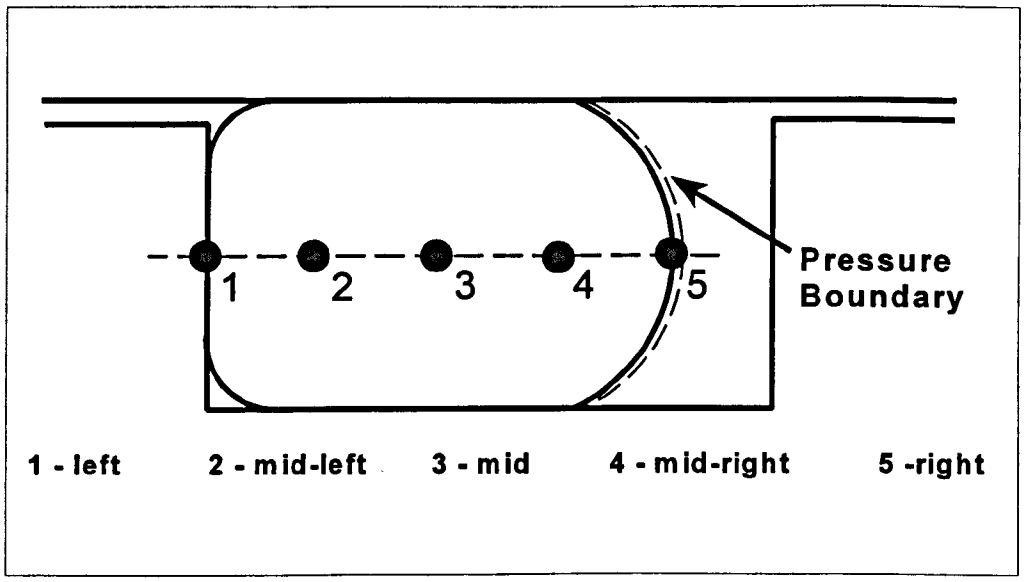

Figure 8.12 - Concentration calculation points

The concentration at point 5 will decay linearly from the initial equilibrium concentration of c_0 to zero over the decompression time. The concentration at the other four points will all decay at a slower rate than point 5. The concentration differential formed during decompression between point 5 and the other four points will increase up to the decompression time and then fall off as the concentration at point five remains constant at zero and the gas continues to diffuse out.

As the concentration of gas is directly related to the pressure by Henry's law, the maximum pressure differential formed is at the end of the decompression period. Owing to diffusion out of the O-ring, the pressure differential formed at the points nearer to the

pressure surface will be less than that formed at point 1. Therefore the conclusion could be drawn that the further away from the pressure surface a void is, the more likely it is to fail.

However, it could be the case that the void will actually fail at a pressure much lower than the total pressure differential at point 1 and will fail at almost any point in the seal.

8.3.3 Analysis Results

The results shown are for an example case of a 5.33mm section seal subjected to 100 bar gas (methane) pressure and 100°C, decompressed linearly over 2 hours. The concentration vs time plot for the five points considered is shown in Figure 8.13. The initial concentration shown (i.e. 4 vol. gas/vol rubber) is calculated from Henry's law (c = sp) using a pressure of 100 bar and a solubility coefficient of 0.04 atm^{-1}, measured from the gas transport testing. The model was run using data at 100°C.

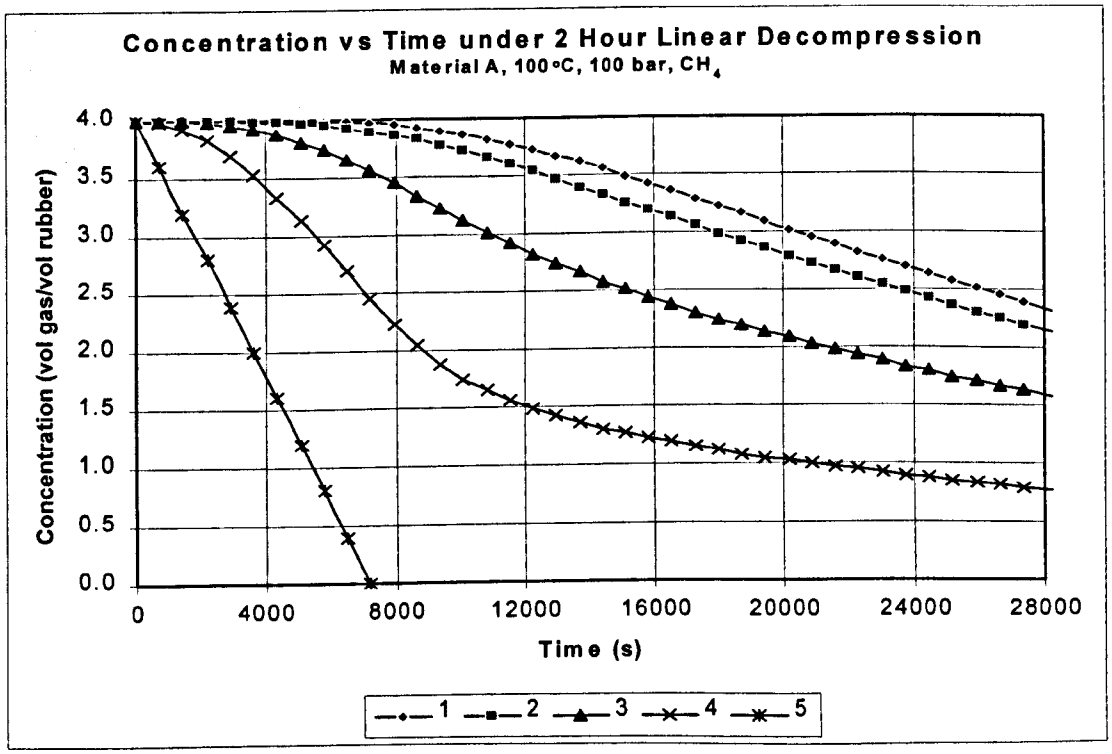

Figure 8.13 - Concentration vs time plot for points 1-5

As can be seen from the results graph the concentration at point 5 drops linearly over the 2 hour decompression period as expected. The other four points show a time lag and the concentration then drops in accordance with diffusion of gas out of the seal.

The concentration differential is calculated by: -

$$\delta c = c_n - c_5 \qquad (8.3.3)$$

Where c_n is the concentration at the analysis point required, i.e. 1 to 4. The evaluation of the concentration differential formed between points 1 to 4 and point 5 over the time period is shown in Figure 8.14.

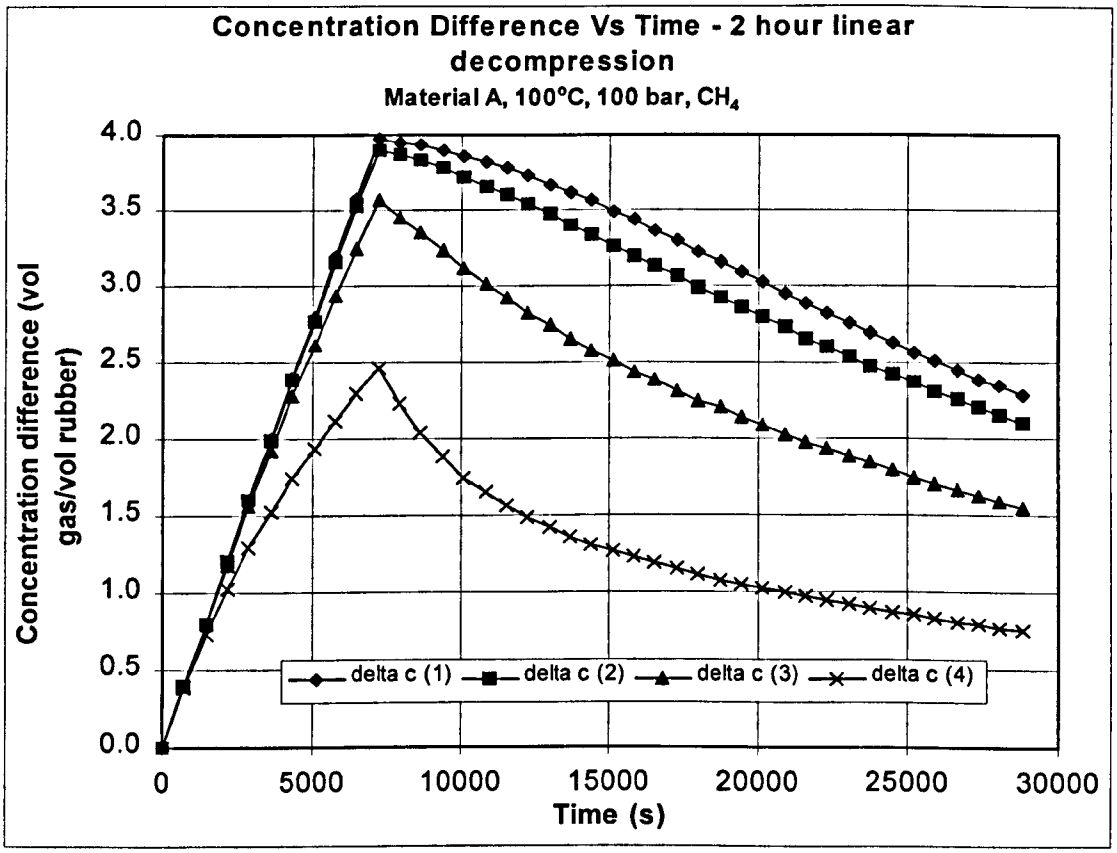

Figure 8.14 - Concentration differential vs time for points 1-4

Figure 8.14 clearly shows that the maximum concentration differential formed at all points occurs exactly at the end of the decompression period (in this case at t = 2 hours). The closer to the pressure surface the lower the concentration differential formed. The

concentration differential profile can now be directly related to the pressure differential formed between each point and the ambient conditions. This is shown in Figure 8.15.

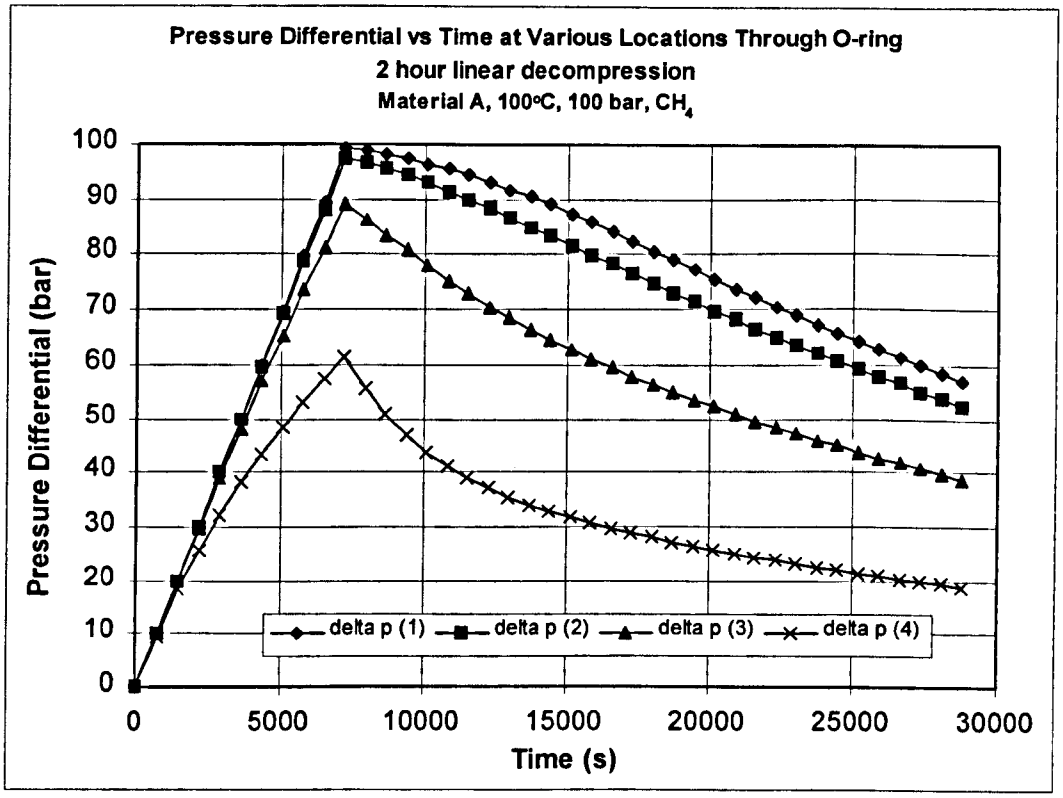

Figure 8.15 - Pressure differential vs time for points 1 to 4

The graph of pressure differential vs time for each point exactly replicates the form of the concentration differential. This would indicate that the maximum pressure differential formed would be at point 1 and the pressure would reduce as points were taken closer to the pressure boundary (point 5)

The analysis was also carried out for the same example, but the temperature was increased to 150°C. This resulted in increased diffusion and higher solubilities as previously shown from the gas transport testing (Chapter 5). The resulting pressure differential vs time plot is shown in Figure 8.16.

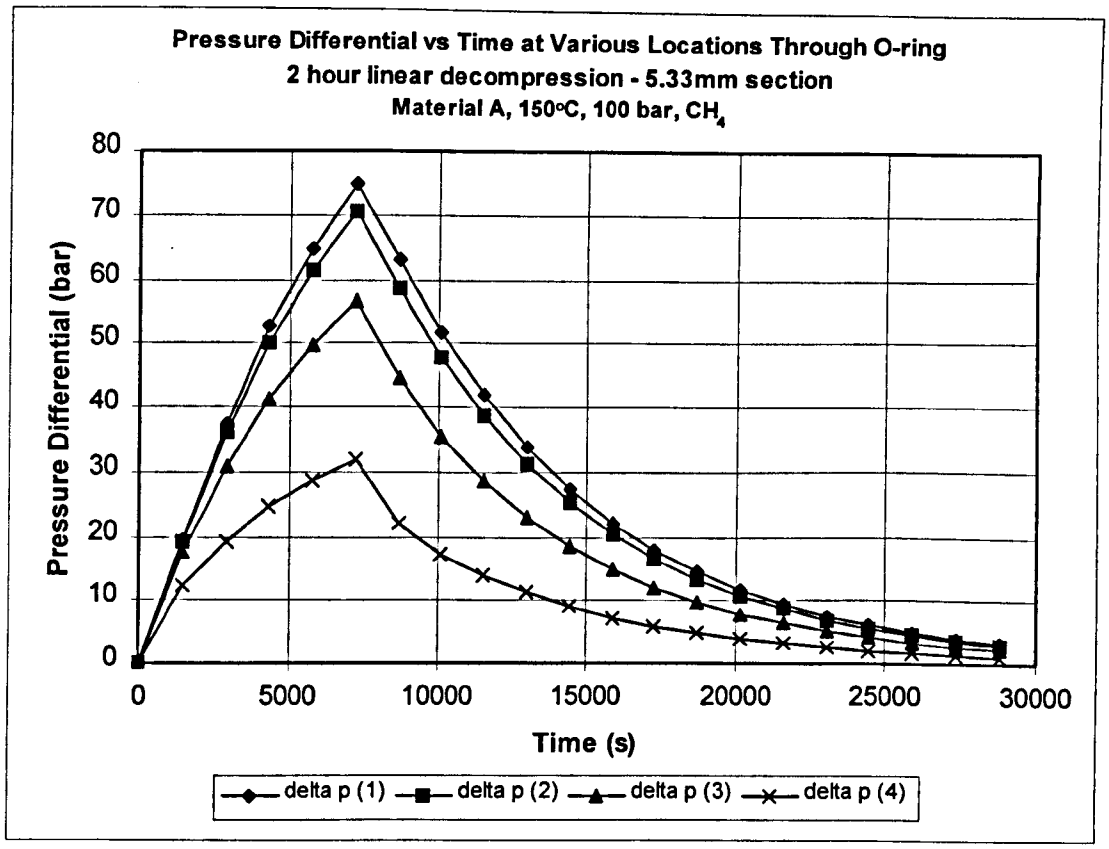

Figure 8.16 - Pressure differential vs time for points 1 to 4 (150°C)

8.3.4 Summary of Results

8.3.4.1 2 Hour Linear Decompression

The maximum pressure differentials formed during each decompression regime are shown in Tables 8.2 to 8.7. In some cases, the results are not available as the appropriate gas transport data was not obtained during the permeation testing programme.

Table 8.2 - Results for 100 bar analysis

MAT ID	SECT DIA. (mm)	Maximum Pressure Differential (bar)							
		1		2		3		4	
		100°C	150°C	100°C	150°C	100°C	150°C	100°C	150°C
A	5.33	99.3	74.8	97.5	70.6	89.0	56.7	61.5	31.9
	10.00	100.0	96.2	100	93.7	98.8	82.3	83.8	53.6
B	5.33	96.0	83.5	93.0	79.5	80.5	65.5	51.5	38.5
	10.00	100.0	98.9	99.5	97.4	96.0	89.3	74.5	62.3
C	5.33	100.0	-	99.4	-	95.2	-	73.0	-
	10.00	100.0	-	100	-	99.8	-	91.4	-

Table 8.3 - Results for 500 bar analysis

MAT ID	SECT DIA. (mm)	Maximum Pressure Differential (bar)							
		1		2		3		4	
		100°C	150°C	100°C	150°C	100°C	150°C	100°C	150°C
A	5.33	495.0	391.7	485.0	370.0	437.5	298.3	297.5	170.0
	10.00	500.0	485.0	500.0	478.3	492.5	421.7	382.5	241.7
B	5.33	500.0	451.1	496.7	433.3	475.0	365.6	367.0	223.3
	10.00	500.0	497.8	500.0	495.6	498.3	466.7	433.3	304.4
C	5.33	-	481.4	-	467.1	-	410.0	-	268.6
	10.00	-	500.0	-	498.6	-	485.7	-	351.4

8.3.4.2 24 Hour Linear Decompression

Table 8.4 - Results for 100 bar analysis (5.33mm section only)

MATERIAL ID	Maximum Pressure Differential (bar)							
	1		2		3		4	
	100°C	150°C	100°C	150°C	100°C	150°C	100°C	150°C
A	41.0	9.7	38.3	9.1	30.0	7.1	16.3	3.8
B	26.7	14.9	25.0	13.9	19.5	10.8	10.5	5.8
C	59.6	-	55.8	-	44.2	-	24.2	-

Table 8.5 - Results for 500 bar analysis (5.33mm section only)

MATERIAL ID	Maximum Pressure Differential (bar)							
	1		2		3		4	
	100°C	150°C	100°C	150°C	100°C	150°C	100°C	150°C
A	188.5	54.5	176.5	51.0	138.0	39.8	74.8	21.3
B	300.0	102.3	281.7	95.7	223.3	74.7	123.2	40.2
C	-	155.7	-	145.7	-	114.1	-	61.6

8.3.4.3 48 Hour Linear Decompression

Table 8.6 - Results for 100 bar analysis (5.33mm section only)

MATERIAL ID	Maximum Pressure Differential (bar)							
	1		2		3		4	
	100°C	150°C	100°C	150°C	100°C	150°C	100°C	150°C
A	21.8	4.9	20.5	4.6	16.0	3.6	8.6	1.9
B	13.6	7.4	12.7	7.0	9.9	5.4	5.3	2.9
C	35.2	-	31.2	-	25.6	-	13.9	-

Table 8.7 - Results for 500 bar analysis (5.33mm section only)

MATERIAL ID	Maximum Pressure Differential (bar)							
	1		2		3		4	
	100°C	150°C	100°C	150°C	100°C	150°C	100°C	150°C
A	99.8	27.3	93.3	25.5	72.8	19.8	39.3	10.7
B	181.7	51.4	170.0	48.1	133.2	37.6	72.0	20.2
C	-	80.6	-	75.4	-	58.9	-	31.6

8.3.5 Discussion

As can be seen from Figure 8.16, the rate of diffusion is much faster immediately after the decompression time has elapsed, this is due to the concentration differential reaching a maximum at the decompression time. As the diffusion rate is much faster at the elevated temperature, the pressure does not have enough time to build up in the material and so the resulting maximum pressure differential at the decompression time is much lower than that at 100°C.

This does not necessarily imply that the material is more likely to fail at 100°C than 150°C as the strength of the materials in this study are greatly reduced at 150°C. Also, as suggested previously, the material may fail at a pressure much less than the maximum pressure differential achieved in both cases.

This model now gives us the information required to determine the safe degassing times for specific gas-elastomer systems. The plots of decompression time vs maximum pressure differential shown in Figures 8.17 to 8.20 show that for a given decompression time a range of pressure differentials are created, depending on location within the seal section.

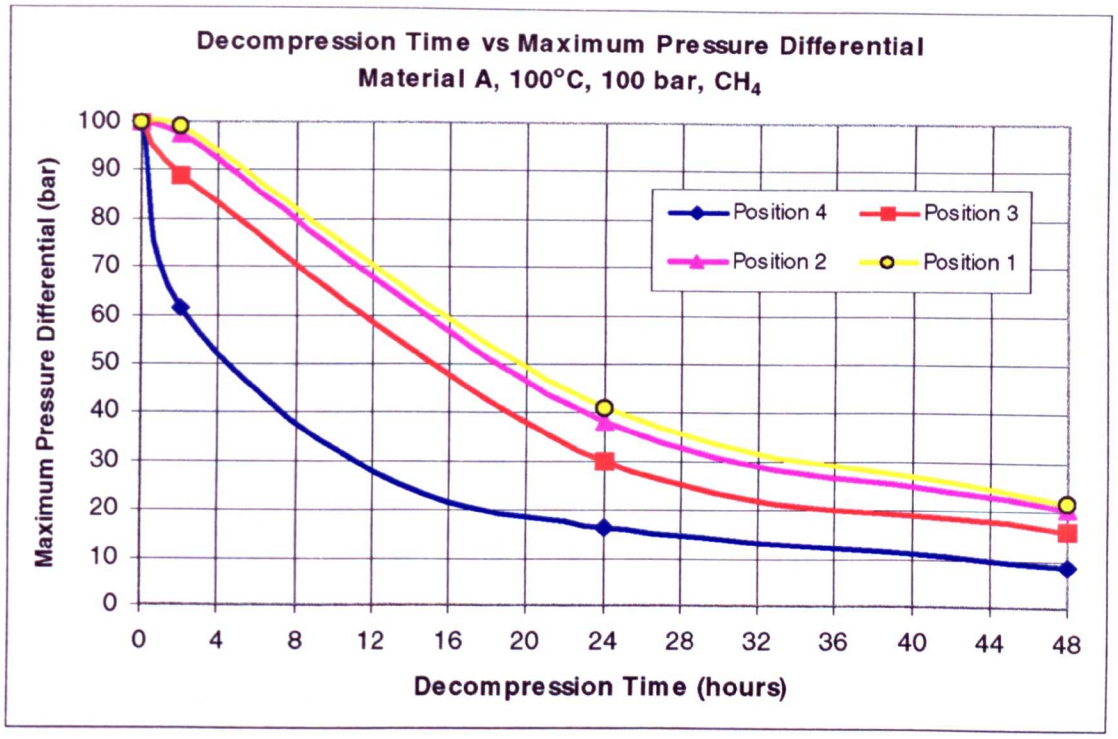

Figure 8.17 - Decompression time vs pressure differential at various locations (100°C)

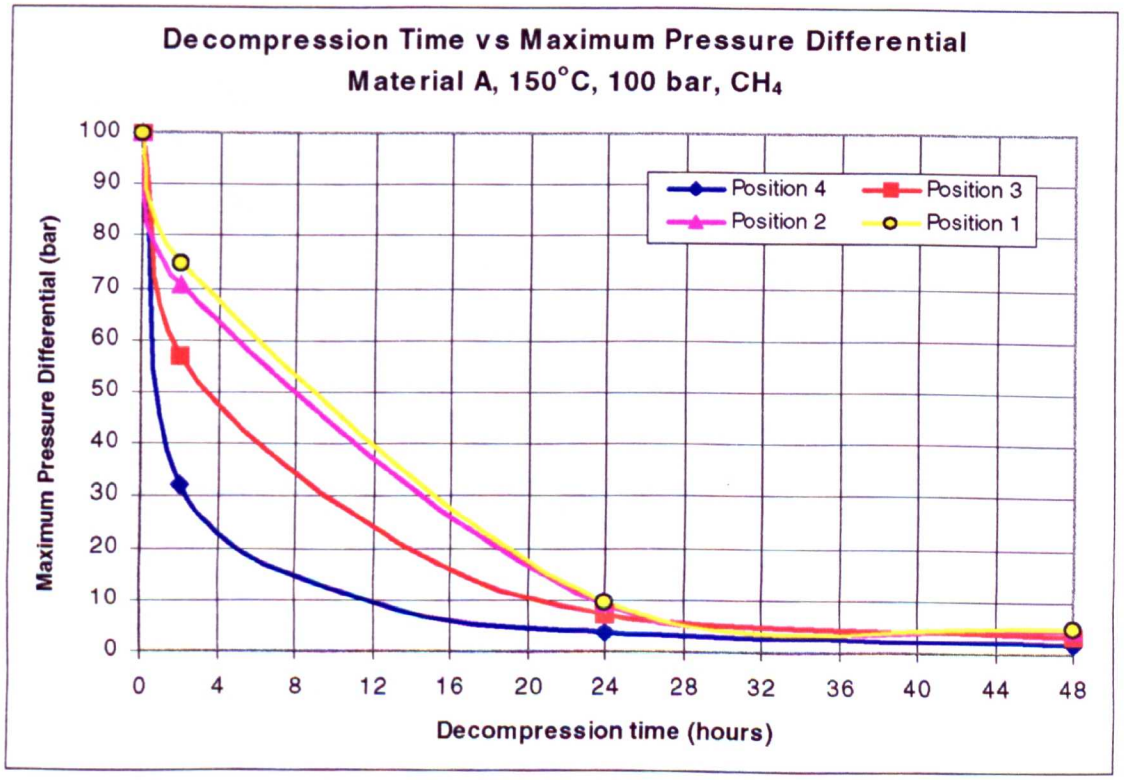

Figure 8.18 - Decompression time vs pressure differential at various locations (150°C)

Therefore, from the void expansion model we know the maximum pressure a void will withstand before failure takes place. We can then relate this pressure to the maximum pressure differential plot to determine the time over which decompression is safe.

For example, if the void expansion model maximum pressure was 70 bar for material A, we would ideally want to decompress over around 13 hours at 100°C to ensure that the critical pressure differential was not exceeded. The corresponding decompression time for 150°C would be around 4 hours, although the strength of the material would be much less.

The analyses of the decompression time vs maximum pressure differential for materials A and B at positions 1 and 4 are shown in Figures 8.19 and 8.20.

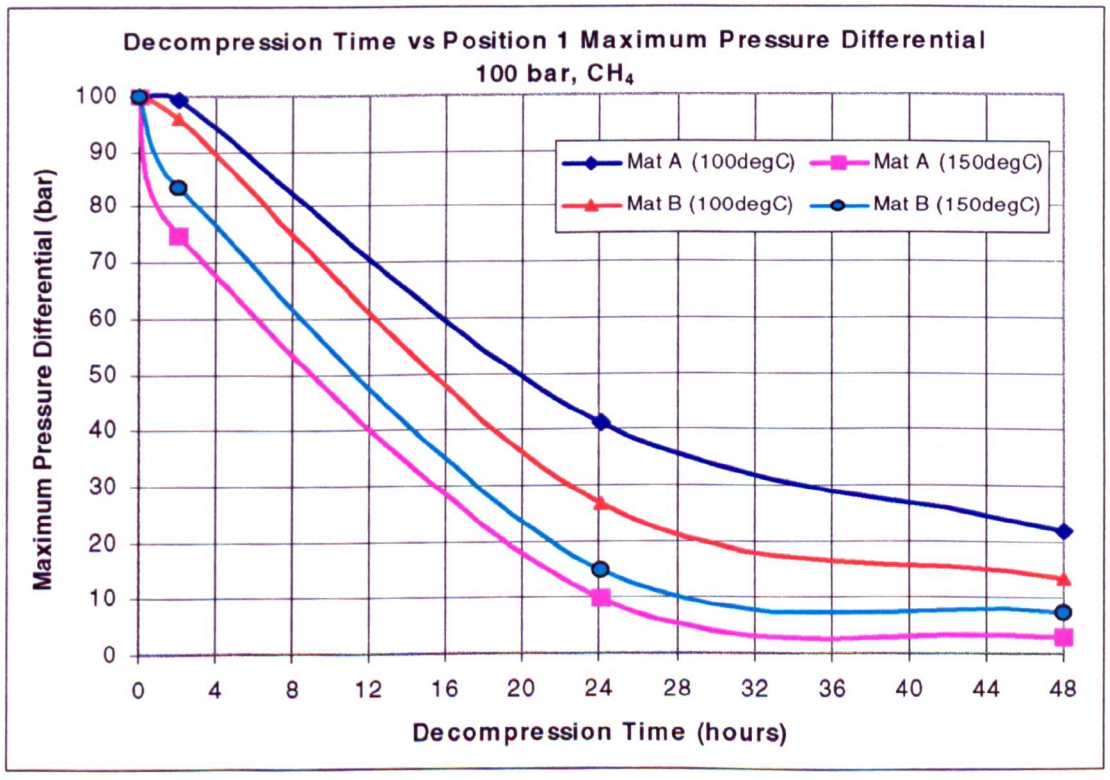

Figure 8.19 - Decompression time vs Position 1 Maximum pressure differential at 100°C and 150°C

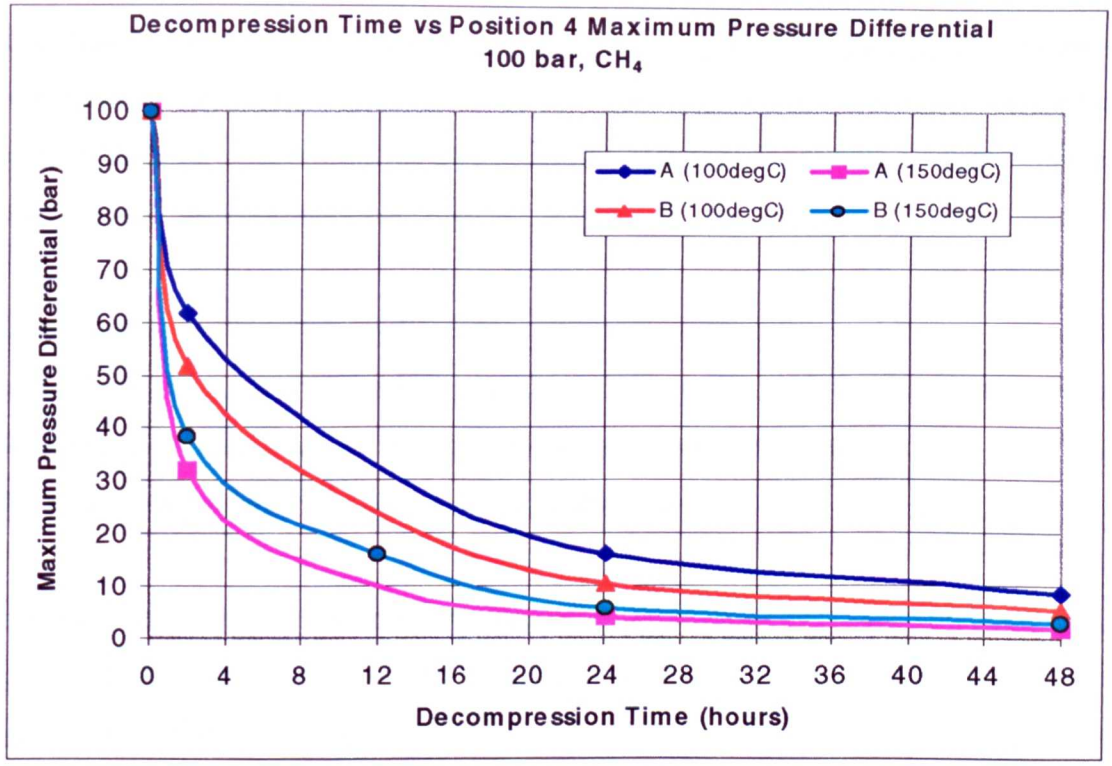

Figure 8.20 - Decompression time vs Position 4 maximum pressure differential at 100°C and 150°C

Interestingly, material A at 100°C shows the highest available critical pressure for void expansion and material A at 150°C shows the lowest available critical pressure. The curves for material B at 100°C and 150°C fall between the two material A curves. This would indicate that material A would perform best at 150°C and less well at 100°C. Material B is the best material on average, but the operational considerations must be taken into account before selecting a material for an explosive decompression application.

8.3.6 Conclusions

This chapter has determined the maximum available pressure differential for void expansion under various decompression regimes. This is achieved using a computer model which solves the differential equation for the axisymmetric transient diffusion of gas.

The model takes into account the decompression time, the material gas transport properties, the seal section diameter, the temperature and the system pressure. The model can also be used to determine the safe decompression time for a system when combined with the void inflation model detailed in Chapter 10.

It was found from the analysis that the maximum pressure differential formed within the seal section always occurred at the end of the decompression period. This is independent of location. The maximum pressure differential also occurs at the point furthest away from the pressure boundary, i.e. the low pressure side of the seal.

Temperature affects the maximum pressure differential formed due to decompression. The gas transport activity increases considerably with increase in temperature, as shown by the gas transport testing. In general, for the same material and section size, the maximum pressure differential is reduced with an increase in temperature. The increase in temperature from 100°C to 150°C had a greater effect on material A than material B. If operating at 100°C, material A showed a much higher pressure differential than material B at the same temperature. However, when the temperature was increased to 150°C, the pressure differential was higher for material B than material A. This suggests that material A is more sensitive to temperature fluctuations than material B.

The analysis showed that section size also affects the maximum available pressure differential. The 10mm section seals produced a higher pressure differential than the 5.33mm section O-rings. This is because the gas has a greater distance to diffuse out the seal in the larger section. Section size effects are most pronounced the nearer to the pressure interface. The maximum pressure differential increased by 18 to 68% by increasing the section size from 5.33mm to 10mm. The actual value in the range depends on material, temperature and pressure.

The 500 bar analyses showed that a higher pressure differential is available after the decompression. This is obviously due to the higher initial saturation pressure.

Once the maximum pressure differential needed to cause fracture initiation in the void is determined from the void inflation model, the safe decompression time can be evaluated from curves such as those shown in Figures 8.17 to 8.20.

8.4 CHAPTER SUMMARY

The modelling of transient diffusion of gas through elastomers under decompression conditions is used to determine the maximum available pressure for void inflation. Depending on the rate of decompression used in the model there are vast differences in the pressure differential available. For instantaneous decompression, the rate of pressure increase within a single void was very rapid, virtually instantaneous.

For linear decompressions over a given time period, the maximum available pressure always occurs at the end of the decompression period. It was found that temperature affects the maximum pressure differential. For material A the effect was more pronounced, showing a significant drop in maximum pressure differential with an increase in temperature. The trend was the same for material B, but less pronounced.

Section size and initial saturation pressure also affect the maximum available pressure differential. The results from this analysis are combined with the stress field model results (Chapter 9) and used as inputs to the void inflation model to determine the probability of fracture at all of the analysis points.

CHAPTER 9 - O-RING STRESS FIELD MODELLING

9.1 INTRODUCTION

When an O-ring is compressed in a standard rectangular groove, the material is subjected to deformations, and therefore stresses. The magnitude and distribution of the stress field are influenced by many controlling parameters. These can be summarised as: -

- Initial compression
- Groove fill
- Physical properties of the elastomer
- Friction
- Seal section size and shape
- Temperature
- Pressure

These parameters must be considered in any model of an elastomer O-ring compressed in a groove to gain a realistic prediction of the stress field induced during decompression.

The purpose of the O-ring stress field model is to determine the stress field induced during O-ring installation and depressurisation. The results of the stress field analysis will be used for a location-based void inflation model, using the stress field as initial conditions. The stress field plays an important role in determining crack initiations, locations and propagation directions.

The model detailed in this chapter provides the complete stress field at all locations throughout the seal section. However, for purposes of the void inflation model, only the stress field at six locations is required. The model results in four stress values for each location. Two values at the compression only phase and two at the end of the gross

volumetric expansion phase are produced:-

- σ_x - direct stress in the x-direction at compression only
- σ_y - direct stress in the y-direction at compression only
- σ_{xexp} - direct stress in the x-direction after gross volumetric expansion
- σ_{yexp} - direct stress in the y-direction after gross volumetric expansion

These are shown graphically in Figure 9.4.

9.2 O-RING BEHAVIOUR UNDER COMPRESSION AND PRESSURE

The elastomer O-ring is used as a fluid boundary for gases and liquids. The O-ring is installed in the groove with the outer radius of the seal in contact, or in close proximity to, the outer radius of the housing, assuming an internal pressurisation. A counter face is then brought down causing the seal to compress and fill the groove. The high elasticity of the seal allows it to deform into the peaks and troughs of the surface roughness of the counter face, therefore effectively forming a barrier to fluid passage (see Figure 9.1).

Various initial compressions and groove fills are employed to provide different sealing functions. The normal values are 15% compression and 70% groove fill. Higher values can be used, but the seal is prone to stress cracking under the increased strain and is therefore undesirable. However, observations of reduced explosive decompression damage from increased groove fill and initial compression have been made.

When the system pressure is applied to the seal, it is pushed towards the outer radius of the housing, therefore increasing the contact stress between the seal and the counterface. Owing to the near incompressibility of the elastomer, the system pressure is translated to a contact stress between the seal and the counter face. The degree of sliding during pressurisation depends on the initial compression and the lubricant used to install the seal.

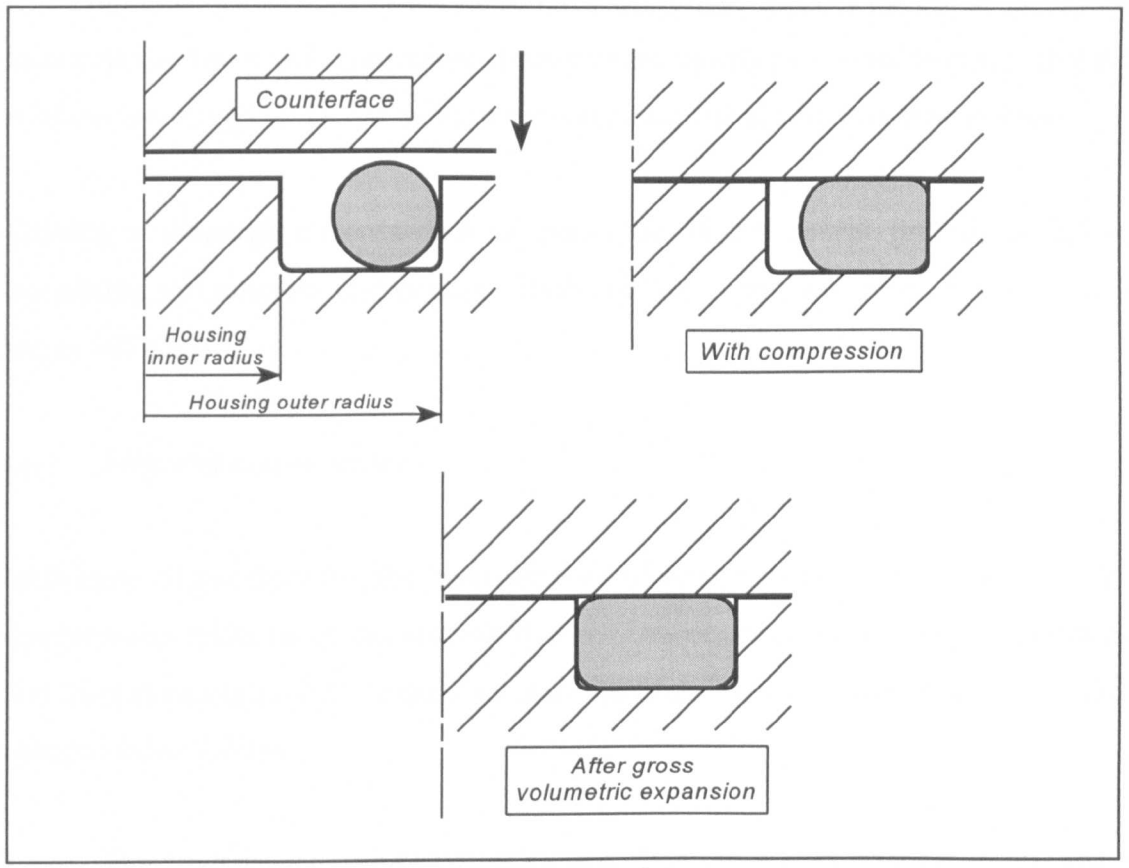

Figure 9.1 - O-ring general arrangements

During decompression, the seal is allowed to relax and the compressive stress field is reduced. However, as the system pressure is reduced, a pressure differential is formed between the interior of the seal and ambient. This causes the inherent voids to inflate, increasing the effective volume of the seal. The seal then expands and the stress field is further increased. The rate of increase of stress is not as significant as the reduction due to depressurisation, therefore an overall drop in compressive stress level is seen by the O-ring.

9.3 NON-LINEAR FINITE ELEMENT SOLUTION PROCEDURES

Non-linear finite element solutions are more complex than linear solutions and can results in many sources of error. In linear analysis, the behaviour of the structure is assumed to be reversible, and solutions for various load cases can be superimposed. The application

of the finite element method to non-linear problems usually requires the use of small load increments and an iterative procedure. Iterations are usually performed to ensure that the solution is convergent, i.e. the error in approximating the equilibrium state is small.

Gaining a thorough understanding of non-linear finite element procedures before attempting any solutions is important. There are four main types of non-linearity, these are as follows: -

(a) Material non-linearity

With material non-linearity, the stress-strain relationships are non-linear, but the strain-displacement relationships are assumed linear. This assumes that the changes in strains and displacements are infinitesimally small. The material non-linearities can be further categorised as follows;

- Time-independent behaviour such as the elasto-plastic behaviour in metals when the material is loaded past the yield point

- Time-dependent behaviour such as creep of metals at high temperatures

- Viscoelastic/viscoplastic behaviour in which both the effects of plasticity and creep are exhibited

(b) Geometric non-linearity

With geometric non-linearity the strain-displacement relationships are non-linear, but the stress-strain relationships are assumed to be linear. This involves large changes in strains and displacements.

(c) Combined material and geometric non-linearity

This is a combination of (a) and (b) above, i.e. non-linear stress-strain relationships as well as large displacements and strains. Examples of combined geometric and material non-linearity include the deformation of rubber-like structures.

(d) Boundary non-linearity (contact)

In contact problems, the deformation and stresses of the contacting bodies are not linearly dependent on the applied forces. The extent of the contact area is not linearly dependent on the applied loads, i.e. doubling the applied loads does not necessarily produce double the displacements. If friction is present between the mating surfaces, then a stick-slip behaviour may occur at the interface that adds another non-linear complexity to the problem.

The deformation of an elastomer seal in a groove is a combination of all of the above. It includes the effects of combined material and geometric non-linearities with the added complication of contact and frictional behaviour.

9.3.1 Non-linear solution procedures

The following solution procedures are taken from Finite Element Analysis of Geometric Non-Linearities and Contact (Becker, 1997). Several solution procedures exist to solve non-linear equations of the form:

$$f(x) = 0 \qquad (9.3.1)$$

One technique commonly employed is the Newton or Newton-Raphson method. This method involves proposing a trial solution, x_i, which is sufficiently close to the exact solution. The next trial solution, x_{i+1}, is estimated using the slope (dy/dx) of the curve at point x_i, as follows:

$$x_{i+1} = x_i - \frac{f(x_i)}{\left(\frac{dy}{dx}\right)} \qquad (9.3.2)$$

The iterations are continued until the exact solution can be found to a specified accuracy or tolerance. This occurs when the right hand side of equation (9.3.1) is close to zero. This method effectively approximates the non-linear curve to a series of tangents.

Normally, convergence to the solution occurs in a small number of iterations. However, in some cases convergence may not be obtained quickly or non-convergence may occur. Non-convergence can occur when the slope of the non-linear curve changes slope from positive to negative. Therefore, the Newton method can easily fail in solutions where there is a maximum or minimum in the curve.

9.3.2 Finite element incremental-iterative procedures

Most finite element formulations involve breaking down the non-linearity into a series of simpler linear steps. The load incrementation and iteration procedures used in commercial finite element codes are often automated by code developers requiring little or no interaction from the user. The user must ensure that the software solution procedures are robust. The nonlinear finite element analysis involves the solution of a large system of non-linear equations, checking the equilibrium in successive iterations.

Often, the modified Newton-Raphson method is used in commercial finite element codes. If the slope of the curve (dy/dx) is kept constant, the stiffness matrix value can be kept constant, therefore reducing computational time. However, using this method, a slower convergence occurs.

The load incrementation procedure can be summarised in the following steps:

1. Start from the initial external loads and initial displacements, e.g. the elastic solution.
2. Divide the total external load into M small increments as follows.

$$F_{total} = F_o + \sum_{i=1}^{M} \Delta F_i \qquad (9.3.3)$$

   The size of the load increment is not necessarily constant, and may be automatically increased or decreased by the program based on an assessment of the changes between successive increments.
3. Apply one load increment ΔF_i and solve the equations to obtain the resulting displacement increment Δu_i as follows:

$$\Delta u_i = [K]_{i-1}^{-1} \Delta F_i \qquad (9.3.4)$$

4. Perform iterations to ensure that equilibrium conditions exist.
5. Apply the next load increment. Calculate a new updated stiffness matrix $[K]_i$, for each new load increment, or alternatively use the old value of [K].
6. Repeat the iterative procedure for each load increment.
7. Stop when the full load is applied.
8. The total displacements are finally obtained by adding all the displacement increments:

$$u_{total} = u_o + \sum_{i=1}^{M} \Delta u_i \qquad (9.3.5)$$

It is important to ensure that with each load increment, equilibrium conditions are satisfied before proceeding to the next step. This is usually achieved by estimating the residual or out of balance forces within the structure and reducing them to a negligible value.

9.3.3 Difficulties in modelling non-linear problems

With complex non-linear problems there is no assurance of convergence. Divergence from the correct solution can easily occur if the initial iterations are inaccurate and the user may interpret the results incorrectly. If the slope of the non-linear curve changes sign during the loading, many standard incremental-iterative procedures may fail.

It is difficult to determine, in advance, what size of load increment and how many increments should be used. However, many modern finite element codes automate this procedure.

Engineering judgement must always be applied to the outputs from a non-linear finite element solution as there is no guarantee that the solution is valid

9.4 SOLUTION METHODOLOGY

9.4.1 Model definition

The modelling programme is closely related to the seal decompression testing (see Chapter 3) to validate the model. The model uses the non-linear finite element method to produce a mesh of an O-ring in a groove. Contact conditions between the seal and the counterface are defined by determining the elements that come into contact as the seal is deformed. The housing counter faces are modelled using rigid surfaces. Rigid surfaces are surfaces that do not deform under any loading condition. Considering the relative strength and stiffness of elastomer seals and steel counter faces, this is a reasonable assumption to make. The mesh is deformed by shifting rigid surfaces to the dimensions of the groove. Based on these deformations, the corresponding direct stress values are calculated by evaluating the strain energy potential and differentiating this function partially with respect to the extension ratio (λ) in the specified direction.

The material is modelled using the polynomial (N = 2) form of the strain energy function: -

$$U = \sum_{i+j=1}^{N} C_{ij}(I_1 - 3)^i(I_2 - 3)^j \qquad (9.4.1)$$

where U is the strain energy potential, C_{ij} are material constants and I_1 and I_2 are the first and second strain invariants respectively. Uniaxial and biaxial material data are used to produce a fitted strain energy function by determining the material constants C_{ij}. The fitted curve matches, as near as possible, the actual stress-strain characteristics of the material.

The elements used in the model are linear, reduced integration elements with a fine mesh. The O-ring mesh has a higher density of elements at the contact surfaces between the seal and the counter face. These surfaces undergo a much higher deformation and therefore a higher density of elements is required to ensure that the solution will converge. The element types used are axisymmetric, to reduce the model complexity and computational time.

The methodology used to determine the stress field at the end of initial compression and after the gross volumetric expansion is shown in Figure 9.2. The two values at compression only and with expansion are necessary as the void inflation model requires both sets of data. The initial compression values are used as initial conditions and the expanded values are used as the pressure is ramped up within the void.

9.4.2 Compression phase

The initial compression is applied by translating the top rigid surface down until it contacts the top of the groove. When the rigid surface contacts the seal, the friction properties introduced in the model come into effect (see Figure 9.1). The seal will be deformed on the bottom of the groove as well as the top and side faces. Therefore there are three main contact areas, all sliding as the counter faces come into contact. Once the gross volumetric expansion is applied to the model, to simulate the decompression, a fourth contact area (the

inner radius) may come into the solution, depending on the groove fill and initial compression.

The application of pressure has been modelled, but it is not required for the analysis of the stress field formed during decompression. At the end of the decompression period, the seal has no pressure activation as the pressure has been completely removed. However, the seal experiences gross volumetric expansion during this depressurisation according to the increase in pressure differential formed in the inherent voids. This causes the seal to expand into the available groove volume, therefore increasing the stress field.

From the void inflation model perspective, the worst case is a minimum compressive stress and maximum available pressure differential. The void will then have minimum resistance to expansion and maximum driving force for inflation. The maximum available pressure differential occurs at the end of the decompression period (see Chapter 8) and the minimum compressive stress also occurs at this time. Therefore, the worst case scenario is at this point. Figure 9.3 shows this phenomenon graphically.

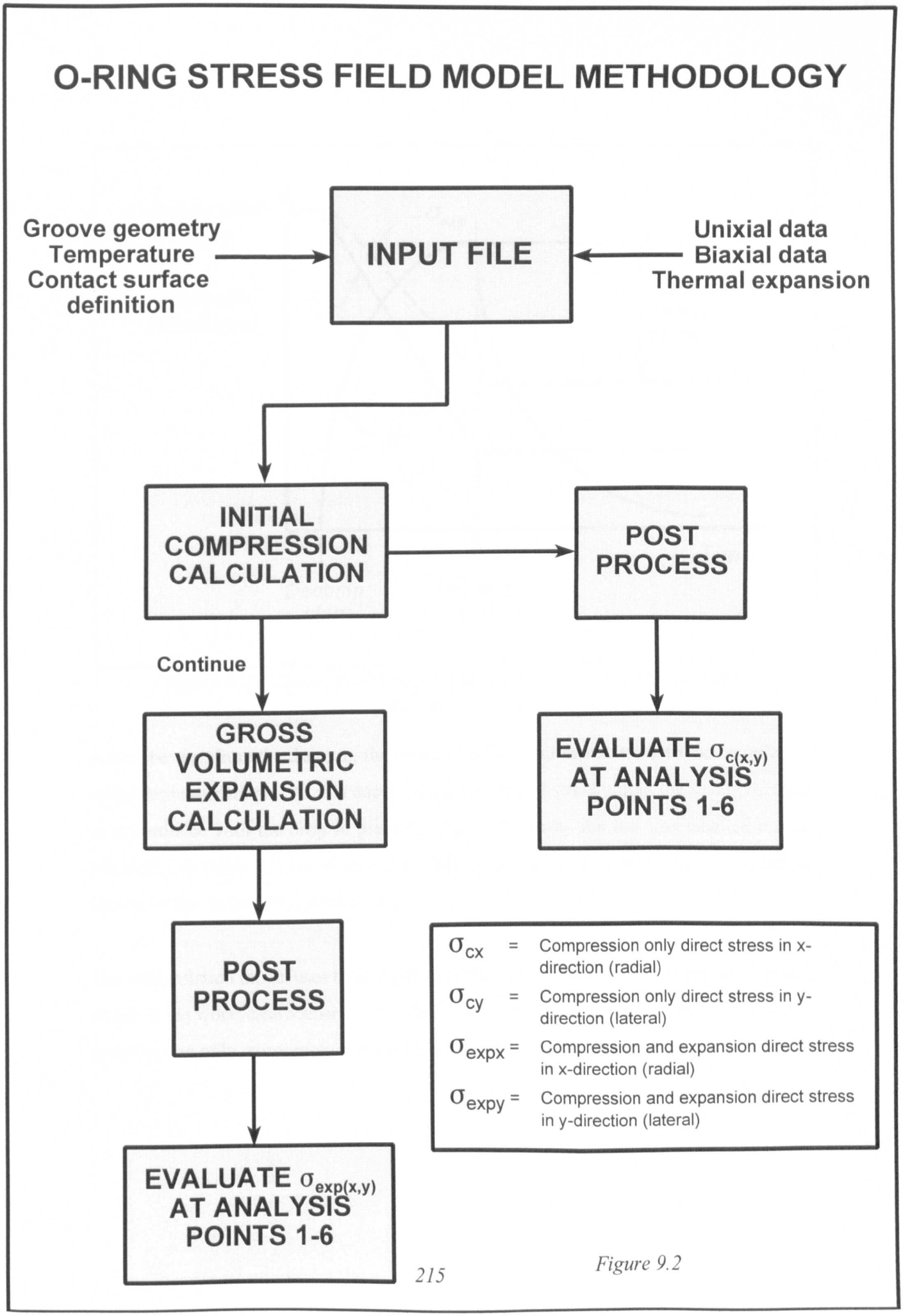
O-RING STRESS FIELD MODEL METHODOLOGY
Groove geometry
Temperature
Contact surface definition
INPUT FILE
Unixial data
Biaxial data
Thermal expansion
INITIAL COMPRESSION CALCULATION
POST PROCESS
Continue
GROSS VOLUMETRIC EXPANSION CALCULATION
EVALUATE $\sigma_{c(x,y)}$ AT ANALYSIS POINTS 1-6
POST PROCESS
EVALUATE $\sigma_{exp(x,y)}$ AT ANALYSIS POINTS 1-6
σ_{cx} = Compression only direct stress in x-direction (radial)
σ_{cy} = Compression only direct stress in y-direction (lateral)
σ_{expx} = Compression and expansion direct stress in x-direction (radial)
σ_{expy} = Compression and expansion direct stress in y-direction (lateral)

Figure 9.2

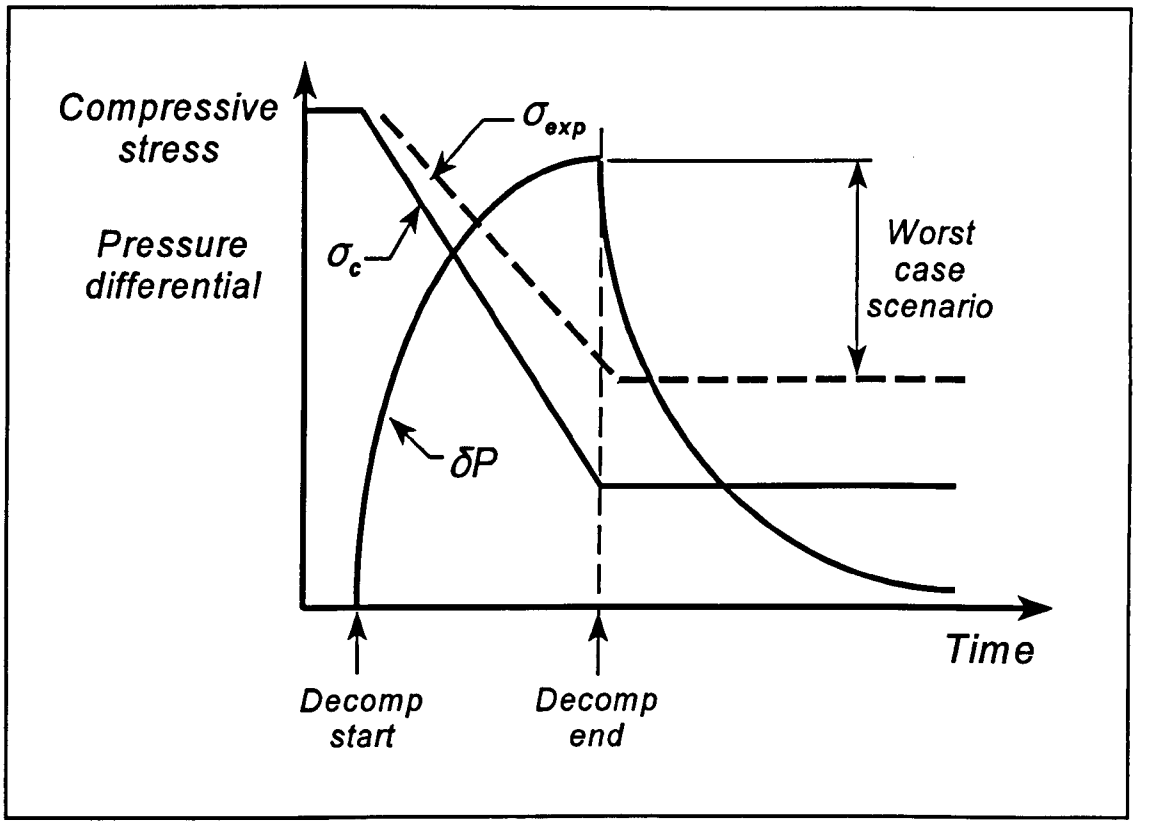

Figure 9.3 - Compressive Stress Field and Pressure Differential during depressurisation

As can be seen from the diagram, the pressure differential increases up to the completion of the depressurisation. As this occurs, the compressive stress within the seal is reduced in accordance with the drop in pressure, this is shown by the full line labelled σ_c. In practice, this stress level is increased slightly by the gross volumetric expansion, this is shown by the dashed line labelled σ_{exp}.

The void inflation model uses three input variables at the end of the decompression period, which is the worst case scenario. The three variables are compressive stress field due to compression only, compressive stress field with expansion and the pressure differential.

9.4.3 Gross volumetric expansion phase

The stress field model takes into account the condition of initial compression and gross volumetric expansion in determining the stress field. The volumetric expansion is applied by using a thermal expansion analogy. The material is given a coefficient of thermal expansion and an additional temperature applied to the seal. The magnitude of this expansion is based on the void and rigid inclusion analysis carried out in Chapter 4. Using this data and assuming a quantity of submicroscopic voids, the estimated volumetric increase can be calculated, based on a critical strain to failure in a void of approximately $\lambda = 3$.

The analysis is performed in two steps and the stress field is calculated at six analysis points. The two steps are:-

- Initial compression and application of analysis temperature across all nodes
- Gross volumetric expansion using thermal expansion analogy (increasing the temperature to induce the required expansion)

The six analysis points are shown in Figure 9.4. The bottom section of the seal is not studied as it is assumed that the stress field is symmetrical about the radial direction. Each of the six analysis points have differing stress fields and differing available pressure differentials under decompression. The direct stress in the x (radial) and y (lateral) directions are calculated and used as initial conditions in the void inflation model.

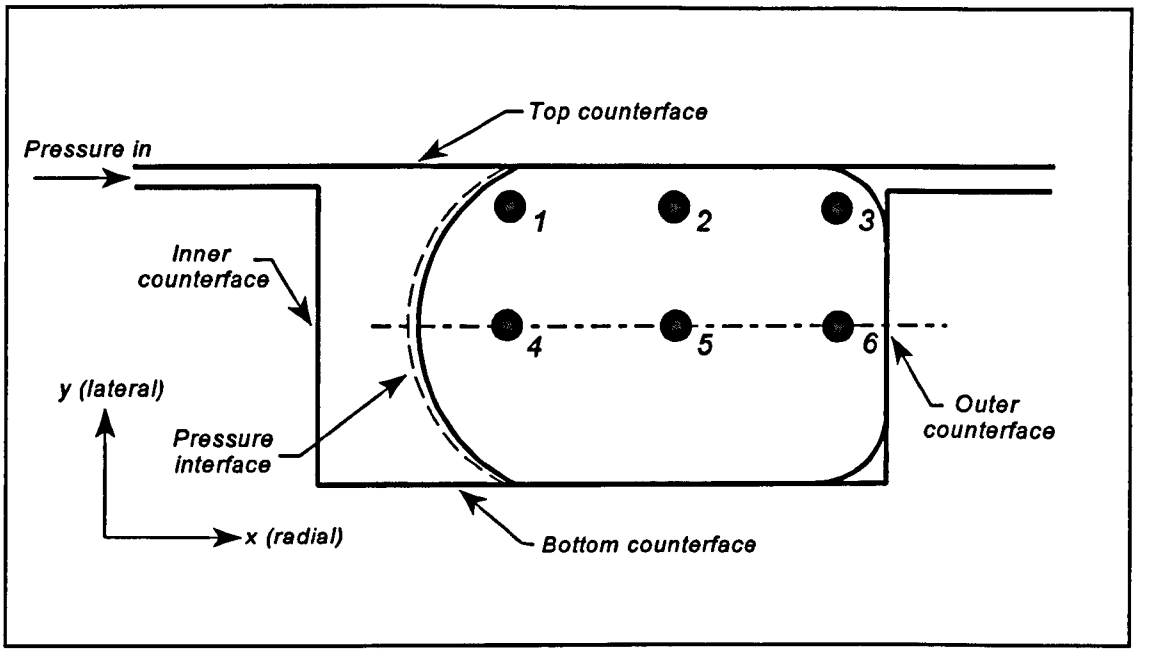

Figure 9.4 - O-ring analysis points and groove arrangement

9.4.4 Modelling the initial compression and groove fill

It has been observed in industry that high groove fill will inhibit crack growth during decompression. As the voids start to inflate and the seal undergoes gross volumetric expansion it contacts the groove wall. This imparts additional compressive stress into the seal and reduces the available surface for gas transport out of the seal section. Therefore, the pressure differential is reduced and the compressive stress field is increased, therefore inhibiting void inflation and crack initiation.

The initial compression also increases the compressive stress within the seal. However, excessive stress due to compression or groove fill can lead to stress cracking as the seal is pushed into the corners of the groove.

For each analysis the positions of the rigid surfaces are modified to change the dimensions of the groove. In doing this, the initial compression and groove fill are varied. Changing the groove depth dimension modifies the initial compression. This dimension, in

combination with the length of the groove determines the available groove area.

In simple terms, the groove fill is the cross sectional area of the seal divided by the available groove area. However, the calculation of initial compression and groove fill used in the model are taken directly from the groove dimensions used in the seal decompression testing programme (see Chapter 3). These dimensions take into account tolerances and the differential thermal expansion of the seal and the housing to provide more accurate dimensions.

9.4.5 The effect of friction

The coefficient of friction, μ, is commonly defined as the ratio of the tangential force F to the normal load N.

$$\mu = \frac{F}{N} \qquad (9.4.2)$$

When dealing with elastomers, the above equation should be considered as a definition of μ and no inference should be drawn regarding the constancy of μ with such variables as load, contact area, velocity of slide and temperature. The value of μ can vary greatly depending on the above parameters, in particular the contact area.

It has been stated in the literature that boundary lubrication is a dominant friction mechanism, although hysteresis losses in the rubber may contribute to friction. During metal to metal contact the surface asperities are deformed and more contact surface area is created, therefore the friction coefficient is dependant upon contact pressure. With elastomer to metal contact the elastomer is deformed into the peaks and troughs with very little pressure, therefore the contact area does not increase. The requirement for slippage is that the shear stress between the elastomer and the counter face is overcome in order for slippage to occur (Nau, 1971).

Therefore during a finite element analysis, the friction coefficient is set to a very high value (~10) and an equivalent shear stress limit set so that, whatever the magnitude of the contact pressure stress, sliding will only occur if the magnitude of the equivalent shear stress reaches this value. The value used in the model is 0.5 MPa, which is quoted by Nau, 1971 as a good approximation for most elastomer sealing applications.

9.4.6 Analysis Matrix

To fully replicate the conditions seen in industry, the analysis matrix needs to cover all eventualities. These analyses have also been replicated in experimental work (see Chapter 3) to determine the decompression performance of each elastomer.

The analysis matrix is shown in Table 9.1. The matrix did originally include a best case analysis and test (number 3). However, it was decided that studying this case was not necessary as no failure would clearly take place owing to the 48 hour decompression period.

Table 9.1 - Analysis matrix

Test Variable	**Analysis Number**					
	1	2	4	5	6	7
Initial comp.	15%	15%	25%	25%	15%	15%
Groove fill	70%	70%	70%	90%	70%	90%
Section dia.	5.33mm	10mm	5.33mm	10mm	10mm	5.33mm
Decomp. time	2 hours	instant	instant	instant	2 hours	2 hours
Temperature	100°C	150°C	100°C	150°C	100°C	150°C
Pressure	100 bar	400 bar	500 bar	100 bar	100 bar	500 bar

9.5 RESULTS

A sample of the resultant stress field for material A, analysis 7 is shown in Figure 9.5. This analysis is for 15% compression and 90% groove fill at 150°C and clearly shows the high compressive stress cones between the top and bottom faces and the increased levels of contact and therefore stress on the inner and outer radii of the housing. During expansion the stress field is increased and the compressive stress cones move further in towards the centre of the seal section. The x and y components of direct stress for compression and expansion are shown in Tables 9.2 to 9.19. Note in some cases the stresses are tensile.

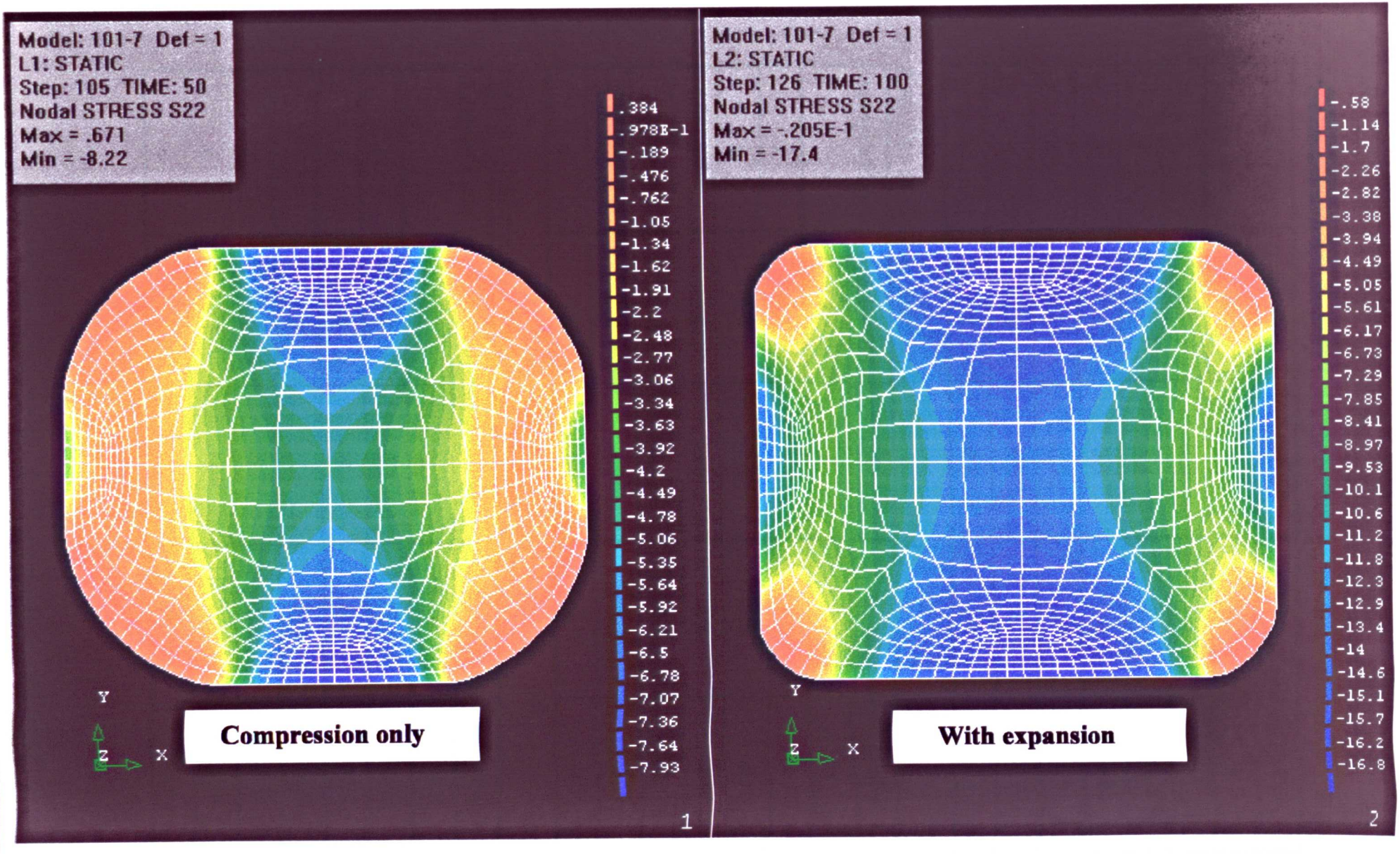

Figure 9.5 - Comparison of O-ring stress field for compression only and with expansion

Table 9.2 - Material A - Analysis 1

Analysis Point	σ_c (compression) (MPa)		σ_{exp} (expansion) (MPa)	
	x	y	x	y
1	-0.8	-1.2	-1.2	-2.2
2	-3.1	-8.4	-4.3	-10.0
3	-1.5	-2.3	-1.8	-4.6
4	-0.1	-0.3	-0.4	-0.3
5	+0.8	-5.2	0	-7.3
6	-3.2	-0.8	-5.6	-2.3

Table 9.3 - Material A - Analysis 2

Analysis Point	σ_c (compression) (MPa)		σ_{exp} (expansion) (MPa)	
	x	y	x	y
1	-0.7	-1.2	-1.0	-2.1
2	-2.9	-7.4	-3.9	-8.8
3	-1.4	-3.0	-1.8	-5.1
4	-0.1	-0.2	-0.3	-0.2
5	+0.7	-4.9	+0.1	-6.7
6	-3.0	-1.0	-4.7	-2.2

Table 9.4 - Material A - Analysis 4

Analysis Point	σ_c (compression) (MPa)		σ_{exp} (expansion) (MPa)	
	x	y	x	y
1	-1.8	-5.1	-3.3	-6.9
2	-7.5	-18.9	-9.7	-22.6
3	-3.7	-12.6	-5.9	-16.5
4	-0.5	-0.7	-0.9	-0.9
5	+2.2	-16.8	+0.3	-21.0
6	-5.2	-2.3	-8.5	-4.6

Table 9.5 - Material A - Analysis 5

Analysis Point	σ_c (compression) (MPa)		σ_{exp} (expansion) (MPa)	
	x	y	x	y
1	-3.4	-7.5	-25.3	-30.5
2	-8.8	-17.2	-31.5	-39.8
3	-5.2	-12.4	-27.3	-35.7
4	-4.7	-2.4	-27.7	-24.5
5	-0.3	-15.1	-21.4	-37.7
6	-7.5	-3.7	-30.7	-24.9

Table 9.6 - Material A - Analysis 6

Analysis Point	σ_c (compression) (MPa)		σ_{exp} (expansion) (MPa)	
	x	y	x	y
1	-0.9	-1.5	-1.2	-2.5
2	-3.6	-9.4	-4.7	-11.0
3	-1.6	-3.5	-2.0	-5.9
4	-0.1	-0.3	-0.3	-0.4
5	+1.0	-6.2	+0.3	-8.3
6	-3.3	-1.0	-5.4	-2.3

Table 9.7 - Material A - Analysis 7

Analysis Point	σ_c (compression) (MPa)		σ_{exp} (expansion) (MPa)	
	x	y	x	y
1	-1.5	-2.0	-7.3	-11.6
2	-4.1	-8.0	-12.7	-16.9
3	-1.7	-2.4	-6.8	-12.2
4	-3.6	-1.0	-13.5	-9.4
5	-0.6	-4.8	-8.4	-12.9
6	-4.5	-1.4	-14.2	-9.2

Table 9.8 - Material B - Analysis 1

Analysis Point	σ_c (compression) (MPa)		σ_{exp} (expansion) (MPa)	
	x	y	x	y
1	-0.7	-1.1	-1.1	-2.4
2	-2.4	-6.1	-3.5	-7.7
3	-1.3	-1.8	-1.7	-3.8
4	-0.1	-0.2	-0.2	-0.1
5	+0.5	-3.6	+0.1	-5.2
6	-3.0	-0.9	-5.2	-2.5

Table 9.9 - Material B - Analysis 2

Analysis Point	σ_c (compression) (MPa)		σ_{exp} (expansion) (MPa)	
	x	y	x	y
1	-0.7	-1.2	-1.0	-2.3
2	-3.3	-8.8	-4.5	-10.8
3	-1.4	-3.3	-1.9	-5.8
4	-0.1	-0.3	-0.3	-0.3
5	+0.7	-6.0	+0.1	-8.3
6	-3.0	-1.0	-5.1	-2.3

Table 9.10 - Material B - Analysis 4

Analysis Point	σ_c (compression) (MPa)		σ_{exp} (expansion) (MPa)	
	x	y	x	y
1	-1.5	-4.8	-2.5	-6.9
2	-5.0	-10.4	-6.4	-12.2
3	-3.2	-8.3	-4.7	-10.8
4	-0.3	-0.2	-0.6	-0.3
5	+1.1	-8.6	+0.1	-10.8
6	-5.7	-2.7	-8.1	-5.0

Table 9.11 - Material B - Analysis 5

Analysis Point	σ_c (compression) (MPa)		σ_{exp} (expansion) (MPa)	
	x	y	x	y
1	-4.2	-9.3	-37.0	-43.6
2	-11.3	-23.8	-45.5	-57.5
3	-6.3	-16.0	-39.6	-51.1
4	-5.9	-3.3	-39.8	-36.5
5	-0.5	-21.1	-31.8	-54.8
6	-8.7	-4.2	-43.4	-35.9

Table 9.12 - Material B - Analysis 6

Analysis Point	σ_c (compression) (MPa)		σ_{exp} (expansion) (MPa)	
	x	y	x	y
1	-0.8	-1.4	-1.0	-2.7
2	-2.8	-6.7	-3.7	-8.1
3	-1.5	-2.7	-1.8	-4.8
4	-0.1	-0.1	-0.2	-0.1
5	+0.6	-4.2	+0.3	-5.8
6	-3.4	-1.2	-5.3	-2.6

Table 9.13 - Material B - Analysis 7

Analysis Point	σ_c (compression) (MPa)		σ_{exp} (expansion) (MPa)	
	x	y	x	y
1	-1.6	-2.2	-9.4	-14.8
2	-4.7	-9.3	-16.2	-21.3
3	-1.8	-2.6	-8.4	-15.6
4	-4.1	-1.2	-17.0	-12.1
5	-0.5	-5.7	-10.9	-16.4
6	-5.0	-1.4	-17.7	-11.6

Table 9.14 - Material C - Analysis 1

Analysis Point	σ_c (compression) (MPa)		σ_{exp} (expansion) (MPa)	
	x	y	x	y
1	-0.7	-1.1	-1.2	-4.5
2	-2.9	-8.0	-4.5	-10.7
3	-1.4	-2.1	-1.8	-2.4
4	-0.1	-0.2	-0.3	-0.4
5	+0.6	-4.9	-0.1	-7.6
6	-3.2	-0.9	-5.8	-2.5

Table 9.15 - Material C - Analysis 2

Analysis Point	σ_c (compression) (MPa)		σ_{exp} (expansion) (MPa)	
	x	y	x	y
1	-1.0	-1.9	-1.5	-3.9
2	-3.6	-8.9	-5.1	-11.1
3	-1.8	-3.7	-2.5	-6.6
4	-0.1	-0.3	-0.3	-0.3
5	+0.8	-5.7	+0.4	-8.0
6	-4.5	-1.5	-7.0	-3.5

Table 9.16 - Material C - Analysis 4

Analysis Point	σ_c (compression) (MPa)		σ_{exp} (expansion) (MPa)	
	x	y	x	y
1	-1.4	-5.2	-2.6	-8.8
2	-4.7	-9.3	-6.8	-12.9
3	-3.2	-6.9	-5.1	-10.4
4	-0.2	-0.1	-0.4	-0.2
5	+0.5	-7.5	-0.1	-11.1
6	-5.9	-3.3	-8.8	-6.2

Table 9.17 - Material C - Analysis 5

Analysis Point	σ_c (compression) (MPa)		σ_{exp} (expansion) (MPa)	
	x	y	x	y
1	-3.7	-9.4	-21.1	-29.2
2	-9.2	-16.8	-28.0	-36.1
3	-6.3	-13.6	-25.1	-34.0
4	-5.8	-2.2	-27.3	-21.1
5	-0.4	-14.2	-19.4	-33.6
6	-9.9	-5.2	-30.5	-24.2

Table 9.18 - Material C - Analysis 6

Analysis Point	σ_c (compression) (MPa)		σ_{exp} (expansion) (MPa)	
	x	y	x	y
1	-0.8	-1.4	-1.2	-2.8
2	-3.5	-9.3	-5.0	-12.0
3	-1.5	-3.2	-2.1	-6.0
4	-0.1	-0.3	-0.3	-0.4
5	+0.7	-6.2	+0.2	-9.0
6	-3.4	-1.8	-5.8	-2.6

Table 9.19 - Material C - Analysis 7

Analysis Point	σ_c (compression) (MPa)		σ_{exp} (expansion) (MPa)	
	x	y	x	y
1	-1.8	-2.5	-7.5	-12.7
2	-4.7	-9.3	-13.3	-19.3
3	-2.0	-2.9	-7.7	-13.5
4	-4.3	-1.3	-15.4	-9.8
5	-0.6	-5.5	-9.0	-14.5
6	-5.7	-1.8	-16.6	-10.7

9.6 DISCUSSION

The void inflation model under compressive constraints clearly shows the importance of the surrounding stress field. The stress field model gives the x and y components of stress. The difference between the x and y components of stress was found to be very important, emphasising the extreme wall stress seen at the lateral poles of an inflating void.

The stress field formed by the deformation of the seal can give some insight into the orientation of cracks formed during decompression. Once a crack begins to propagate, it will take the path of least resistance. If the stress field is highly compressive in a certain region, it is likely that the crack will divert to avoid this high compressive stress. Observations of cracks formed in elastomer seals have shown that, usually, cracks are formed perpendicular to the direction of applied pressure. Close observation of these cracks show that they are not perfectly perpendicular, but are slightly angled. This may be due to the cone shaped region of high compressive stress diverting the crack as it propagates.

The O-ring stress field model uses uniaxial and biaxial data generated during testing. The model is only as accurate as the data used to generate the strain energy function for the material. Therefore, the stress field results will only be as accurate as this data. The material properties are also extremely variable owing to the intrinsically variable behaviour of elastomers in general. Taking into account this variability, the resulting stress field may also be variable. The stress-strain data used to generate the model are the nominal values only.

The stress field may also be affected by the friction between the seal and the counter face. Elastomer seals are commonly installed using a lubricant that aids the sliding between the seal and the housing. After a period of time, this lubricant is absorbed into the surface of the O-ring and no longer acts as a lubricating boundary. The model assumes that no lubrication is present between the seal and counter face. However, if decompression

occurs before the lubricant is absorbed into the surface the resulting stress field may differ. Other effects such as compression set, stress relaxation and swell due to liquid uptake are not considered in this model.

The dimensions of the groove used in the model are nominal values. Obviously, during manufacture, tolerances are applied to the dimensions. Small variations in tolerance can affect the initial compression and groove fill. The seal dimensions are also nominal values and small variations in section size or seal diameter can have a similar effect on the stress field. The groove is assumed to have sharp corners, rather than fillet radii as specified in the relevant British Standard (BS 4518 - Metric dimensions of toroidal sealing rings and their housings).

The temperature across the seal is assumed to be uniform during decompression. Rapid depressurisation can result in the formation of temperature gradients across the seal section due to the adiabatic expansion of the gas at the pressure interface. However, the thermal conductivity of the elastomer is much lower than the housing. The thermal inertia of the housing is also much greater, therefore rapidly increasing the temperature at the pressure interface due to conduction and convection.

The magnitude of the gross volumetric expansion is assumed to be 11%. This value will obviously vary depending on the quantity of voids and their average size. The value will also vary if the inflated void fails and the crack continues to propagate, resulting in a much larger void. In the cases of high groove fill, this value could be significant.

In the cases of extreme deformation of the finite element mesh the elements are pushed into the corners of the housing. This may result in inaccurate stress levels at the corners as the elements are distorted. This was solved using a higher mesh density at these points, but in the extreme cases of 25% initial compression and 90% groove fill, the problem was still apparent.

The model assumes that the stress field is symmetrical about the radial centre line of the seal. This is not entirely the case because when the seal is compressed, the bottom of the seal rapidly pushes into the corner of the groove, whereas the top of the seal is being compressed initially by a flat surface. This introduces a slightly non-symmetric stress field, but for the purposes of the model, this is assumed to be symmetric. There will also be a small extrusion gap at the top of the groove that will also cause the stress field to be non-symmetric.

9.7 CONCLUSIONS

The O-ring stress field model has produced the necessary initial conditions for the void inflation model. It is clear from the results that the maximum compressive stress occurs at analysis point 2 where the seal contacts the counterface. However the worst case, as far as void inflations are concerned, is at analysis point 5. This is because the difference between the x and y components of compressive stress is the maximum. In most cases the x component is tensile in nature. The magnitude of the compressive stress field will also be important as this will resist the pressure differential inflating the void.

The model shows that initial compression and groove fill significantly affect the magnitude of the compressive stress field, increasing it in all directions in the case of high groove fill.

9.8 CHAPTER SUMMARY

This chapter has determined the stress field induced in an elastomer O-ring under various operational environments and groove dimensions. The data generated is now used as initial conditions for the void inflation model discussed in the next chapter.

The stress field can also be used to draw conclusions regarding the orientation of cracks formed in the seal during decompression.

CHAPTER 10 - VOID INFLATION MODELLING

10.1 INTRODUCTION

During depressurisation, the voids that are inherent to the material are subject to an internal pressure increase owing to the pressure differential created between the seal interior and the ambient. The void is inflated by this pressure increase until a critical stress is reached in the void wall, after which fracture will initiate. If the pressure inside the void is not large enough to cause fracture, the void will inflate and then deflate as the gas diffuses out of the void wall.

The void inflation model is used to determine the size and shape of voids expanded due to gas pressure. From the deformation of the void, the maximum wall stress can be determined. The maximum wall stress can then be compared with the strength of the material to determine if failure will take place. The prediction of the rate of void growth is dependent on many factors, including: -

- rate of depressurisation
- elastic properties of the elastomer matrix
- gas transport properties
- initial size of void or rigid inclusion
- surrounding voids and rigid inclusions
- temperature effects

The model consists of two parts. The first is a model of void inflation without the effect of compressive stress field. This enables the void to inflate freely and uniformly, with no constraints. The second model includes the effects of compressive stress field to determine the influence on wall stress and the shape of the expanded void. Obviously, failure can initiate from other sources such as surfaces of weakness or badly bonded filler particles,

but the inherent voids are thought to be the primary cause of failure. The extent of crack growth after initiation is subject to many factors that will not be considered in this chapter.

The stress field near a rigid inclusion may cause premature failure of an elastomeric material subject to large deformations under decompression conditions. The stress field also affects the rate of growth of a void. The shape of the void growth will also be affected by the stress distribution, which could promote a non-uniform wall stress and therefore premature failure.

The probability of an occurrence of failure is dependent on the quantity and density of voids and inclusions and also the physical properties of the elastomer.

10.2 THE VOID INFLATION MODEL

The purpose of the void inflation model is to determine under what conditions the void will rupture. The void will inflate according to the pressure differential developed, which is in turn affected by the diffusion and temperature dependant properties of the elastomer. The rate of diffusion of gas into or out of the void is dependent on whether another void is within the vicinity and the location of the void in the seal section. If there is another void close by it may act as a sink or a source depending on the pressure gradient produced. This is an important concept as it will affect the rate of growth of the bubble.

As the bubble grows it increases in volume, therefore reducing the pressure within the void. If the diffusion into the bubble is more dominant than the diffusion out of the bubble, the pressure will be increased by the influx of gas. If this diffusion rate is rapid enough, the pressure within the void as it expands can be assumed to be constant.

The model of transient diffusion into an expanding void under instantaneous decompression shows that the time taken for the system to reach equilibrium is very rapid

and the void will therefore maintain an approximate constant pressure during inflation. The available pressure for longer decompression times depends on the temperature and decompression rate, see Chapter 8.

The transient gas diffusion modelling showed that the maximum pressure differential formed during depressurisation is at the end of the decompression period. If the decompression is instantaneous, the available pressure differential equals the system pressure. If the decompression is linear over a set time period, the concentration and therefore the pressure profiles formed in the seal reach a maximum at the end of the decompression period.

The radial strain in the void is assumed to be equal to the strain in the wall of the void. Figure 10.1 shows a void inflated from initial radius r_1 to r_2.

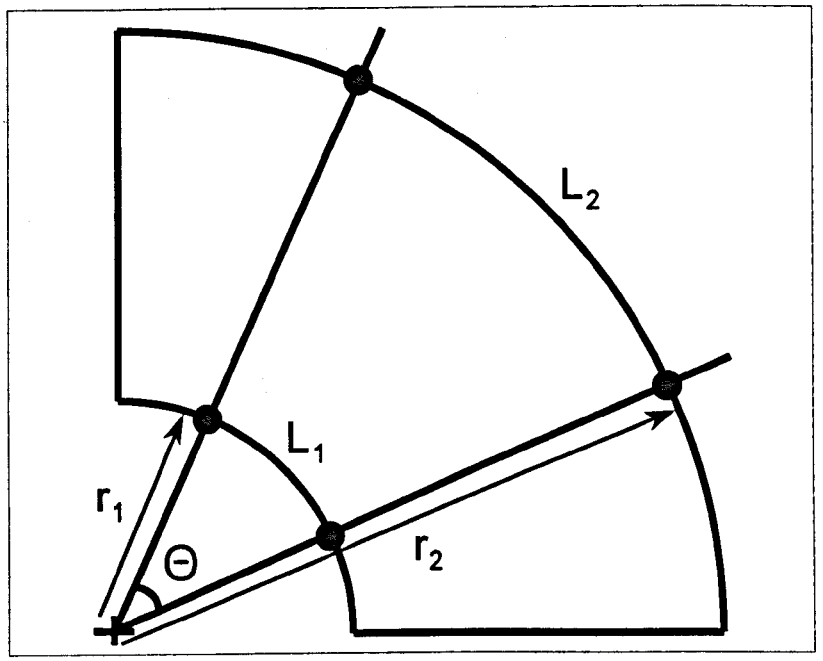

Figure 10.1 - Relationship between radius and arc length in an expanded void

If we take two arbitrary points on the initial void wall at angle θ_1 apart, the arc length will be L_1. The corresponding arc length of the expanded void is given by L_2. The lengths of the two arcs are given by

$$L_1 = r_1\theta \quad ; \quad L_2 = r_2\theta \qquad (10.2.1)$$

If we take the ratio of the arc lengths, L_2/L_1

$$\frac{L_2}{L_1} = \frac{r_2\theta}{r_1\theta} \qquad (10.2.2)$$

Cancelling the angle θ, the ratio of arc lengths is equal to the ratio of radii. Therefore, the two measures of strain are proportional.

There were some assumptions made when developing the void inflation model, these are as follows: -

- The initial shape of the void is assumed to be spherical
- Void internal gas pressure is assumed to be constant due to the rapid inward diffusion of gas (see Chapter 8)
- No variation of physical properties across the seal section
- Initial void size is a worst case of 40μm in diameter
- The compressive stress field is applied at a distance of 0.2mm from the void
- The effects of other voids in close proximity are not included in the model
- No swelling due to liquid uptake occurs in the vicinity of the void

8.2.1 Void inflation model without compressive constraints

The model consists of one quadrant of a spherical void modelled axisymmetrically. The mesh used to model the void expansion is a fine mesh of reduced integration, hyperelastic, linear continuum elements. Figure 10.2 shows the model definition.

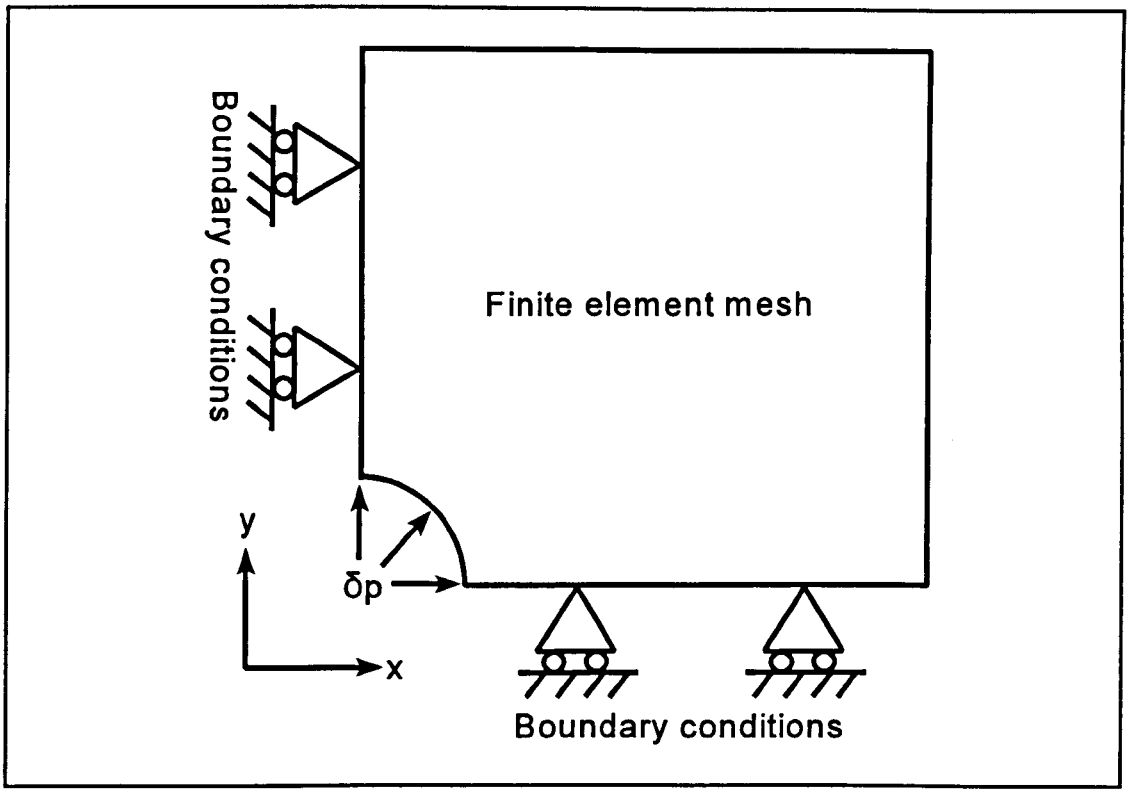

Figure 10.2 - Void Inflation Model Definition Without Compressive Constraints

The pressure is applied to the surfaces of the void elements. This is applied in steps up to the maximum available pressure differential calculated from the transient gas diffusion model. The steps are applied as ramp functions. The gas pressure is assumed to be a constant value as the rate of diffusion into the void is dominant over the outward diffusion rate (see diffusion model).

The boundary conditions that are applied to the model are used to simulate as closely as possible what occurs during void inflation and to restrict rigid body motion in free space. The boundary condition on the left-hand side of the model allows this face to move freely in the y-direction but restricts motion in the x and z directions in addition to all rotational degrees of freedom. The boundary condition applied to the bottom face of the model allows free movement in the x direction with all other degrees of freedom constrained.

The model uses nonlinear geometry definitions and a nonlinear material model. The material model used is the second order form of the polynomial strain energy function (see section 2.3).

The materials constants are calculated from material test data as entered in the finite element input file. The software fits the polynomial strain energy function by varying the two constants to give a best fit for a combination of the uniaxial and biaxial test data. The Mooney-Rivlin formulation is used as the strain magnitudes in the void inflation model are likely to exceed 100% by a considerable amount. Therefore, a higher order polynomial function is required.

10.2.2 Void inflation model with compressive constraints

Initially, the model was carried out without considering the effects of the local stress field. This is to ensure that the model would behave as expected. The void should inflate uniformly with an equal stress distribution in the void wall.

Once the behaviour of the model was established, the effects of local stress field were included. The magnitude of the local stress was determined from the global stress field model. The model resulted in x and y direct stresses at various locations within the seal (figure 10.4). These stresses are applied to the void inflation model to determine how the void expands in reality (see Figure 10.3)

Consider the condition of stress within an elastomer seal during decompression. The maximum compressive stress occurs when the seal is installed in the groove and the pressure is applied. Due to the elastomer incompressibility assumption used in the model, the seal transmits the hydrostatic pressure to the counterfaces of the housing, therefore increasing the overall stress levels.

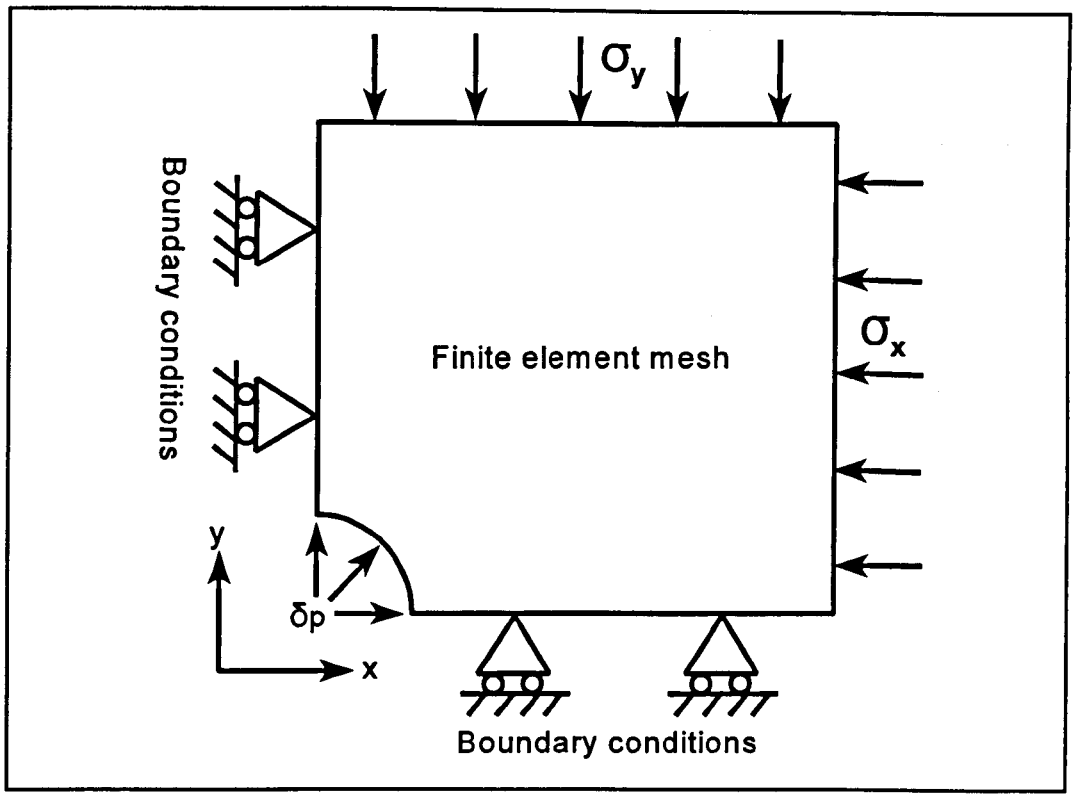

Figure 10.3 - Finite element void inflation model definition with compressive constraints

During decompression, the pressure is reduced over the decompression time period. At the end of the decompression period the stress field is the same as the stress field under installation compression only, assuming no significant swelling has occurred.

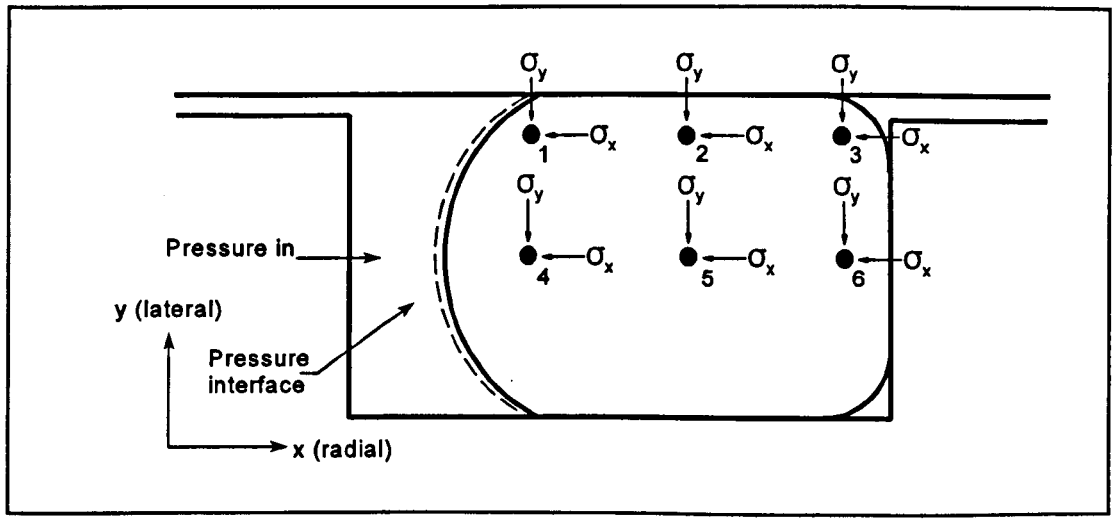

Figure 10.4 - Void Inflation Model with Compressive Constraints Analysis Locations

The worst condition for a void in an elastomer seal under decompression is when the available pressure differential is a maximum and the surrounding compressive stress field is a minimum, which occurs at the end of the decompression period. This will enable the void to expand with limited resistance from compressive constraints. Another worst case condition is when the x and y compressive stresses applied are very different. This will allow the void to expand into an elliptical shape and introduce non-uniform wall stress distributions. This will magnify the stress at one point on the void wall and cause premature fracture.

The void inflation model with compressive constraints is therefore carried out with the compressive stresses taken from the initial compression model. The maximum pressure differential available for void expansion is determined from the transient gas diffusion model. Taking both initial conditions, it is possible to determine the wall stress vs applied pressure differential plot for individual cases. From the plot, the probability of fracture initiation can be determined by comparing the wall stress values with the physical strength of the elastomer in biaxial extension.

The void inflation model is used for each analysis point, in each of the three materials and for each of the test environments. This results in 108 separate analyses to determine the wall stress under each condition.

For the purposes of modelling, only the worst case is considered. During void inflation the volume of the seal is increased and there is a tendency for the seal to fill the groove. This increases the overall stress field in the seal section to σ_{exp}. Therefore, the compressive stress field applied to the void inflation model is applied as a linear increase with increasing pressure differential from σ_c to σ_{exp}. Figure 10.5 shows the compressive stress field increase from stress at compression only, to stress after gross volumetric expansion. Equations (10.2.3) and (10.2.4) show how the compressive stress field is applied to the finite element model.

$$\sigma_x = \sigma_{cx} + \left[\frac{\delta p}{\delta p_{max}} \cdot \left(\sigma_{expx} - \sigma_{cx} \right) \right] \qquad (10.2.3)$$

$$\sigma_y = \sigma_{cy} + \left[\frac{\delta p}{\delta p_{max}} \cdot \left(\sigma_{expy} - \sigma_{cy} \right) \right] \qquad (10.2.4)$$

Where $\sigma_{x,y}$ is the total compressive stress in the x (radial) and y (lateral) directions, $\sigma_{cx,y}$ is the compression only stress value, $\sigma_{expx,y}$ is the compressive stress with gross volumetric expansion, δp is the applied intermediate pressure differential and δp_{max} is the maximum applied pressure differential.

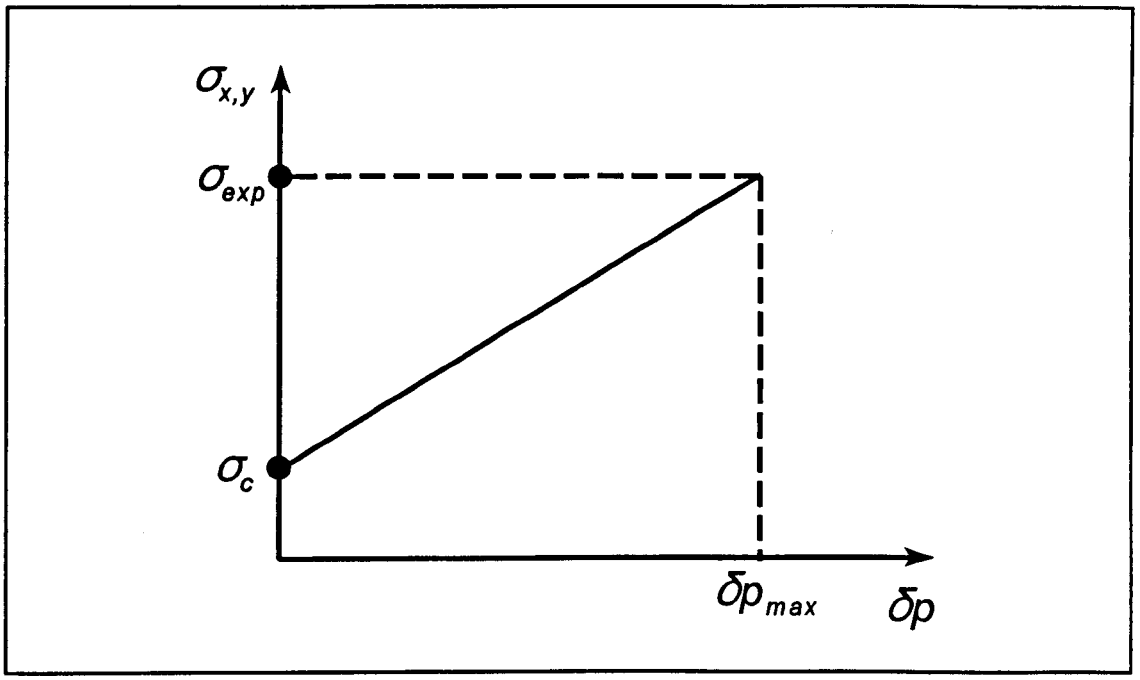

Figure 10.5 - Linear increase of compressive stress field with increase in pressure differential

Sometimes, the pressure differential exceeds a critical value and the model becomes unstable as the element deformation is too large. When this is the case, the model achieves an actual pressure that is then extrapolated to the higher pressure. The resulting stress values are then also extrapolated. This was proven to be valid by modelling a case where

the system is stable. The first four data points were taken from this solution and extrapolated to the final pressure value. The extrapolation was then compared with the actual model prediction and was found to be accurate. This is shown in Figure 10.6.

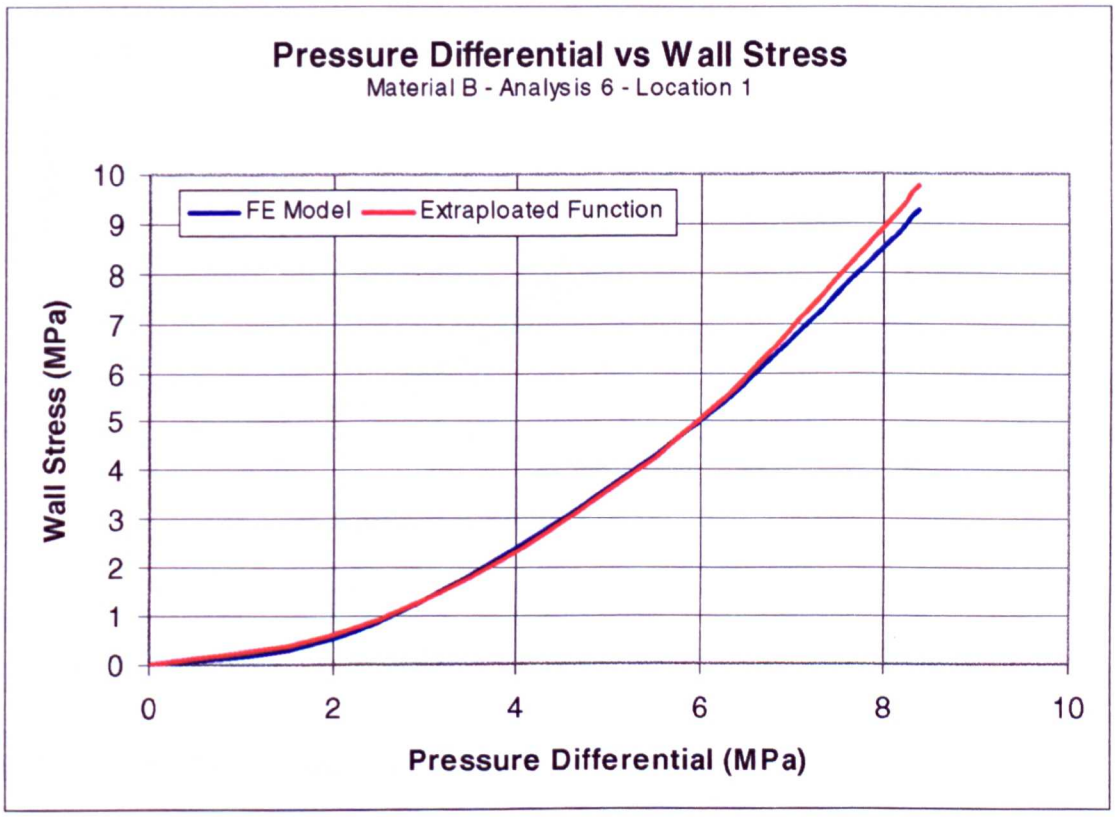

Figure 10.6 - Comparison of FE Model and Extrapolated Prediction

10.3 ANALYSIS RESULTS

10.3.1 Void inflation model with no compressive constraints

Figure 10.7 shows the relationship between applied pressure and maximum wall stress in the void. This analysis is carried out for each material (A, B, and C) using 100°C material data only to establish the general trends.

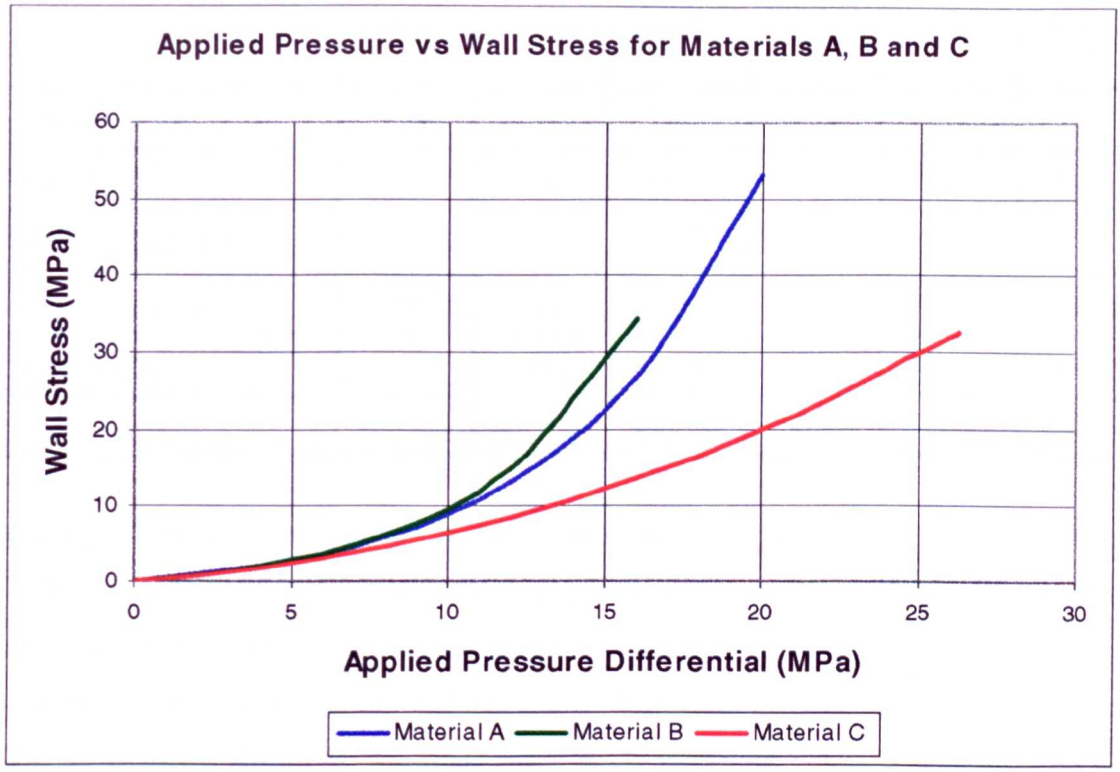

Figure 10.7 - Applied Pressure vs Maximum Wall Stress for Materials A,B and C

10.3.2 Void inflation model with compressive constraints

The void inflation analyses were carried out to match the decompression testing programme to validate the results. The programme of analyses is shown in Table 10.1.

Table 10.1 - Void inflation model analysis matrix

Analysis Parameter	Analysis Number					
	1	2	4	5	6	7
Compression	15%	15%	25%	25%	15%	15%
Groove fill	70%	70%	70%	90%	70%	90%
Section diameter (mm)	5.33	10.0	5.33	10.0	10.0	5.33
Decompression time	2 hours	Instant	Instant	2 hours	2 hours	Instant
Temperature	100°C	150°C	100°C	150°C	100°C	150°C
Pressure	100 bar	400 bar	500 bar	100 bar	100 bar	500 bar

Figure 10.8 shows a typical finite element model output. The figure shows the direct stress in the x (radial) direction for material B under a pressure differential of 93 bar. The analysis was carried out at location 3 with 15% initial compression and 70% groove fill. The areas coloured red indicate high tensile stresses and the blue areas indicate compressive stresses. The model clearly shows the deformed shape of the void to be elliptical in nature with the maximum wall stress occurring at the top of the void.

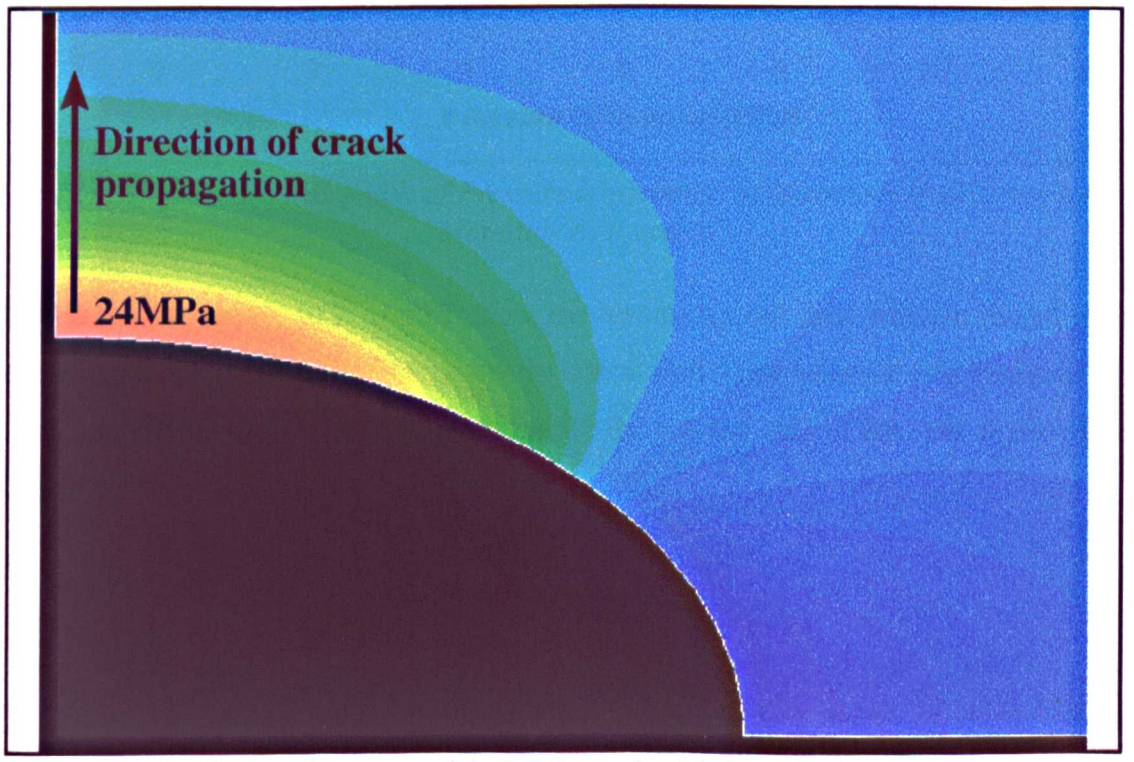

Figure 10.8 - Finite element model of deformed void showing direct stress contours

Figure 10.9 shows a typical output graph from the void inflation model showing pressure differential vs maximum wall stress for three materials. The results show that the relationship between applied pressure differential is a second order polynomial (quadratic). The results indicate that the more elastic the material, the more pronounced the rapid increase in wall stress with increase pressure differential.

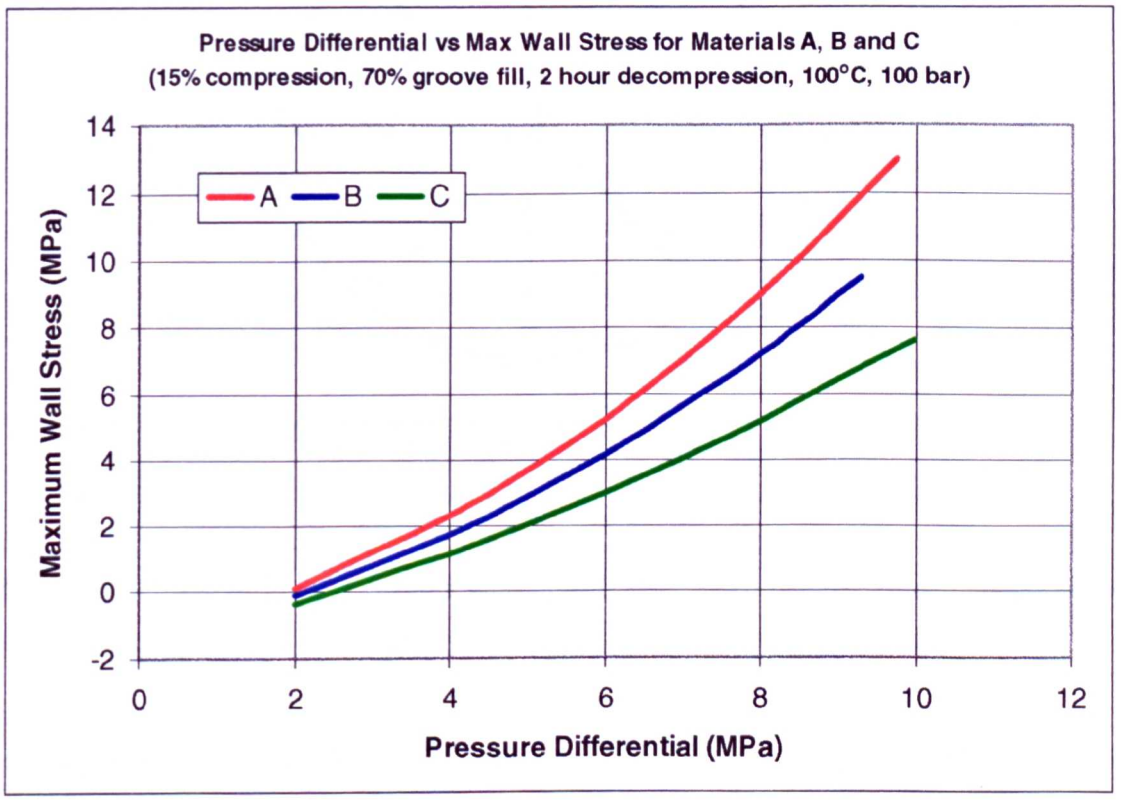

Figure 10.9 - Typical graph of Pressure Differential vs Maximum Wall Stress for Materials A, B and C

The following tables 10.2 to 10.7 show the results for the void inflation model with compressive constraints. The tables show the critical wall stress values at two positions for each analysis location. The two positions are the top and side of the void as shown in Figure 10.10.

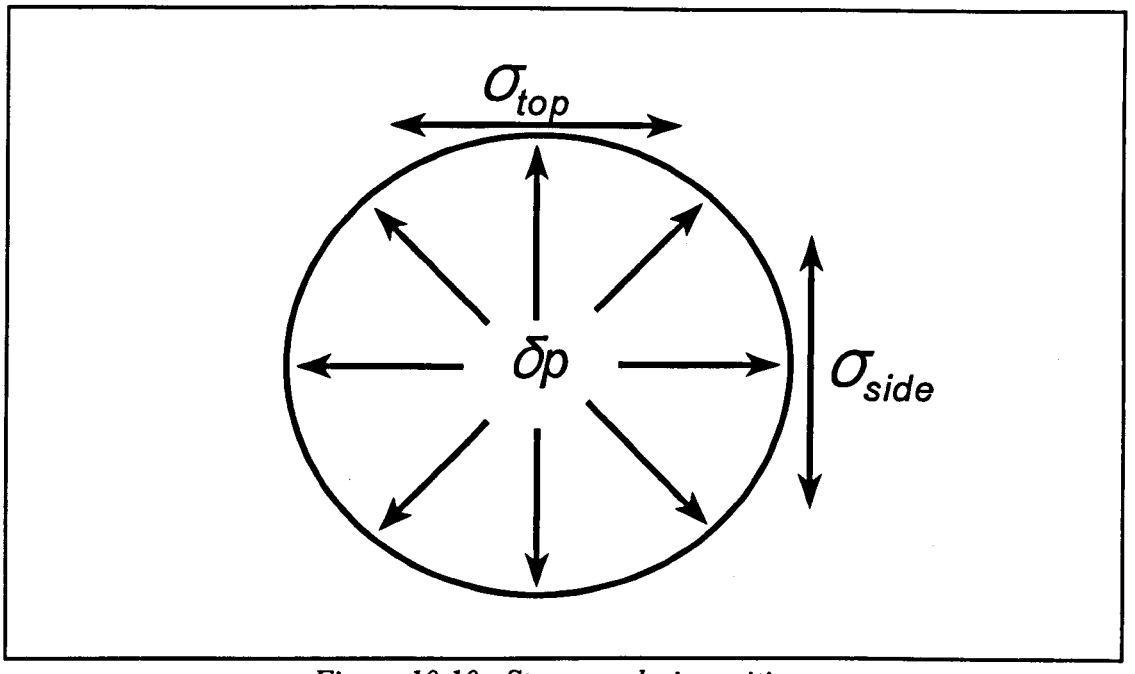

Figure 10.10 - Stress analysis positions

Figure 10.11 shows the growth of a void in four stages. The increased wall stress at the top of the void can be clearly seen as the void inflates to the elliptical form.

The results tables show the actual pressure differential and the value achieved by the model. If the desired pressure differential is not reached by the model, extrapolated wall stress values are given. Note that 'u.t.e' denotes 'unable to extrapolate'. There was no need to model analysis case 5 as the compressive stress field is much higher than the available pressure differential. Therefore, the pressure within the void cannot overcome the compressive constraints and the void will not inflate.

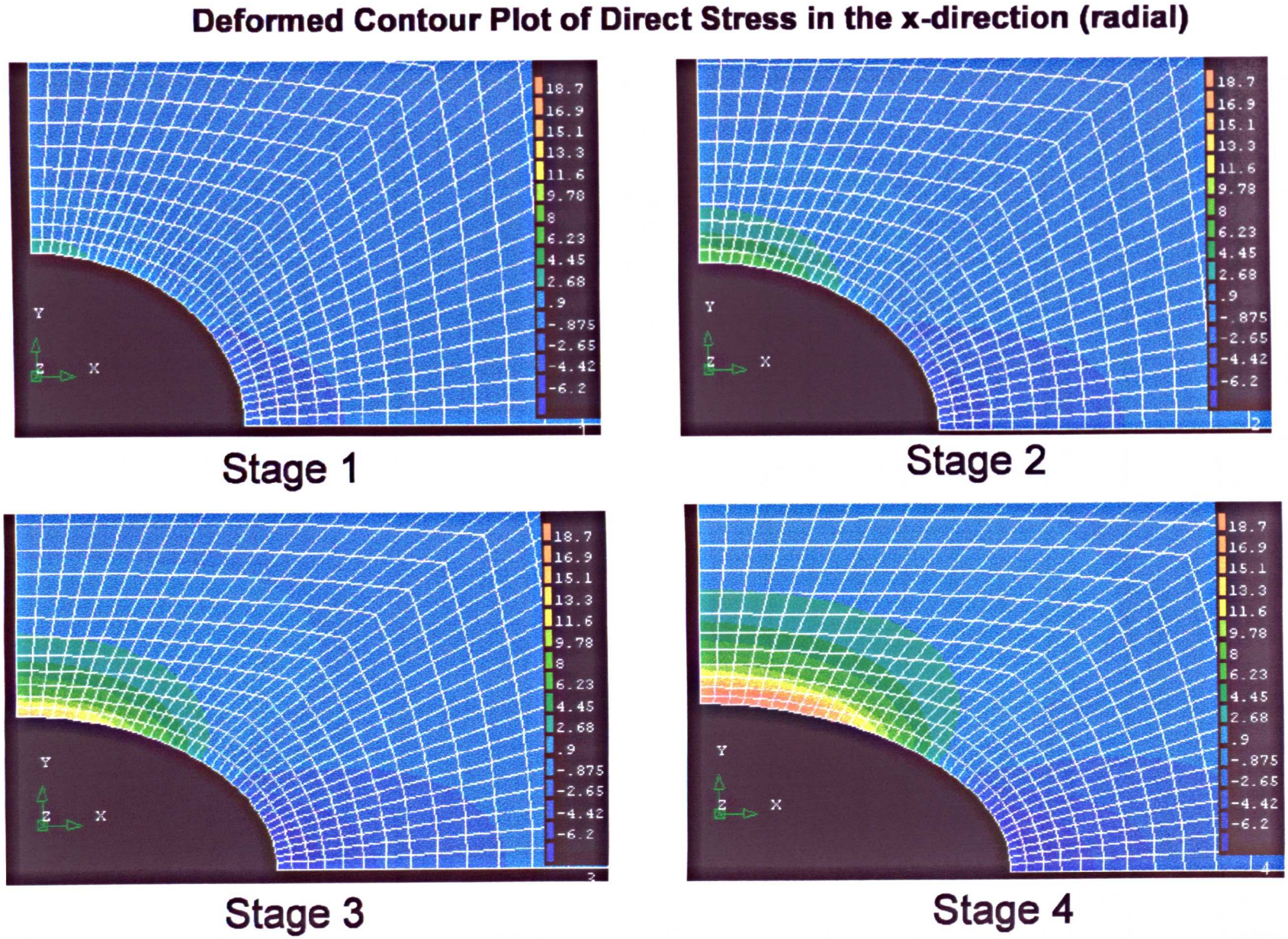

Figure 10.11 - Growth of void at analysis location 5 - analysis number 1

Table 10.2 - Analysis 1 *(All units in MPa)*

Compression = 15%	*Section diameter = 5.33mm*	*Pressure = 100 bar*
Groove fill = 70%	*Decompression time = 2 hours*	*Temperature = 100°C*

Material A *Biaxial strength = 22.7MPa*

Analysis Point	δp	δp achieved	σ_{top} achieved	σ_{side} achieved	σ_{top} extrapolated	σ_{side} extrapolated	FAIL?
1	6.15	6.15	7.1	1.2	-	-	No
2	8.90	8.90	8.7	-15.1	-	-	No
3	9.75	9.75	13.0	-0.1	-	-	No
4	6.15	6.15	5.2	5.3	-	-	No
5	8.90	8.90	24.2	-9.3	-	-	Yes
6	9.75	9.75	5.5	-9.6	-	-	No

Material B *Biaxial strength = 15.9MPa*

1	5.15	5.15	3.8	-0.9	-	-	No
2	8.05	8.05	6.3	-10.0	-	-	No
3	9.30	9.30	9.5	-1.1	-	-	No
4	5.15	5.15	3.7	4.0	-	-	No
5	8.05	7.90	17.5	-4.8	18.0	-4.6	Yes
6	9.30	9.30	-6.2	3.5	-	-	No

Material C *Biaxial strength = 27.3MPa*

1	9.14	9.14	14.1	-2.1	-	-	No
2	9.98	9.98	12.2	-16.1	-	-	No
3	10.00	10.00	7.6	4.6	-	-	No
4	9.14	9.14	8.6	8.4	-	-	No
5	9.98	9.98	27.0	-10.1	-	-	No
6	10.00	10.00	-9.7	5.2	-	-	No

Table 10.3 - Analysis 2 *(All units in MPa)*

Compression = 15%	*Section diameter = 10mm*	*Pressure = 400 bar*
Groove fill = 70%	*Decompression time = instantaneous*	*Temperature = 150°C*

Material A *Biaxial strength = 14.9MPa*

Analysis Point	δp	δp achieved	σ_{top} achieved	σ_{side} achieved	σ_{top} extrapolated	σ_{side} extrapolated	FAIL?
1	40	14.0	24.7	22.7	183	216	Yes
2	40	14.0	24.7	-0.5	166	u.t.e	Yes
3	40	13.4	25.0	12.3	198	u.t.e	Yes
4	40	14.5	26.5	27.0	147	209	Yes
5	40	9.8	29.2	-1.9	2000+	u.t.e	Yes
6	40	15.1	8.7	20.0	176	140	Yes

Material B *Biaxial strength = 10.3MPa*

1	40	11.1	11.1	9.4	96	u.t.e	Yes
2	40	10.2	13.0	-11.8	102	75	Yes
3	40	10.6	15.4	2.5	192	114	Yes
4	40	10.7	11.2	11.4	113	130	Yes
5	40	5.2	18.0	-12.2	u.t.e	u.t.e	Yes
6	40	9.9	-2.5	6.1	63	67	Yes

Material C *Biaxial strength = 19.1MPa*

1	40	16.0	22.9	16.0	155	117	Yes
2	40	16.0	21.5	-5.7	137	u.t.e	Yes
3	40	16.0	22.6	9.5	154	85	Yes
4	40	16.0	23.2	22.7	144	152	Yes
5	40	12.0	27.1	-4.1	u.t.e	u.t.e	Yes
6	40	22.0	13.3	32.2	61	150	Yes

Table 10.4 - Analysis 4 *(All units in MPa)*

Compression = 25%	*Section diameter = 5.33mm*	*Pressure = 500 bar*
Groove fill = 70%	*Decompression time = instantaneous*	*Temperature = 100°C*

Material A *Biaxial strength = 22.7MPa*

Analysis Point	δp	δp achieved	σ_{top} achieved	σ_{side} achieved	σ_{top} extrapolated	σ_{side} extrapolated	FAIL?
1	50	13.8	23.7	5.7	230	u.t.e	Yes
2	50	9.9	10.8	-26.6	163	-261	Yes
3	50	10.3	16.9	-18.9	226	-116	Yes
4	50	13.9	22.9	22.8	268	305	Yes
5	50	5.8	21.2	-15.4	672	u.t.e	Yes
6	50	15.8	-2.1	13.6	90	160	Yes

Material B *Biaxial strength = 15.9MPa*

1	50	10.7	14.3	-0.3	157	155	Yes
2	50	13.3	11.9	-11.1	165	u.t.e	Yes
3	50	11.5	14.0	-8.6	167	66	Yes
4	50	11.5	12.7	13.8	190	195	Yes
5	50	7.1	18.1	-6.7	426	u.t.e	Yes
6	50	12.5	-6.1	5.2	69	111	Yes

Material C *Biaxial strength = 27.3MPa*

1	50	14.0	23.0	0.5	104	98	Yes
2	50	17.2	20.0	-5.8	160	u.t.e	Yes
3	50	16.1	20.8	-0.9	123	98	Yes
4	50	17.0	18.5	19.8	101	102	Yes
5	50	9.2	29.5	-13.0	u.t.e	u.t.e	Yes
6	50	18.5	-4.0	10.2	59	77	Yes

Table 10.5 - Analysis 5 *(All units in MPa)*

Compression = 25%	*Section diameter = 10mm*	*Pressure = 100 bar*
Groove fill = 90%	*Decompression time = 2 hours*	*Temperature = 150°C*

Material A *Biaxial strength = 14.9MPa*

Analysis Point	δp	δp achieved	σ_{top} achieved	σ_{side} achieved	σ_{top} extrapolated	σ_{side} extrapolated	FAIL?
1	5.35	-	No analysis required				No
2	8.23	-	No analysis required				No
3	9.37	-	No analysis required				No
4	5.35	-	No analysis required				No
5	8.23	-	No analysis required				No
6	9.37	-	No analysis required				No

Material B *Biaxial strength = 10.3MPa*

1	6.20	-	No analysis required	No
2	8.90	-	No analysis required	No
3	9.90	-	No analysis required	No
4	6.20	-	No analysis required	No
5	8.90	-	No analysis required	No
6	9.90	-	No analysis required	No

Material C *Biaxial strength = 19.1MPa*

1	<10	-	No analysis required	No
2	<10	-	No analysis required	No
3	<10	-	No analysis required	No
4	<10	-	No analysis required	No
5	<10	-	No analysis required	No
6	<10	-	No analysis required	No

Table 10.6 - Analysis 6 *(All units in MPa)*

Compression = 15%	*Section diameter = 10mm*	*Pressure = 100 bar*
Groove fill = 70%	*Decompression time = 2 hours*	*Temperature = 100°C*

Material A *Biaxial strength = 22.7MPa*

Analysis Point	δp	δp achieved	σ_{top} achieved	σ_{side} achieved	σ_{top} extrapolated	σ_{side} extrapolated	FAIL?
1	8.38	8.38	9.3	3.5	-	-	No
2	9.88	9.88	10.2	-16.6	-	-	No
3	10.00	10.00	15.1	-3.3	-	-	No
4	8.38	8.38	9.3	9.3	-	-	No
5	9.88	9.26	28.1	-10.5	31.6	u.t.e	Yes
6	10.00	10.00	-7.0	6.0	-	-	No

Material B *Biaxial strength = 15.9MPa*

1	7.45	7.45	7.6	1.0	-	-	No
2	9.60	9.60	8.3	-9.2	-	-	No
3	9.95	9.95	11.7	-0.4	-	-	No
4	7.45	7.45	6.8	7.3	-	-	No
5	9.60	7.34	18.2	-6.3	25.8	u.t.e	Yes
6	9.95	9.95	-5.7	4.1	-	-	No

Material C *Biaxial strength = 27.3MPa*

1	9.14	9.14	10.4	2.4	-	-	No
2	9.98	9.98	11.9	-19.3	-	-	No
3	10.00	10.00	14.6	-4.6	-	-	No
4	9.14	9.14	8.9	8.3	-	-	No
5	9.98	9.00	29.7	-15.0	u.t.e	u.t.e	Yes
6	10.00	10.00	-9.6	5.0	-	-	No

Table 10.7 - Analysis 7 *(All units in MPa)*

Compression = 15%	*Section diameter = 5.33mm*	*Pressure = 500 bar*
Groove fill = 90%	*Decompression time = instantaneous*	*Temperature = 150°C*

Material A *Biaxial strength = 14.9MPa*

Analysis Point	δp	δp achieved	σ_{top} achieved	σ_{side} achieved	σ_{top} extrapolated	σ_{side} extrapolated	FAIL?
1	50	15.8	23.1	14.2	256	251	Yes
2	50	18.3	20.3	-1.9	194	u.t.e	Yes
3	50	16.0	24.5	13.2	266	254	Yes
4	50	16.9	-1.9	15.7	u.t.e	147	Yes
5	50	13.6	25.1	1.4	124	-45	Yes
6	50	8.0	-9.7	2.9	u.t.e	131	Yes

Material B *Biaxial strength = 10.3MPa*

1	50	13.0	12.5	2.4	188	104	Yes
2	50	15.5	7.1	-12.9	85	31	Yes
3	50	12.6	13.2	0.8	203	97	Yes
4	50	11.6	-10.0	2.5	7	37	Yes
5	50	10.2	28.1	-8.2	432	65	Yes
6	50	9.7	-11.9	2.2	u.t.e	14	Yes

Material C *Biaxial strength = 19.1MPa*

1	50	18	20.6	9.5	109	102	Yes
2	50	18	15.6	-10.4	111	16	Yes
3	50	18	20.5	8.0	113	100	Yes
4	50	18	-6.8	19.8	35	165	Yes
5	50	16	22.5	-1.5	u.t.e	75	Yes
6	50	18	-11.9	17.2	3	159	Yes

10.4 DISCUSSION

Voids, which are inherent to the elastomer, are thought to be the primary cause of failure initiations within seals subject to rapid decompressions. There are other possible sources of damage initiation such as surfaces of weakness and the presence of rigid inclusions. The void inflation model studies the effects of pressure differential on the growth of the void, initially with no compressive constraints. The void inflation model with compressive constraints replicates the actual conditions seen by a void within an elastomer seal compressed in a groove.

The model without compressive constraints is a location independent analysis which shows that the void inflates in a uniform manner as expected. The rate of growth of the void with an increase in pressure differential accelerates. The previous modelling approach taken by Gent states that the radius of the void tends to infinity at a pressure differential of 5E/6, where E is the small strain elastic modulus of the elastomer.

The results of the finite element model show that there is a tendency towards the Gent model, but the acceleration is less pronounced and does not tend off towards infinity. The Gent model assumes that the strains are small and linear and does not take into account the geometric and material non-linearities of the system. The small strain elastic modulus is effectively the slope of the stress-strain curve at up to 20% strain. At failure, the strain can be in the region of λ=3, at which point the slope of the stress-strain curve can be very different. The results show that the more elastic the elastomer (i.e. the softer materials), the more closely the curve follows Gent's model.

The void inflation model with compressive constraints is a location dependant analysis includes the effect of the stress field within the seal section. The inflation of the voids causes gross volumetric expansion in the seal. The void inflation model simulates this effect by linearly increasing the compressive stress field from the compression only value to the stress field after volumetric expansion.

From the O-ring stress field model there is clearly a significant difference between the radial and lateral direct stress values. This causes a non-uniform strain and therefore stress in the void wall. The void typically inflates to an elliptical form. In general the displaced form is as shown in Figure 10.12.

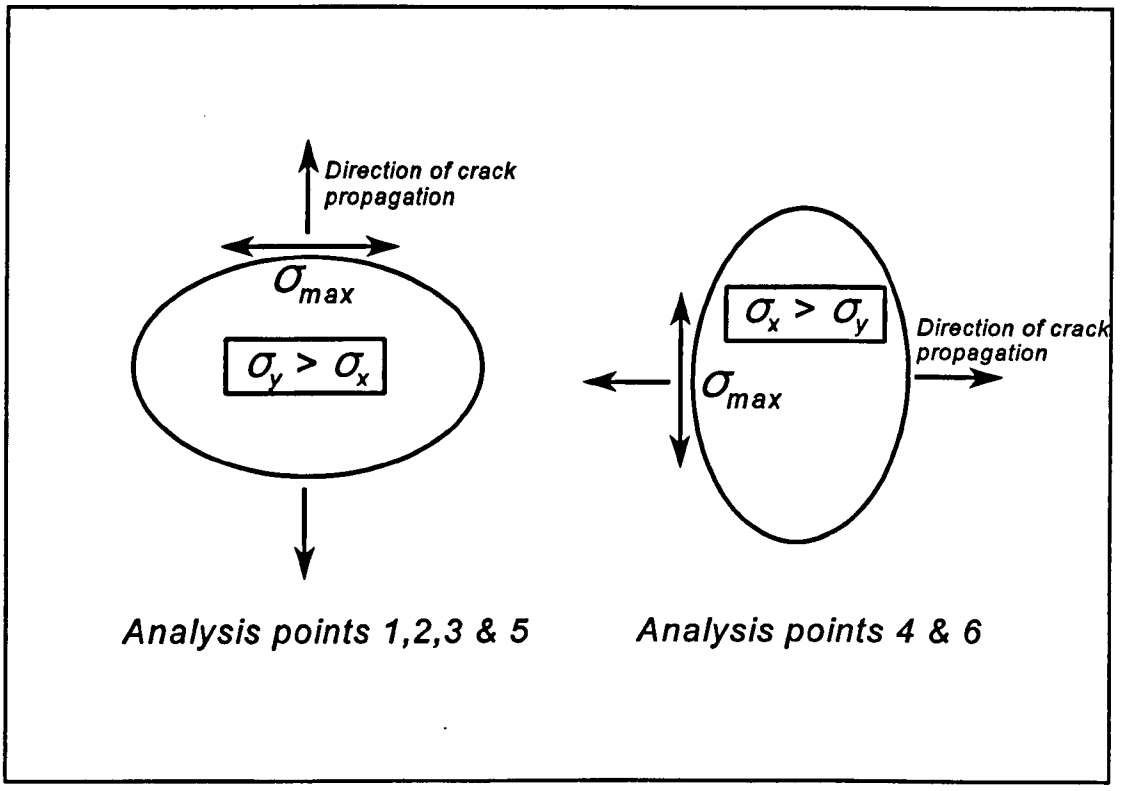

Figure 10.12 - Deformed shape of inflated void under compressive constraints

For analysis points 1, 2, 3 and 5, the compressive stress in the y-direction (lateral) is greater than the stress in the x-direction (radial). In some cases the radial stress is tensile. For analysis points 4 and 6, the opposite is the case. The maximum tensile wall stress occurs in the direction of minimum stress field. Therefore the crack will initiate and then propagate in the direction shown in Figure 10.12. Therefore, in general, the expected crack patterns are shown in Figure 10.13.

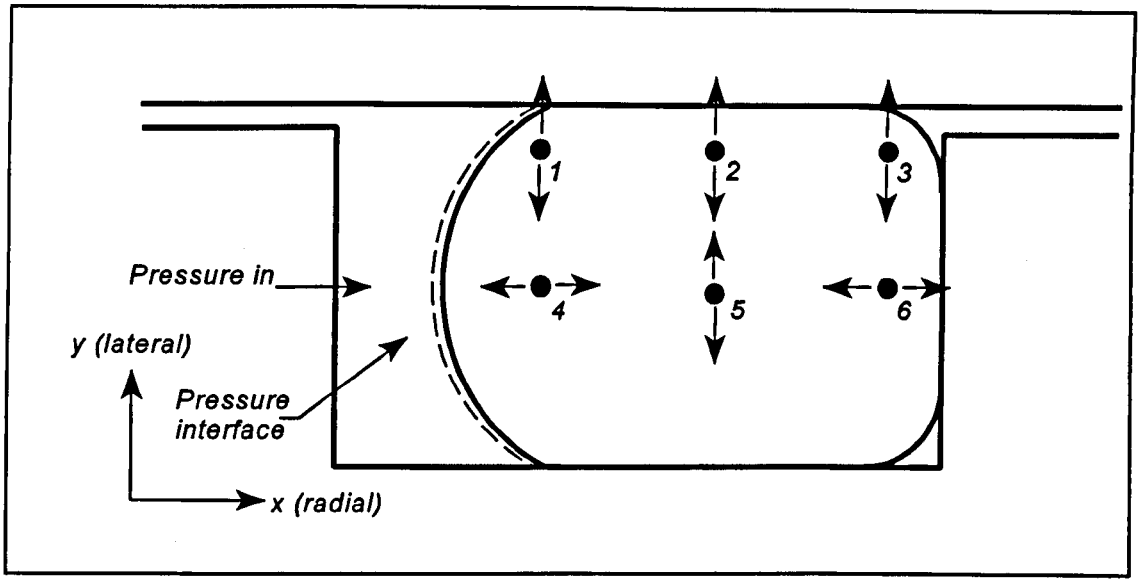

Figure 10.13 - Expected crack patterns within a standard groove configuration

The analysis of the resulting pressure differential vs void wall stress curves show a second order polynomial (quadratic) relationship as a function of the pressure differential of the form: -

$$\sigma_w = C_1(\delta p)^2 + C_2(\delta p) + C_3 \qquad (10.4.1)$$

where σ_w is the wall stress, δp is the pressure differential and $C_{1,2,3}$ are constants.

The shape of the inflated void not only depends on the magnitude of the stress field, but also the difference between the lateral and radial values. This difference effectively determines the shape function of the ellipse and therefore the stress concentration that causes crack initiation. The worst case condition is where difference between σ_x and σ_y is the greatest. This usually occurs at analysis point 5 where σ_y is compressive and σ_x is tensile.

After initiation the crack will start to propagate through the seal section if sufficient energy is available. Once the crack initiates from the void wall, the stress condition relaxes and there must be sufficient energy in the system to continue the crack propagation. This has

not been considered in this model as it would make the solution too complex. The crack propagation model could be incorporated into the overall modelling methodology to predict not only crack initiations, but the extent of damage.

The model makes some assumptions that are necessary to determine the relationship between pressure differential and void wall stress. The model assumes that there is a void present at the analysis point. Obviously this will not always be the case, but from studies of void location it seems that there is a high probability that a void will be present. If the model were to be further developed, the probability of a void being present could be included to add a statistical approach to the solution.

From the transient gas diffusion model it was shown that during void expansion, the rate of gas diffusion into the void is rapid. As the void expands, its volume increases, therefore reducing the pressure within the void. The rate of gas diffusion into the void is rapid. Therefore, the pressure within the void will remain approximately constant. The void inflation model assumes that this is the case.

The model assumes that there are no other voids in the proximity of the void under analysis. The voids in the model are assumed to be equally spaced on a square matrix for simplicity. However, in reality the voids can be clustered together and may cause coalescence during inflation. The rate of diffusion into and out of the void will also be affected by neighbouring voids, depending on their size.

The void inflation model also assumes that the void size is a worst case of 40μm diameter at a distance of 0.2mm from the next void in the square matrix. The void is assumed to be spherical. Most of the voids discovered during the void and rigid inclusion analyses were near-spherical in nature. Only a small minority were different shapes, some of which had sharp edges. Further work in this field could consider the effects of different shaped voids and rigid inclusions.

The solution of the void inflation at higher pressures uses an extrapolation of the solution at lower pressures. However, it is not clear that this principle applies at higher pressures. It is not known how the elastomer behaves at the higher strains and pressures. Therefore, the solution is only approximate. It must be noted that the elastomer has usually failed before this high pressure has been achieved.

The resulting wall stress from the model is compared with the biaxial strength of the elastomer to determine if failure takes place. It must be remembered that the strength of elastomers is inherently variable and may be ±20-30% of the nominal value. Therefore if the final wall stress calculated by the model falls within the range of biaxial strengths, the probability must be considered a marginal case.

10.4.1 Model validation

The results of the modelling methodology have been compared with the results of the decompression testing programme for validation. The methodology results in three predictions. These are: -

- Damage
- No damage
- Marginal case

The decompression testing results can be formed into a probability of a crack occurrence. The following table compares the results of the model with the tests. The percentage value used in the table for the tests gives the percentage of samples where cracks were found.

Table 10.8 - Model validation

Test Number	MATERIAL					
	A		B		C	
	Test	Model	Test	Model	Test	Model
1	0%	Marginal	17%	Marginal	0%	No damage
2	100%	Damage	100%	Damage	100%	Damage
4	42%	Damage	75%	Damage	100%	Damage
5	0%	No damage	13%	No damage	50%	No damage
6	19%	Marginal	25%	Marginal	50%	Damage
7	100%	Damage	0%	Damage	0%	Damage

In general, the model predicts the occurrence of damage relatively accurately. The results for analysis 5 give ambiguous results, as the cracks formed in the tests are thought to be due to stress cracking. The initial compression for this test was 25% and the groove fill was 90%. To prove this, a void inflation model was produced with no applied pressure differential. The stress field from this analysis was applied to the model and it was found that the biaxial strength of the material was exceeded, even without the pressure differential.

Test number 7 is the case of 15% compression and 90% groove fill. The model predicts that failure will occur in all materials. However, the test results show that no damage occurred in materials B and C. It is thought that the estimate of 11% gross volumetric expansion has been underestimated and the actual stress field formed is much higher. This will inhibit the growth of the voids and therefore reduce damage. The manufacturer of material B has stated that it is particularly prone to swelling which would add to the overall stress field.

Including the effects of stress cracking in test 5, the model predicts correctly in 14 out of the 18 analyses. This translates to an accuracy of 78%. If the effects of test 5 are not

considered, the accuracy increases to 13 out of 15 analyses, which translates to 87% accuracy.

The model also accurately predicted the locations of cracks within the seal section. In general, the predictions of cracks initiating at the centre of the specimen and propagating in the lateral direction were confirmed by the decompression testing. In some cases, the radial cracks at locations 4 and 6 were observed, which also matches the model prediction.

The decompression testing results showed that the vast majority of cracks were formed at the centre. The model predicts that cracks will form at more locations in the seal. The model assumes that the voids and their locations are considered independently. In practice, the seal will fail at the worst case location (the centre) and the remainder of the seal will relax when failure occurs. In the worst cases of decompression (i.e. high pressure, rapid decompression), the cracks are observed to be formed throughout the section in the orientations predicted by the model.

Obviously, no firm conclusions can be drawn regarding the accuracy of the modelling methodology at this stage. Further tests and analyses would be required to include a range of variables to validate the model fully. However, the initial results suggest that the model performs well, predicting the initiation of cracks and their orientations.

10.5 CONCLUSIONS

The results of the void inflation model clearly show that cracks are likely to form perpendicular to the direction of pressure application at analysis points 1, 2, 3 and 5. The cracks are formed in-line with the pressure at points 4 and 6. The reason for orientation of the cracks is the nature of the stress field induced during installation of the O-ring. The difference between the radial and lateral stress field values are important as these determine the shape function of the expanded void.

The voids are inflated into an elliptical form due to the localised stress field. The causes stress concentrations in the void wall which could cause premature failure. If the void is free to expand with no compressive constraints, failure can occur at any point in the void wall. Therefore, the crack orientations would be more random.

The results show that the relationship between the applied pressure differential and the void wall stress is a quadratic function. The model includes the effects of material and geometric non-linearity to establish the behaviour of the elastomer at high strains. To model the higher strains seen at high pressure, the solution is extrapolated to the desired pressure differential.

The comparison of the model output with the decompression testing results show that the model predicts crack initiations accurately.

10.6 CHAPTER SUMMARY

A void inflation model has been developed that determines the maximum wall stress in an inflating void under various operational conditions. This wall stress is compared directly with the biaxial strength of the elastomer to determine failure.

The finite element method is used to determine failure, including the effects of stress field induced by installation of the O-ring and gross volumetric expansion seen during decompression.

CHAPTER 11 - DISCUSSION

11.1 THE NEW MODEL

This research was driven by a need in the oil and gas industry to predict when failure will occur to reduce maintenance down times and gaseous emissions. This would result in considerable cost savings, estimated at hundreds of thousands of pounds per annum.

As a result of the work described in this thesis, the oil and gas industry can now predict with some confidence the performance of elastomer sealing systems subject to rapid decompression. The modelling methodology can be used to predict the effects of various parameters including seal and housing geometries. This will have a significant impact on the oil and gas industry as it can confidently predict the onset of damage and therefore reduce maintenance down times and leakage.

Through this methodology, industry can evaluate the performance of seals supplied by manufacturers. The manufacturers will then have to respond by improving the performance of their seals by improved sealing system design, quality and compounding. The improvement can take place as this research has clearly identified the controlling parameters for failure.

The modelling methodology can be used to evaluate the performance of existing sealing systems or to aid the development of new systems. For example, an operator could evaluate the safe decompression time for a system such that no damage occurs or a manufacturer could make recommendations regarding sealing system design.

The results of the model are to be incorporated into a user-friendly software interface to predict explosive decompression in elastomer seals. This is currently under development and will be used in the oil and gas industry as a predictive tool. The tool will be based on

the results of the current research and will be developed as more information and data from the model are made available.

If the new modelling methodology developed during this programme were not available to industry the probability of failure occurrences would continue to rise as elastomer seals are being pushed into more aggressive environments and critical applications. This could have significant implications for safety issues and gaseous emissions. The nuclear power generation industry has attempted to reduce explosive decompression damage for many years and this tool will assist in the reduction of radioactive emissions through improved system design and safety.

The work has demonstrated the reliability of the model for the decompression conditions studied during this research programme. However, before it is adopted in industry as a predictive tool, more validation is required. Based on the results of this research, industry has expressed an interest in developing the model further.

This research could stimulate interest from standards organisations for the specification of elastomer seals in explosive decompression sensitive applications. If the modelling methodology results in a fully validated predictive tool, the standards organisations might take up this method as a quality control procedure. If this method is adopted, industry could be forced to conform to the standards to continue to use and manufacture elastomer seals for this type of application.

The solution to the problem involved reducing a difficult problem to a series of less complex elements and combining them to form a prediction methodology. The modelling methodology was developed to predict the occurrence of cracks within elastomer seals subject to real operational conditions using materials that are commonly used for these highly sensitive applications.

The new modelling methodology can be applied to any elastomer sealing system. The geometry of the seal and housing can be easily modified and the data can be generated for any operational condition. The principles of the model can also be applied to other applications such as the prediction of collapse of lined pipelines. Metal pipes are commonly lined with a polyethylene liner to reduce corrosion. The gas in the pipeline eventually diffuses through the liner and pressure builds up at the annulus between the liner and the pipe. If the pipeline is rapidly decompressed, the pressure differential causes the liner to collapse. The pipe can become blocked and the liner ceases to function as an anti-corrosion aid.

Another application of the research is the prediction of explosive decompression failure in flexible joints for sub-sea pipelines. These joints are used to take up the angular movement of the pipeline due to movement of the topside processing equipment. This is achieved by using a rubber cylinder reinforced with metal layers. Gas diffuses into the elastomer and causes significant cracking when the system is decompressed. The volume of rubber in a flex-joint is much more than that of a seal, so the problem is further emphasised. Future research will involve the development of a model to predict damage in flexible joints.

11.2 FAILURE ASPECTS

The research programme started by gaining a thorough understanding of the explosive decompression failure mode and elastomer material behaviour from the open literature. It was noted from this study that previous research focussed on materials, pressures and temperatures that are not used in practical applications. The mechanisms of failure had been researched and reasonably well understood. However, each mechanism was considered as separate functions, without giving any consideration of how they interact with each other. One author, Briscoe, discussed how the different parameters would interact, but did not attempt to model the interaction.

The literature also does not give any physical property data for the materials of interest. All analytical models used to predict the pressure differential at which failure occurs assumes linear material models using a small strain elastic modulus, which is effectively irrelevant at higher strains. The models also do not consider the effects of decompression time, seal constraints or how damage affects the seal's integrity. Various other parameters such as seal section size, initial compression, groove fill and the size and quantity of inherent voids and rigid inclusions were not considered in the open literature.

It was clear from the literature that the previous approaches did not consider the sealing system as a whole. The studies did not use high enough pressures and temperatures that would be of interest to industry. The literature showed that the failure mode is extremely complex, but it was thought that primary variables existed which controlled the failure process. This is where the development of the prediction model started. The solution procedure involved the identification of the primary controlling variables through studying the failure process and previous test results. The primary controlling variables were then applied to a modelling methodology that reduces the complex failure mode to a series of more simplistic models.

The modelling programme involved the development of a methodology that would predict the initiation of cracks within elastomer seals due to various decompression regimes. It was thought that attempting to model the extent of damage by modelling the crack propagation would be too ambitious for a project of this size. Therefore, only crack initiations are modelled. Crack propagations are important as they will determine the extent of damage within the seal. The extent of damage will affect the overall structural integrity of the seal and therefore the probability of leakage. This is an area of particular interest to industry as it will determine whether safety regulations are breached and whether gaseous emissions have occurred. The definition of seal failure and leakage is difficult to define. In general, if the contact stress between the seal and the counterface falls below the system pressure, leakage may occur. Extensive cracking could reduce this contact stress by relieving the stress field. However, the additional effort required to

model crack propagations would not be justified as the seal user would require zero crack damage. Any cracking in the seal section would be undesirable and therefore crack propagation modelling could not be justified.

The primary factors that are responsible for the development of cracks were considered in detail. The primary factors which cause failures are the available pressure differential, the stress field and the presence of voids. Each of the primary factors have secondary variables that also affect the probability of failure.

The final output of the methodology is the maximum void wall stress. This is compared directly with the biaxial tensile strength of the elastomer to determine whether damage will occur. Figure 1.1 shows the inputs and outputs for each model and how they interact with each other.

The methodology uses the worst case scenario for failure prediction. The worst case for an elastomer seal under decompression conditions is at the end of the decompression period. The available pressure differential is a maximum and the compressive stress field is a minimum. This allows the void to expand freely. The stress field is increased during the void inflation stage as the seal undergoes gross volumetric expansion and the seal is pushed into the groove.

11.3 THE EFFECTS OF DIFFUSION

The model to determine the rate of inward diffusion of gas into a void is based on a thermal diffusivity analogy. The model is based on the finite element method and determines the change in concentration as the void expands, and therefore the concentration gradient surrounding a void. This initiates gas diffusion into the void until equilibrium conditions exist. The model determines the time for the pressure within the void to reach 90% of the original pressure. This time was relatively short. Therefore, the pressure within the void can be assumed to be constant. If this process was not as rapid,

the model would have to include a time dependant element to vary the void internal pressure.

Seal section diameter had an impact on the pressure differential formed within the seal section. The gas has a greater distance to diffuse out of the seal in a larger section. In many applications where explosive decompression is a problem, the seal section could easily be reduced if the equipment was designed with the problem in mind. However, equipment is designed and the seals are specified afterwards, rather than being an integral part of the design process. The results of this research will be made available to equipment manufacturers with the aim of reducing the seal sections used in critical applications.

The model assumes that the seal section is fully saturated with gas. If the seal section is only partially saturated, the available pressure differential at the analysis locations will be different. This could be the case if the seal has only been installed for a short period of time. Many systems in the oil and gas industry are pressurised for a considerable period of time before decompression takes place, therefore this assumption is valid. However, some applications such as compressor seals, may only be partially saturated, therefore the initial conditions of this model would have to change.

The decompression profile is assumed to be linear over the decompression period. In practice, when systems are decompressed, the reduction in pressure usually follows an exponential curve with time. However, as the maximum pressure differential is formed at the end of the decompression period and this is the worst case, the manner in which the system decompresses is irrelevant. Only if the system were partially decompressed would this be of interest. Some systems in the oil and gas industry are partially decompressed and would therefore require a revised decompression regime in the model.

The model assumes that the only surface available for gas diffusion out of the seal is the pressure interface. This interface is the surface available after 15% compression of the seal. Obviously, for cases when the initial compression is 25%, the available surface for

outward gas diffusion is smaller. Other degassing surfaces such as the low pressure side surface are relatively small and can be considered insignificant. When the initial compression is increased to 25%, the available surface is reduced resulting in a slower diffusion of gas from the seal section. This would cause the pressure differential in the seal section to be higher. Most applications use a compression of approximately 15%. The 25% tests and analyses were used to determine the effects of higher compression.

Industry can use this method to evaluate operational procedures and schedule maintenance. The method can be used to determine the safe decompression time of the system if the pressure differential at which damage occurs is known. The rate at which the pressure system is decompressed can be incorporated into the operating procedure to ensure that no damage takes place. The analysis was carried out at various temperatures, pressures and decompression periods with materials of differing section size. The decompression periods were linear over 2, 24 and 48 hours. Although the void inflation model and decompression testing studies only instantaneous and two hour linear decompressions, the transient gas diffusion model included the longer decompression regimes.

11.4 STRESS FIELD

The O-ring stress field model determines the stress field due to initial compression and gross volumetric expansion. The data from this model are used as initial conditions for the void inflation model.

The difference between the x (radial) and y (lateral) stress values at the analysis locations were considerable. The difference determines the shape function of the void as it inflates. The magnitude of the stress is also important as it resists the applied pressure differential, therefore inhibiting void inflation. The difference between the radial and lateral stress values could be reduced by changing the seal and housing geometries. If a back-up ring arrangement was used with a curved surface, the contact stresses would be more evenly distributed through the section as the seal would almost maintain near circular shape. This

would reduce the tendency for the voids to inflate to an elliptical form and cause stress concentrations. The back-up rings would also increase groove fill that has been shown to inhibit crack formation. This suggested arrangement is shown schematically in Figure 11.1.

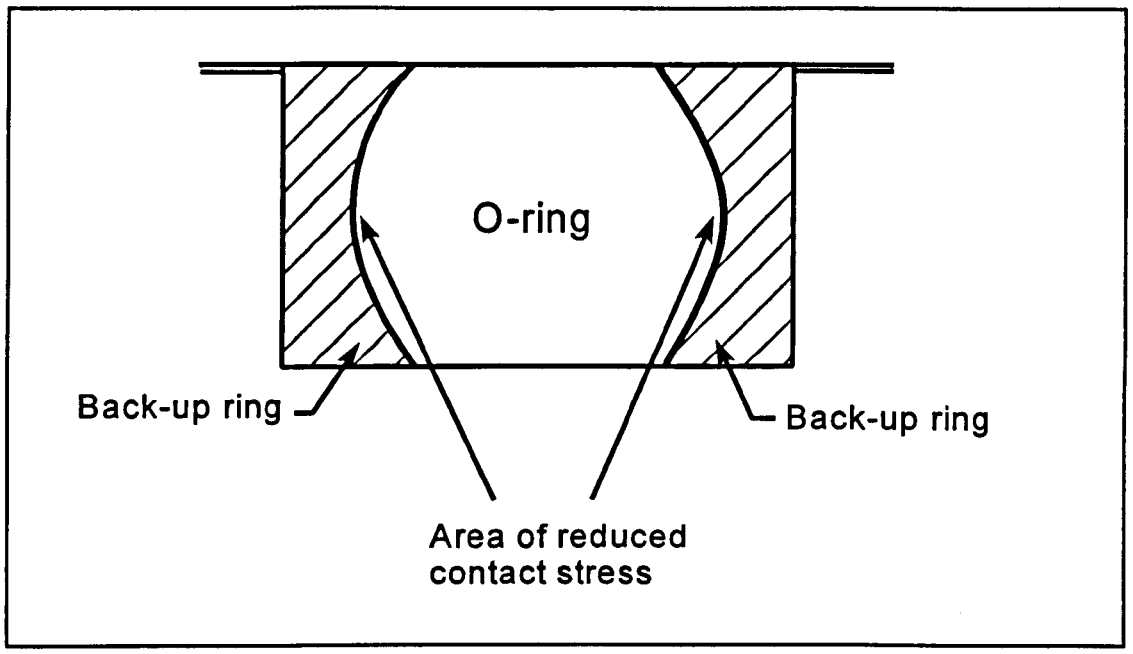

Figure 11.1 - Proposed groove design with back-up rings

The magnitude of the gross volumetric expansion was estimated based on the void and rigid inclusion analysis. However, this value could be easily underestimated as there are many smaller voids present in the elastomer that could not be detected. The submicroscopic voids that are present in the seal will also inflate and cause volumetric expansion.

The effect of friction was considered in the stress field model. However, in practice, the friction could be extremely variable depending on the lubrication used and the period of time before installation. The lubricant is dissolved into the surface of the elastomer after a period of time and this could affect the stress field formed during decompression. The type of lubricant used during installation is extremely variable and could have a significant impact on the performance of the seal. The lubricant could affect the physical properties

as well as friction and requires further investigation.

11.5 VOID INFLATION

The results show that the void wall stress accelerates with increasing pressure differential, the rate depending on the compressive stress field. In all cases, the curve is quadratic in nature. The values of the constants in the quadratic equation depend on all of the parameters previously considered in the transient gas diffusion model and the O-ring stress field model. Therefore, determining the values of these constants theoretically is extremely difficult. It would be of interest to establish relationships between the variables that would calculate the values of the constants in the quadratic equation, but this is a complex problem and would require considerable effort.

There are some limitations with the void inflation model. The model assumes that there is a void present at the analysis location. This may not be the case and a probability model would have to be introduced to the methodology to consider this. The void and rigid inclusion analysis showed that, at the analysis locations in the seal section, a void was nearly always present.

It is assumed that there are no other voids in the immediate vicinity of the void under analysis. Obviously, the presence of other voids would affect the gas diffusion and the surrounding stress field. The voids considered in this model were a worst case of 40μm diameter and spherical in nature. The void sizes could be different introducing surface tension effects. The shape of the void could be different, possibly with sharp corners that would introduce stress raisers and therefore cause premature failure.

An interesting hypothesis is that if the voids were distributed evenly through the seal section, equally spaced and near the same size, the expansion of the voids could conceivably cancel each other out. Many structures in industry and nature are honeycomb type structures and balance the stresses upon loading. A possibility for further work could

be to carry out tests and analyses to determine if this is the case.

The critical wall stress in the void from the model is compared with the biaxial strength of the elastomer. This will determine whether crack initiations will occur. It must be noted that the strength of the elastomer is inherently variable and if the critical wall stress falls within the range of tensile strengths, the probability of failure must be considered marginal.

The comparison between the void wall stress and the biaxial strength of the elastomer may be a source of error in the prediction. The deformation modes are different because of the thickness of the test membrane compared with the material surrounding a void. The membrane is relatively thin, and the thickness reduces during the inflation test. The thickness of elastomer surrounding an expanding void can be assumed to be infinitely thick. Therefore, a direct comparison cannot be made.

Using the modelling methodology in reverse, the pressure differential at which failure occurs can be determined from the curve of pressure differential vs void wall stress. This can be compared with the decompression time versus maximum pressure differential curve to determine the safe decompression time.

The research programme included many tests used to determine the input properties required for the model and to validate the results. This involved the design and development of specialist test facilities as the necessary equipment was not available on the commercial market.

The importance of the presence of voids and rigid inclusions in elastomer seals has been shown in this study to be a critical factor in the explosive decompression failure process. Without these defects it would be near impossible for failure to occur because there would be no initiation points for cracks. There are currently no data available regarding the nature of defects in elastomers and this study provided the information required to model

explosive decompression failure.

In general, analysis of void locations showed that the highest density of voids usually occurred near the centre of the seal section. This may be due to the curing process used during manufacture. During cure, gases are released by the material that can diffuse out of the bulk more easily if the molecules are nearer the surface. The distribution of rigid inclusions is more random. The elastomer seal manufacturing process has been studied in some detail and recommendations regarding the reduction of voids and rigid inclusions were supplied to the manufacturer. However, most of the recommendations cannot be released due to commercial confidentiality. One suggestion for the reduction of voids would be to cure the O-ring in a vacuum. This would create a pressure differential during curing and draw out the trapped gases, therefore reducing the void content.

Observations from the decompression testing show that most cracks initiate at the centre of the specimen. Although the model predicts that this is the worst-case location in relation to the stress field, the void and rigid inclusion analysis shows there is also a higher density of voids at the centre of the seal.

In summary, it is clear from the analysis that the observations of voids and rigid inclusions correlate well with the observations made during the decompression testing and in industry. If industry can concentrate on reducing the size and number of voids and rigid inclusions within elastomer seals, the problem of explosive decompression can be greatly reduced. However, the costs involved in manufacturing seals in a clean environment with additional quality control procedures would cause the cost of explosive decompression resistant seals to rise considerably. Elastomer seals are often the most critical component in a pressure driven system and therefore require significant thought when designing equipment. However, industry in general considers elastomer seals to be cheap components that are virtually negligible when compared with the cost of the equipment and would therefore not be responsive to a considerable price increase.

11.6 OTHER FACTORS AFFECTING FAILURE

Industry can use the gas transport test facility to generate the necessary data to model any polymeric gas transport activity. It can be used for the development of ageing models for polymers that are dependent on the concentration of gas diffusing through the material versus time and the temperature.

The permeation testing facility is unique in that simple elastomer sheet samples are used. There is one other testing facility known of that can measure permeation at high pressures and temperatures, but this requires the provision of specially bonded samples. These samples can be costly and cannot sometimes be manufactured due to the metal bonding process. The permeation testing facility can be used for other applications such as determining the permeation rate for polyethylene lined steel pipes. The rig can be easily adapted to measure the properties of polymer sheets.

The variables used during the decompression testing were standard, but including back-up rings to determine their effect on decompression resistance would be interesting.

There are a number of limitations to the present model and test programmes that need to be addressed in more detail. However, they are not thought to affect the solution of the problem significantly. Other possible failure modes in the elastomer seal during decompression have been identified as surfaces of weakness and the presence of rigid inclusions. Surfaces of weakness are said to exist within the elastomer structure that, when subjected to large deformations, cause cracks to initiate. During gross volumetric expansion, the elastomer is deformed around rigid inclusions that are inherent to the material. It is thought that the rigid inclusions act as stress raisers and cause cracking.

During the research programme several simple models of rigid inclusions were produced. During decompression the primary deformation direction is radial. Therefore, for a rigid inclusion that is not bonded to the elastomer matrix, the maximum tensile stress occurs at

the top and bottom of the elastomer surrounding the inclusion. Therefore the elastomer will fail in much the same mode as the inflated void, with the cracks forming perpendicular to the direction of applied pressure (see Figure 11.2).

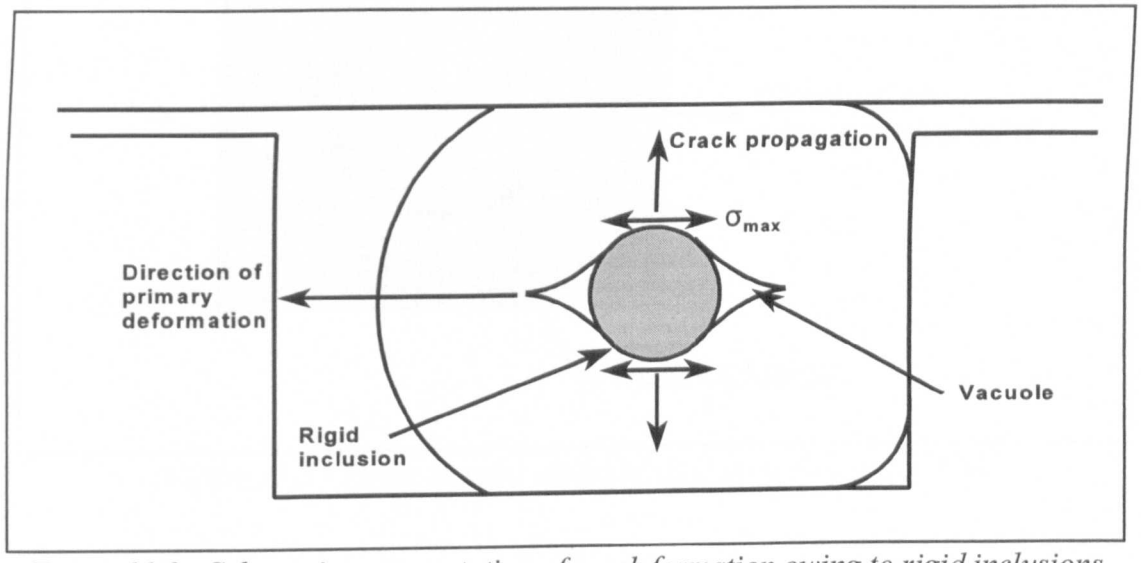

Figure 11.2 - Schematic representation of crack formation owing to rigid inclusions

If the rigid inclusion is not firmly bonded to the elastomer, detachment may occur and vacuoles may also be formed. These vacuoles will act in much the same way as an inflating void. The finite element model of the rigid inclusion stress field is shown in Figure 11.3 and clearly shows the region of high tensile stress at the contact surface.

The results of this research programme are limited in that the study concentrated on certain elastomers subjected to methane gas pressure. Obviously, other gases and elastomers would perform very differently under decompression conditions. However, the fundamental principles can be applied to any sealing system.

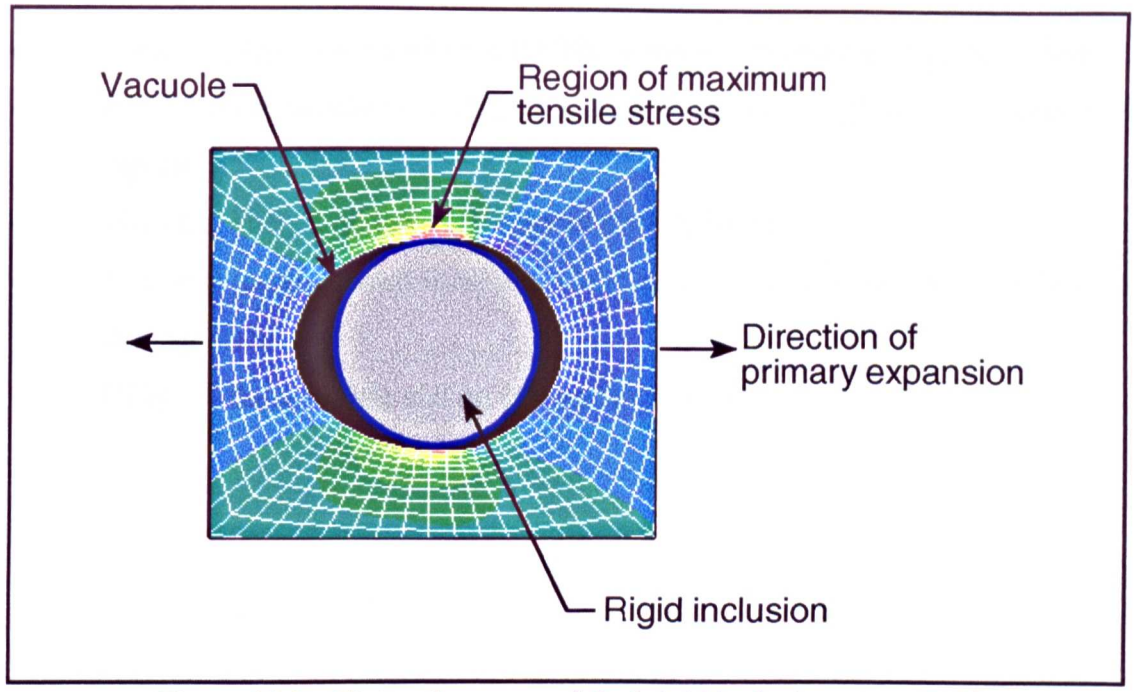

Figure 11.3 - Finite element model of rigid inclusion stress field

The knowledge gained during this research programme can be summarised to produce a series of general recommendations to seal users and manufacturers to reduce the probability of damage due to explosive decompression. The recommendations are given below and if as many as possible are used in the development of a sealing system, explosive decompression damage will be limited.

As a result of this investigation the following recommendations can be made:

- Decompress the system as slowly as possible, based on model outputs
- Use a small section seal if possible
- The groove should be designed with the lowest compression practically possible
- The groove should be designed with high groove fill
- The elastomer should have a low void and rigid inclusion content
- Use back-up rings or a formed groove to reduce stress concentrations
- The elastomer should have a high physical strength
- The elastomer should have a high elongation to break

- Select an elastomer with low solubility to inhibit the amount of gas absorbed
- Choose an elastomer with a high diffusion coefficient to allow gas to diffuse out rapidly during decompression
- Use elastomers with low variability of physical properties
- Use only recommended installation lubricants and install carefully, ensuring no damage occurs
- Consider the complete sealing system, not only the elastomer seal

CHAPTER 12 - CONCLUSIONS

This research has provided a quantitative approach to the prediction of explosive decompression damage in elastomer seals that was not previously available. The research programme has developed a methodology to model the failure process and predict the onset of damage. The model considers the sealing system as a whole, including the effects of material behaviour, seal section and groove design. The need to understand and predict explosive decompression damage in elastomer seals has become very important to the oil and gas and nuclear power generation industries.

The modelling methodology is currently being translated into a user-friendly software tool to predict damage. The tool will be used by industry to predict damage occurrences, determine safe decompression times and aid the development of new materials.

Any elastomer sealing system can be evaluated using the modelling methodology to determine whether explosive decompression damage will take place. This includes differences in seal section shape and size, housing design and materials.

Crack damage due to explosive decompression is critically dependent on the presence of voids and rigid inclusions in the elastomer seal. The presence of these defects has been characterised in terms of shape, size and location. In general, larger section seals contained larger voids. These defects are introduced in the manufacturing process and recommendations have been given about how to reduce their presence.

The void inflation model predicts that cracks will occur preferentially at the centre of the seal section and propagate in the lateral direction. When the pressure differential is high, the model predicts damage at all locations within the seal. Analysis points 1, 2, 3 and 5 form cracks perpendicular to the direction of applied pressure (lateral), whereas analysis points 4 and 6 generally form radial cracks.

The decompression testing programme showed that most cracks initiate from the centre of the section and propagate in a direction perpendicular to the direction of pressure application. Larger section seals were found to be less resistant to damage. Increasing the groove fill reduced the level of damage within the seals tested.

The new model has excellent prediction capabilities. Comparing the results of the decompression tests and the modelling methodology shows an 87% accuracy on occurrence of cracks. The location and orientation of cracks were also correctly predicted by the model.

The analysis showed that the maximum pressure differential always occurs at the end of the decompression period and at the outer radius of the seal section. Decompression time was shown to have a significant impact on the pressure differential available to cause void expansion. The temperature of the system reduces the overall pressure differential formed within the seal section, but also reduces the physical strength of the elastomer.

The worst case condition for an elastomer O-ring under decompression occurs at the end of the decompression period when the pressure differential is highest and the compressive stress field is a minimum. This gives maximum driving force for void inflation with minimum resistance from the compressive stress field.

The location in a seal section where failure takes place is also determined by the stress field. The worst case location is the centre where the stress in the y-direction (lateral) is compressive and the stress in the x-direction (radial) is tensile. The stress field significantly affects the formation of cracks as it determines the shape function of an inflating void. The stress field for each material was evaluated for initial compression and after gross volumetric expansion.

Cracks form perpendicular to the pressure application direction because voids inflate to an elliptical form under applied pressure differential and stress field constraints. This has

been shown by the void inflation model.

Crack initiations occur at a critical void wall stress generated by the pressure differential. The relationship between applied pressure differential and void wall stress was found to be quadratic function. The constants of the quadratic equation depend on the seal geometry, material, constraint and operational conditions and are therefore difficult to predict. The constants can be found from the modelling methodology.

High initial compression and groove fill reduces the damage caused by explosive decompression by increasing the stress field. If the compressive stress field surrounding a void is greater than the applied pressure differential, the void cannot inflate. However, high initial compression and groove fill can cause stress cracking due to high strains. An ideal case would be low initial compression (15%) and high groove fill (90%).

The rate of inward diffusion of gas into an inflating void is very rapid and therefore the pressure differential can be considered constant. This was determined by developing a transient gas diffusion model of an inflating void.

Gas transport activity has a significant effect on decompression damage. The rate of diffusion of gas out of the seal section during decompression will determine the available pressure differential for void inflation. To determine the gas transport activity a permeation testing facility has been developed to determine the solubility, diffusion and permeation characteristics of unique gas-elastomer combinations. The test facility has been developed for ease of use and requires only the standard sheet form of the elastomer.

The quality control statistical analysis showed that the physical properties of elastomers are extremely variable, which significantly affects the performance of an elastomer seal in marginal cases.

The research has identified areas that require further study such crack initiations near rigid inclusions, the effects of material variability, and factors affecting crack propagation, which will determine the overall integrity of the seal.

CHAPTER 13 - FURTHER WORK

The testing programme and the modelling methodology developed as part of the research has determined the damage occurrences in elastomer seals due to explosive decompression. However, some areas require further investigation to understand their contribution to the damage process. The areas identified for further work have been identified as follows.

13.1 MATERIAL VARIABILITY

The physical properties of elastomers are inherently variable and can cause errors in prediction. The effects of material variability would be a significant advance on the current model. The effect of the use of the maximum or minimum stress-strain curve for the finite element models may affect the model output. Also, the variation in tensile strengths of the elastomers has to be considered.

13.2 THE EFFECT OF GEOMETRY

The current study only considers the damage caused in an O-ring arranged in a flange type groove. There are many other arrangements of grooves and seal sections that would affect the resistance of the sealing system to explosive decompression damage. If for example the groove were dovetail shaped, how would this affect the stress field and therefore crack initiations?

Seal sections such as V-rings have more surface area for the gas to diffuse from, therefore possibly reducing the pressure differential within the seal. The inclusion of curved back up rings that support the seal within the groove would distribute the stress field more evenly. This would minimise the difference between the lateral and radial stress values, therefore reducing the tendency for the void to inflate to an ellipse.

13.3 CRACK PROPAGATIONS

The next logical development from this research would be to consider the effects of crack propagations. Currently the model predicts the initiations of cracks. Determining the extent of damage would be desirable and therefore how this affects the seal integrity. The presence of a crack does not necessarily imply that the seal will cause leakage. The modelling of crack propagations due to gas decompression would be extremely complex. The crack propagation is energy driven and the extent of damage would be based on evaluating the energy in the system. The crack may also be driven by gas pressure as gas rapidly diffuses into the crack as it propagates.

13.4 THE EFFECT OF DECOMPRESSION CYCLES

The current model only considers a single decompression. In practice, the seal may be decompressed many times and this may result in a fatigue type failure through continued crack propagations.

13.5 SATURATED MATERIAL PROPERTIES

The material properties used in this model are evaluated with no gas pressure. Previous studies by Davies (1997) showed that the physical strength of elastomers is greatly reduced when saturated with a pressurising medium at temperature. This depends on the gas and the temperature at which the seal is operating, but this could have a significant impact on the stress-strain characteristics of the elastomer. Therefore, a possibility for further work would be to consider the effects of gas pressure on the physical properties of the elastomer.

Ideally, all of the above ideas for further work should be incorporated into the modelling methodology to gain further understanding of the explosive decompression failure process.

REFERENCES

ABAQUS Users Manual. Version 5.6. (1996) *Hibbit, Karlsson & Sorensen Inc.*, Pawtucket, RI, USA.

Andrews, E.H. & Stevenson, A. [1978], **'Fracture Energy of Epoxy Resin under Plane Strain Conditions'**. *J.Mater.Sci*, **13**, 1680.

Assink, R.A. [1974], *J.Polym.Sci.Polym Phys Ed*, **12**, 2281

Austin, R.M. & Nau, B.S. [1974]. **'The Seal Users Handbook'**. *Published BHRA, Fluid Engineering, Cranfield, Bedfordshire, England.*

Becker, A.A., [1997], **'Finite Element Analysis of Geometric Non-Linearities and Contact'**. *University of Nottingham Course Notes.*

Bowns, D.E., Ballard, R.L. & Starling, J.E. [1975], **'Measurement of Seal Friction in Pneumatic Actuators Using an On-line Digital Computer'**. Paper C3, *7th Int Conf on Fluid Sealing*, BHRA, Cranfield, Bedfordshire, England.

Briscoe, B.J. & Liatsis, D. [1989], **'Internal Crack Symmetry Phenomena During Gas Induced Rupture of Elastomers'**. *Submitted to Rubber Chemistry and Technology.*

Briscoe, B.J., Savvas, T. & Kelly, C.T. [1994], **'Explosive Decompression Failure of Rubbers : A Review of the Origins of Pneumatic Stress Induced Rupture in Elastomers'**. *Rubber Chem.Technol*, **67**, No.3, 384

Briscoe, B.J. & Zakaria, S. [1990a], **'Polymer Gas Interactions at High Pressure : The Use of Ultrasonic Probes'**. *Polymer*, **31**, 440.

Briscoe, B.J. & Zakaria, S. [1990b], **'Polymer Gas Interactions at High Pressure : The Use of Ultrasonic Techniques for Material Testing'**. *Polym.Test*, **9**, 103.

Briscoe, B.J. & Zakaria, S. [1990c], **'Role of Interfacial Quality on Gas Induced Damage of Elastomeric Composites'**. *Proc Int Conf on Composite Interfaces*, Ohio, May 1990.

Briscoe, B.J. & Zakaria, S. [1990d], **'Why Rubber Explodes'**. *Chemtech, Innovators Magazine, Aug 1990*, 492.

Briscoe, B.J. & Zakaria, S. [1990e], **'Gas Induced Damage in Elastomeric Composites'**. *J.Mater.Sci*, **25**, 3017.

Briscoe, B.J. & Zakaria, S. [1992], **'Sorption and Dilation of Silicone Elastomer Composites at High Gas Pressures : The Role of Interfacial Quality'**. *J.Polym.Sci Part B: Poly.Phys.Ed*, **30**, 959

Campion, R.P. [1990], **'Explosive Decompression in Elastomers'.** *Cellular Polymers*, **9**, 206.

Chivers, T.C. & Hunt, R.P. [1978], **'The Achievement of Minimum Leakage from Elastomeric Seals'.** Paper F3, *8th Int Conf on Fluid Sealing*, BHRA, Cranfield, Bedfordshire, England.

Cho, K. & Gent, A.N. [1988], **'Cavitation in Model Elastomeric Composites'.** *J.Mater.Sci*, **23**, 141.

Cho, K., Gent, A.N. & Lam, P.S. [1987], **'Internal Fracture in an Elastomer Containing a Rigid Inclusion'.** *J.Mater.Sci*, **22**, 2899.

Cox, V.A. [1985], **'Service Failures - A Users View of Explosive Decompression in Oilfield Elastomers'.** *Conf Proc 'Offshore Engineering with Elastomers'*, June 1985, Aberdeen.

Crank, J. [1975], **'The Mathematics of Diffusion'.** 2nd Edition, Clarendon Press, Oxford

Daley, J.R. & Mays, S. [1997], **'The Complexity of Material Modelling in the Design Optimisation of Elastomeric Seals'**, *Finite Element Analysis of Elastomers Conference, IMechE, London, October 1997.*

Davies, O.M. [1997], **'The Effect of High Pressure CO_2 on the Mechanical Properties of Elastomeric Materials'**, *Fluid Sealing Conference, Maastricht, Sept 1997*, BHR Group Limited, Cranfield, Bedfordshire, England.

Edwards, S.F. & Vilgis, T. [1986], **'The effect of entanglements in rubber elasticity'**, *Polymer*, **27**, 483.

Ender, D.H. [1986], **'Elastomeric Seals'.** *Chemtech*, January 1986, 52.

Fleming, G.K. & Koros, W.J. [1986], **'Dilation of Polymers and Sorption of Carbon Dioxide at Elevated Pressures. 1. Silicone Rubber'.** *Macromolecules*, **19**, 2285.

Flint & Naunton. [1937] *Trans.Inst.Rubber.Ind*, **12**, 367

Gent, A.N. [1980], **'Detachment of An Elastic Matrix From A Rigid Spherical Inclusion'.** *J.Mater.Sci*, **15**, 2884

Gent, A.N. & Lindley, P.B. [1958], **'Internal Rupture of Bonded Rubber Cylinders in Tension'**, *Proc.R.Soc.London*, **A249**, 195

Gent, A.N. & Marteny, P. [1982], **'Crack Velocities in Natural Rubber'.** *J.Mater.Sci*, **17**, 2955.

Gent, A.N. & Park, B. [1984], **'Failure Processes in Elastomers at or Near a Rigid Spherical Inclusion'.** *J.Mater.Sci*, **19**, 1947.

Gent, A.N. & Tompkins, D.A. [1969a], **'Nucleation and Growth of Gas Bubbles in Elastomers'**. *J.Appl.Physics*, **Vol 40, No.6**, 2520.

Gent, A.N. & Tompkins, D.A. [1969b], **'Surface Energy Effects for Small Holes or Particles in Elastomers'**. *J.Polym.Sci.Part A2*, 7, 1483.

Gent, A.N. & Wang, C. [1991], **'Fracture Mechanics and Cavitation in Rubber Like Solids'**. *J.Material.Sci*, **26**, 3393.

Green, A.E. & Zerna, W [1954], **'Theoretical Elasticity'**. *Clarendon Press, Oxford*

Greensmith, H.W. [1956], **'Rupture of Rubber IV. Tear Properties of Vulcanizates Containing Carbon Black'**. *J.Polym.Sci.*, **21**, 175.

Griffiths, A.D. [1985], **'Materials Selection and Product Design for Resistance to Explosive Decompression'**. *Disc Forum & Exhib on 'Offshore Engineering with Elastomers'*, Paper 20, Aberdeen, May 1985.

Hepburn, C. & Reynolds , R.J.W.[1979], **'Elastomers : Criteria for Engineering Design'**, *Applied Science Publications*, London.

Ho, E. [1993], **'Theoretical and Computational Modelling of Polymer Seal Life'**. *PhD Thesis, Department of Fluid Engineering and Instrumentation, Cranfield University.*

Ho, E. & Nau, B.S. [1996], **'Gas Emission by Permeation through Elastomeric Seals'**. *Tribology Transactions*, **39**, 1, 180.

Ho, E., Nau, B.S., Stevenson, A., Campion, R., Derham, C.J. and Morgan, G [1989-1997] **'Seal Life Project Reports'**, *BHR Group, Cranfield, Beds. and Materials Engineering Research Laboratory, Hertford, Herts, England.*

Hörl, L. & Haas, W. [1997], **'O-rings at pulsating pressure'**, *15th International Conference on Fluid Sealing, Maastricht, BHR Group Ltd.*

Hou, H & Abeyaratne, R [1992], **'Cavitation in Elastic and Elastic-Plastic Solids'**, *J.Mech Phys Solid*, **40**, no.3, 571.

Jackson, A. [1996], **'Explosive Decompression Testing of Elastomeric O-ring Seal Materials'**, *Statoil Research Centre Report* - Classified.

James, A.G., Green, A. & Simpson, G.M. [1975], *J.Appl.Poly.Sci*, **19**, 2033.

Lake, G.J., Samsuri, A., Teo, S.C. & Vaja, J. [1991], **'Time Dependant Fracture in Vulcanised Elastomers'**, *Polymer*, **Vol 32**, 2963.

Lake, G.J., Thomas, A.G. & Lawrence, C. [1992], **'Effects of Hydrostatic Pressure on Crack Growth in Elastomers'**, *Polymer*, **33**, 4069.

Leefe, S.E. [1993], **'Elastomeric Diaphragm Life Prediction Methodology'**. *BHR Group Report RR 3313,* BHR Group Limited, Cranfield, Bedfordshire, England.

Liatsis, D. [1989], **'Gas Induced Rupture of Elastomers'**. PhD Thesis, Imperial College, University of London.

Lindsey, G.H. [1967], **'Triaxial Fracture Studies'**. *J.Appl.Physics*, **38**, No.12, 4843.

Melikhova, N.A., Reitlinger, S.A. & Kuzina, E.N. [1959], **'Effects of Fillers on the Gas Permeability of Synthetic Rubbers'**. *Soviet Rubber.Tech*, **18**, 34

Shade, W.N. & Legg, D.W. [1988], **'Explosive decompression Resistance of Centrifugal Compressor O-Ring Seals : a Comparative Test Summary and Procedure'**. *Journal of Engineering for Gas Turbines and Power*, **110**, 289.

Shah, V.M., Hardy, B.J. & Stern, S.A. [1978], *J.Polym.Sci. Polym Phy Ed*, **16**, 735

Sick, H.H. [1975], **'Measurement and reduction of friction of reciprocating piston seals for hydraulic and pneumatic application'**. Paper C2, *7th Int Conf on Fluid Sealing*, BHRA, Cranfield, Bedfordshire, England.

Stewart, C.W. [1970], **'Nucleation and Growth of Bubbles in Elastomers'**. *J.Polym.Sci Part A2*, **8**, 937.

Treloar, L.R.G [1975], **'The Physics of Rubber Elasticity'**. *3rd Edition, Clarendon Press, Oxford.*

Van Amerongen, G.J. [1964], **' Diffusion in Elastomers'**. *Rubber Chem.Technol*, **37**, 1065

Williams, M.L. & Schapery, R.A. [1965], **'Spherical Flaw Instability in Hydrostatic Tension'**. *Int.J.Fract.Mech*, **1**, 64

APPENDIX A - SOLUTION OF TRANSIENT AND STEADY STATE DIFFUSION IN A PLANE SHEET

APPENDIX A

Solution of Transient and Steady-State Diffusion in a Plane Sheet

The following solution was sourced from "The Mathematics of Diffusion" by J.Crank (1975).

Consider one dimensional diffusion in a medium bounded by 2 parallel plane, at x=0 and x=l. The plane sheet is so thin that effectively all the diffusing substance enters through the plane faces and a negligible amount through the edges.

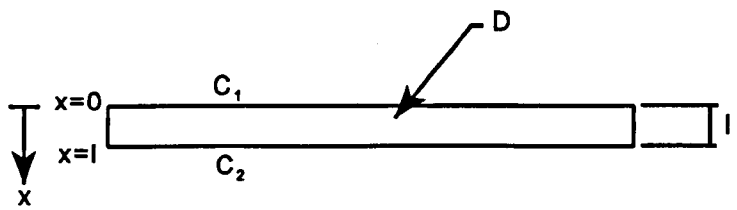

Steady State condition

Consider the case of diffusion through a plane sheet or membrane of thickness l, diffusion coefficient D, whose surfaces, x=0, x=l, are maintained at constant concentrations C_1, C_2 respectively. After a finite period of time, a steady state condition is reached where all points of the remain at a constant concentration. The diffusion equation in one dimension then reduces to

$$\frac{d^2C}{dx^2} = 0 \qquad (A.1)$$

providing that the diffusion coefficient D is constant. If we integrate this function with respect to x we have

$$\frac{dC}{dx} = constant \qquad (A.2)$$

If we integrate again and introduce the conditions at x=0 and x=l

$$\frac{C - C_1}{C_2 - C_1} = \frac{x}{l} \qquad (A.3)$$

This shows that the concentration varies linearly from C_1 to C_2 through the sheet. The rate of transfer of diffusing substance is the same across all sections of the membrane and is given by

$$F = -D\frac{dC}{dx} = \frac{D\,(C_1 - C_2)}{l} \qquad (A.4)$$

If the new surface x=0 is maintained at a constant concentration C_1 and at x=l there is evaporation into the atmosphere for which the equilibrium concentration just within the surface is C_2, so that

$$\frac{\partial C}{\partial x} + h\,(C - C_2) = 0, \qquad x = l$$

then we find

$$\frac{C - C_1}{C_2 - C_1} = \frac{hx}{1 + hl'} \qquad (A.3a)$$

and

$$F = \frac{Dh\,(C_1 - C_2)}{1 + hl} \qquad (A.4a)$$

If the surface conditions are

$$\frac{\partial C}{\partial x} + h_1\,(C_1 - C) = 0, \qquad x = 0$$

$$\frac{\partial C}{\partial x} + h_2\,(C - C_2) = 0, \qquad x = l$$

then

$$C = \frac{h_1 C_1 \left[1 + h_2(l-x)\right] + h_2 C_2 (1 + h_1 x)}{h_1 + h_2 + h_1 h_2 l} \qquad (A.3b)$$

and

$$F = \frac{D h_1 h_2 (C_1 - C_2)}{h_1 + h_2 + h_1 h_2 l} \qquad (A.4b)$$

Permeability constant

If the surface concentrations are unknown, which is often the case in practical situations, and the gas pressures on the two sides of the membrane are known, the rate of transfer in the steady state can be written

$$F = \frac{Q (p_1 - p_2)}{l} \qquad (A.5)$$

where the constant Q is referred to as the permeability constant.

If the diffusion coefficient is constant, and if the sorption isotherm is linear, i.e. if there is a linear relationship between the external gas pressure and the corresponding equilibrium concentration within the membrane, then equations (A.4) and (A.5) are equivalent. The linear isotherm may be written

$$C = Sp \qquad (A.6)$$

and is sometimes referred to as Henry's law. C is the concentration of gas within the membrane material in equilibrium with external gas pressure p, and S is the solubility. Since C_1, p_1, C_2 and p_2 in (A.4) and (A.5) are related by (A.6) it follows that

$$Q = DS \qquad (A.7)$$

Transient diffusion

The solution to the transient condition of diffusion through an elastomer membrane can be obtained either by the method of separation of variables or by the Laplace transform. The following is the solution of uniform initial distribution and surface concentrations different, which is the case of flow through a membrane.

If one face x=0 of a membrane is maintained at constant concentration C_1 and the other x=l at C_2, and the membrane is initially at uniform concentration C_0, there is a finite interval of time during which the steady state condition is achieved. During this period the concentration changes according to the following relation

$$C = C_1 + (C_2 - C_1)\frac{x}{l} + \frac{2}{\pi}\sum_{n=1}^{\infty}\frac{C_2\cos n\pi - C_1}{n}\sin\frac{n\pi x}{l}\exp\left(\frac{-Dn^2\pi^2 t}{l^2}\right)$$

$$+ \frac{4C_0}{\pi}\sum_{m=0}^{\infty}\frac{1}{2m+1}\sin\frac{(2m+1)\pi x}{l}\exp\left(\frac{-Dn^2\pi^2 t}{l^2}\right) \qquad (A.8)$$

As t approaches infinity, the exponential terms disappear and we are left with the linear concentration distribution obtained in (A.2). If M_t denotes the total amount of diffusing substance which enters the sheet during time t, and M_∞ the corresponding amount during infinite time, then

$$\frac{M_t}{M_\infty} = 1 - \frac{8}{\pi^2}\sum_{n=0}^{\infty}\frac{1}{(2n+1)^2}\exp\left(\frac{-D(2n+1)^2\pi^2 t}{l^2}\right) \qquad (A.9)$$

In this case:-

$$M_\infty = l\left(\frac{1}{2}(C_1 + C_2) - C_0\right)$$

and the total content of the membrane at time t is given by $M_t + lC_o$.

The rate at which the gas or other diffusing substance emerges from unit area of face x=l of the membrane is given by

$$-D\left(\frac{\partial C}{\partial x}\right)_{x=l}$$

which is easily determined from (5A.8). By intergrating with respect to t, we obtain the total amount of diffusing substance Q_t which has passed through the membrane in time t.

$$Q_t = D\,(C_1 - C_2)\,\frac{t}{l} + \frac{2l}{\pi^2}\sum_{1}^{\infty}\frac{C_1\cos n\pi - C_2}{n^2}\left(1 - \exp\left(\frac{-Dn^2\pi^2 t}{l^2}\right)\right)$$

$$+ \frac{4C_0 l}{\pi^2}\sum_{m=0}^{\infty}\frac{1}{(2m+1)^2}\left(1 - \exp\left(\frac{-D(2m+1)^2\pi^2 t}{l^2}\right)\right) \qquad (A.10)$$

In the commonest experimental arrangement, both C_0 and C_2 are zero, i.e. the membrane is initially at zero concentration and the concentration at the face through which the gas will emerge is also at zero concentration. Therefore, we find that

$$\frac{Q_t}{lC_1} = \frac{Dt}{l^2} - \frac{1}{6} - \frac{2}{\pi^2}\sum_{1}^{\infty}\frac{(-1)^n}{n^2}\exp\left(\frac{-Dn^2\pi^2 t}{l^2}\right) \qquad (A.10a)$$

which, as $t\to\infty$, approaches the line

$$q_t = \frac{DC_1}{l}\left(t - \frac{l^2}{6D}\right) \qquad (A.11)$$

This has an intercept τ on the t-axis given by

$$\tau = \frac{l^2}{6D} \qquad (A.12)$$

From observation of the intercept, τ, the diffusion coefficient can be obtained by equation (A.12). From the steady-state flow rate, the permeability constant Q can be obtained from equation (A.5). The solubility can then be obtained using equation (A.7).

APPENDIX B - PERMEATION TESTING FACILITY DRAWINGS

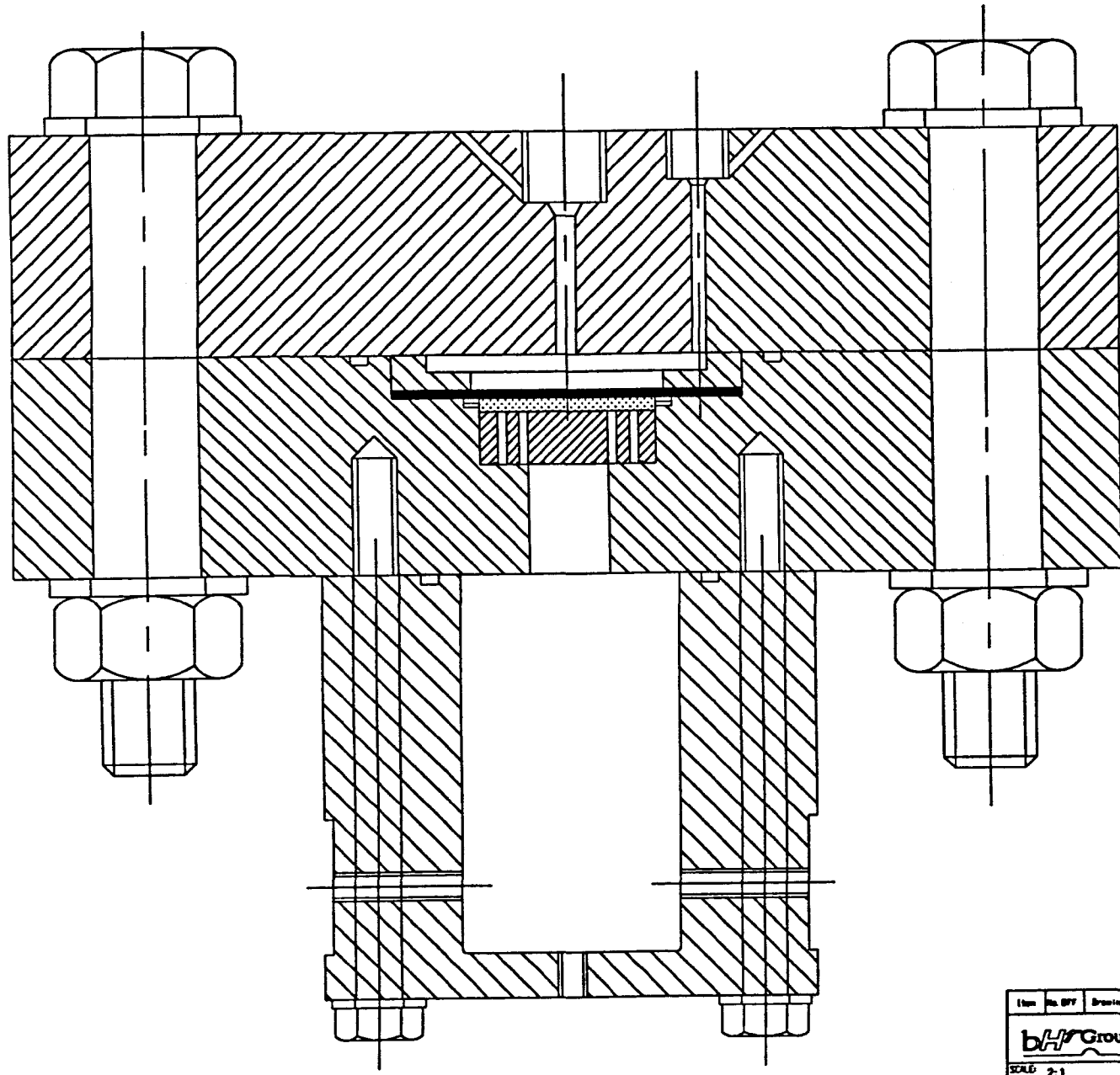

Item	No. OFF	Drawing/Part No.	Description

bHP Group

Registered Office -
Cranfield, Bedford. MK43 0AL England.
Telephone +44-(0)1234-750422
FAX +44-(0)1234-750074

SCALE 2:1	All dims are in mm unless stated otherwise. General tolerance - Linear - up to ? over ? Angles ? unless stated otherwise.
DRAWN BY JAMES ROUTH	
DATE 19/2/97	
CHECKED BY	
DATE	
APPROVED BY	
DATE	

TITLE

ASSEMBLY

DRAWING No.

ISSUE

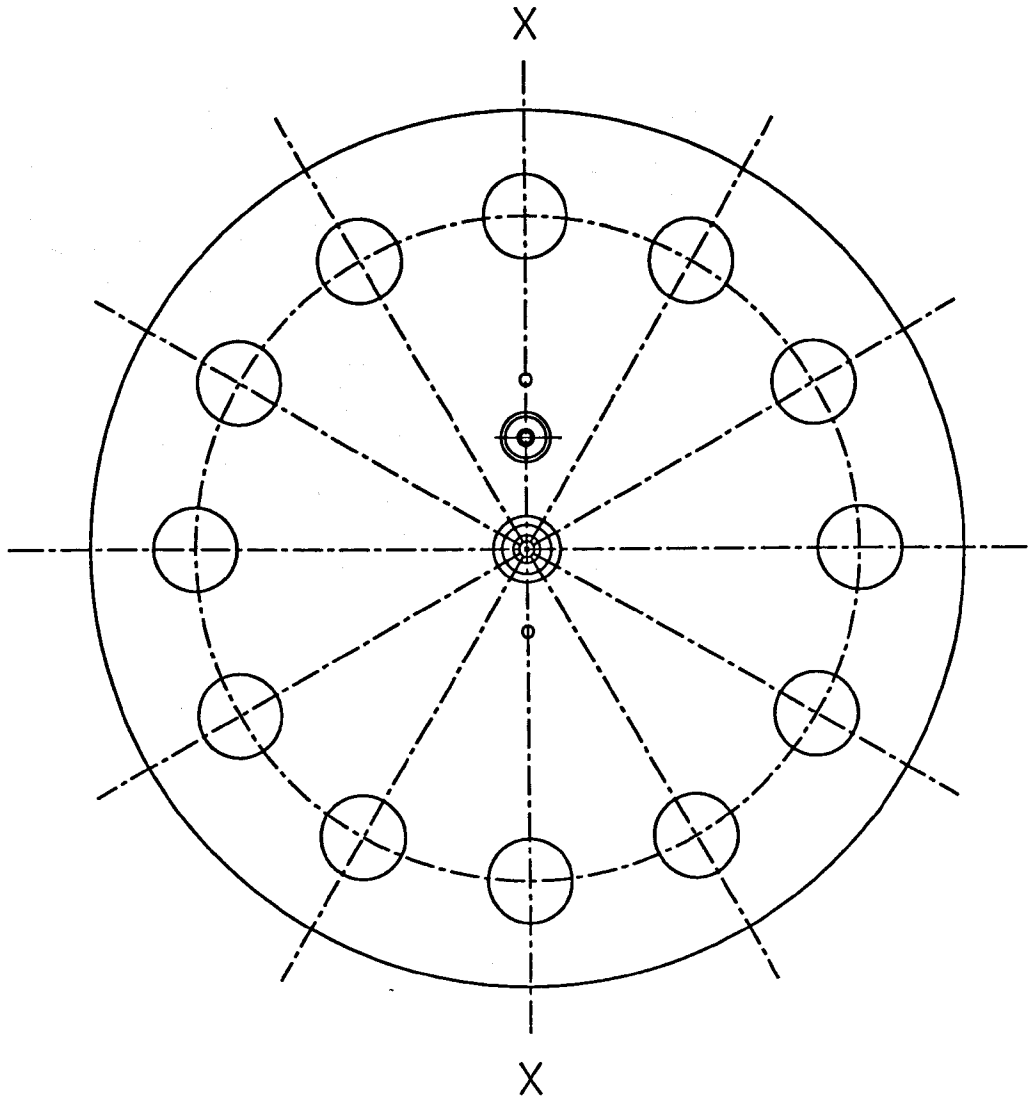

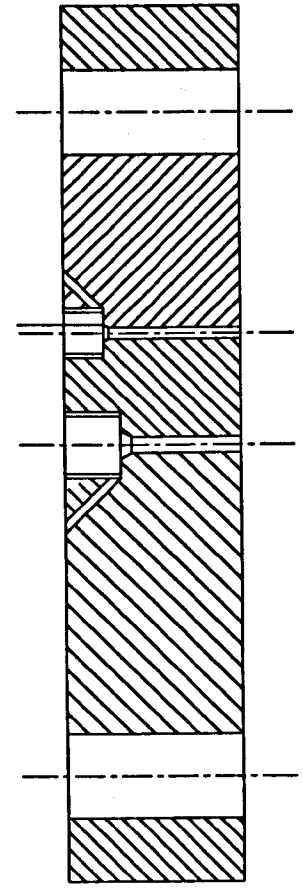

SECTION X–X

NOTE : ALL DIMENSIONS REMOVED FOR CONFIDENTIALITY

MATERIAL : STAINLESS STEEL 316

Item	No. Off	Drawing/Part No.	Description
bHR Group			Registered Office - Cranfield, Bedford. MK43 0AJ. England. Telephone +44-(0)1234-750422 FAX: +44-(0)1234-750074
SCALE: 1:1.5	All dims are in mm unless stated otherwise. General tolerances - 1 decimal - ±0.2 up to ? over ? Angles ? unless stated otherwise.		TITLE: PERMEATION RIG TOP
DRAWN BY: JAMES ROUTH			
DATE: 19/2/97			
CHECKED BY: DATE:			DRAWING No. ISSUE
APPROVED BY: DATE:			

THIRD ANGLE PROJECTION - DO NOT SCALE - FOR ALL QUERIES, CONTACT DESIGN OFFICE.

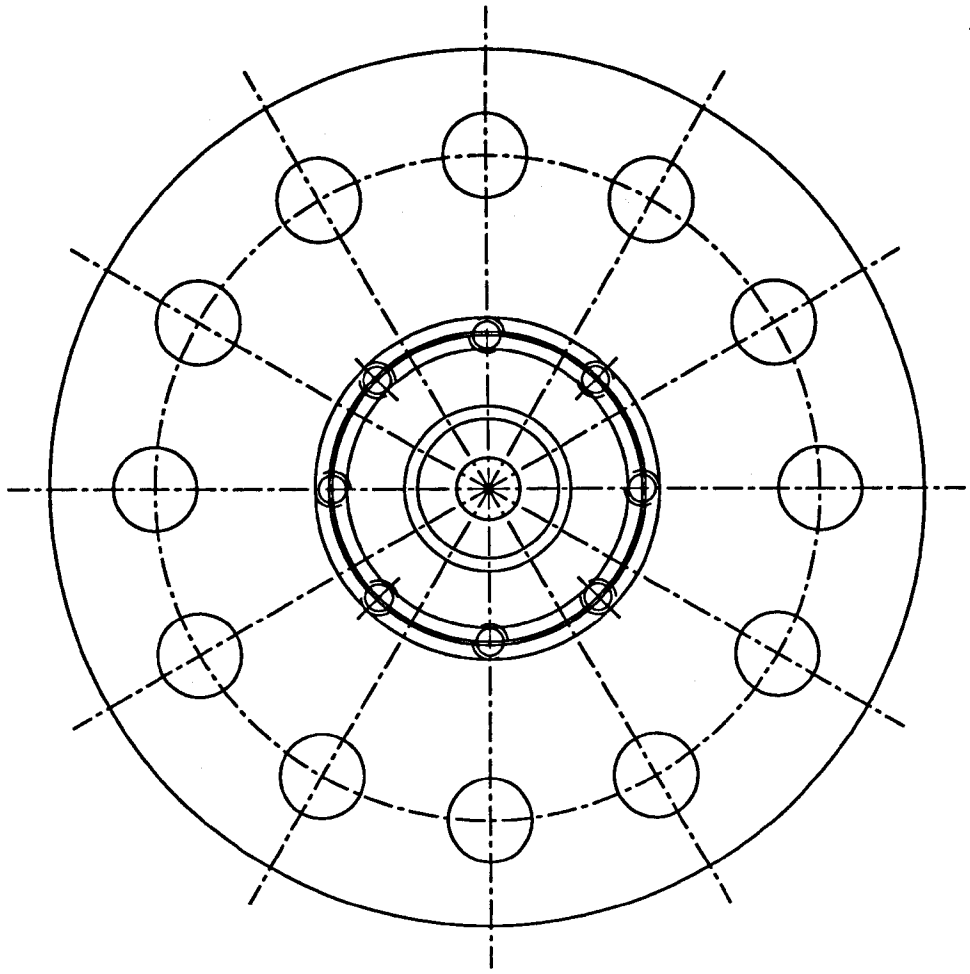

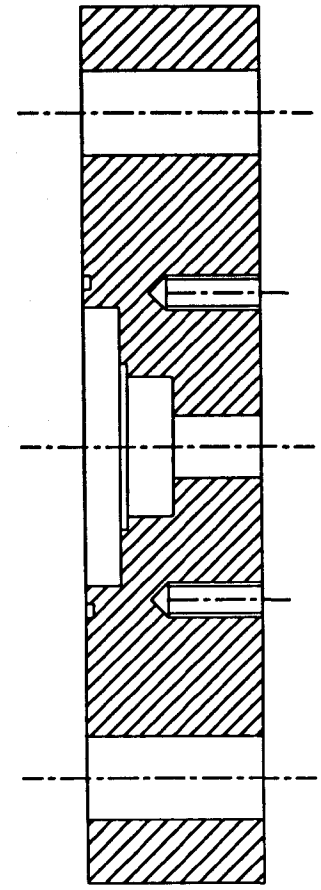

NOTE : ALL DIMENSIONS REMOVED FOR CONFIDENTIALITY

MATERIAL : STAINLESS STEEL 316

Item	No OFF	Drawing/Part No.	Description

bHR Group
Registered Office -
Cranfield, Bedford, MK43 0AJ, England
Telephone: +44-(0)1234-750422
FAX: +44-(0)1234-750074

SCALE: 1:1.5	All dims are in mm unless stated otherwise. General tolerances - Linear - ±0.2 up to ? over ? Angles ? unless stated otherwise.	TITLE: PERMEATION RIG BOTTOM
DRAWN BY: JAMES ROUTH		
DATE: 19/2/97		
CHECKED BY:		
DATE:		
APPROVED BY:		DRAWING No. / ISSUE
DATE:		

3

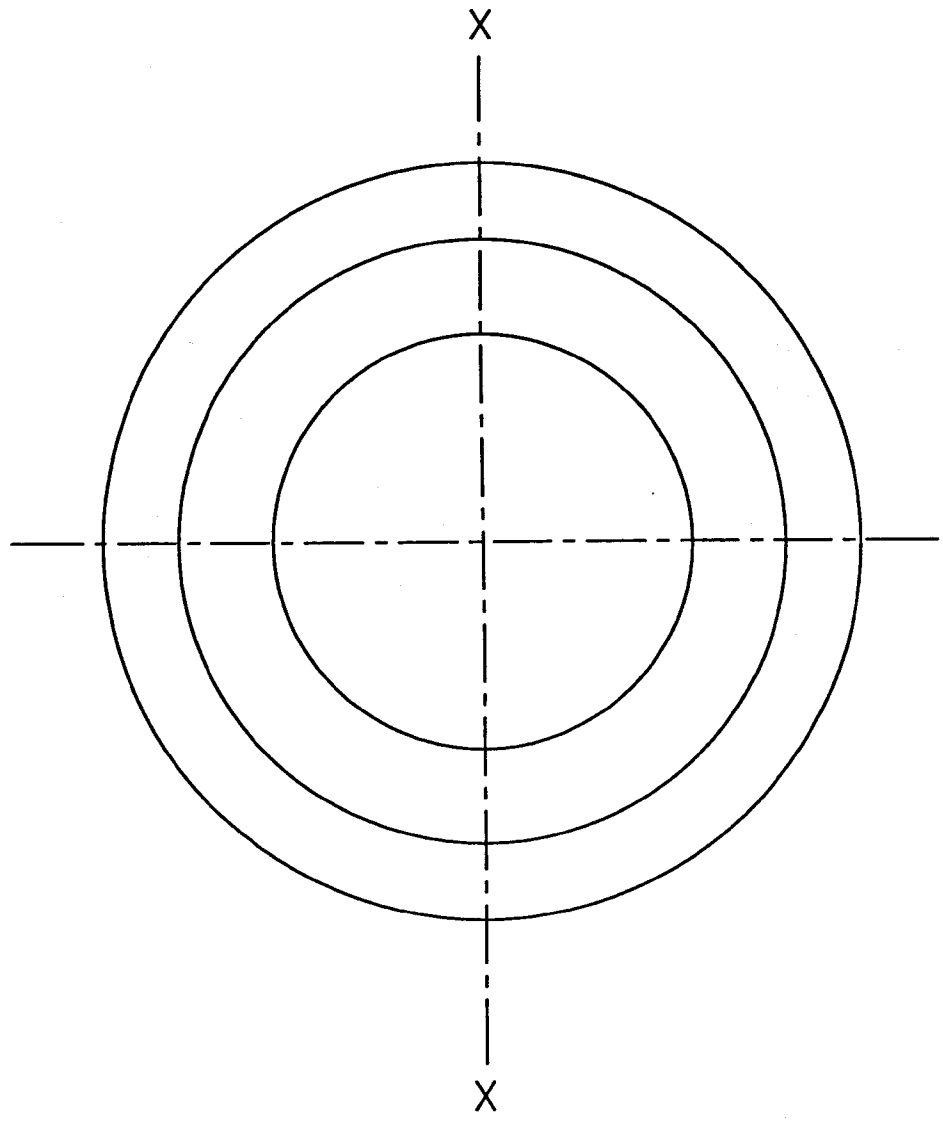

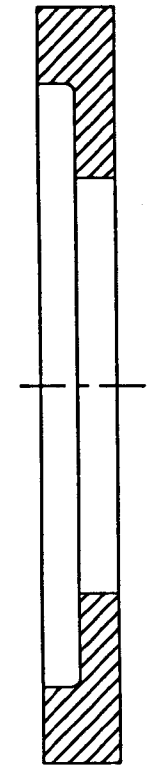

SECTION X–X

MATERIAL : STAINLESS STEEL 316

NOTE : ALL DIMENSIONS REMOVED FOR CONFIDENTIALITY

Item	No Off	Drawing/Part No.	Description

bHP Group

Registered Office :-
Cranfield, Bedford MK43 0AJ England
Telephone +44-(0)1234-750422
Fax +44-(0)1234-750034

SCALE: 1:1

DRAWN BY: JAMES ROUTH

DATE: 19/2/97

CHECKED BY:

DATE:

APPROVED BY:

DATE:

All dims are in mm unless stated otherwise.
General tolerances -
Linear -±0.2
up to ?
over ?
Angles ?
unless stated otherwise.

TITLE:

SUPPORT RING

DRAWING No.

ISSUE

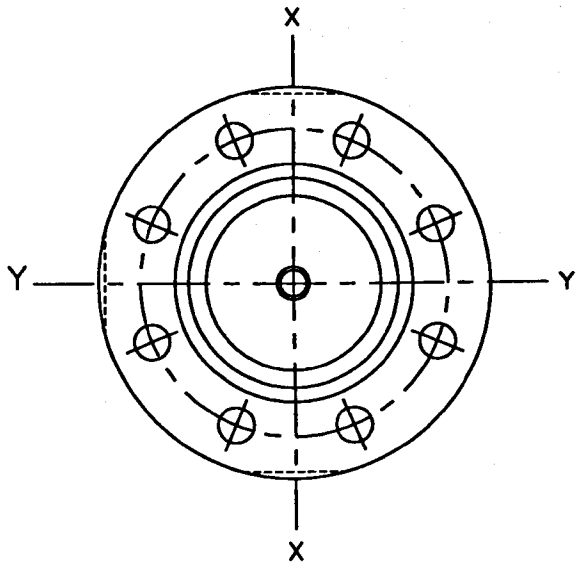

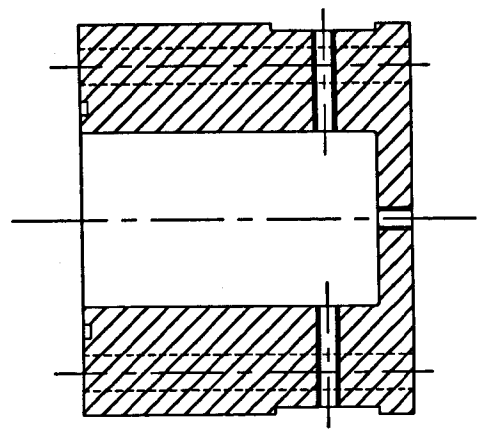

SECTION X–X

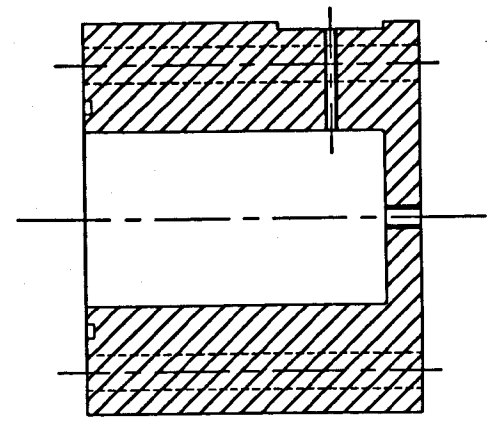

SECTION Y–Y

NOTE : ALL DIMENSIONS REMOVED FOR CONFIDENTIALITY

Item	No. Off	Drawing/Part No.	Description

bHP Group

Registered Office -
Crawley, Bedford, MK43 0AL England
Telephone +44-(0)1234-750422
FAX +44-(0)1234-750004

SCALE: 2:1

DRAWN BY: JAMES ROUTH

DATE: 19/2/97

CHECKED BY

DATE:

APPROVED BY

DATE:

All dims are in mm unless stated otherwise.
General tolerances -
Linear -
up to ?
over ?
Angles ?
unless stated otherwise.

TITLE:

Low Pressure Cup

DRAWING No.

ISSUE

THIRD ANGLE PROJECTION - DO NOT SCALE - FOR ALL QUERIES, CONTACT DESIGN OFFICE.

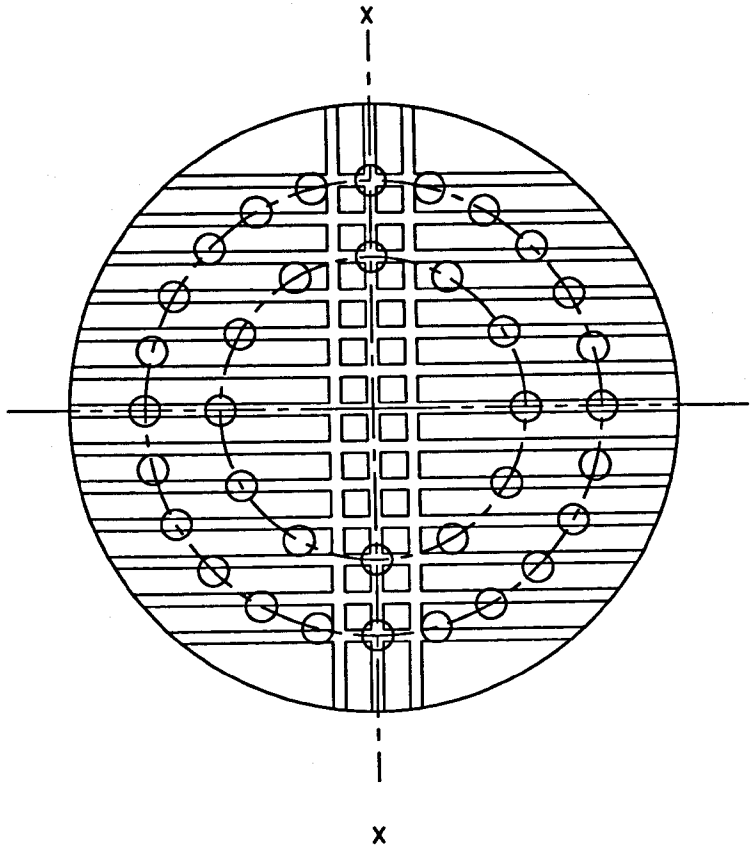

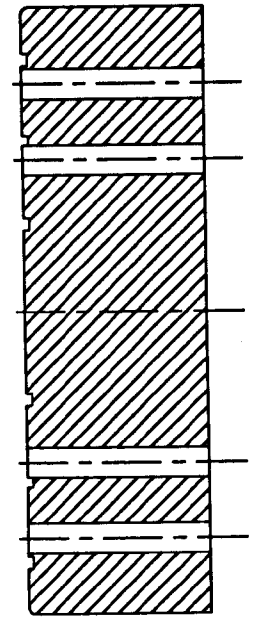

SECTION X–X

MATERIAL : STAINLESS STEEL 316

NOTE : ALL DIMENSIONS REMOVED FOR CONFIDENTIALITY

Item	No Off	Drawing/Part No.	Description

bHP Group
Registered Office -
Crawford, Bedford, MK43 0AJ England
Telephone +44-(0)1234-750422
FAX +44-(0)1234-750074

SCALE 1:1	All dims are in unless stated otherwise. General tolerance - Linear - up to ? over ? Angles ? unless stated otherwise	TITLE: SUPPORT
DRAWN BY JAMES ROUTH		
DATE 19/2/97		
CHECKED BY		
DATE		
APPROVED BY		DRAWING No. / ISSUE
DATE		

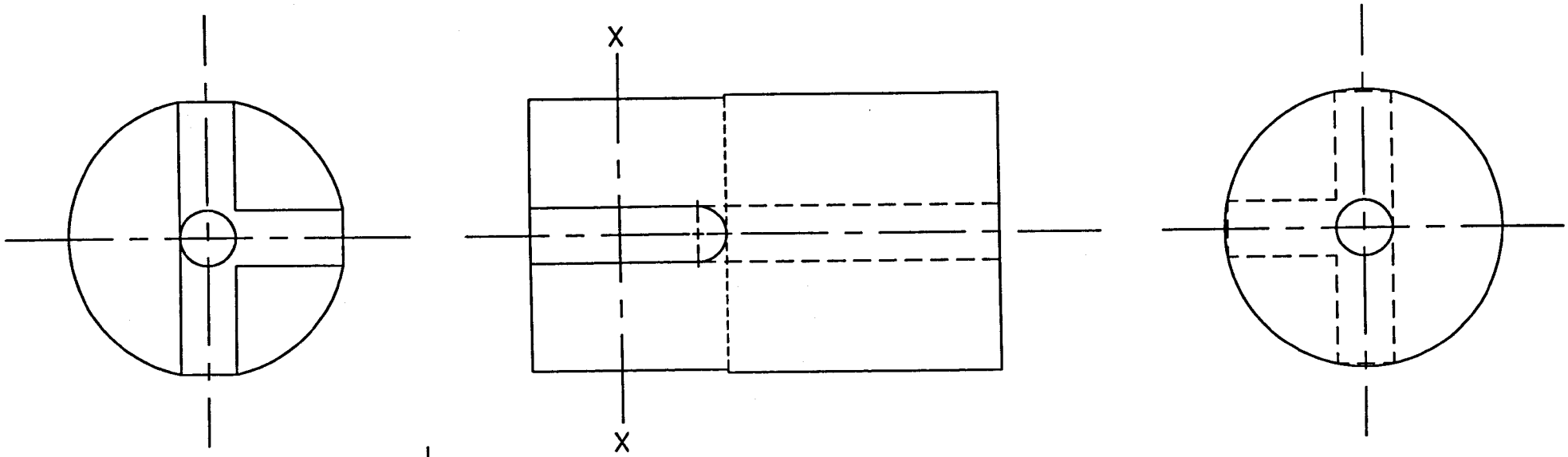

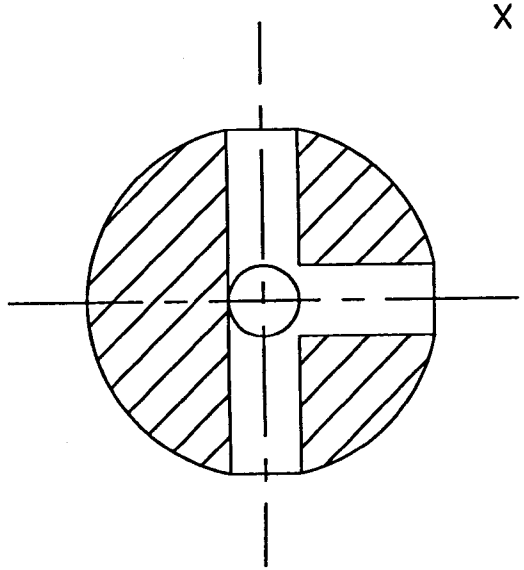

SECTION X–X

NOTE : ALL DIMENSIONS REMOVED FOR CONFIDENTIALITY

Item	No. Off	Drawing/Part No.	Description
bHR Group			Registered Office - Cranfield, Bedford. MK43 0AL England. Telephone +44-(0)1234-750422 FAX +44-(0)1234-750074
SCALE: Not to scale			TITLE: Low Pressure Volume Reducer
DRAWN BY: JAMES ROUTH			
DATE: 24/4/98			
CHECKED BY DATE:			
APPROVED BY DATE:			DRAWING No. ISSUE

All dims are in mm unless stated otherwise. General tolerances - Linear: up to ? over ? Angles ? unless stated otherwise.

THIRD ANGLE PROJECTION - DO NOT SCALE - FOR ALL QUERIES, CONTACT DESIGN OFFICE.

APPENDIX C - DECOMPRESSION RIG DRAWINGS

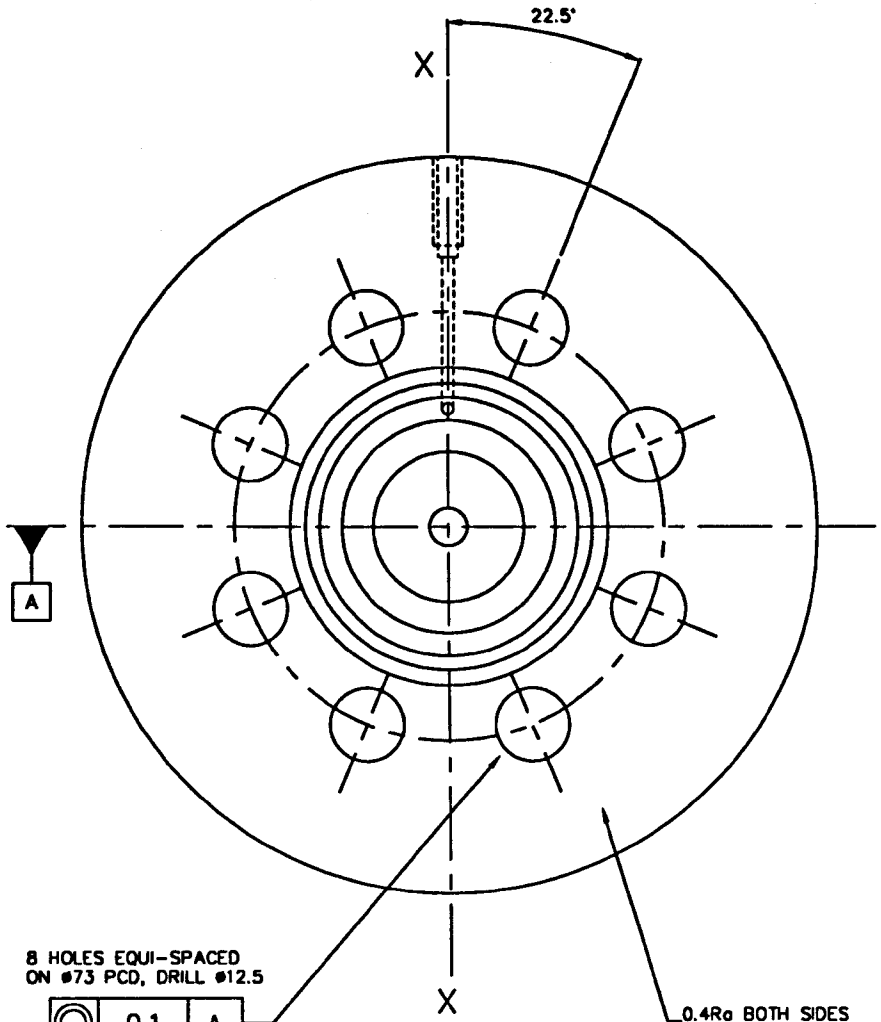

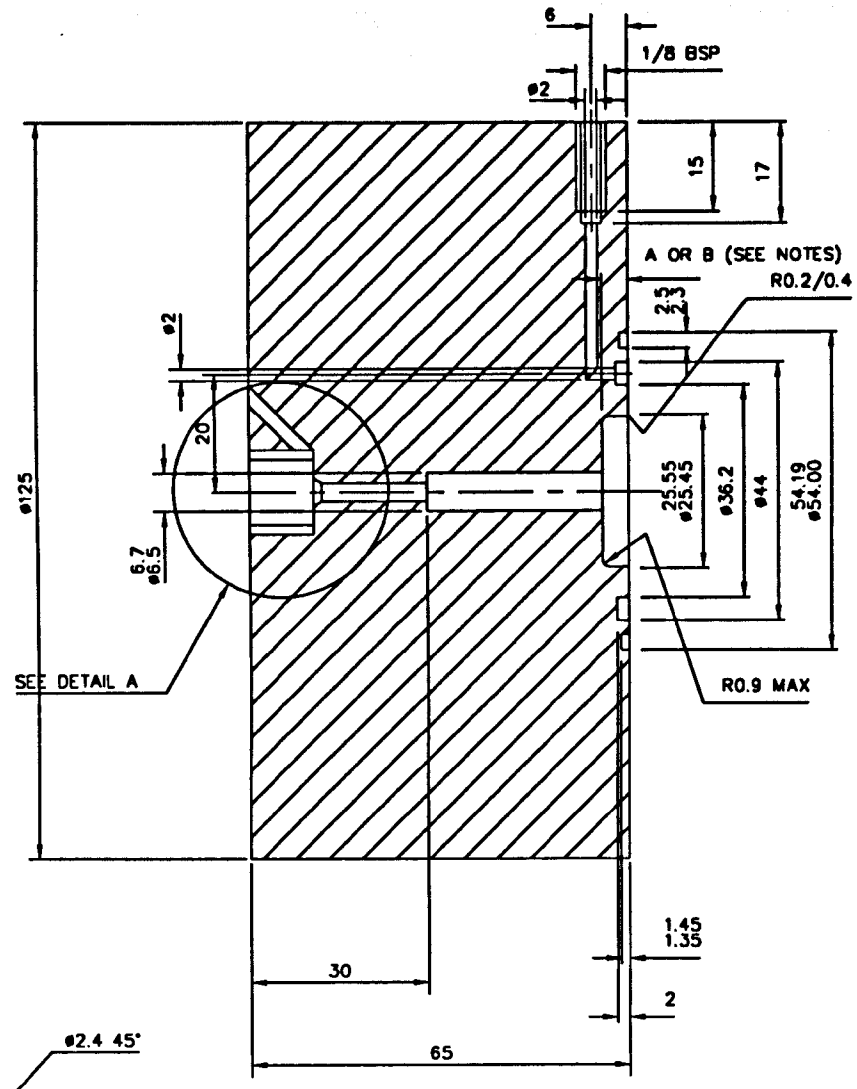

SECTION X–X

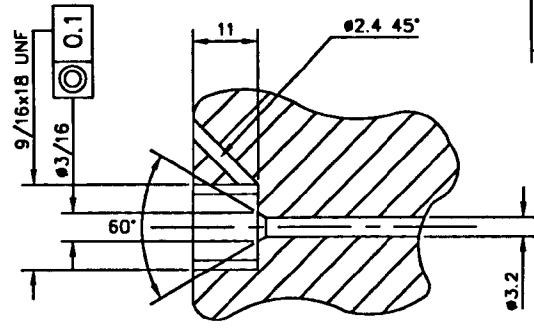

DETAIL A

NOTES:
MATERIAL : STAINLESS STEEL
1 OFF @ A = 4.55/4.65
1 OFF @ B = 4.05/4.15

Item	No. Off	Drawing/Part No.	Description
bHR Group			Registered Office - Cranfield, Bedford. MK43 0AL England. Telephone +44-(0)1234-750422 FAX +44-(0)1234-750074
SCALE: 1:1		All dims are in unless stated otherwise. General tolerances - Linear - ±0.2 up to ? over ? Angles ? unless stated otherwise.	TITLE: DECOMPRESSION RIG BOTTOM PLATE
DRAWN BY: JAMES ROUTH			
DATE: 9/11/98			
CHECKED BY DATE:			DRAWING No. ISSUE
APPROVED BY DATE:			

THIRD ANGLE PROJECTION - DO NOT SCALE - FOR ALL QUERIES, CONTACT DESIGN OFFICE

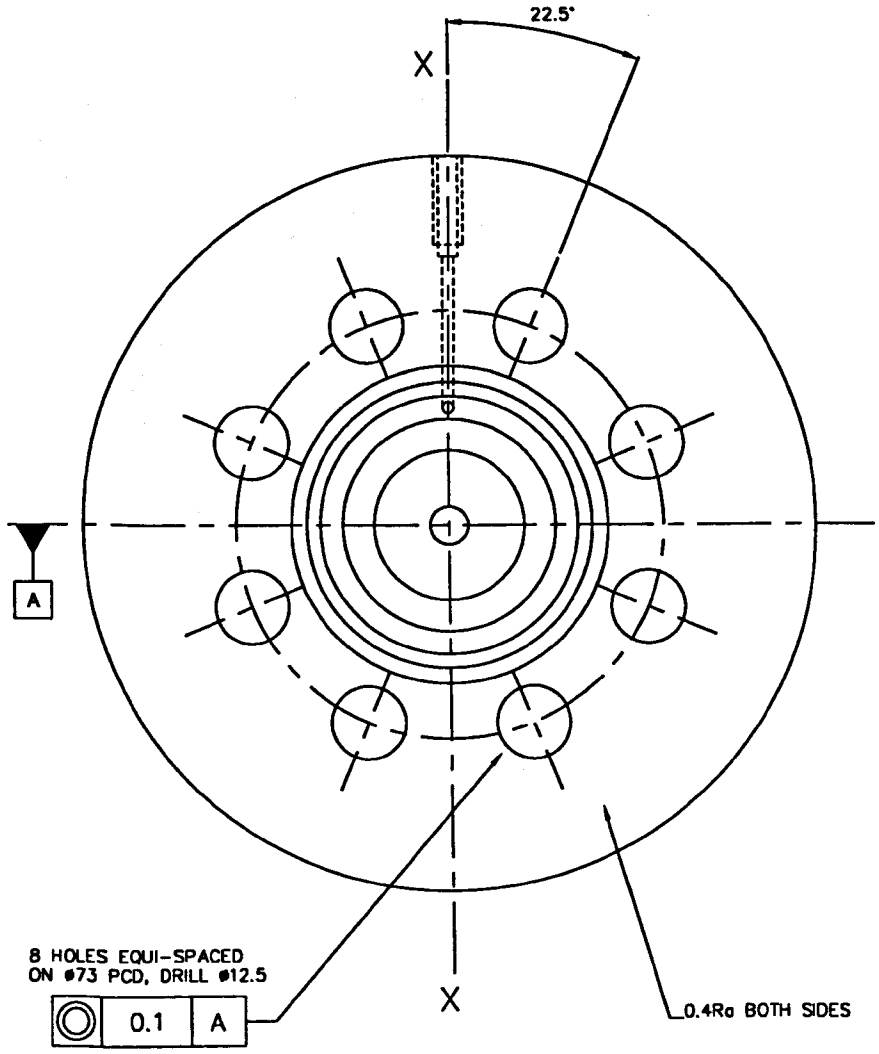

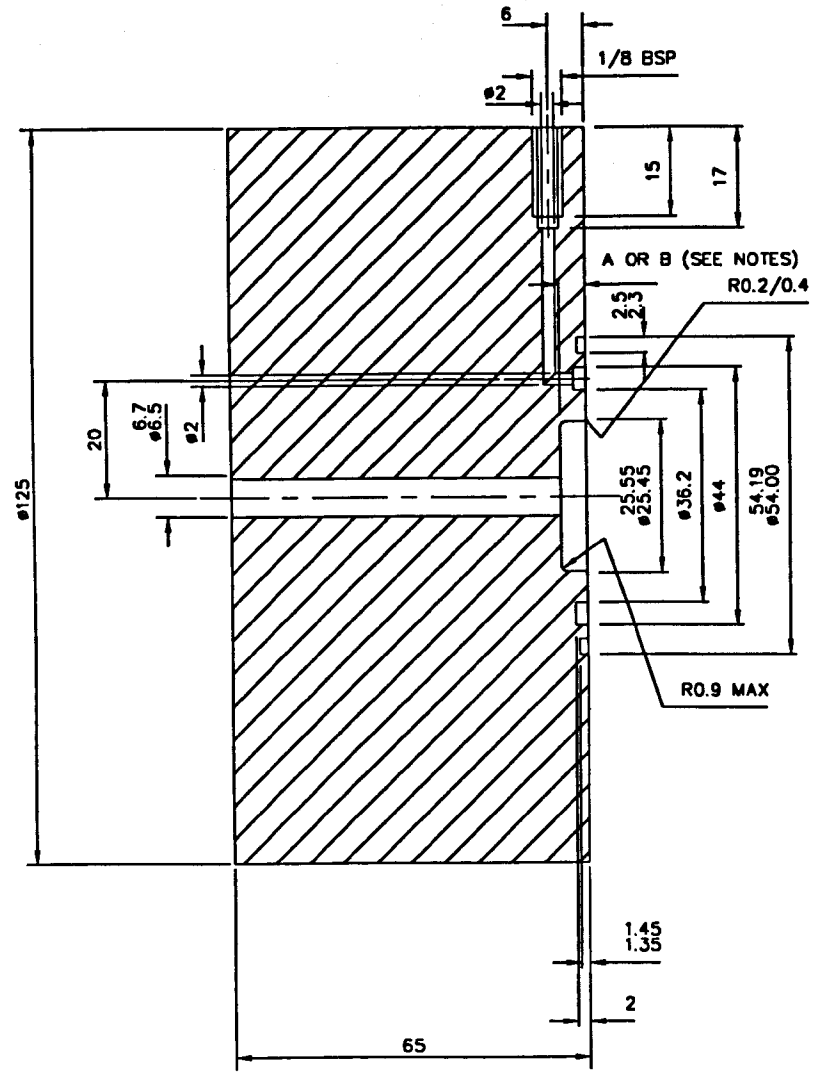

SECTION X–X

NOTES:
MATERIAL : STAINLESS STEEL
1 OFF @ A = 4.55/4.65
1 OFF @ B = 4.05/4.15

Item	No. Off	Drawing/Part No.	Description
bhr Group			Registered Office: Cranfield, Bedford MK43 0AL England. Telephone +44-(0)1234-750422 FAX +44-(0)1234-750074
SCALE: 1:1	All dims are in mm unless stated otherwise. General tolerances - Linear -±0.2 up to 1 over 1 Angles 1 unless stated otherwise.		TITLE: DECOMPRESSION RIG MID PLATE
DRAWN BY: JAMES ROUTH			
DATE: 9/11/98			
CHECKED BY: DATE:			DRAWING No. ISSUE
APPROVED BY: DATE:			

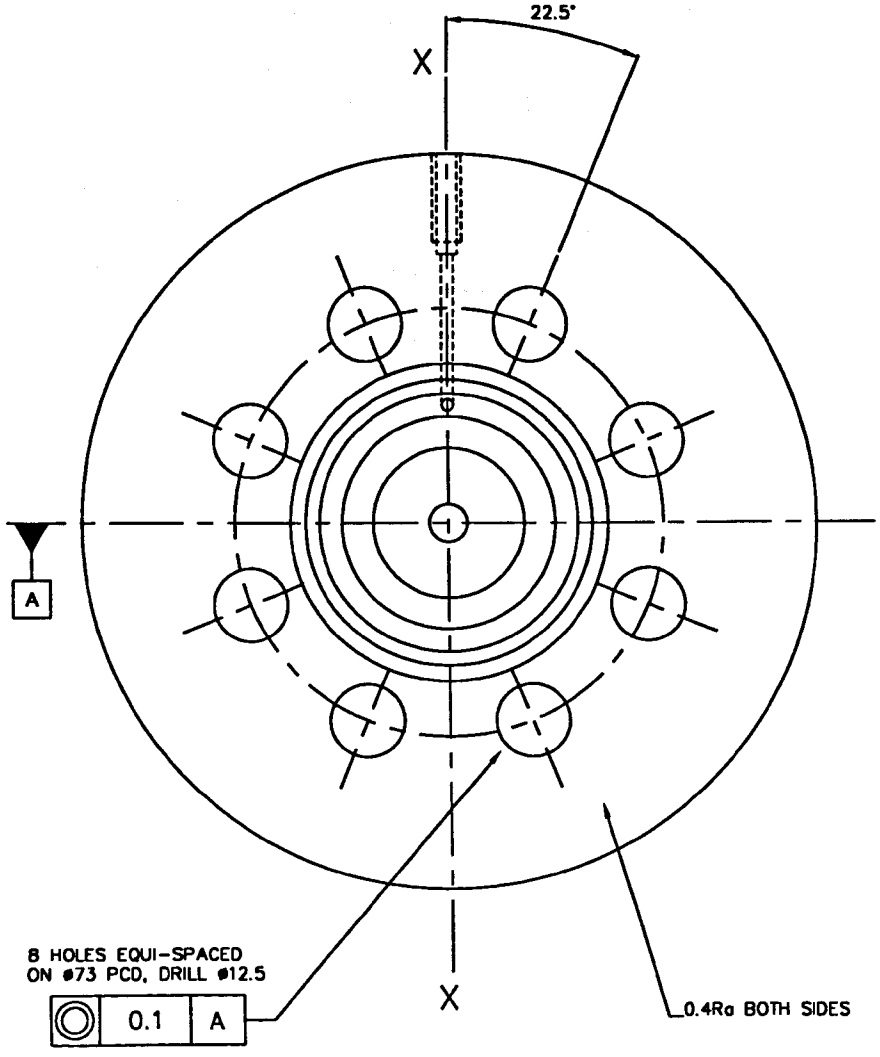

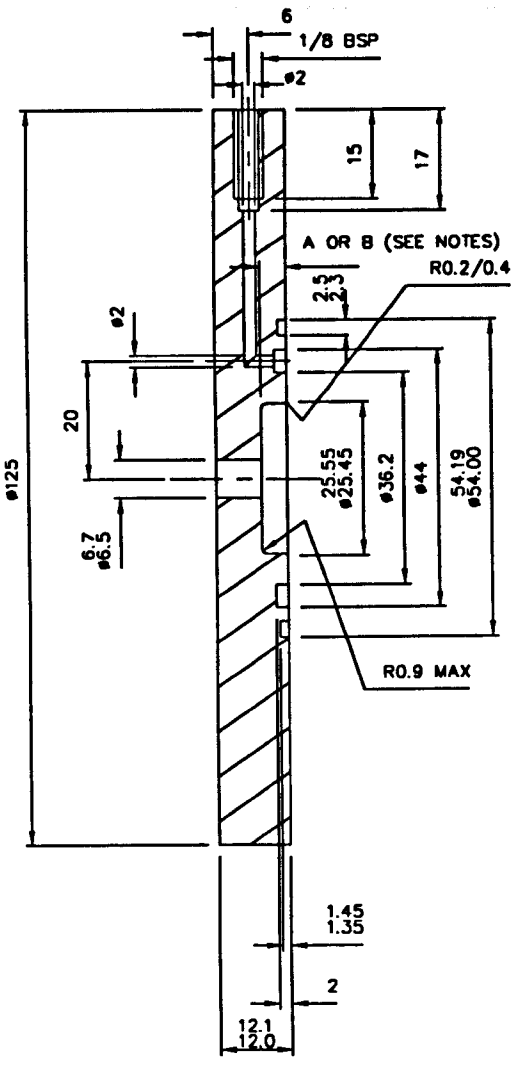

SECTION X–X

NOTES:
MATERIAL : STAINLESS STEEL

5 OFF @ A = 4.55/4.65
10 OFF @ B = 4.05/4.15

5 OFF MODIFICATIONS OF EXISTING PLATES
TO DIMENSION A PLUS EXTRA HOLES

Item	No. OFF	Drawing/Part No.	Description

BHP Group
Registered Office:-
Cranfield, Bedford MK43 0AL England
Telephone +44-(0)1234-750422
FAX: +44-(0)1234-750074

SCALE: 1:1	All dims are in mm unless stated otherwise. General tolerances - Linear -±0.2 up to 1 over 1 Angles 1 unless stated otherwise.
DRAWN BY: JAMES ROUTH	
DATE: 9/11/98	
CHECKED BY:	
DATE:	
APPROVED BY:	
DATE:	

TITLE: DECOMPRESSION RIG PLATE

DRAWING No. | ISSUE

THIRD ANGLE PROJECTION - DO NOT SCALE - FOR ALL QUERIES, CONTACT DESIGN OFFICE

3

Modifications			
Letter	Change	Date	Mod By

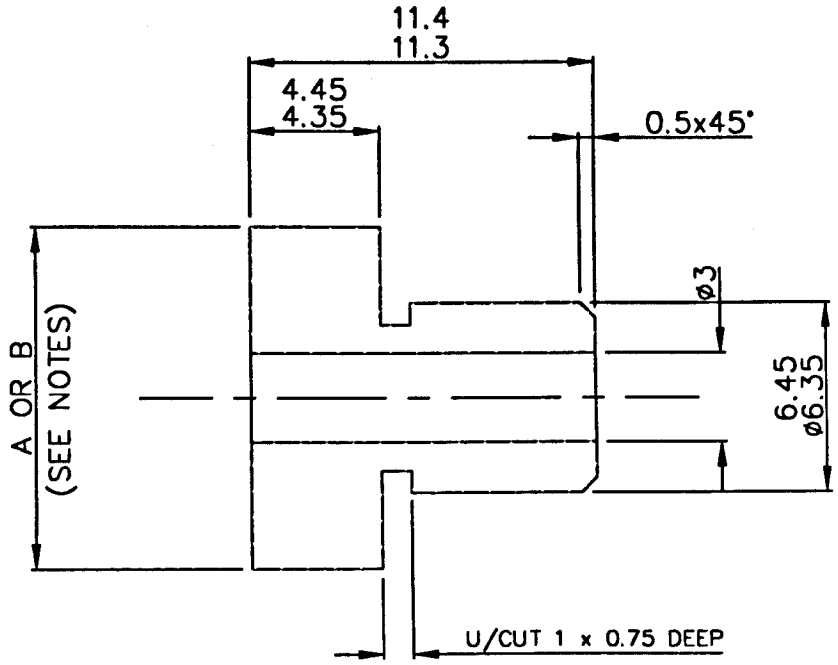

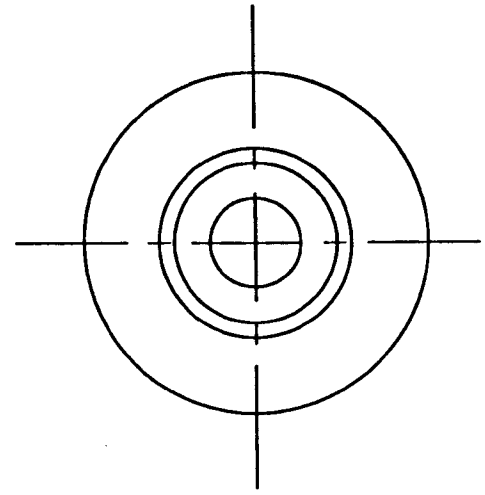

NOTES:
MATERIAL : STAINLESS STEEL
12 OFF @ A = ø8.05/8.15
12 OFF @ B = ø11.05/11.15

Item	No. Off	Drawing/Part No.	Description

bHR Group
Registered Office: -
Cranfield, Bedford. MK43 0AJ. England.
Telephone: +44-(0)1234-750422
FAX: +44-(0)1234-750074

SCALE:	All dims are in mm unless stated otherwise. General tols - Linear - up to ? over ? Angles ? U.S.O.	TITLE: GROOVE FILL PIN
DRAWN BY: J.ROUTH		
DATE: 16/11/98		
CHECKED BY: DATE:		DRAWING No. / ISSUE
APPROVED BY: DATE:		

THIRD ANGLE PROJECTION - DO NOT SCALE -

Modifications			
Letter	Change	Date	Mod By

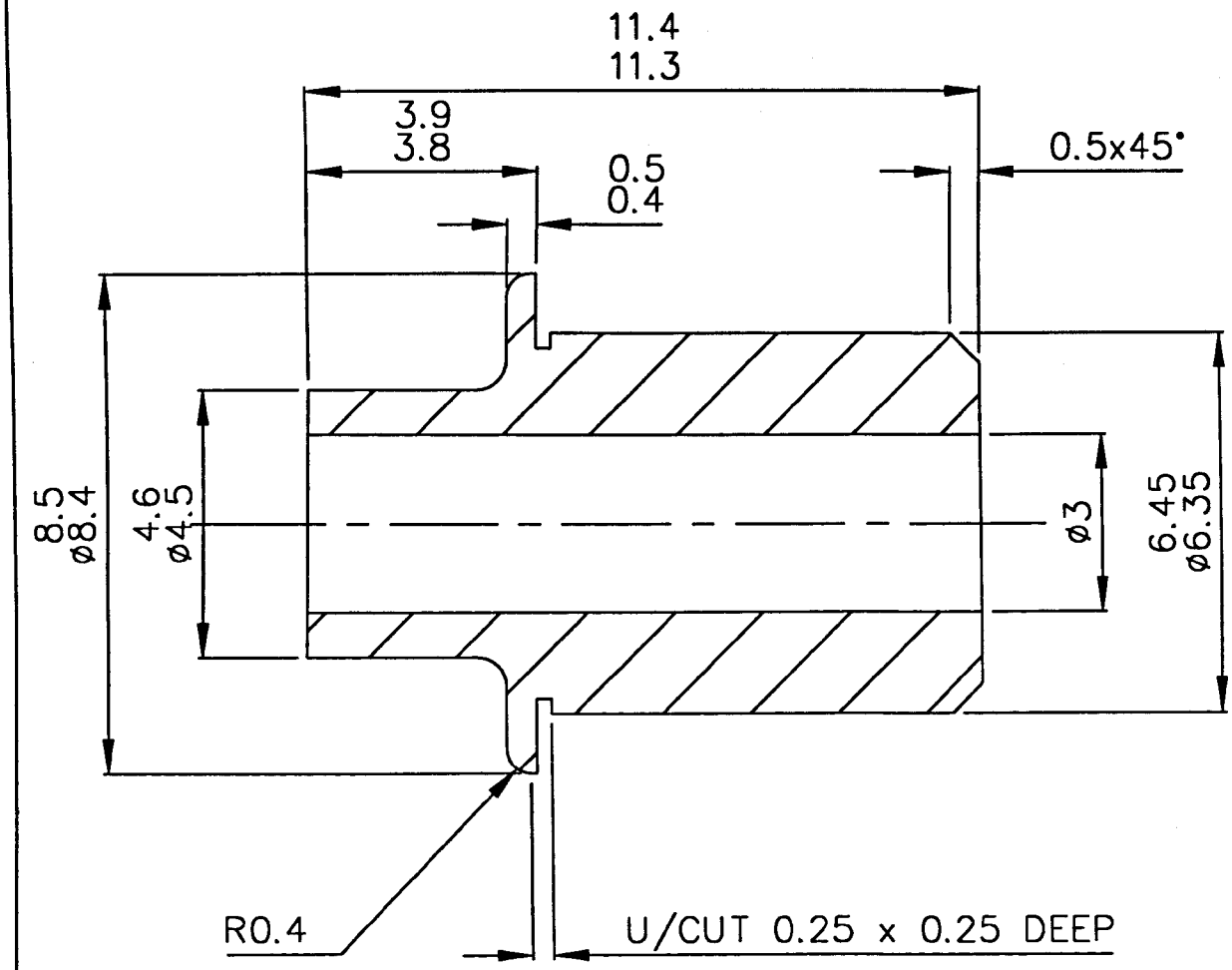

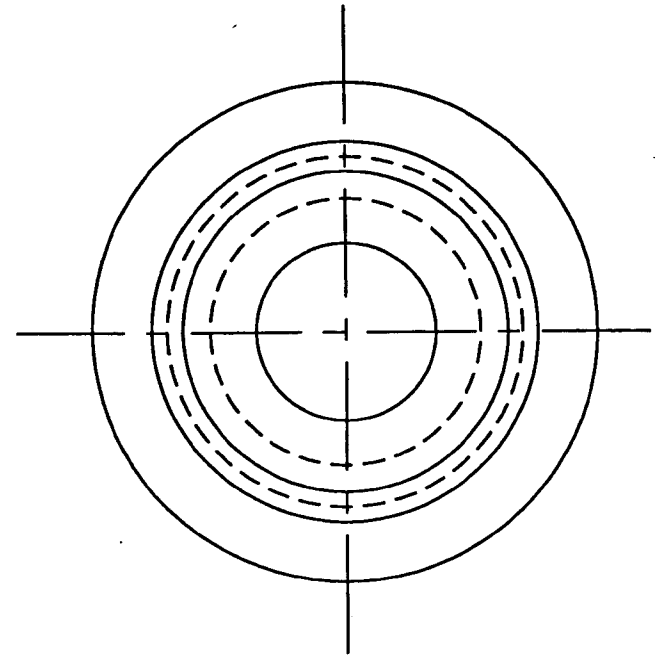

NOTES:
MATERIAL : STAINLESS STEEL

THIRD ANGLE PROJECTION - DO NOT SCALE -

Item	No. OFF	Drawing/Part No.	Description

bHR Group
Registered Office: -
Cranfield, Bedford. MK43 0AJ. England.
Telephone: +44-(0)1234-750422
FAX: +44-(0)1234-750074

SCALE:	All dims are in mm unless stated otherwise. General tols - Linear - up to ? over: ? Angles ? d. s. o.	TITLE: GROOVE FILL PIN TEST 4 VARIANT
DRAWN BY: J.ROUTH		
DATE: 16/11/98		
CHECKED BY: DATE:		DRAWING No. / ISSUE
APPROVED BY: DATE:		